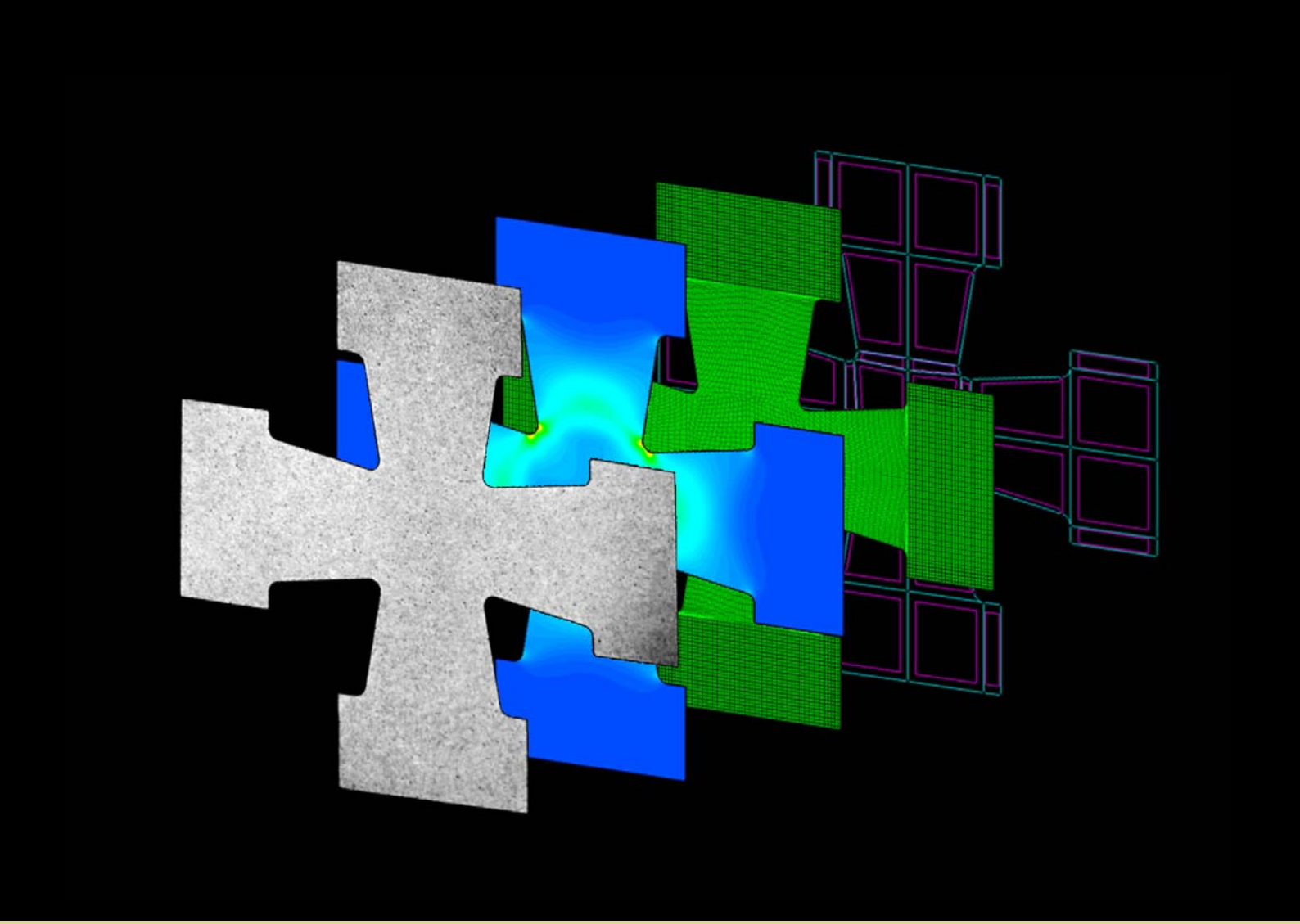

Pedro André Dias Prates

INVERSE METHODOLOGIES FOR IDENTIFYING CONSTITUTIVE PARAMETERS OF METAL SHEETS

Doctoral Thesis in Mechanical Engineering, specialisation in Production Technologies, supervised by Professor José Valdemar Bidarra Fernandes and Professor Marta Cristina Cardoso de Oliveira, submitted to the Department of Mechanical Engineering, Faculty of Sciences and Technology of the University of Coimbra.

September 2014

· U C ·

UNIVERSIDADE DE COIMBRA

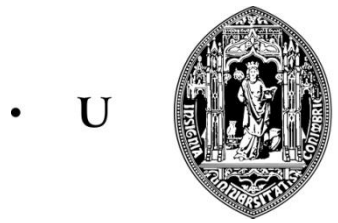

Inverse Methodologies for Identifying Constitutive Parameters of Metal Sheets

Dissertation presented to the Department of Mechanical Engineering of the University of Coimbra, as a requirement to obtain the doctoral degree in Mechanical Engineering, carried out under the supervision of Professor José Valdemar Bidarra Fernandes and Professor Marta Cristina Cardoso de Oliveira, University of Coimbra.

Pedro André Dias Prates

Department of Mechanical Engineering
Faculty of Sciences and Technology
University of Coimbra

Coimbra

2014

"A theory is something nobody believes,
except the person who made it, while
an experiment is something everybody believes,
except the person who made it."

Albert Einstein

[Erhard Scheibe, Between Rationalism and Empiricism: Selected Papers in the Philosophy of Physics, Edited by Brigitte Falkenburg, Springer - Verlag, New York Berlin Heidelberg, 2001, page 73 of 627 pages – ISBN 0-367-98520-4]

(Page intentionally left blank)

Acknowledgements

Above all, I want to express my deepest gratitude to my supervisors, Professor José Valdemar Fernandes and Professor Marta Oliveira, for their admirable guidance throughout my research, providing me the best of both their worlds. Their endless patience, enthusiastic encouragement, valuable insights, passionate discussions, readiness and friendship greatly contributed to the accomplishment of this thesis and, most significantly, the continuous improvement towards excellence.

I am also grateful for the support of the research unit in which this thesis was conducted, CEMUC - *Centro de Engenharia Mecânica da Universidade de Coimbra* (Centre for Mechanical Engineering of the University of Coimbra). My sincere thanks to all current and former colleagues from *Grupo de Tecnologia Experimental e Computacional (ECAT - Experimental and Computational Aided Technology*, currently named *Advanced Manufacturing Systems)*, for the encouragement, good mood and friendship.

To publishers, copyright holders and scientific journals editors, my acknowledgement for providing the licences allowing the print and electronic reuse of the papers published under the scope of this research.

Finally, I wish to thank my family and Elisabete, for their unconditional support, patience, encouragement and presence during this journey.

This thesis is sponsored by national funds from the Portuguese Foundation for Science and Technology (FCT) via the projects PTDC/EME–TME/113410/2009, PEst-C/EME/UI0285/2011 and PEst-C/EME/UI0285/2013; and by FEDER funds through the program COMPETE – Programa Operacional Factores de Competitividade, under the project CENTRO -07-0224 -FEDER -002001 (MT4MOBI). This thesis is also supported by a PhD studentship from FCT with reference SFRH/BD/68398/2010. All supports are gratefully acknowledged.

Abstract

The accurate modelling of the plastic behaviour of metal sheets is a fundamental aspect to be considered in the numerical simulation of sheet metal forming processes. The non-linear nature of the plastic behaviour of metal sheets makes their characterisation quite complex, depending on factors such as: (i) the constitutive model used to describe the material hardening and anisotropic behaviour; (ii) the experimental tests performed, comprising the sample geometry and testing conditions, and the analysis methodologies (iii) the strategy for identifying the constitutive parameters.

The main objective of this thesis is to establish inverse identification strategies for the parameters of constitutive models that describe the plastic behaviour of metal sheets. In this context, inverse strategies are proposed for the simultaneous identification of yield criteria and isotropic hardening laws parameters, from the results of a unique biaxial tensile test of a cruciform-shaped sample. The identification of the constitutive parameters is based on the following results of the cruciform tensile test: (i) the evolution of the load during the test, for both axes of the sample; the distributions of the (ii) equivalent strain and (iii) strain path, along the axes of the sample, at a given moment during the test. The optimisation procedures for identifying constitutive parameters are performed in a pre-specified sequence and use a gradient-based optimisation algorithm, the Levenberg-Marquardt method. The proposed inverse identification strategies are compared with two other: a classical strategy, making use of the results from simple mechanical tests, and an inverse strategy, making use of a unique cost function that includes all the constitutive parameters and different types of results of the cruciform test at once. The proposed identification approaches were shown to be competitive with these other strategies. Additionally, a strategy for the inverse identification of kinematic hardening parameters is outlined, allowing the full description of the plastic behaviour of metal sheets when coupled with the inverse strategy using the cruciform test. It uses load *versus* displacement results from the reverse shear test of a modified sample with a cylindrical fillet, along the axis, in order to confine the plastic deformation within the entire gauge section and allowing the easy and suitable numerical representation of the boundary conditions of the experimental shear test. All the inverse identification strategies were designed and their performance was assessed by means of finite element simulations, using the in-house code DD3IMP, devoted to sheet metal forming processes, developed and continuously updated in CEMUC.

Keywords Parameters Identification, Inverse Strategies, Yield Criterion, Isotropic Hardening Law, Kinematic Hardening Law, Metal Sheets.

Resumo

A modelação rigorosa do comportamento plástico de chapas metálicas é um aspeto fundamental a considerar na simulação numérica de processos de conformação de chapas metálicas. A natureza não-linear do comportamento plástico de chapas metálicas torna a sua caracterização bastante complexa, dependendo de fatores tais como: (i) o modelo constitutivo, usado para descrever o encruamento e comportamento anisotrópico do material; (ii) os ensaios experimentais realizados, englobando a geometria de provete e as condições de ensaio, e as metodologias de análise e (iii) a estratégia para identificação de parâmetros constitutivos.

O principal objetivo desta tese é estabelecer uma estratégia de identificação inversa dos parâmetros dos modelos constitutivos, que descrevem o comportamento plástico de chapas metálicas. Neste contexto, são propostas estratégias inversas para identificação simultânea dos parâmetros de critérios de plasticidade e de leis de encruamento isotrópico, a partir dos resultados de um único ensaio de tração biaxial de um provete cruciforme. A identificação dos parâmetros constitutivos baseia-se nos seguintes resultados do ensaio cruciforme: (i) a evolução da força durante o ensaio, para ambos os eixos do provete; as distribuições da (ii) deformação equivalente e (iii) da trajetória de deformação, ao longo dos eixos do provete, num dado momento do ensaio. Os procedimentos de otimização para a identificação de parâmetros constitutivos são realizados numa sequência pré-determinada e recorre a um algoritmo de otimização baseado no gradiente, o método de Levenberg-Marquardt. As estratégias propostas, de identificação inversa, são comparadas com outras duas estratégias de identificação de parâmetros: uma clássica, que utiliza os resultados de ensaios mecânicos simples, e uma estratégia inversa, que recorre a uma única função de custo incluindo todos os parâmetros constitutivos e diferentes tipos de resultados do ensaio cruciforme. A abordagem de identificação proposta mostrou ser competitiva com estas duas estratégias. Além disso, delineou-se uma estratégia para a identificação inversa de parâmetros de encruamento cinemático, permitindo a descrição completa do comportamento plástico de chapas metálicas quando associada com a estratégia inversa que recorre ao ensaio cruciforme. Utiliza resultados de força *versus* deslocamento das amarras de um provete de corte modificado, com um entalhe cilíndrico paralelo ao eixo, de modo a confinar a deformação plástica no entalhe e permitir a representação numérica fácil e adequada das condições de fronteira do provete de corte experimental. Todas as estratégias de identificação inversas foram concebidas e testadas com recurso a simulações por elementos finitos utilizando o código DD3IMP, dedicado a processos de conformação de chapas metálicas, desenvolvido e continuamente atualizado no CEMUC.

Palavras-chave: Identificação de Parâmetros, Estratégias Inversas, Critério de Plasticidade, Lei de Encruamento Isotrópico, Lei de Encruamento Cinemático, Chapas Metálicas.

Contents

List of Figures

(Page intentionally left blank)

List of Tables

(Page intentionally left blank)

Acronyms and Symbology

Acronyms

BCC	Body Centred Cubic
CB2001	Cazacu-Barlat 2001 yield criterion
CEMUC	Centro de Engenharia Mecânica da Universidade de Coimbra
DD3IMP	Deep-Drawing 3D IMPlicit code
DIC	Digital Image Correlation
DOE	Design of Experiments
Drucker+L	Drucker yield criterion with the linear transformation **L**
FCC	Face Centred Cubic
FE	Finite Element
FEA	Finite Element Analysis
FEMU	Finite Element Model Updating method
Hill'48	Hill 1948 yield criterion
IPE	Isotropic Plasticity Equivalent stress space concept
KB'93	Karafillis and Boyce yield criterion
RD	Rolling Direction (Axis of orthotropy in a rolled metal sheet)
TD	Transverse Direction (Axis of orthotropy in a rolled metal sheet)
ND	Normal Direction (Axis of orthotropy in a rolled metal sheet)
RSM	Response Surface Methodology
VFM	Virtual Fields Method
Yld'91	Barlat 1991 yield criterion

Symbology

α	Parameters of the yield criterion; weighting parameter for the combined isotropic hardening laws: Swift - Voce and Swift - Hockett & Sherby
β	Parameters of the hardening law
$\bar{\varepsilon}^{p}$	Equivalent plastic strain
ε_0	Parameter of isotropic hardening laws: Swift, Ghosh and Fernandes
ε_p	Equivalent pre-strain value for the Fernandes isotropic hardening law
$\boldsymbol{\varepsilon}$	Strain tensor
$\boldsymbol{\varepsilon}^{p}$	Plastic strain tensor
λ	Stabilising parameter for the Levenberg-Marquardt algorithm
$\bar{\sigma}$	Equivalent stress
σ_0	Yield stress determined from the uniaxial tensile test for the RD
$\boldsymbol{\sigma}$	Cauchy stress tensor
$\boldsymbol{\sigma}'$	Deviatoric Cauchy stress tensor
τ_0	Critical value for the shear stress
Φ_1, Φ_2	Functions of the KB'93 yield criterion
a	Parameter of the Hockett & Sherby kinematic hardening law
$\mathbf{A}$	Vector of constitutive parameters
$a_1,...,a_6$	Anisotropy parameters of the CB2001 yield criterion
$b_1,...,b_{11}$	Anisotropy parameters of the CB2001 yield criterion
c	Isotropic weight parameter of yield criteria: Drucker, Drucker+L and CB2001
C	Parameter of the Ghosh isotropic hardening law
$C_1,...,C_6$	Anisotropy parameters of the yield criteria: Drucker+L, KB'93 and Yld'91

C_{X}	Parameter of kinematic hardening laws: Armstrong & Frederick and Chaboche
C_{Y}	Parameter of isotropic hardening laws: Voce and Hockett & Sherby
F	Parameter of the Hill'48 yield criterion
$F(\mathbf{A})$	Cost function
$\mathcal{F}$	Function defining the yielding condition
g	Parameter of the Fernandes isotropic hardening law
G	Parameter of the Hill'48 yield criterion
h	Parameter of the Fernandes isotropic hardening law
H	Parameter of the Hill'48 yield criterion
J_2	Second invariant of the deviatoric stress tensor, $\boldsymbol{\sigma}'$
J_3	Third invariant of the deviatoric stress tensor, $\boldsymbol{\sigma}'$
J_2^0	Generalised second invariant of the deviatoric stress tensor, $\boldsymbol{\sigma}'$
J_3^0	Generalised third invariant of the deviatoric stress tensor, $\boldsymbol{\sigma}'$
$\mathbf{J}$	Jacobian matrix of Gauss-Newton and Levenberg-Marquardt algorithms
k	Isotropic exponent of the KB'93 yield criterion
K	Parameter of isotropic hardening laws: Hollomon, Ludwick, Swift, Ludwigson, Ghosh and Fernandes
K_1	Parameter of the Ludwigson isotropic hardening law
L	Parameter of the Hill'48 yield criterion
$\mathbf{L}$	Linear transformation tensor defining the IPE stress state
m	Isotropic exponent for yield criteria: Hosford and Yld'91; total number of experiments
M	Parameter of the Hill'48 yield criterion
n	Parameter of isotropic hardening laws: Hollomon, Ludwick, Swift, Ludwigson, Ghosh and Fernandes; total number of measurement points
n_1	Parameter of the Ludwigson isotropic hardening law
n_p	Total number of constitutive parameters
n_r	Dimension of the vector of residuals

N	Parameter of the Hill'48 yield criterion
N_t	Total number of time steps
$\mathbf{P}^{\mathrm{Exp}}$	Vector of experimental load results
$\mathbf{P}^{\mathrm{Num}}$	Vector of numerically predicted load results
q_{P}	Parameter of the Prager kinematic hardening law
q_{Z}	Parameter of the Ziegler kinematic hardening law
r_0	Anisotropy coefficient from the uniaxial tensile test at RD
r_{45}	Anisotropy coefficient from the uniaxial tensile test at 45° with RD
r_{90}	Anisotropy coefficient from the uniaxial tensile test at TD
$\mathbf{r}(\mathbf{A})$	Vector of residuals between numerically predicted and the experimental results
s_i	Residual scale factor
$\mathbf{s}$	IPE stress state
$\mathbf{u}^{\mathrm{Exp}}$	Vector of experimental results
$\mathbf{u}^{\mathrm{Num}}$	Vector of numerically predicted results
$\mathbf{w}$	Vector of the cost function weighting factors
$\mathbf{W}$	Vector of weighting factors for Gauss-Newton and Levenberg-Marquardt algorithms
X_{Sat}	Parameter of the Armstrong & Frederick kinematic hardening law
$\mathbf{X}'$	Deviatoric back-stress tensor
Y	Flow stress; yield stress
Y_0	Yield stress; initial yield stress
Y_{Sat}	Parameter of kinematic hardening laws: Voce and Hockett & Sherby

Chapter 1

General Introduction

This chapter concerns the motivation for investigating the topics addressed in the thesis. The key objectives and achievements in the context of the identification of constitutive parameters of metal sheets are highlighted and the outline of the text is presented.

(Page intentionally left blank)

1.1. Motivation

Finite Element Analysis (FEA) is now a well-established computational tool in industry for the optimisation of sheet metal forming processes. The accurate modelling of these processes is a complex task due to the nonlinearities involved, such as those associated with: (i) the kinematics of large deformations; (ii) the contact between the sheet and the tools and (iii) the plastic behaviour of the metal sheet.

The description of the plastic behaviour of metal sheets is usually performed using phenomenological constitutive models. In this context, the development of new metallic alloys and their increasingly widespread use in the automotive and aeronautical industries has encouraged the development of more reliable models, with increasing flexibility, associated with a larger number of parameters to identify. The classical identification strategies for the constitutive parameters make use of a large number of standardised mechanical tests, with well-defined geometry and loading conditions, such that homogeneous stress and strain distribution develop in the region of interest. However, sheet metal forming processes are carried out under strongly non-homogeneous stresses and strains fields. Therefore, limiting the characterisation of the mechanical behaviour of metal sheets to a restricted number of tests with linear strain paths and homogeneous deformation can lead to a somewhat incomplete characterisation of the overall plastic behaviour of the material.

Recent developments and accessibility of optical full-field measurement techniques, such as Digital Image Correlation (DIC) technique coupled with FEA, make the inverse identification strategies a common current place. The full-field measurements allow the acquisition of enriched information from mechanical tests, such as displacement and strain fields. This makes it possible to attenuate the constraints on the geometry and loading conditions of the mechanical tests used for identification of materials parameters, so that non-homogeneous stress and strain distributions can be developed in the region of interest. In this sense, the identification of constitutive parameters from non-homogeneous strain fields and complex loading conditions provides a more reliable description of the material behaviour during real sheet metal forming processes. In such complex mechanical tests, it is no longer possible to identify the constitutive parameters based on simple assumptions on the stress and/or strain states, as in the classical identification strategies. Instead, a finite element model of the mechanical test is established and cost functions are defined to minimise the gap between numerical and experimental

results of the mechanical test, which demands efficient optimisation algorithms. However, the efficiency of any inverse identification strategy directly depends on the information contained by the objective function. In the context of constitutive parameters identification, this is related with the type of experimental results included (e.g. loads, displacements, strains) but also with the strain paths and levels of deformation attained by the experimental test. It turns out that there is no consensus about the experimental tests (sample geometry and loading conditions), the cost functions and the optimisation procedure that will lead to accurate constitutive parameters identification. Also, a major obstacle to the widespread use of advanced constitutive models in industrial simulations seems to result from the lack of an efficiency strategy for parameters identification. In this sense, the developed strategy must be simple, from an experimental point of view, and allow evaluating to what extent the selected constitutive model allows to perfectly describe the behaviour of a given material.

1.2. Objectives and Achievements

The aim of this thesis is to establish efficient inverse strategies for identifying the parameters of complex constitutive models, which describe the plastic behaviour of metal sheets. It is intended resorting to mechanical tests leading to non-uniform strain and stress states, as alternative to the classical identification strategies. Pushing this idea forward, the objectives were to retrieve the plastic constitutive parameters from the minimum number of tests (a unique test, if possible) with convenient design in order to induce inhomogeneous deformation and multiaxial strain paths, including strain path changes. This presumes the use of a large amount of data, i.e. measured quantities, such as loads, displacements and strains, provided by classical measurement devices and optical full-field multi-local measurement technique. The idea is to design mechanical tests (samples geometry and loading conditions) and explore the above-mentioned data in the framework of an inverse analysis methodology. This methodology combines experimental results, finite element simulations and a minimisation strategy, and takes into account the distinguishability and uniqueness of the constitutive models parameters. To achieve this purpose, a widespread computational direct analysis must be performed considering different sample geometries and loading conditions. The selected tests should cover, as far as possible, a wide range of in-plane stress states, from pure shear to balanced biaxial stretching, and out-of-plane stress states mainly considering shear normal to the sheet plane. Also, the test should allow conducting strain path changes, such as orthogonal or reversal.

In the above context, inverse strategies are proposed for the simultaneous identification of parameters of complex yield criteria and isotropic hardening laws,

from the results of a unique biaxial tensile test of a cruciform-shaped sample. The identification of the constitutive parameters is performed in a pre-specified sequence, minimising firstly the results of load *versus* displacement and then the equivalent strain and strain path distributions along the axes of the sample. This sequence was established from a forward analysis study on the sensitivity of results of the test to variations of the constitutive parameters. The results of the proposed strategies are compared with classical identification strategies and with recently proposed inverse identification strategies that make use of a unique cost function, which includes all constitutive parameters and different type of results. The possibility of simultaneously identifying the parameters of kinematic hardening laws from the cruciform tensile test was also explored, although this exploratory work is not included this document. For this purpose, a number of sequential loading combinations of the cruciform sample were studied, so that strain path changes occur in the sample. The results of these sequential loading combinations, composed of asymmetric biaxial tensions, indicate that none is sensitive enough to the parameters of the kinematic law. Alternatively, it is established an inverse strategy for identifying the parameters of the kinematic hardening law, from the results of a unique reverse shear test. This strategy, coupled with the above mentioned for identification of the parameters of the yield criteria and isotropic hardening laws, allows achieving the full plastic description of the material behaviour, using only two mechanical tests.

The numerical simulations were carried out with the in-house finite element code DD3IMP, developed for simulating sheet metal forming processes. This program is the result of the research activity carried out in the research group for Advanced Manufacturing Systems, of the Centre for Mechanical Engineering of the University of Coimbra (CEMUC).

1.3. Thesis Outline

Following this general introduction, the thesis consists of two main parts. The first part contains the literature review and is made up of two chapters: Chapter 2 addresses constitutive modelling, i.e. some relevant yield criteria, isotropic and kinematic hardening laws are described; Chapter 3 focuses on strategies for the parameter identification of constitutive models, with emphasis on inverse identification strategies. The second part contains the innovative research conducted within the framework of this thesis and is composed by two chapters: Chapter 4 is a collection of four papers and Chapter 5 presents the conclusions and perspectives. Details regarding the modelling of the cruciform sample are presented in Appendix.

(Page intentionally left blank)

Chapter 2

Constitutive Modelling

This chapter provides an overview of the literature on the modelling of the plastic behaviour of metal sheets. In the first subchapter, a brief introduction to the most common constitutive models is presented. The description of some yield criteria and hardening laws is made in the second and third subchapters, respectively. Finally, the fourth subchapter contains the closing remarks and some considerations on the use of constitutive models in the sheet metal forming industry.

(Page intentionally left blank)

2.1. Introduction

The accurate modelling of the plastic behaviour of metal sheets is a fundamental aspect to be considered in the numerical simulation of sheet metal forming processes. For this reason constitutive models with increased complexity have been developed to accurately predict the onset and evolution of the plastic deformation in a deformable body undergoing a general state of stress. A phenomenological constitutive model is typically a combination of the following components:

- Yield criterion that describes the yield surface of the material in a multidimensional stress space. The metal sheets are usually assumed as orthotropic, with invariant anisotropy during plastic deformation.
- Hardening laws that express the evolution of the yield surface during plastic deformation. The isotropic hardening law refers to the homothetic expansion of the yield surface while the kinematic hardening law describes its translation in the stress space.
- Flow rule, to establish a relationship between the stress state and the plastic strain increment; typically, an associate flow rule is adopted, as performed in this work, although some exceptions can be found in literature (see e.g. [1]).

The general representation of a constitutive model can be described through a function $\mathcal{F}$:

$$\mathcal{F}(\boldsymbol{\sigma}' - \mathbf{X}', \bar{\varepsilon}^{\mathrm{p}}, \alpha, \beta) = \bar{\sigma}(\boldsymbol{\sigma}' - \mathbf{X}', \alpha) - Y(\bar{\varepsilon}^{\mathrm{p}}, \beta), \tag{2.1}$$

where $\bar{\sigma}(\boldsymbol{\sigma}' - \mathbf{X}', \alpha)$ is the equivalent stress defined by a given yield criterion, and $Y(\bar{\varepsilon}^{\mathrm{p}}, \beta)$ is the hardening law that represents the evolution of the yield stress during the deformation. The equivalent stress, $\bar{\sigma}(\boldsymbol{\sigma}' - \mathbf{X}', \alpha) = \bar{\sigma}$, is a function of the effective stress tensor, $(\boldsymbol{\sigma}' - \mathbf{X}')$, that includes the parameters of the yield criterion, α, for describing the anisotropy ($\boldsymbol{\sigma}'$ and $\mathbf{X}'$ are the deviatoric Cauchy stress and the deviatoric back-stress tensors, respectively) and $Y(\bar{\varepsilon}^{\mathrm{p}}, \beta) = Y$ is a function of the equivalent plastic strain, $\bar{\varepsilon}^{\mathrm{p}}$, in which the parameters are represented by β. The yielding is defined based on the function $\mathcal{F}$ of equation Eq. (2.1) and can be written:

$$\mathcal{F} = \bar{\sigma} - Y = 0 \Rightarrow \bar{\sigma} = Y. \tag{2.2}$$

If $\bar{\sigma} < Y$, the stress state of the material remains inside the yield surface and only elastic deformation occurs. When plastic deformation occurs, the associated flow rule states that the increment of the plastic strain tensor is normal to the yield surface, for a stress state such that $\bar{\sigma} = Y$. The normality condition, defined by the associated

flow rule, assumes that the increment of the plastic strain tensor is normal to the yield surface and is expressed:

$$\mathrm{d}\boldsymbol{\varepsilon}^{\mathrm{p}} = \mathrm{d}\lambda \frac{\partial \bar{\sigma}(\boldsymbol{\sigma}' - \mathbf{X}')}{\partial(\boldsymbol{\sigma}' - \mathbf{X}')}, \tag{2.3}$$

where $\mathrm{d}\boldsymbol{\varepsilon}^{\mathrm{p}}$ is the increment of the plastic strain tensor, $\mathrm{d}\lambda$ is a scalar multiplier that is equal to the increment of equivalent plastic strain and $\bar{\sigma}(\boldsymbol{\sigma}' - \mathbf{X}') = \bar{\sigma}$ is the equivalent stress function, representing the plastic potential.

The next subchapters present examples of relevant yield criteria (see 2.2. Yield Criteria) and hardening laws (see 2.3. Hardening Laws) found in literature.

2.2. Yield Criteria

The yield criteria allow characterising the state of stress by a scalar, whatever the involved stress path, simple or complex. In this context, several yield criteria have been proposed that allow describing the yielding behaviour of materials under a general state of stress. Tresca [2] and von Mises [3] developed pioneering yield criteria, based on the following general statements [4]:

(i) The state of stress at a point can be completely described by the magnitude and orientation of the principal stresses. For isotropic materials, the orientation of the principal axes of stress does not affect the yielding.

(ii) Hydrostatic states of stress do not generate plastic deformation of metallic materials. Therefore, a yield criterion should be formulated based not on the absolute value of the principal stresses, but rather on the magnitude of the differences between the principal stresses. This assumption implies that the plastic deformation is caused by the deviatoric component of the stress tensor.

In the following, a restricted number of three-dimensional (3D) yield criteria are described (the in-house code DD3IMP has only 3D criteria implemented). Actually, there is an extensive list of literature reviews on the subject (e.g [5 - 8]). In the following subchapter only the criteria that are somehow related to the work of this thesis are mentioned, with one exception, which emphasizes the increasing number of parameters associated with recent models.

2.2.1. Isotropic yield criteria

Tresca yield criterion [2] is based on the statement that, in metallic materials, the yielding occurs when the shear stress, in a plane and direction (slip system), reaches a critical value, τ_0, to ensure the plastic deformation by promoting slip of dislocations. Under this condition and assuming that, in polycrystalline metallic materials, there is

always a slip system where the maximum shear stress occurs, whatever the state of stress, the Tresca yield criterion is written:

$$\max\left\{\left|\sigma_1-\sigma_2\right|,\left|\sigma_2-\sigma_3\right|,\left|\sigma_3-\sigma_1\right|\right\}=2\tau_0\,, \tag{2.4}$$

where σ_1, σ_2 and σ_3 are the Cauchy principal stresses. The value of τ_0 can be determined using the shear test. Eq. (2.4) can also be expressed as a function of the yield stress in uniaxial tension, σ_0 (the most commonly used). In fact, in uniaxial tension, the tensile stress is twice the maximum shear stress and so σ_0 is equal to $2\tau_0$, and Eq. (2.4) becomes:

$$\max\left\{\left|\sigma_1-\sigma_2\right|,\left|\sigma_2-\sigma_3\right|,\left|\sigma_3-\sigma_1\right|\right\}=\sigma_0\,. \tag{2.5}$$

The von Mises yield criterion [3] states that the yielding occurs when the elastic energy of distortion reaches a critical value. Two other ways of looking at the same outcome are: (i) von Mises criterion is represented by a cylinder that circumscribes the regular hexagonal Tresca prism, in the principal stresses space; (ii) yielding occurs when the second deviatoric stress invariant (or maximum octahedral shear stress) reaches a critical value. Under these conditions, von Mises criterion can be written:

$$(\sigma_1-\sigma_2)^2+(\sigma_2-\sigma_3)^2+(\sigma_1-\sigma_3)^2=2{\sigma_0}^2\,. \tag{2.6}$$

For the 0xyz system, Eq. (2.6) is written:

$$(\sigma_{yy}-\sigma_{zz})^2+(\sigma_{zz}-\sigma_{xx})^2+(\sigma_{xx}-\sigma_{yy})^2+6\tau_{yz}^2+6\tau_{xz}^2+6\tau_{xy}^2=2{\sigma_0}^2\,, \tag{2.7}$$

where σ_{xx}, σ_{yy}, σ_{zz}, τ_{xy}, τ_{xz} and τ_{yz} are the components of Cauchy stress tensor.
At a given moment of the deformation, the yield stress is Y and Eqs. (2.6) and (2.7) can be written, respectively:

$$(\sigma_1-\sigma_2)^2+(\sigma_2-\sigma_3)^2+(\sigma_1-\sigma_3)^2=2Y^2\,, \tag{2.8}$$

$$(\sigma_{yy}-\sigma_{zz})^2+(\sigma_{zz}-\sigma_{xx})^2+(\sigma_{xx}-\sigma_{yy})^2+6\tau_{yz}^2+6\tau_{xz}^2+6\tau_{xy}^2=2Y^2\,. \tag{2.9}$$

Figure 2.1 shows the schematic representation of Tresca and von Mises yield criteria in the plane of principal stresses (σ_1; σ_2). Tresca criterion is represented by a hexagonal-shaped surface that is inside the elliptical surface described by von Mises equation. Tresca yield criterion predicts the yielding earlier than von Mises criterion, except for simple tension and compression, and for equibiaxial stress states, where the yielding occurs in the same way for both criteria.

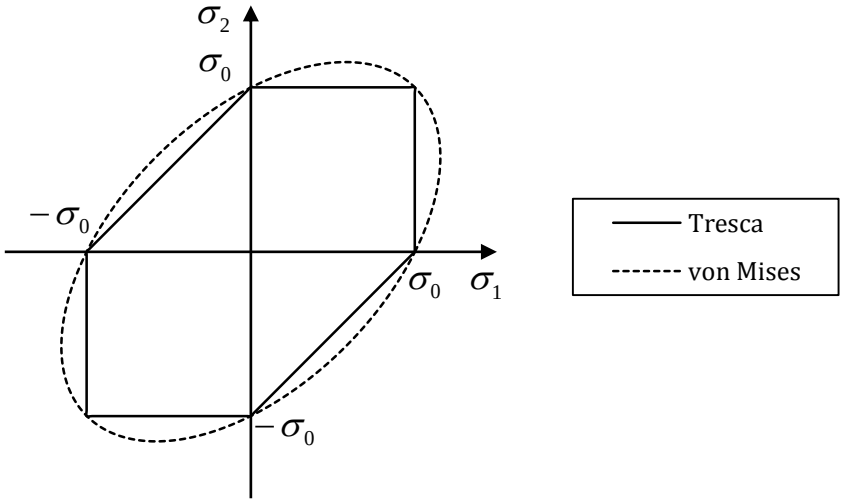

Figure 2.1. Representation of Tresca and von Mises yield surfaces in the (σ_1 ; σ_2) plane.

Further developments concerning the isotropic yield criteria were performed by Drucker [9] and Hosford [10]. Drucker [9] proposed a yield criterion taking into account the second and third invariants of the deviatoric stress tensor, J_2 and J_3, respectively:

$$J_2^3 + cJ_3^2 = 27\left(\frac{Y}{3}\right)^6, \tag{2.10}$$

where c is a weight parameter, ranging from -3.375 to 2.25 to ensure the convexity of the yield surface. Otherwise, a non-convex yield surface, allowing negative plastic work, could be generated, which violates the Drucker postulate that ensures the stability of plastic deformation coupled to the normality condition [11].

The equations for J_2 and J_3 in function of the Cauchy stress components are, respectively:

$$J_2 = \frac{1}{6}\left[(\sigma_{xx}-\sigma_{yy})^2+(\sigma_{yy}-\sigma_{zz})^2+(\sigma_{xx}-\sigma_{zz})^2\right]+\tau_{xy}^2+\tau_{xz}^2+\tau_{yz}^2, \tag{2.11}$$

$$\begin{aligned} J_3 = {} & \frac{2}{27}\left[\sigma_{xx}^3+\sigma_{yy}^3+\sigma_{zz}^3\right]+\frac{4}{9}\sigma_{xx}\sigma_{yy}\sigma_{zz}+2\tau_{xy}\tau_{yz}\tau_{xz} \\ & -\frac{1}{9}\left[(\sigma_{yy}+\sigma_{zz})\sigma_{xx}^2+(\sigma_{zz}+\sigma_{xx})\sigma_{yy}^2+(\sigma_{xx}+\sigma_{yy})\sigma_{zz}^2\right] \\ & -\frac{1}{3}\left[\tau_{xz}^2(2\sigma_{yy}-\sigma_{zz}-\sigma_{xx})+\tau_{xy}^2(2\sigma_{zz}-\sigma_{yy}-\sigma_{xx})+\tau_{yz}^2(2\sigma_{xx}-\sigma_{yy}-\sigma_{zz})\right] \end{aligned} \tag{2.12}$$

This yield criterion allows modelling a wide range of isotropic surfaces, from near Tresca surface (for $c = 2.25$) to von Mises surface (for $c = 0$) and from this surface to outside the von Mises surface (for $c = -3.375$), as shown in Figure 2.2 for the plane $(\sigma_1;\ \sigma_2)$.

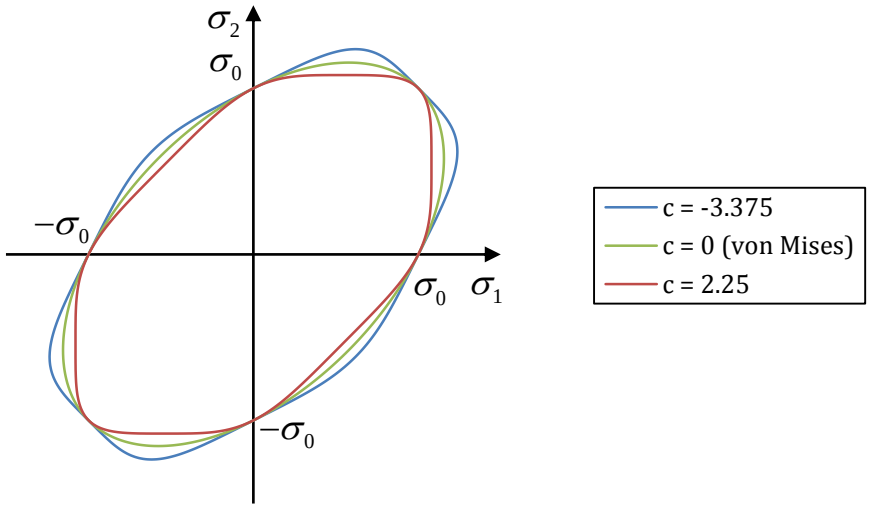

Figure 2.2.Representation of Drucker yield surfaces in the (σ_1 ; σ_2) plane, for c values equal to -3.375, 0 (von Mises surface) and 2.25.

Hosford yield criterion [10] is a reformulation of von Mises yield criterion, where the square of each part of the sum in Eq. (2.8) is replaced by an exponent m, as follows:

$$(\sigma_1-\sigma_2)^m+(\sigma_2-\sigma_3)^m+(\sigma_1-\sigma_3)^m=2Y^m \tag{2.13}$$

The exponent m can take any real value above unity. This yield criterion allows modelling isotropic surfaces ranging from von Mises surface (for $m=2$) to Tresca surface (for $m=+\infty$). Hosford proposes values of m depending on the crystallographic structure of the material, with m equal to 6 and 8, for metals with BCC (body centred cubic) and FCC (face centred cubic) structures, respectively [10]. Figure 2.3 shows the yield surfaces in the plane (σ_1 ; σ_2) for m values equal to 2 (von Mises surface), 6, 8 and +∞ (Tresca surface).

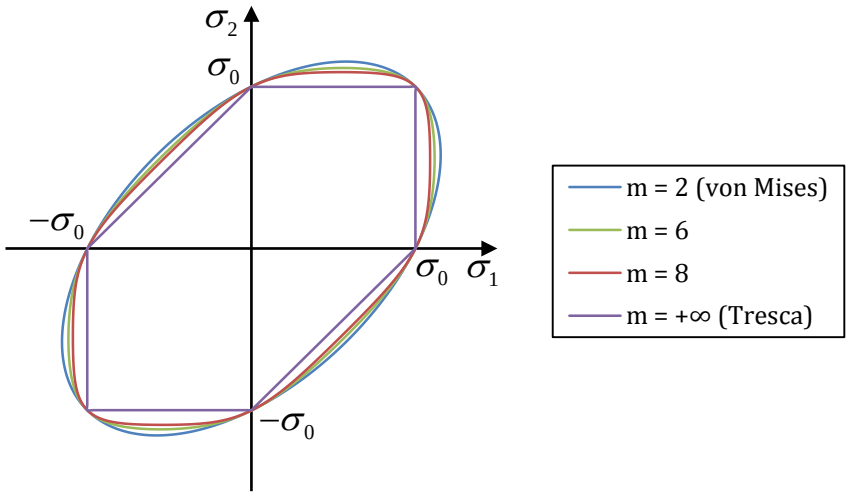

Figure 2.3. Representation of Hosford yield surfaces in the (σ_1 ; σ_2) plane, for m values equal to 2 (von Mises surface), 6, 8 and +∞ (Tresca surface).

2.2.2. Anisotropic yield criteria

The yield criteria above described were developed under the assumption of isotropic plastic behaviour of the material. However, such yield criteria are inadequate for describing the behaviour of metal sheets produced by rolling. This process generally leads to favouring certain crystallographic orientations of the grains within the metal sheet (crystallographic texture), which causes anisotropy [12]. Consequently, the yielding of materials becomes orientation-dependent, in contrast to isotropic materials. Since the sheet metal forming processes are carried out under multiaxial solicitations, the accurate modelling of anisotropy is of paramount importance.

With high incidence in the last decades, it has been witnessed the emergence of anisotropic yield criteria with an increasing number of material parameters. They provide the flexibility required for accurately modelling the plastic behaviour of advanced metallic alloys, which are frequently used in automotive and aeronautical industries. For deriving such yield criteria several approaches have been used:

- high-order polynomial yield criteria (e.g. [13, 14]);
- yield criteria based on the generalisation to anisotropy of the second and third invariants of the deviatoric stress tensor, J_2 and J_3, respectively(e.g. [15]);
- yield criteria based on one or more isotropic yield functions, using the linear Isotropic Plasticity Equivalent (IPE) stress space concept (e.g. [15 - 21]);
- yield criteria constructed as a weighted sum of an anisotropic yield criterion (e.g. [19]);
- yield criteria able to model the tension-compression asymmetry, particularly devoted to specific magnesium and titanium alloys (e.g. [15, 18, 22]);
- yield criteria able to model kinematic hardening (e.g. [23]);
- yield criteria based on the interpolation of second-order Bézier curves (e.g. [24]).

The anisotropy of rolled metal sheets is orthotropic, i.e. has three symmetry planes, normal to each other. The intersections of these planes are known as principal axes of orthotropy. This axis system correspond to the rolling, transverse and normal to the sheet plane directions, as illustrated in Figure 2.4.

In the following, some anisotropic yield criteria are presented, from classical ones, such as Hill'48 yield criterion [25], to more recent developments, such as Yoshida yield criterion [19].

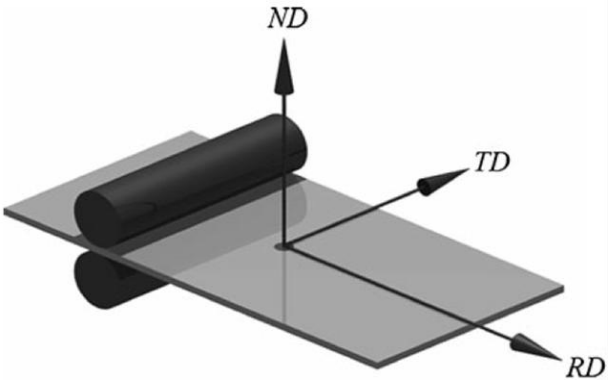

Figure 2.4. Axes of orthotropy in a rolled metal sheet: RD - rolling direction, TD - transverse direction, and ND - normal direction [7].

Hill'48 is one of the most widely used anisotropic yield criteria, due to its simplicity. Hill [25] deduced this simple yield criterion from von Mises yield criterion (Eq. (2.9)), multiplying the parts of the sum in the first member of this criterion by factors, the so-called anisotropy parameters. This leads to the following formulation:

$$F(\sigma_{yy}-\sigma_{zz})^2+G(\sigma_{zz}-\sigma_{xx})^2+H(\sigma_{xx}-\sigma_{yy})^2+2L\tau_{yz}^2+2M\tau_{xz}^2+2N\tau_{xy}^2=Y^2, \qquad (2.14)$$

where σ_{xx}, σ_{yy}, σ_{zz}, τ_{xy}, τ_{xz} and τ_{yz} are the components of the Cauchy stress tensor, in the principal axes of orthotropy, and F, G, H, L, M and N are the anisotropy parameters of the material. In this context, von Mises yield criterion is retrieved when the relationship between the anisotropy parameters is $F=G=H=L/3=M/3=N/3=0.5$. The identification of the F, G, H, L, M and N anisotropic parameters can be performed using at least 6 (as many as the parameters of anisotropy) or more different types of experimental results. However, the identification of the anisotropic parameters L and M is difficult due to dimensional restrictions of the sheets, since requires performing tests with shear components τ_{yz} and τ_{xz}, respectively. Classically, the easy and prompt identification of the parameters F, G, H and N uses three uniaxial tensile tests at 0°, 45° and 90° with the rolling direction, to determine the anisotropy coefficients r_0, r_{45} and r_{90}, respectively, and at least the yield stress in the rolling direction, σ_0, for example. For a more extensive material characterisation, additional tests are often used, such as biaxial tension, shear and compression normal to the sheet plane. To overcome the difficulty for identifying L and M, their values are typically assumed as in isotropy, i.e. $L=M=1.5$, although other conditions for the values of these parameters were proposed [26]. These conditions for the parameters associated with the stress components τ_{yz} and τ_{xz}, are also generally adopted, whatever the anisotropic yield criteria.

The advantage of using Hill'48 yield criterion, regarding others more complex mentioned below comes from its simple formulation and easy implementation in numerical simulation codes. The small number of experimental tests needed for

identifying the anisotropy parameters is quite convenient in industrial laboratories. However, the major drawback of Hill'48 criterion is the lack of flexibility to describe the plastic behaviour of some materials under biaxial stress states, for which the anisotropy coefficient is lower than 1, as in case of some aluminium alloys [7].

To overcome the limitations of Hill'48 criterion, a class of anisotropic yield criteria based on the extension of isotropic yield criteria to anisotropy was developed. This is generally performed through a linear transformation of the Cauchy stress tensor, given rise to an isotropic plasticity equivalent (IPE) stress state, which enters into isotropic yield criteria [6]. This leads to more flexible yield surfaces, containing isotropic and anisotropic parameters. Examples of yield criteria using an IPE stress state, developed by Barlat et al. [20], Karafillis & Boyce [21] and Cazacu & Barlat [15] are described below.

The yield criterion proposed by Barlat et al. [20], now referred as Yld'91 criterion, is the extension of Hosford isotropic criterion [10] to anisotropy, using an IPE stress state, $\mathbf{s}$, as follows:

$$\mathbf{s} = \mathbf{L} : \boldsymbol{\sigma}, \tag{2.15}$$

where $\mathbf{L}$ is the linear transformation operator proposed by Barlat et al. [20]:

$$\mathbf{L} = \begin{bmatrix} (C_2+C_3)/3 & -C_3/3 & -C_2/3 & 0 & 0 & 0 \\ -C_3/3 & (C_3+C_1)/3 & -C_1/3 & 0 & 0 & 0 \\ -C_2/3 & -C_1/3 & (C_1+C_2)/3 & 0 & 0 & 0 \\ 0 & 0 & 0 & C_4 & 0 & 0 \\ 0 & 0 & 0 & 0 & C_5 & 0 \\ 0 & 0 & 0 & 0 & 0 & C_6 \end{bmatrix}, \tag{2.16}$$

in which C_i, are the anisotropy parameters, with $i = 1,...,6$; C_i is equal to 1 for the isotropy condition. Then, Yld'91 yield criterion is written:

$$|s_1 - s_2|^m + |s_2 - s_3|^m + |s_3 - s_1|^m = 2Y^m, \tag{2.17}$$

where s_1, s_2 and s_3 are the principal IPE stress state components. Exponent m has the same meaning as in Hosford criterion; also, the convexity of this criterion is guaranteed for $m \geq 1$. Moreover, Hill'48 criterion is retrieved when $m = 2$.

Karafillis & Boyce yield criterion [21], now referred to as KB'93 criterion, is a generalisation of Yld'91, using the IPE stress state for describing the anisotropy as follows:

$$(1-a)\Phi_1 + a\frac{3^{2k}}{2^{2k-1}+1}\Phi_2 = 2Y^{2k}, \tag{2.18}$$

where a is a weighting parameter, ranging between 0 and 1; $2k$ is an isotropic exponent, with k integer and positive to ensure the convexity of the yield surface and Φ_1 and Φ_2 are defined:

$$\Phi_1 = (s_1 - s_2)^{2k} + (s_2 - s_3)^{2k} + (s_3 - s_1)^{2k}, \tag{2.19}$$

$$\Phi_2 = s_1^{2k} + s_2^{2k} + s_3^{2k}. \tag{2.20}$$

Any yield surface described by Eq. (2.18) lies between the lower bound of the Φ_1 function, for $a = 0$ (for the Φ_1 function the lower bound occurs for $k = +\infty$ - Tresca yield surface - and upper bound for $k = 1$ - von Mises yield surface) and the upper bound of Φ_2 function for $a = 1$ (for the Φ_2 function the lower bound occurs for $k = 1$ - von Mises yield surface - and upper bound for $k = +\infty$ - outside von Mises yield surface). Karafillis & Boyce [21] proposed to set k equal to a high enough value ($k =$ 15), which enables approximately describing any surface between the lower bound and the upper bound defined by Eq. (2.18), varying only the value of the weighting factor *a*.

Figure 2.5 shows the yield surfaces in the plane (σ_1; σ_2) for $k = 15$ and a values equal to 0, 0.97 (close to von Mises surface, also shown in the figure) and 1.

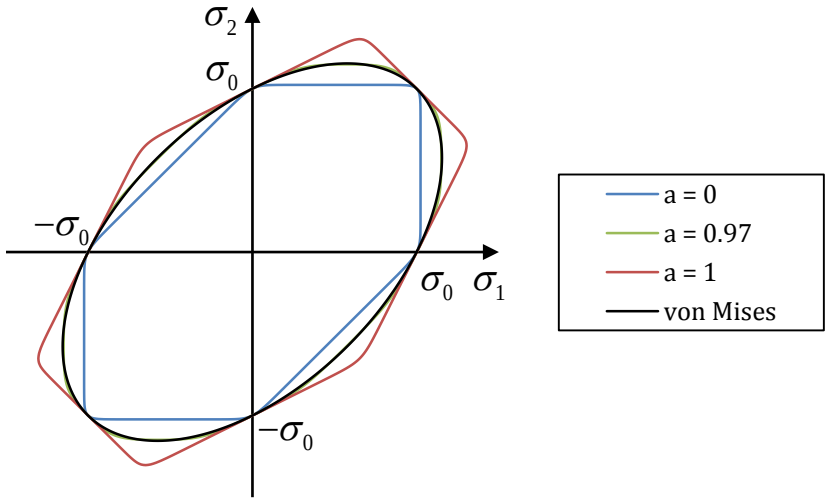

Figure 2.5. Representation of KB'93 yield surfaces in the (σ_1; σ_2) plane, for $k = 15$ and *a* values equal to 0, 0.97 and 1. The von Mises surface is also plotted.

Cazacu & Barlat [15] proposed an extension of Drucker isotropic criterion to anisotropy using the IPE stress state (Eqs. (2.15) and (2.16)) mentioned above. This criterion is now referred to as Drucker+L criterion and can be expressed as:

$$\left[1/2\,\mathrm{tr}(\mathbf{s}^2)\right]^3 - c\left[1/3\,\mathrm{tr}(\mathbf{s}^3)\right]^2 = 27\left(\frac{Y}{3}\right)^6, \tag{2.21}$$

where $\mathrm{tr}(\mathbf{s})$ is the trace of the stress tensor $\mathbf{s}$, and c is a weighting parameter with the same meaning as for Drucker isotropic criterion, ranging between -3.375 and 2.25, to ensure the convexity of the yield surface. Hill'48 yield criterion is retrieved for $c = 0$.

Cazacu & Barlat [15] also developed a method for generalising to anisotropy the invariants of the deviatoric stress tensor J_2 and J_3 into Drucker isotropic yield criterion. The resulting yield function is now referred to as CB2001 criterion, expressed:

$$\left(J_2^0\right)^3 + c\left(J_3^0\right)^2 = 27\left(\frac{Y}{3}\right)^6, \tag{2.22}$$

where J_2^0 and J_3^0 are the generalised second and third invariants of the deviatoric stress tensor, respectively, and c is a weight parameter. The expression for J_2^0 is given by:

$$J_2^0 = \frac{a_1}{6}(\sigma_{xx}-\sigma_{yy})^2 + \frac{a_2}{6}(\sigma_{yy}-\sigma_{zz})^2 + \frac{a_3}{6}(\sigma_{xx}-\sigma_{zz})^2 + a_4\tau_{xy}^2 + a_5\tau_{xz}^2 + a_6\tau_{yz}^2, \tag{2.23}$$

where the coefficients a_i ($i=1$ to 6) are the anisotropy parameters related to the generalised second invariant. The expression for J_3^0 is:

$$\begin{aligned} J_3^0 = {} & \frac{1}{27}(b_1+b_2)\sigma_{xx}^3 + \frac{1}{27}(b_3+b_4)\sigma_{yy}^3 + \frac{1}{27}\left[2(b_1+b_4)-b_2-b_3\right]\sigma_{zz}^3 \\ & -\frac{1}{9}(b_1\sigma_{yy}+b_2\sigma_{zz})\sigma_{xx}^2 - \frac{1}{9}(b_3\sigma_{zz}+b_4\sigma_{xx})\sigma_{yy}^2 \\ & -\frac{1}{9}\left[(b_1-b_2+b_4)\sigma_{xx}+(b_1-b_3+b_4)\sigma_{yy}\right]\sigma_{zz}^2 \\ & +\frac{2}{9}(b_1+b_4)\sigma_{xx}\sigma_{yy}\sigma_{zz} - \frac{\tau_{xz}^2}{3}\left[2b_9\sigma_{yy}-b_8\sigma_{zz}-(2b_9-b_8)\sigma_{xx}\right] \\ & -\frac{\tau_{xy}^2}{3}\left[2b_{10}\sigma_{zz}-b_5\sigma_{yy}-(2b_{10}-b_5)\sigma_{xx}\right] \\ & -\frac{\tau_{yz}^2}{3}\left[(b_6+b_7)\sigma_{xx}-b_6\sigma_{yy}-b_7\sigma_{zz}\right] + 2b_{11}\tau_{xy}\tau_{yz}\tau_{xz} \end{aligned}, \tag{2.24}$$

where the coefficients b_i ($i=1$ to 11) are the anisotropy parameters concerning the generalised third invariant. This criterion is reduced to Hill'48 yield criterion, for $c=0$, and to Drucker yield criterion, for $a_i = b_i = 1$.

The complete description of CB2001 yield criterion involves the identification of 18 parameters. The value of the parameters associated with the out-of-plane stress components τ_{yz} and τ_{xz} are generally assumed as in isotropy, i.e. $a_5 = a_6 = b_6 = b_7 = b_8 = b_9 = b_{11} = 1$, thus reducing the total number of parameters to 11. While the convexity for Drucker yield criterion is ensured for $-3.375 \le c \le 2.25$, the range of c values that ensure the convexity of CB2001 criterion is not yet established. For this purpose, Chaparro [6] explored the convexity of the CB2001 yield surface, by varying each parameter of CB2001 criterion and keeping the remaining parameters

unchanged with their values as in isotropy. Under these conditions, the identified values for the limits of the parameters that ensure the convexity are: $a_1 \geq 0.5$; $a_2 \geq 0.5$; $a_3 \geq 0.5$; $a_1 \geq 0.4$; $-2.1 \leq b_1$; $-1.0 \leq b_2$; $b_3 \leq 3.2$; $b_4 \leq 1.8$; $-2.0 \leq b_5 \leq 4.0$ and $-1.0 \leq b_{10} \leq 1.5$. Nevertheless, the parameters optimisation must contemplate the surface convexity check, in order to penalise non-convex surfaces [27].

According to Yoshida et al. [19], a user-friendly yield criterion should: (i) accurately describe the planar anisotropy coefficients and the in-plane flow stress directionality as well as the shape of the yield surface; (ii) allow a 3D representation of the stresses, and not only plane stress description (2D); (iii) be convex; (iv) only require standard experimental data for the material parameter identification, from simple mechanical tests, i.e. uniaxial tension (anisotropy coefficients and yield stress values at different orientations in the sheet plane) and equibiaxial yield stress data; (v) take into account additional experimental data, if available, such as near plane strain, pure shear stresses, among others. To achieve this, Yoshida et al. [19] proposed a yield criterion based on the sum of a number of components of Drucker+L yield criterion [15]:

$$\frac{27}{n}\sum_{i=1}^{n}\left\{\left(\frac{1}{2}\mathrm{tr}\left(\mathbf{s}^{(i)}\right)^2\right)^3 - c^{(i)}\left(\frac{1}{3}\mathrm{tr}\left(\mathbf{s}^{(i)}\right)^3\right)^2\right\} = Y^6, \tag{2.25}$$

where $i = 1, \ldots, n$ are the components for the yield criterion. Each component i of the sum in Eq. (2.25) has a distinct set of material parameters, as tensor $\mathbf{s}^{(i)}$ is obtained through $\mathbf{s}^{(i)} = \mathbf{L}^{(i)} : \boldsymbol{\sigma}$, where $\mathbf{L}^{(i)}$ is written:

$$\mathbf{L}^{(i)} = \begin{bmatrix} (C_2^{(i)} + C_3^{(i)})/3 & -C_3^{(i)}/3 & -C_2^{(i)}/3 & 0 & 0 & 0 \\ -C_3^{(i)}/3 & (C_3^{(i)} + C_1^{(i)})/3 & -C_1^{(i)}/3 & 0 & 0 & 0 \\ -C_2^{(i)}/3 & -C_1^{(i)}/3 & (C_1^{(i)} + C_2^{(i)})/3 & 0 & 0 & 0 \\ 0 & 0 & 0 & C_4^{(i)} & 0 & 0 \\ 0 & 0 & 0 & 0 & C_5^{(i)} & 0 \\ 0 & 0 & 0 & 0 & 0 & C_6^{(i)} \end{bmatrix}. \tag{2.26}$$

In this sense, the sum of several yield function components generates new yield functions with guaranteed convexity [19], which are able to describe the anisotropy of metal sheets with higher flexibility than using only one component, as in Drucker+L criterion. This yield criterion is presented to highlight the increase in the number of parameters associated with the latest advanced models, which require at least the same number of simple mechanical tests to identify them.

2.3. Hardening Laws

Metals and alloys show hardening behaviour during plastic deformation, i.e. the stress increases when occurring further plastic deformation. This sub-chapter analyses the hardening laws, which describe the evolution of the yield surface during the plastic deformation. These laws are essentially of two types, isotropic and kinematic. Isotropic hardening laws formulate mathematically the change in size of the yield surface, during plastic deformation, without affecting its shape. Kinematic hardening laws express the translational motion of the yield surface centre, during plastic deformation, and are therefore recommended for describing plastic deformation under strain path changes, mainly strain path reversal, in materials that exhibit Bauschinger effect. Therefore, the combination of isotropic and kinematic hardening laws provides a flexible model, for simultaneously describing the change in size and position of the centre of the yield surface, during plastic deformation. Figure 2.6 schematises the isotropic (Figure 2.6(a)) and kinematic (Figure 2.6(b)) hardening of a generic yield surface.

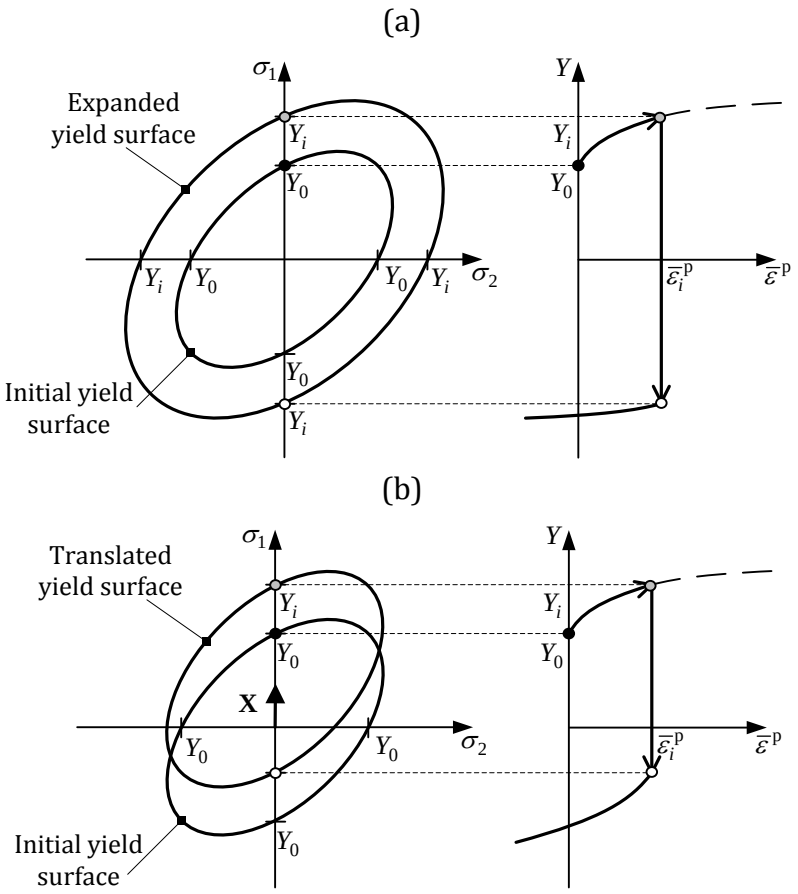

Figure 2.6. Representation of the plastic behaviour of materials in tension - compression. The left side shows generic yield surfaces in the plane (σ_1 ; σ_2) and, the right side, corresponding stress *vs.* plastic strain curves: (a) isotropic hardening and (b) kinematic hardening. Adapted from [28].

2.3.1. Isotropic hardening

A simple isotropic hardening model was proposed by Hollomon [29]:

$$Y = K(\bar{\varepsilon}^{\mathrm{p}})^{n}, \tag{2.27}$$

where Y and $\bar{\varepsilon}^{\mathrm{p}}$ are the flow stress and the equivalent plastic strain, respectively; K and n are material parameters to identify. It is clear that Eq. (2.27) is suitable when low values for the yield stress are observed (i.e. $\bar{\varepsilon}^{\mathrm{p}} = 0 \Rightarrow Y = 0$), and/or when high enough values of plastic deformation are attained, so that inconsistencies at the beginning of plastic deformation can be neglected.

Variants of Eq. (2.27), consisting of more flexible and complex power laws proposed by Ludwick [30], Swift [31], Ludwigson [32], Ghosh [33] and Fernandes et al. [34], are, respectively:

$$Y = Y_0 + K(\bar{\varepsilon}^{\mathrm{p}})^{n}, \tag{2.28}$$

$$Y = K(\varepsilon_0 + \bar{\varepsilon}^{\mathrm{p}})^{n}, \tag{2.29}$$

$$Y = K(\bar{\varepsilon}^{\mathrm{p}})^{n} + \exp(K_1 + n_1\bar{\varepsilon}^{\mathrm{p}}), \tag{2.30}$$

$$Y = C + K(\varepsilon_0 + \bar{\varepsilon}^{\mathrm{p}})^{n}, \tag{2.31}$$

$$Y = K\left[g(\varepsilon_0 + \varepsilon_{\mathrm{p}}) + h\bar{\varepsilon}^{\mathrm{p}} \right]^{n}, \tag{2.32}$$

where Y_0, ε_0, K_1, n_1, g and h are material parameters and ε_{p} in Eq. (2.32) represents an equivalent pre-strain value [34]. However, none of these power laws takes into account the stress saturation at large deformations, which occurs in face centred cubic (FCC) metallic materials as for example aluminium and copper alloys [35]. In this regard, isotropic hardening laws with stress saturation were developed, such as the ones proposed by Voce [36] and Hockett & Sherby [37], written in the following equations, respectively:

$$Y = Y_0 + (Y_{\mathrm{Sat}} - Y_0)[1 - \exp(-C_{\mathrm{Y}}\bar{\varepsilon}^{\mathrm{p}})], \tag{2.33}$$

$$Y = Y_0 + (Y_{\mathrm{Sat}} - Y_0)[1 - \exp(-C_{\mathrm{Y}}(\bar{\varepsilon}^{\mathrm{p}})^{a})], \tag{2.34}$$

where Y_0, Y_{Sat}, C_{Y}, and a are material parameters.

The next equations describe weighted combinations of isotropic hardening laws such as Swift - Voce [38] and Swift - Hockett & Sherby [7], respectively, which allow increasing flexibility for fitting material curves:

$$Y=(1-\alpha)[K(\varepsilon_0+\bar{\varepsilon}^{\mathrm{p}})^n]+\alpha\{Y_0+(Y_{\mathrm{Sat}}-Y_0)[1-\exp(-C_{\mathrm{Y}}\bar{\varepsilon}^{\mathrm{p}})]\}, \quad (2.35)$$

$$Y=(1-\alpha)[K(\varepsilon_0+\bar{\varepsilon}^{\mathrm{p}})^n]+\alpha\{Y_{\mathrm{Sat}}+(Y_0-Y_{\mathrm{Sat}})\exp[-a(\bar{\varepsilon}^{\mathrm{p}})^b]\}, \quad (2.36)$$

where α is a weighting parameter, ranging between 0 and 1. Accordingly, when $\alpha=$ 0, both Eqs. (2.35) and (2.36) become Swift law (see Eq. (2.29)); when $\alpha=$ 1, Eq.(2.35) becomes Voce law (see Eq. (2.33)) and Eq.(2.36) becomes Hockett & Sherby law (see Eq. (2.34)).

2.3.2. Kinematic hardening

The modelling of the kinematic hardening plays a significant role when phenomena such as the Bauschinger effect and permanent softening, due to strain path change, are relevant. Figure 2.7 shows an example of a stress-strain curve for an in-plane tensile-compression test of a JIS SPCC steel sheet [39], with pronounced Bauschinger effect. The reloading in compression shows three stages: (i) the transient Bauschinger effect, with early yielding after strain path reversal and a smooth transition between the elastic and plastic deformation regimes; (ii) with eventual subsequent work-hardening stagnation followed by increase of work-hardening rate; (iii) permanent softening, which is expressed by a shift in the stress values relatively to the ones predicted for pure isotropic hardening. Depending on the material, these stages can be more or less noticeable.

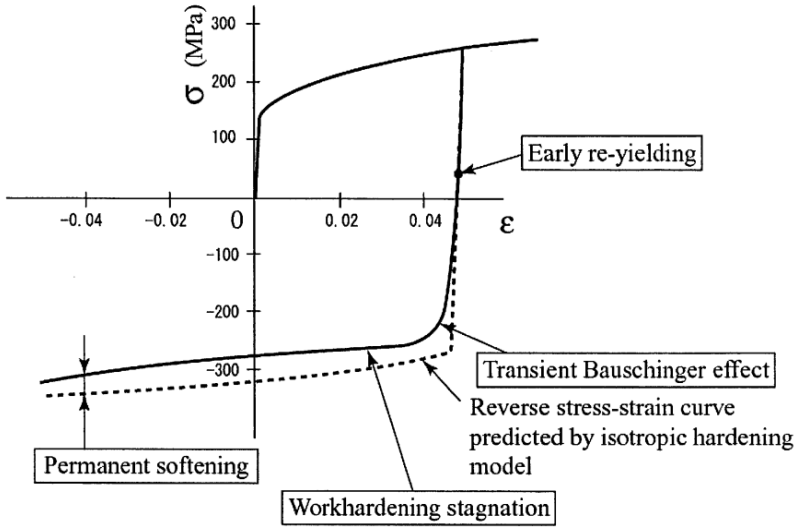

Figure 2.7. Work-hardening behaviour during a tension-compression test of a JIS SPCC steel sheet, showing the stages associated with the Bauschinger effect [39].

Kinematic hardening is relevant in deep-drawing processes with occurrence of abrupt inversions of strain path, which influence the plastic deformation behaviour. The Bauschinger effect is also associated with the springback, due to premature yielding after reverse strain path [39]. Springback is the elastic strain recovery when

forming loads are removed, and its magnitude depends on the flow stress value [23]. Therefore, the proper modelling of the kinematic hardening is important in order to efficiently predict the springback.

The Bauschinger effect is modelled through kinematic hardening laws. Prager [41] and Ziegler [42] proposed linear kinematic hardening laws, introducing the deviatoric back-stress tensor $\mathbf{X}'$ in the constitutive model (as shown in Eq. (2.1)). The deviatoric back-stress tensor $\mathbf{X}'$ is coaxial with the tensor $\boldsymbol{\sigma}'$, and defines the translation of the centre of the yield surface, during plastic deformation.

The linear kinematic hardening model proposed by Prager [41] is written as follows:

$$\mathrm{d}\mathbf{X}' = q_{\mathrm{P}}\mathrm{d}\boldsymbol{\varepsilon}^{\mathrm{p}}, \tag{2.37}$$

where q_{P} is a material parameter.

In Ziegler's linear model, the kinematic hardening is given by [42, 43]:

$$\mathrm{d}\mathbf{X}' = q_{\mathrm{Z}}\mathrm{d}\bar{\varepsilon}^{\mathrm{p}}(\boldsymbol{\sigma}'-\mathbf{X}'), \tag{2.38}$$

where q_{Z} is a material parameter. The assumption of a linear kinematic hardening behaviour is advantageous in terms of numerical implementation and computational efficiency. However, it fails to predict the non-linear kinematic hardening behaviour of real materials. This disadvantage led to the development of non-linear kinematic models as proposed by Armstrong & Frederick [44], which can be written:

$$\mathrm{d}\mathbf{X}' = C_{\mathrm{X}}\left[\frac{X_{\mathrm{Sat}}}{\bar{\sigma}}\left(\boldsymbol{\sigma}'-\mathbf{X}'\right)-\mathbf{X}'\right]\mathrm{d}\bar{\varepsilon}^{\mathrm{p}}, \tag{2.39}$$

where C_{X} and X_{Sat} are material parameters. This model allows describing the transient Bauschinger effect during abrupt changes in strain path.

Chaboche [45, 46] proposed an improvement of the Armstrong & Frederick model, which is the sum of several parts, each one described as in Eq. (2.39):

$$\mathrm{d}\mathbf{X}' = \sum_{i=1}^{\mathrm{N}}\mathrm{d}\mathbf{X}_i',\ \mathrm{d}\mathbf{X}_i' = C_i\left[\frac{X_i}{\bar{\sigma}}\left(\boldsymbol{\sigma}'-\mathbf{X}_i'\right)-\mathbf{X}_i'\right]\mathrm{d}\bar{\varepsilon}^{\mathrm{p}}, \tag{2.40}$$

where N is the number of parts of the sum, C_i and X_i are the material parameters for each part of the sum.

Teodosiu & Hu [47, 48], Geng & Wagoner [49] and Yoshida & Uemori [39, 50] developed flexible models to describe the stages shown in Fig. 2.7. However, such flexibility requires high number of material parameters to identify, compared with the kinematic models described above. For example, Teodosiu & Hu model has 13 parameters (8, for the simplified model, adequate for some materials, such as aluminium [6]) and Yoshida & Uemori model has at least 7 parameters (the number depends on the type of isotropic and kinematic hardening laws).

2.4. Final Remarks

The yield criteria and hardening laws reviewed above and others not mentioned show that a great investment has been made for modelling the plastic deformation of materials, in part due to the emergence of new steels, aluminium, magnesium and superplastic alloys, in automotive and aeronautical industry [7]. Whereas a number of advanced constitutive models are available in literature, sheet metal forming simulations are still mainly performed in industry with the well-known Hill'48 yield criterion, which parameters identification can be easily supported by uniaxial tensile tests, and usually not taking into account kinematic hardening. Mattiasson & Sigvant [51] mentioned some plausible explanations, still valid today, for this reality:

- the relative simplicity of the Hill'48 model makes it attractive to use;
- the availability of industry analysts for understanding to what extent the modelling of the material influences the simulation results;
- there is lack of knowledge, time, and money for performing the multiaxial material tests needed to identify reliable hardening curves and parameters of more advanced yield criteria;
- the additional cost in terms of CPU-time for using more advanced constitutive models is considered to be an effort that is not worth it.

A major obstacle to the widespread use of advanced constitutive models in industrial simulations comes from the large number of linear strain path tests required for the parameters identification. To overcome this barrier, a potential approach is to seek new constitutive parameters identification strategies, alternative to the classical. In this sense, an accurate description of the material plastic behaviour could be attained from: (i) a minimum number of material tests and experimental data; (ii) flexible and user-friendly constitutive models and (iii) a accessible identification procedure for the constitutive parameters, coupled with robust optimisation algorithms.

The next chapter will discuss some identification procedures for the constitutive parameters based on inverse analysis, as an alternative to the classical approach.

References

[1] Khalfallah A, Bel Hadj Salah H, Dogui A (2002) Anisotropic parameter identification using inhomogeneous tensile test. European Journal of Mechanics A/Solids, 21, 927–942.

[2] Tresca H (1864) Memoir on the flow of solid bodies under strong pressure. Comptes Rendus de l'Académie des Sciences Paris, 59, 754–758.

[3] von Mises RV (1913) Mechanik der festen korper im plastic-deformablen zustand. Nachrichten vos der koniglichen gellesschaft des winssenschaften zu Gottingen, Mathematisch-physikalische klasse, 582–592.

[4] Lardner TJ, Archer RR (1994) Mechanics of solids: an introduction. McGraw-Hill international editions.

[5] Alves JL (2003) Simulação numérica do processo de estampagem dee chapas metálicas – modelação mecânica e métodos numéricos. PhD Thesis. University of Minho.

[6] Chaparro BM (2006) Comportamento plástico de materiais metálicos: identificação e optimização de parâmetros. PhD Thesis. University of Coimbra.

[7] Banabic D (2010) Sheet Metal Forming Processes – Constitutive Modelling and Numerical Simulation. Springer-Verlag.

[8] Banabic D, Barlat F, Cazacu O, Kuwabara T (2010) Advances in anisotropy and formability. International Journal of Material Forming, 3, 165–189.

[9] Drucker DC (1949) Relation of experiments to mathematical theories of plasticity. Journal of Applied Mechanics, 16, 349–357.

[10] Hosford WF (1972) A generalized isotropic yield criterion. Journal of Applied Mechanics - Transactions ASME, 39, 607–9.

[11] Drucker DC (1959) A definition of a stable inelastic material. ASME Journal of Applied Mechanics, 26, 101–195.

[12] Yamashita T (1996) Analysis of Anisotropic Material. MSc Thesis. Ohio University.

[13] Hu W (2005) An orthotropic yield criterion in a 3-D general stress state. International Journal of Plasticity, 21, 1771–1796.

[14] Soare S (2007) On the use of homogeneous polynomials to develop anisotropic yield functions with applications to sheet metal forming. PhD Thesis, University of Florida.

[15] Cazacu O, Barlat F (2001) Generalization of Drucker's yield criterion to orthotropy. Mathemathics and Mechanics of Solids, 6, 613–630.

[16] Bron F, Besson J (2004) A yield function for anisotropic materials –

application to aluminum alloys. International Journal of Plasticity, 20, 937–963.

[17] Barlat F, Aretz H, Yoon JW, Karabin ME, Brem JC, Dick RE (2005) Linear transformation-based anisotropic yield functions. International Journal of Plasticity, 21, 1009–1039.

[18] Plunkett B, Cazacu 0, Barlat F (2008) Orthotropic yield criteria for description of the anisotropy in tension and compression of sheet metals. International Journal of Plasticity, 24, 847–866.

[19] Yoshida F, Hamasaki H, Uemori T (2013) A user-friendly 3D yield function to describe anisotropy of steel sheets. International Journal of Plasticity, 45, 119–139.

[20] Barlat F, Lege DJ, Brem JC (1991) A 6-component yield function for anisotropic materials. International Journal of Plasticity, 7, 693–712.

[21] Karafillis AP, Boyce MC (1993) A general anisotropic yield criterion using bounds and a transformation weighting tensor. Journal of the Mechanics and Physics of Solids, 41, 1859–1886.

[22] Cazacu O, Plunkett B, Barlat F (2006) Orthotropic yield criterion for hexagonal close packed metals. International Journal of Plasticity, 22, 1171–1194.

[23] Barlat F, Gracio JJ, Lee MG, Rauch EF, Vincze G (2011) An alternative to kinematic hardening in classical plasticity. International Journal of Plasticity, 27, 1309–1327.

[24] Vegter H, van den Boogaard AH (2006) A plane stress yield function for anisotropic sheet material by interpolation of biaxial stress states. International Journal of Plasticity, 22, 557–580.

[25] Hill R (1948) A theory of yielding and plastic flow of anisotropic metals. Proc. R. Soc. London, 193, 281–297.

[26] Prates PA, Oliveira MC, Fernandes JV (2013) How to Combine the Parameters of the Yield Criteria and the Hardening Law. Key Engineering Materials, 554-557, 1195–1202.

[27] Soare S, Yoon JW, Cazacu O and Barlat F (2007) Applications of anisotropy yield functions to sheet metal forming. Advanced Methods in Material Forming, Banabic D (eds.), Springer, 131-149.

[28] Dunne F, Petrinic N (2005) Introduction to Computational Plasticity. Oxford University Press.

[29] Hollomon JH (1945) Tensile deformations. Transactions of the Metallurgical Society of AIME, 162, 268-290.

[30] Ludwick P (1909) Elemente der technologischen Mechanik. Springer Verlag Berlin.

[31] Swift HW (1952) Plastic instability under plane stress. Journal of the Mechanics and Physics of Solids, 1, 1–18.

[32] Ludwigson DC (1971) Modified stress–strain relation for FCC metals and alloys. Metallurgical Transactions, 2, 2825–2828.

[33] Ghosh AK (1977) Tensile instability and necking in materials with strain hardening and strain-rate hardening. Acta Metallurgica, 25, 1413-1424.

[34] Fernandes JV, Rodrigues DM, Menezes LF, Vieira MT (1998) A modified swift law for prestrained materials. International Journal of Plasticity, 14, 537–550.

[35] Sivaprasad PV, Venugopal S, Venkadesan S (1997) Tensile flow and work-hardening behavior of a Ti-modified austenitic stainless steel. Metallurgical and Materials Transactions A, 28, 171–178.

[36] Voce E (1948) The relationship between stress and strain for homogeneous deformation, Journal of the Institute of Metals, 74, 537–562.

[37] Hockett JE, Sherby OD (1975) Large strain deformation of polycrystalline metals at low homologous temperatures. Journal of the Mechanics and Physics of Solids, 23, 87–98.

[38] Larour P (2010) Strain rate sensitivity of automotive sheet steels: influence of plastic strain, strain rate, temperature, microstructure, bake hardening and pre-strain. PhD Thesis. RWTH Aachen University.

[39] Yoshida F, Uemori T (2003) A model of large-strain cyclic plasticity and its application to springback simulation. International Journal of Mechanical Sciences, 45, 1687–1702.

[40] Oliveira MC, Alves JL, Chaparro BM, Menezes LF (2007) Study on the influence of work-hardening modelling in springback prediction. International Journal of Plasticity, 23, 516–543.

[41] Prager W (1949) Recent developments in the mathematical theory of plasticity. Journal of Applied Physics, 20, 235–241.

[42] Ziegler H (1959) A modification of Prager's hardening rule. Applied Mathematics, 17, 55–65.

[43] Eggertsen P-A, Mattiasson K (2009) On the modelling of the bending–unbending behaviour for accurate springback predictions. International Journal of Mechanical Sciences, 51, 547–563.

[44] Armstrong PJ, Frederick CO (1966) A mathematical representation of the multiaxial Bauschinger effect. GEGB Report RD/B/N 731.

[45] Chaboche JL (1989) Constitutive equations for cyclic plasticity and cyclic viscoplasticity. International Journal of Plasticity, 5, 247–302.

[46] Chaboche JL (2008) A review of some plasticity and viscoplasticity constitutive theories. International Journal of Plasticity, 24, 1642–1693.

[47] Teodosiu C, Hu Z (1995) Evolution of the intragranular microstructure at moderate and large strains: modelling and computational significance. Proceedings of 5th International Conference on Numerical Methods in Industrial Forming Processes – NUMIFORM'95, 173–182.

[48] Teodosiu C, Hu Z (1998) Microstructure in the continuum modelling of plastic anisotropy, 19th Riso International Symposium on Materials Science: Modelling of Structure and Mechanics of Materials from Microscale to Products, Riso National Laboratory, 149–168.

[49] Geng L, Shen Y, Wagoner R H (2002) Anisotropic hardening equations derived from reverse-bend testing. International Journal of Plasticity, 18, 743–67.

[50] Yoshida F, Uemori T (2002) A model of large-strain cyclic plasticity describing the Bauschinger effect and workhardening stagnation. International Journal of Plasticity, 18, 661–686.

[51] Mattiasson K, Sigvant M (2008) An evaluation of some recent yield criteria for industrial simulations of sheet forming processes. International Journal of Mechanical Sciences, 50, 774–787.

Chapter 3

Inverse Identification Strategies

This chapter presents a literature overview on strategies for inverse identification of constitutive parameters of metal sheets. The first subchapter describes formulations for the standard cost-function and the optimisation algorithms commonly found in the literature for inverse identification of constitutive parameters. In the second subchapter, general remarks on the classical methodologies for constitutive parameters identification are made and an introduction to the inverse identification strategies is presented. The third subchapter emphasises inverse strategies, examining case studies from literature, involving the identification of constitutive parameters supported by finite element simulations.

(Page intentionally left blank)

3.1. The Optimisation Problem

The accuracy of numerical results of sheet metal forming processes depends of the constitutive model selected for describing the material behaviour. This implicitly includes the strategy for identifying the model parameters, which is generally seen as an optimisation problem. The purpose is to minimise the difference between computed and experimental results of one or more experiments. This difference is expressed by a cost function and its minimisation is performed using optimisation algorithms, which automatically operate on the values of the constitutive parameters.

3.1.1. Cost function

A wide number of cost function formulations for the identification of constitutive parameters have been proposed in literature (e.g. [1, 2]). According to Cao & Lin [1], a cost function should operate as an "efficient guide" of the optimisation procedure, in order to search for the best fit to the experimental results. Also, the ideal cost function should comprise the following conditions:

- All measured points of a given experiment should be part of the optimisation procedure and have equal opportunity to be optimised, provided that experimental errors are eliminated;
- All experiments should have equal opportunity to be equally optimised, and so the optimisation should not depend on the number of points considered in each experiment;
- Different units of measure in the cost function should not affect the performance of the optimisation;
- The identification procedure should not be dependent of the user, and so the values of the weighting factors should be optimised to achieve the above conditions.

Cost functions are typically formulated under the concept of weighted least-squares, as follows:

$$F(\mathbf{A}) = \sqrt{\frac{1}{m}\frac{1}{n}\sum_{i=1}^{m} w_i \sum_{j=1}^{n} w_j \left[r_{ij}(\mathbf{A}) \right]^2} \,, \tag{3.1}$$

where $F(\mathbf{A})$ is the cost function to minimise; $\mathbf{A}$ is the vector of constitutive parameters to optimise; m is the total number of experiments and n is the total number of points, considered in each experiment i; $r_{ij}(\mathbf{A})$ is the residual between the

numerically predicted and the results of experiment i at point j; w_i and w_j are the weighting factors for each experiment i and for each point j, respectively.

The residuals can be expressed in terms of relative differences,

$$r_{ij}(\mathbf{A}) = \frac{u_{ij}^{\text{Num}}(\mathbf{A}) - u_{ij}^{\text{Exp}}}{u_{ij}^{\text{Exp}}}, \text{ with } i = 1, \ldots, m \text{ and } j = 1, \ldots, n, \tag{3.2}$$

or in terms of absolute differences,

$$r_{ij}(\mathbf{A}) = u_{ij}^{\text{Num}}(\mathbf{A}) - u_{ij}^{\text{Exp}}, \tag{3.3}$$

where u_{ij}^{Num} and u_{ij}^{Exp} are, respectively, the numerically predicted and the experimental results at point j of experiment i. Residuals are often expressed using relative differences, which allows the use, in the same cost function, of several kinds of quantities exhibiting various orders of magnitude and units of measure [3]. When u_{ij}^{Exp} admits values close or equal to zero the residuals should be expressed using absolute differences.

3.1.2. Optimisation algorithms

The minimisation of the least-squares cost-function, presented in Eq. (3.1), requires efficient and robust optimisation algorithms, due to its strongly non-linear nature [4]. For this purpose, several optimisation algorithms are described in the literature, which are commonly divided into two categories: gradient-free algorithms and gradient-based algorithms. Hybrid optimisation strategies using both gradient-free and gradient-based algorithms are also proposed (e.g. [4, 5]).

Gradient-free algorithms, such as evolutionary algorithms, have a great probability of achieving a global minimum due to their random search capability. They require a large number of cost-function evaluations (i.e. iterations) and therefore the convergence can be very time-consuming. Because of this, gradient-free algorithms are not recommended within the context of inverse identification strategies, since they require a large number of finite element simulations and analysis [6].

Gradient-based algorithms are most popular within inverse identification strategies, as they require far less cost function evaluations than gradient-free methods. As local optimisers, these algorithms use information of the gradient to update the vector of constitutive parameters in an adequate search direction [7]. As a result, there is no guarantee that these methods converge to the global minimum, with the possibility of converging to undesirable local minima. This makes the optimisation procedure dependent on the initial estimate for the parameters, and therefore convenient initial estimates for the constitutive parameters are essential.

Examples of gradient-based algorithms are Gauss-Newton and Levenberg-Marquardt algorithms. The Gauss-Newton algorithm is described as follows:

$$\mathbf{A}^{s+1} = \mathbf{A}^{s} - (\mathbf{J}^{\mathrm{T}}\mathbf{W}\mathbf{J})^{-1}\mathbf{J}^{\mathrm{T}}\mathbf{W}\mathbf{r}(\mathbf{A}^{s}), \tag{3.4}$$

where s is the iteration step, $\mathbf{A}$ is the vector of constitutive parameters, $\mathbf{W}$ is the vector of weighting factors, $\mathbf{J}$ is the Jacobian matrix and $\mathbf{r}(\mathbf{A}^{s})$ is the vector of residuals, which can be expressed in terms of relative or absolute differences (see Eq.(3.2) and Eq. (3.3), respectively). The dimension of the vector of residuals depends on the total number of experiments m and the total number of points n, in each experiment, i.e. the dimension $n_r = m \times n$. Considering that the total number of constitutive parameters to be identified is n_p, with $n_r \geq n_p$, the Jacobian matrix, which contains the partial derivatives of the residuals with respect to the constitutive parameters, is defined:

$$J_{l,p} = \frac{\partial r_l(A_p)}{\partial A_p}, \text{ with } l = 1,\ldots, n_r \text{ and } p = 1, \ldots, n_p. \tag{3.5}$$

It expresses the sensitivity of the computed results to the constitutive parameters. An efficient method to compute the Jacobian matrix is finite differentiation. When the residuals are expressed in terms of relative differences, the expressions for backward, centred and forward finite differentiation are, respectively:

$$J_{l,p} = \frac{\partial r_l(A_p)}{\partial A_p} \approx \frac{u_l^{\mathrm{Num}}(A_p) - u_l^{\mathrm{Num}}(A_p - \delta A_p)}{\delta A_p u_l^{\mathrm{Exp}}}; \tag{3.6}$$

$$J_{l,p} = \frac{\partial r_l(A_p)}{\partial A_p} \approx \frac{u_l^{\mathrm{Num}}(A_p + \delta A_p) - u_l^{\mathrm{Num}}(A_p - \delta A_p)}{2\delta A_p u_l^{\mathrm{Exp}}}; \tag{3.7}$$

$$J_{l,p} = \frac{\partial r_l(A_p)}{\partial A_p} \approx \frac{u_l^{\mathrm{Num}}(A_p + \delta A_p) - u_l^{\mathrm{Num}}(A_p)}{\delta A_p u_l^{\mathrm{Exp}}}, \tag{3.8}$$

and when the residuals are expressed in terms of absolute differences, respectively:

$$J_{l,p} = \frac{\partial r_l(A_p)}{\partial A_p} \approx \frac{u_l^{\mathrm{Num}}(A_p) - u_l^{\mathrm{Num}}(A_p - \delta A_p)}{\delta A_p}; \tag{3.9}$$

$$J_{l,p} = \frac{\partial r_l(A_p)}{\partial A_p} \approx \frac{u_l^{\mathrm{Num}}(A_p + \delta A_p) - u_l^{\mathrm{Num}}(A_p - \delta A_p)}{2\delta A_p}; \tag{3.10}$$

$$J_{l,p} = \frac{\partial r_l(A_p)}{\partial A_p} \approx \frac{u_l^{\mathrm{Num}}(A_p + \delta A_p) - u_l^{\mathrm{Num}}(A_p)}{\delta A_p}, \tag{3.11}$$

with $l = 1,\ldots, n_r$ and $p = 1,\ldots, n_p$, where $u_l^{\mathrm{Num}}(A_p)$ is the numerically predicted result for the point i of experiment j, with the set of constitutive parameters A_p, u_l^{Exp} is the experimental result at point i of experiment j and δ is the perturbation value for

the constitutive parameters, chosen small enough. The Jacobian matrix is updated at each iteration step s, in order to improve the convergence. However, the calculation in each step requires high computational cost (at least one numerical simulation per constitutive parameter). To overcome this inconvenient, Cooreman [7] studied the possibility of computing the sensitivity matrix analytically, concluding that it is impossible use this approach for complex and/or heterogeneous deformation [7].

In some cases, the Gauss-Newton algorithm can become unstable in the neighbourhood of the minimum, and so a stabilisation procedure is required. The Levenberg-Marquardt algorithm [8] is similar to Gauss-Newton, but includes a stabilising term, as follows:

$$\mathbf{A}^{s+1} = \mathbf{A}^{s} - (\mathbf{J}^{\mathrm{T}}\mathbf{W}\mathbf{J} + \lambda \mathbf{diag}(\mathbf{J}^{\mathrm{T}}\mathbf{W}\mathbf{J}))^{-1}\mathbf{J}^{\mathrm{T}}\mathbf{W}\mathbf{r}(\mathbf{A}^{s}). \tag{3.12}$$

λ is the stabilising parameter that is updated in each iteration according to the convergence rate [8]. When the Levenberg-Marquardt method shows stability, small values for λ are recommended for fast convergence; otherwise, large values of λ usually allow stable convergence, although slower, towards the minimum. Note that for λ = 0 the Levenberg-Marquardt algorithm is equal to the Gauss-Newton.

A different type of optimisation technique that has been recently used in the identification of constitutive parameters is the Response Surface Methodology (RSM) (e.g. [9, 10]). RSM is an optimisation technique for generating smooth approximations of complex functions in a multidimensional design space. In the context of parameter identification, the design space contains all possible combinations for the constitutive parameters and related values of the cost function. The prohibitive size of the full design space requires a design of experiments (DOE), to efficiently construct an approximated design space from a few number of representative points (i.e. sets of constitutive parameters). The responses of the representative points (i.e. the values of the cost function) are used to fit a response surface, which is typically obtained from second-order polynomial regression, for the sake of simplicity. Finally, the minimum of the response surface is calculated using a gradient-based optimisation procedure, which leads to an estimate of the optimal set of constitutive parameters. In brief, the RSM technique can be summarised as follows:

1. Initial guess for the design space for the material parameters;
2. Numerical simulations with the different sets of parameters, representing the experimental design points needed for filling the design space;
3. For each simulation, the predicted results are compared with the experimental ones, and the cost-function values are calculated according to Eq. (3.1);
4. A response surface is constructed to approximate the values of the cost-function. Typically, least squares approximations are used to determine second-order polynomials;

5. An optimisation algorithm is applied to determine the minimum point of the response surface (i.e. where $F(\mathbf{A})$ is minimum), providing the optimal set of material parameters;
6. If a converged solution is not found, the process starts all over again, adding a new region of interest to the design space.

3.2. Identification Strategies

Two main types of strategies for the identification of the constitutive parameters can be recognised in literature: classical and inverse strategies, the latter being the main target of this work.

3.2.1. Classical strategies

Classical strategies for constitutive parameters identification involve performing standardised mechanical tests, such as the well-known uniaxial tension, plane strain, hydraulic bulge and shear tests. Non-standard mechanical tests can also be performed to properly describe other biaxial stress states in the sheet plane (e.g. [11]). The variables analysed, such as loads, pressures and displacements are then used to analytically determine the values of stresses and strains under the assumption of homogeneous stress and strain fields in the region of interest in the sample, which in turn constitute the database of experimental results, $\mathbf{u}^{\mathrm{Exp}}$, enabling the estimation of the constitutive parameters using Eq. (3.1). The classical identification of the constitutive parameters has been extensively explored in the literature (e.g. [5, 12]), and is a commonplace industrial strategy for identification of constitutive parameters of simple models, mainly due to the convenience of performing uniaxial tension tests. For this reason, these strategies are not addressed in detail herein. Nevertheless, this strategy shows serious drawbacks:

- the increasing flexibility and accuracy of the constitutive models, achieved by raising the number of parameters to be identified, leads to an increase in the number and complexity of the mechanical tests required to characterise the material behaviour [13];
- the parameter identification is restricted to simple strain path tests with quasi-homogeneous deformation in the region of interest, which is far from the heterogeneous deformation under multiaxial loading occurring in metal sheets during complex forming operations;
- for samples with states of stress and strain not entirely homogeneous in the region of interest, the identified values of the constitutive parameters under

homogeneous assumption may not be accurate; in this context, local stress measurements were performed using x-ray diffraction technique [14];
- the identification requires a laborious and delicate post-treatment of the experimental results.

3.2.2. Inverse strategies

While classical strategies make use of global measurements from experiments to infer the values of the constitutive parameters, using simple analytical relations to estimate the material response under the assumption of homogeneous stress and strain fields in the region of interest, the inverse identification strategies are much more flexible [15]. They make use of experiments allowing heterogeneous deformation and/or strain path changes, as close as possible of the conditions usually found during real sheet metal forming processes. In this perspective, some authors even proposed tests involving contact with friction, such as the punch stretch test (e.g. [16]) and the cylindrical cup test (e.g. [17]), for performing the inverse parameter identification. In these latter cases, the adequate description of the local contact with friction is of paramount importance because it can affect the final results of the parameter identification (e.g. see [18]).

The inverse identification strategies make use of global measurements, such as tool loads and tool displacements, which are usually coupled with local measurements, represented as full-field states of displacements and/or strains on the surface of the sample. Then, a numerical analysis of the mechanical test is performed, assuming a constitutive model chosen *a priori* and an initial estimate for its parameters. Finally, the experimental results of the mechanical test are iteratively compared with numerical by acting on the values of the constitutive parameters until there is an adequate correspondence between experimental and numerical results.

The advantages of this identification approach include:

- substantial amount of reliable data extracted from a single mechanical test, using full-field measurements, which enables the accurate identification of large sets of constitutive parameters taking into account a wide range of strain levels and strain paths;
- therefore, it does not require uniform stress and strain distributions, in the region of interest, and no particular restrictions to the sample geometry and/or loading conditions are imposed.

Nevertheless, due to the design of the sample geometry, loading conditions and induced strain paths, the inverse identification requires proper computational strategies [15]. The most common strategy uses Finite Element Model Updating (FEMU), and consists on performing successive finite element (FE) simulations of the physical experiment; the set of parameters are obtained by minimising the gap between the experimental and the numerical results. Usually, this strategy compares the experimental and simulated loads and full-field measurements using a single cost

function (e.g. [19–23]); less frequently, authors propose to use only the load (e.g. [9, 10]), or full-field displacements (e.g. [24]) or strains (e.g. [25, 26]), at a given moment of loading, as schematised in Figure 3.1.

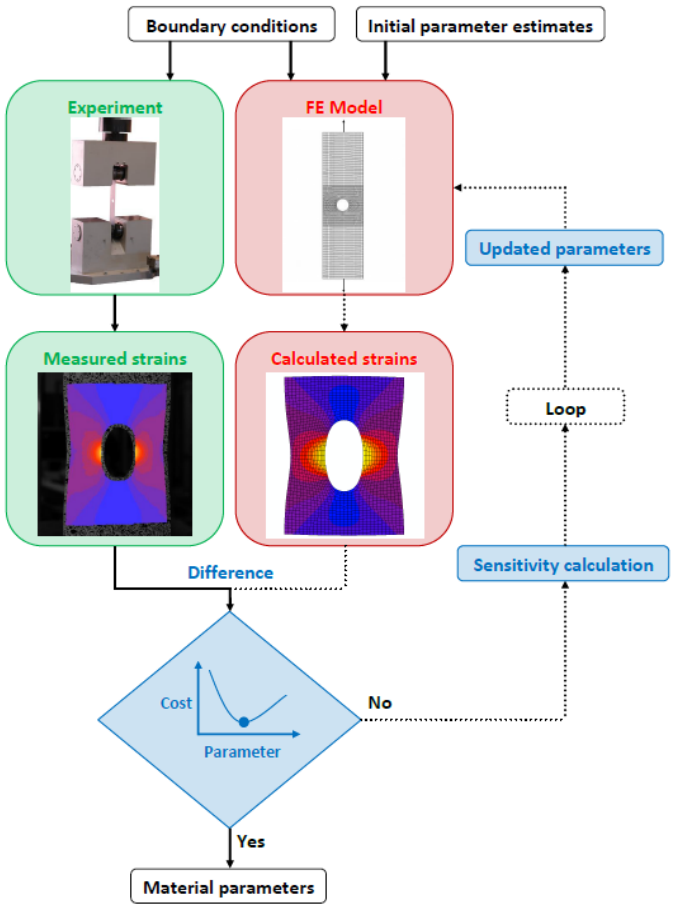

Figure 3.1. Flowchart of inverse identification strategy based on the comparison between the measured and FE simulated strain fields [7].

A promising alternative to the use of FEMU is the Virtual Fields Method (VFM), which is based on the principle of virtual work. Under this approach, the set of unknown constitutive parameters is identified by minimising the difference between the external work and the internal virtual work of the sample. This approach does not require using time-consuming FE analysis and therefore avoids potential drawbacks related to the accuracy of FE models namely the representation of the geometry and boundary conditions [27]. The VFM was successfully used in the identification of the parameters of a non-linear isotropic hardening law [28], the parameters of a linear isotropic hardening law combined with a non-linear kinematic hardening law [27] and the constitutive parameters of the Hill'48 yield criterion with Swift isotropic hardening law [29], resorting to experiments involving small heterogeneous deformations in the region of interest. However, the accuracy of the parameter identification depends on the adequate choice of the virtual field, which is currently a

challenge for problems involving large heterogeneity of deformation of anisotropic materials, as well as large plastic deformations. In fact, in this type of problems the optimal virtual field has to be evaluated for each time increment, which makes it less attractive than for linear problems.

3.3. Inverse strategies - Case Studies

This subchapter describes four representative case studies regarding the identification of constitutive parameters based on inverse strategies coupled with FE simulations. These cases highlight that the identification procedure is dictated by the loading conditions, the geometry of the sample, the type of experimental results selected, the cost functions used and the optimisation algorithm. The first three case studies concern the inverse identification of the parameters of yield criteria and isotropic hardening laws that, in a new approach, is the focus of the work developed in Chapter 4, subchapters 4.3 and 4.4, while the last case study concerns the parameter identification of kinematic hardening laws, which is the topic of the work of the Chapter 4, subchapter 4.5. The first case study [21] concerns the simultaneous identification of the yield criterion and isotropic hardening law parameters from the results of an out-of-plane test. The cost function takes into account the difference between the measured and simulated loads and displacement fields at different time steps of the test, and its minimisation is performed with the Levenberg-Marquardt algorithm. The second and third case studies [24, 25] concern also the simultaneous identification of the yield criterion and the isotropic hardening law parameters, but using biaxial tensile tests of cruciform samples. The cost functions quantify the differences between the measured and the simulated displacement and strain fields, for the second and third case, respectively, and their minimisation is performed with the Levenberg-Marquardt algorithm. The last case study [9] concerns the identification of parameters of kinematic hardening laws from a three-point bending test. The cost function quantifies the difference between the measured and simulated loads during the test, and the optimal solution is determined with a Response Surface Methodology.

3.3.1. Pottier et al. [21]

Pottier et al. [21] developed an out-of-plane testing procedure for the simultaneous identification of Hill'48 yield criterion and Ludwick hardening law parameters of a rolled titanium sheet. Figure 3.2 illustrates the experimental set-up and the geometry of the sample developed by the authors. A hemispherical punch applies a prescribed displacement normal to the sheet plane, at the centre of the surface of the sample, using a simple uniaxial tensile test machine. Two cameras are

located on the opposite side of the sample and the components of the displacement fields along the 0x, 0y and 0z axes are captured during the test using stereo digital image correlation. The sample was designed in order to exhibit multiaxial stress states, including shear, tension and biaxial stretching.

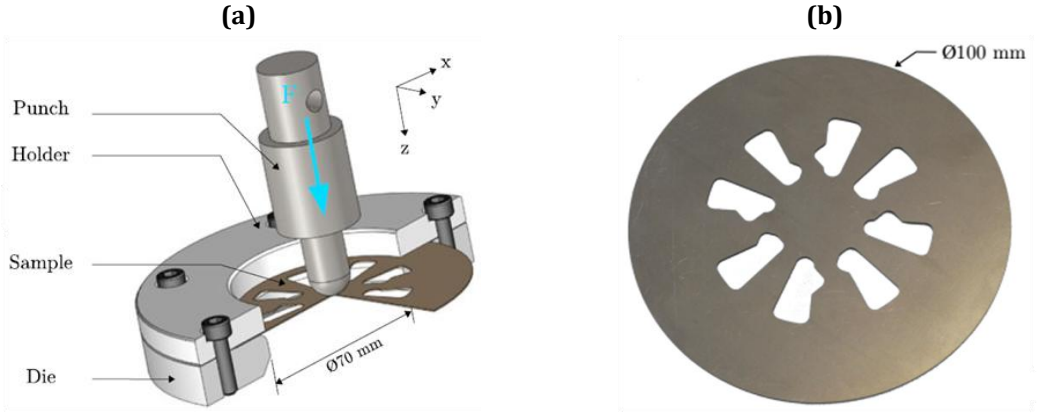

Figure 3.2. Schematic representation of the out-of-plane test: (a) experimental set-up [21] and (b) geometry of the sample [30].

The identification strategy is based on FEMU approach. The numerical displacements fields along the 0x, 0y and 0z axes and the global load are obtained from a model of the test and compared to the experimental ones, through the following least-squares cost function:

$$F(\mathbf{A}) = \left[\sum_{i,j=1}^{N_t,n} \left(\frac{u_{x,ij}^{Num}(\mathbf{A}) - u_{x,ij}^{Exp}}{\max_{i,j}(u_x^{Exp})} \right)^2 + \sum_{i,j=1}^{N_t,n} \left(\frac{u_{y,ij}^{Num}(\mathbf{A}) - u_{y,ij}^{Exp}}{\max_{i,j}(u_y^{Exp})} \right)^2 + \sum_{i,j=1}^{N_t,n} \left(\frac{u_{z,ij}^{Num}(\mathbf{A}) - u_{z,ij}^{Exp}}{\max_{i,j}(u_z^{Exp})} \right)^2 + n \left(\frac{P_i^{Num}(\mathbf{A}) - P_i^{Exp}}{\max_{i}(P^{Exp})} \right)^2 \right]^{\frac{1}{2}}, \quad (3.13)$$

where N_t is the number of time steps considered and n is the number of measured points; u_x, u_y and u_z are the displacements along the 0x, 0y and 0z axes, respectively, P is the global load and $\mathbf{A}$ is the vector of parameters to identify; the subscripts Num and Exp refer to numerical and experimental results, i and j refer to the number of time steps and measured points, respectively. The minimisation of the cost function is performed with the Levenberg-Marquardt algorithm.

The initial estimate of parameters corresponds to isotropy, for the yield criterion, and the initial values of the Ludwick hardening law parameters were chosen according to their known orders of magnitude. For keeping the computation time within reasonable limits, only six loading steps of the test were considered ($N_t = 6$). The iterative procedure stops when the greatest update value, within all parameters,

is less than 1% of the previous value of each parameter. The simultaneous identification of Hill'48 criterion and Ludwick hardening law parameters was reached after eleven iterations of the updating process, and the corresponding results are compared with experimental as shown in Figure 3.3.

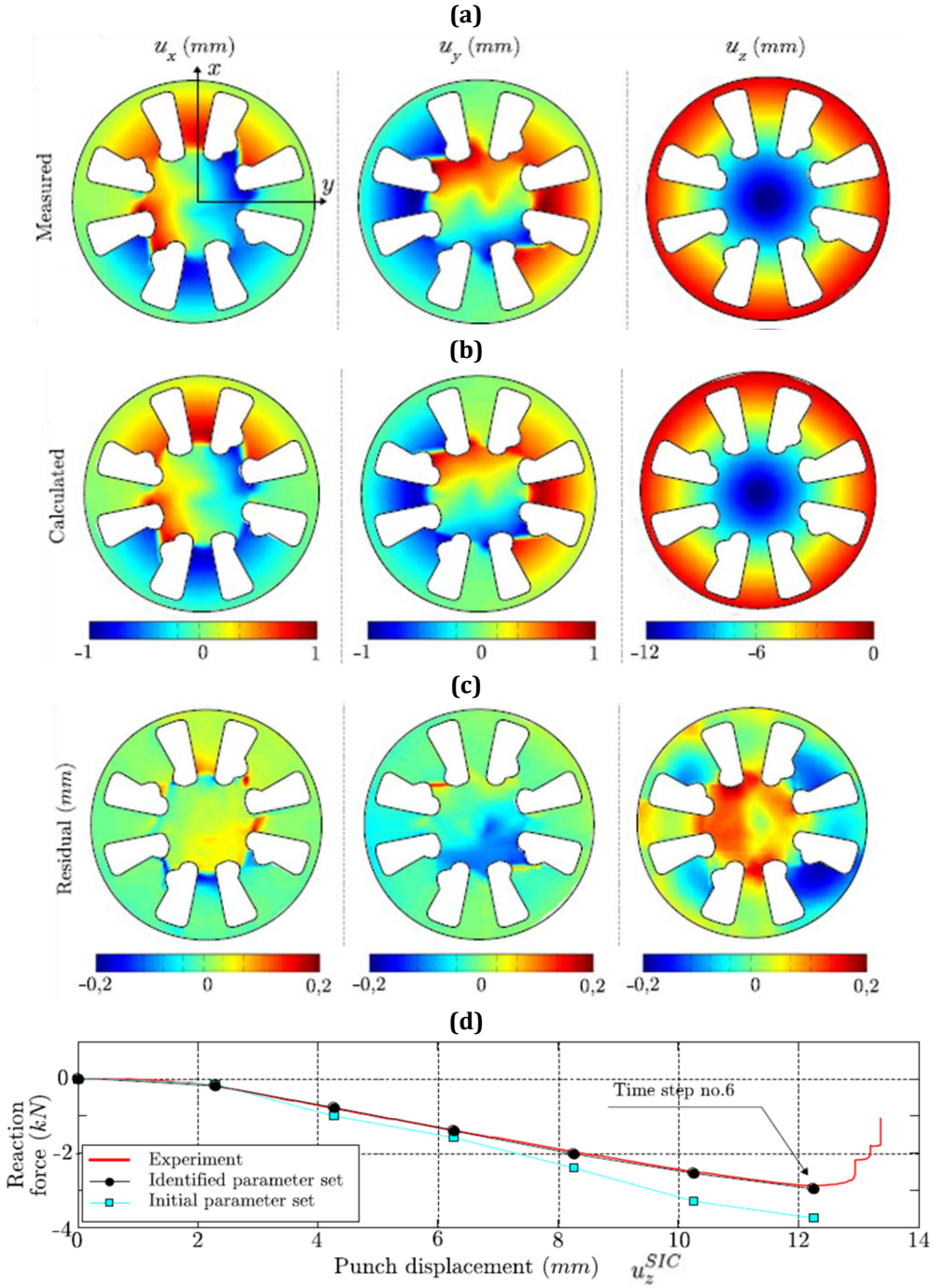

Figure 3.3. Results of the out-of-plane test: (a) and (b) experimental and numerically generated (at the end of the identification) displacement fields along the 0x, 0y and 0z axes, (c) corresponding residual differences and (d) global load *vs.* punch displacement results, as determined experimentally and from the two sets of parameters, initial and at the end of the identification [21]. The results in (a), (b) and (c) concern the loading step 6.

To assess the quality of the identified set of constitutive parameters, the authors performed deep-drawing tests of a circular cup. Moreover, additional identifications of the constitutive parameters of the material were performed, following two different strategies: a classic, based on three tensile tests cut along three different directions in the sheet plane, and an inverse identification strategy using heterogeneous planar shear-like tests, previously proposed [20]. The experimental results of the earing profile of the circular cup were then compared with the numerically predicted from the different parameter identification strategies, as shown in Figure 3.4. The authors concluded that the use of the non-planar sample allows a more accurate prediction of the earing profile than the planar shear-like tests and the three tensile tests, since the non-planar sample test covers a wider range of strain paths.

This inverse identification procedure allows the simultaneous identification of the constitutive parameters (Hill'48 criterion and Ludwick hardening law) using the results of a unique mechanical test. However, the chosen mechanical test shows a relative degree of complexity and has the inconvenience of presenting contact with friction between the punch and the metal sheet, which always raises questions concerning the impact of contact with friction on the identification of the constitutive parameters.

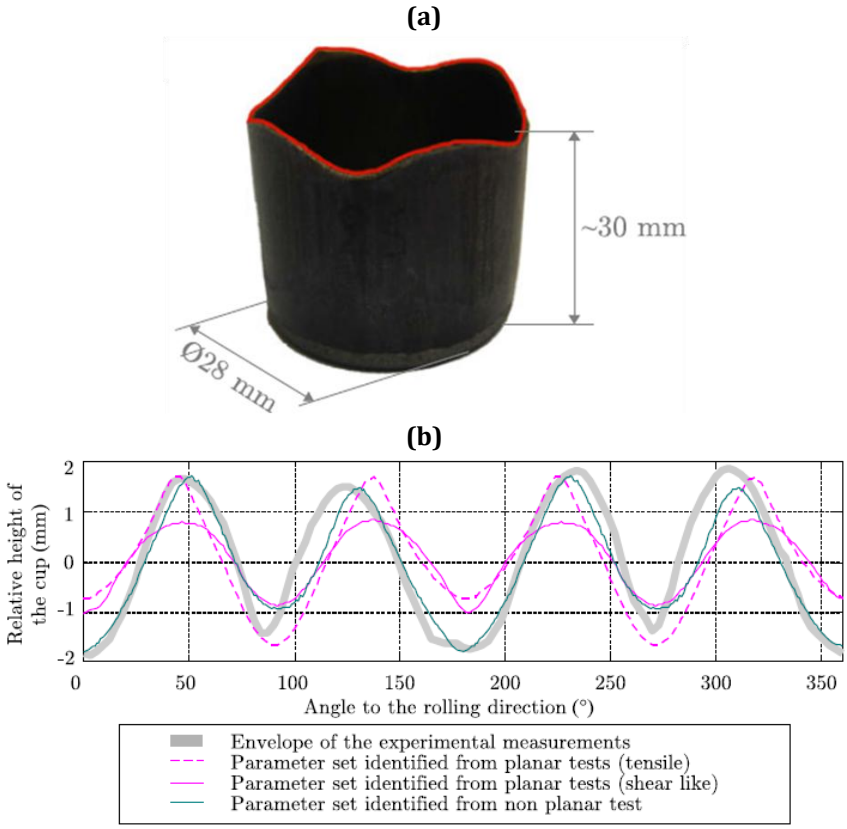

Figure 3.4. Circular cup test [21]: (a) earing profile (in red) and (b) experimental and simulated earing profiles.

3.3.2. Schmaltz & Willner [24]

Schmaltz & Willner [24] explored the usability of the cruciform biaxial test for the identification of constitutive parameters of metal sheets. Three sample geometries and two types of loading conditions were used. The material in this study was a 2.0-mm-thick DC04 sheet steel. The plastic behaviour was modelled via Hill'48 yield criterion and Hockett-Sherby hardening law. The identification of the constitutive parameters is based on FEMU procedure, and the cost-function is defined:

$$F(\mathbf{A}) = \sum_{l=1}^{2}\sum_{i=1}^{n}\left[(u_l^{\mathrm{Exp}})_i - (u_l^{\mathrm{Num}}(\mathbf{A}))_i\right]^2, \tag{3.14}$$

where $(u_l^{\mathrm{Exp}})_i$ and $(u_l^{\mathrm{Num}}(\mathbf{A}))_i$ are the experimentally determined and the numerically predicted values of the displacements at point i, respectively, in the 0x and 0y directions of the sheet plane (l = 1, 2). The minimisation of the cost-function is performed with the Levenberg-Marquardt algorithm, which starts with three different sets of initial parameters for each sample geometry to check if all cases converge to a similar result suggesting that the global optimum was reached. The identification procedure is split into two steps: the first step identifies the hardening law parameters assuming that the material is isotropic (i.e. von Mises), as commonly used in classical identification strategies [31]; in the second step, the anisotropic parameters are identified. The cost-function given by Eq. (3.14) is used in both steps. Afterwards, the results of the inverse identification are compared with those from homogeneous experimental tests.

The identification of the constitutive parameters was performed for 3 distinct geometries of the cruciform sample, using symmetrical biaxial loading conditions, with references "G#1", "G#2" and "G#3", as shown in Figures 3.5 (a), (b) and (c), respectively. The geometry "G#1" seeks to favour homogeneous strain distributions in the central area of the sample. The geometry "G#2" is similar to "G#1", but with a hole inserted in the centre of the sample to promote heterogeneous strain distributions. The geometry "G#3" is anti-symmetrical, so that the centre region rotates under biaxial tensile loading, allowing the occurrence of tension, shear and compressive states of stress, which enrich the inverse identification. Moreover, the authors use a fourth geometry of the test, called "G#4", which involves using the sample geometry of the test "G#2", but with compressive loads in the 0x direction and tensile loads in the 0y direction.

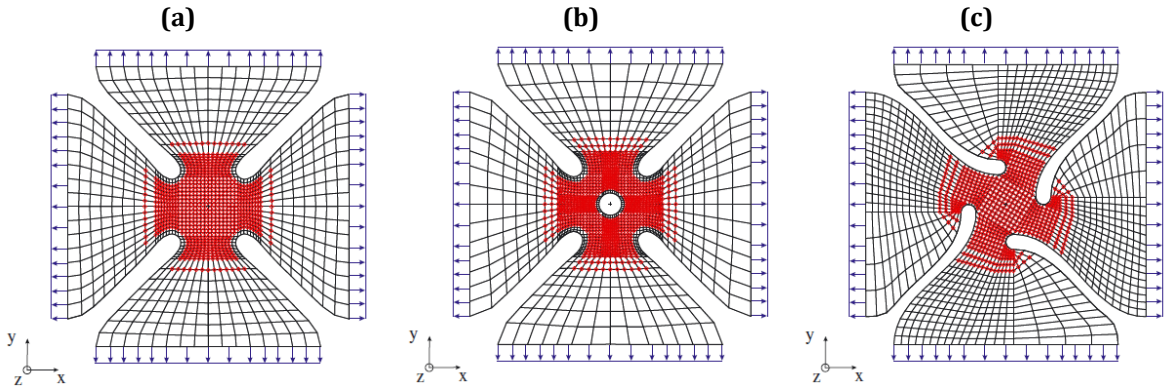

Figure 3.5. Modelling of the three cruciform sample geometries, with boundary conditions and measurement points (in red): (a) G#1; (b) G#2 and (c) G#3 [24].

The authors numerically evaluated the stress paths occurring for the four test geometries. Figure 3.6 shows the stresses at the mentioned loading values, for the horizontal, F_x, and vertical, F_y, axes of the sample, 0x and 0y, respectively. For the test "G#1" and "G#2" (Figure 3.6 (a) and (b)), the stress points are located in the first quadrant, but test "G#3" also shows compressive stresses. Figure 3.6 (d) highlights the occurrence of a wide range of points with compressive stresses for test "G#4", due to loading conditions that involve compressive loads in the 0x direction. The authors conclude that the test "G#4" is the most appropriate for the inverse parameter identification, since it covers the widest range of stress states. However, this test is difficult to accomplish experimentally, since metal sheets are prone to buckling. Therefore, the experimental loading conditions of test "G#4" were not equal to those of the numerical test, which results are shown in Fig. 3.6 (d).

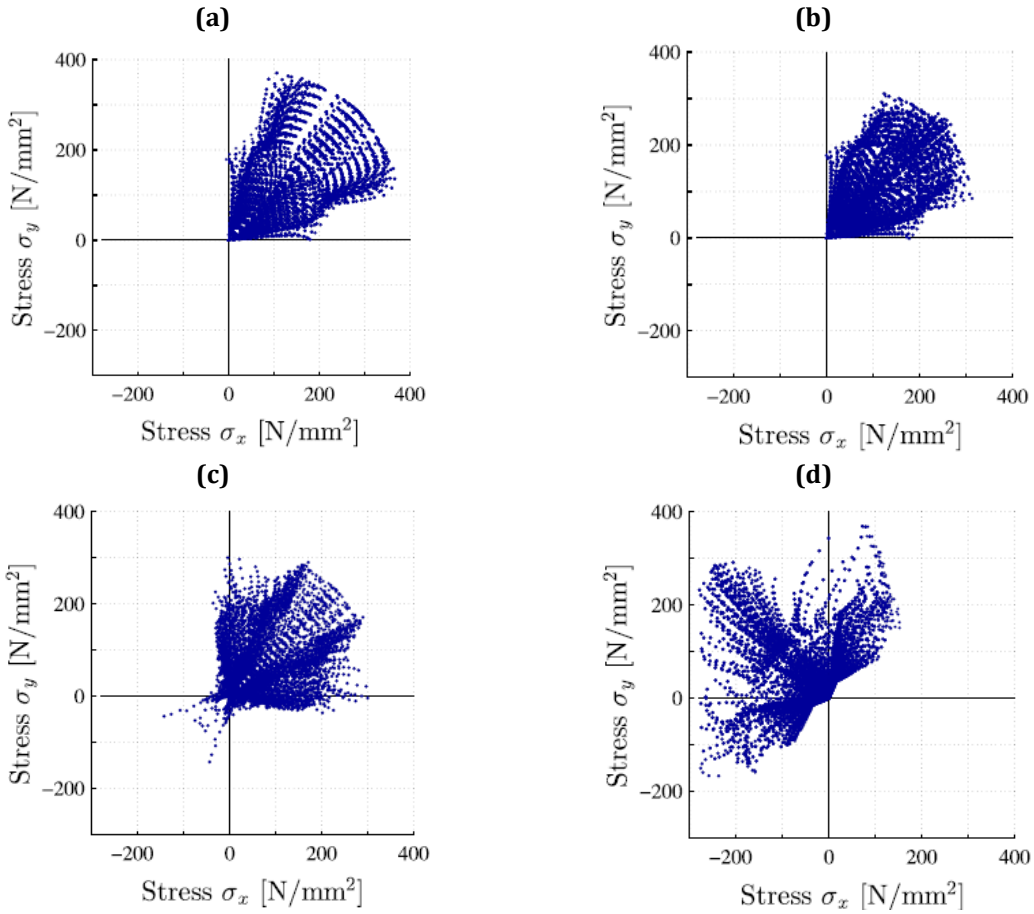

Figure 3.6. Numerically predicted stress distribution in the plane (σ_{xx} ; σ_{yy}): (a) G#1 $F_x = F_y = 10.0$ kN); (b) G#2 ($F_x = F_y = 8.0$ kN); (c) G#3 ($F_x = F_y = 5.0$ kN)and (d) G#4 ($-F_x = F_y = 6.0$ kN) [24].

Experimental tests were carried out for all test geometries and the 0x, 0y and 0z displacement fields were captured using an optical full-field measurement system. Figure 3.7 shows the measured equivalent displacement fields at the mentioned loading values.

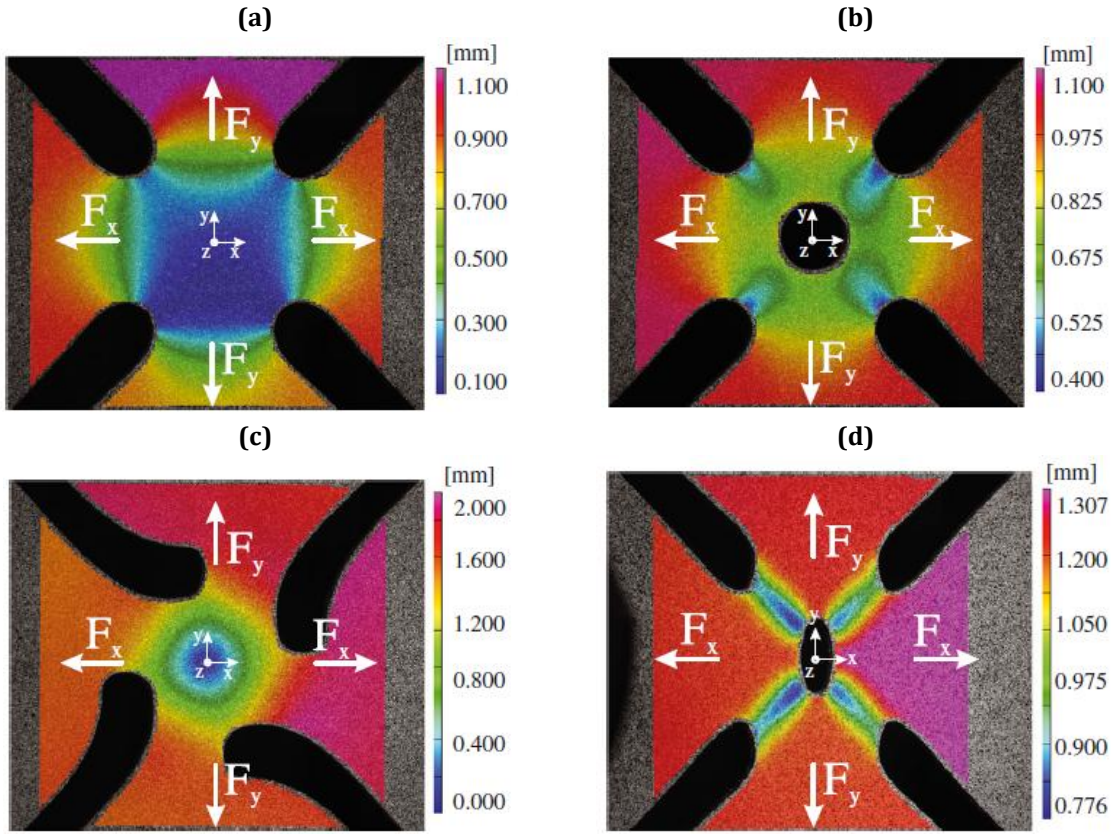

Figure 3.7. Experimental full-field measurements of equivalent displacements: (a) G#1 (F_x = 10.028 kN, F_y = 10.181 kN); (b) G#2 (F_x = 8.633 kN, F_y = 8.692 kN); (c) G#3 (F_x = 4.934 kN, F_y = 4.890 kN) and (d) G#4 (F_x = -3.830 kN, F_y = 5.603 kN) [24].

The experimental results of the major and minor strains, in the sheet plane, were plotted for all test geometries, as shown in Figure 3.8, for the loading conditions as in Figure 3.7. The geometries "G#2" and "G#3" show a wider range of strain distributions than the remaining geometries.

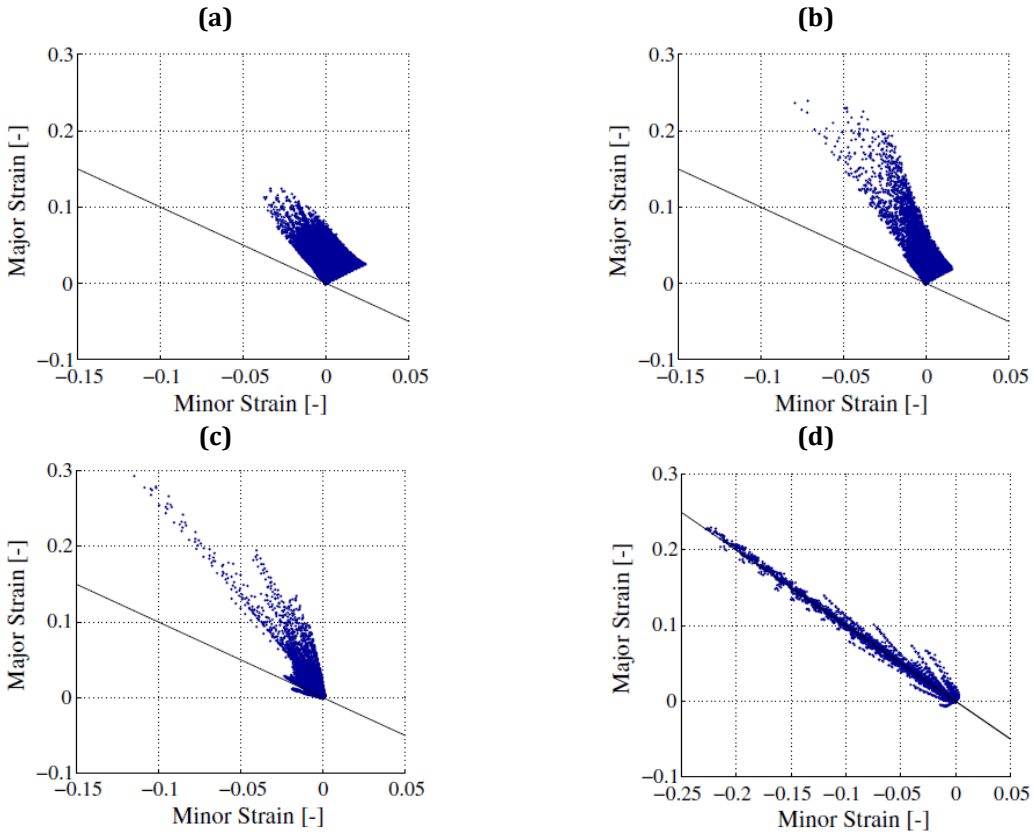

Figure 3.8. Experimentally measured major *vs.* minor strain plots: (a) G#1; (b) G#2; (c) G#3 and (d) G#4 [24].

The first step of the identification procedure only optimises two parameters of the Hockett-Sherby hardening law (Y_0 and Y_{Sat}), while keeping the values of the remaining two parameters (C_Y and a) equal to those obtained by fitting the experimental results determined from the biaxial tensile test (and extrapolated for large strain values). The optimisation procedure was started with three different initial sets of parameters that lead to quite similar optimised values, for each test geometry. Nevertheless, the results displayed in Figure 3.9 shows that the identified hardening curves depend on the test geometry. The authors affirm that the identified curve from test "G#3" is not reasonable due to premature damage of the material and so this geometry was excluded from the second step of the inverse identification procedure. They state that the identified hardening curves are different due to the distinct loading conditions and geometry of the tests. Nevertheless, it is important to mention that the C_Y and a parameters were identified using biaxial tensile test, for very small strain values, as shown in Figure 3.9, and were kept fixed during the identification procedure. Surely, this option is adopted because it is unreasonable to estimate the hardening parameters using displacement fields at a single loading step.

Consequently, the procedure shows low capability to reproduce the experimental stress-strain curves.

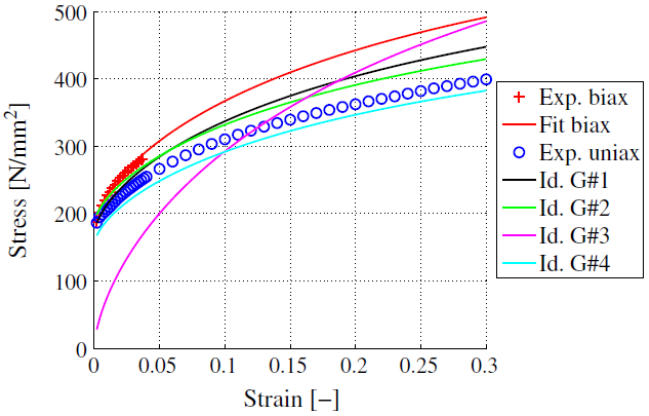

Figure 3.9. Identified stress-strain curves from all test geometries and experimental curves of the biaxial tensile test [24].

After the identification of the hardening law parameters, the authors use the same cost function (Eq. 3.14) for identifying the parameters of the Hill'48 criterion, assuming that the material is isotropic in the direction normal to the sheet plane, i.e. concerning the parameters associated with the out-of-plane shear stresses. Figure 3.10 plots the identified yield surfaces in the plane (σ_{xx} ; σ_{yy}), obtained from the three tests ("G#1", "G#2" and "G#3"), after the second step of the identification procedure, and the experimentally determined yield values, from homogeneous experimental tests. The yield surfaces for the tests "G#1" and "G#2" are quite similar, while the yield surface identified using test "G#4" presents lower yield stress values, which seems to be related to the spread of results in the identification of the hardening curves.

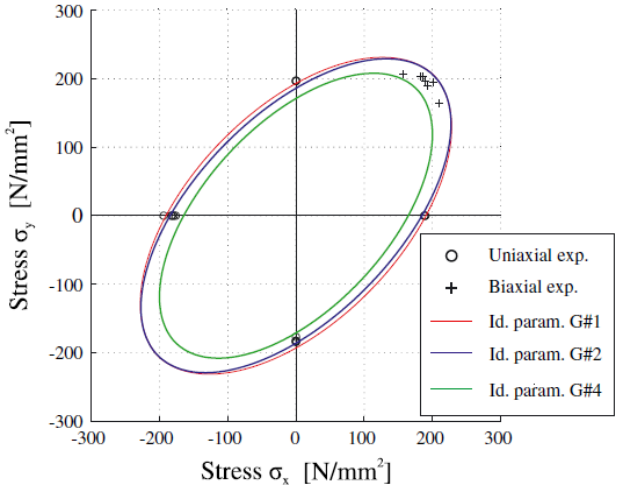

Figure 3.10. Identified yield surfaces in the plane (σ_{xx} ; σ_{yy}) from the geometries G#1, G#2 and G#3 and experimental yield values [24].

3.3.3. Cooreman et al. [25]

Cooreman et al. [25] proposed a FEMU strategy, for the simultaneous identification of Hill'48 yield criterion and Swift hardening law parameters. The experimental plastic behaviour of a 0.8-mm-thick DC06 sheet steel is determined based on a biaxial tensile test of a perforated cruciform sample (see Figure 3.11 (a)), and using full-field strain measurements at distinct load steps (7, in the case): 3.5, 3.76, 4.02, 4.08, 4.14, 4.22 and 4.25 kN (see Figure 3.11 (b)).

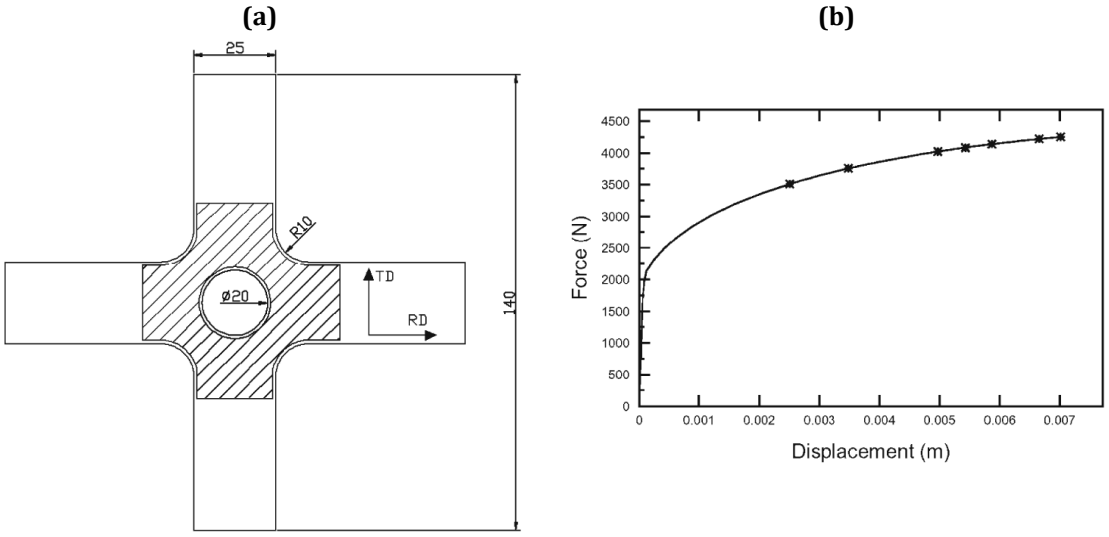

Figure 3.11. (a) Geometry of the cruciform sample and region of interest (shaded area); (b) load-displacement curve and loading steps for identification ("∗", in the curve) [25].

The cost function is defined:

$$F(\mathbf{A})=\frac{1}{3n}\left\{\sum_{i=1}^{n}\left[\left((\varepsilon_{xx}^{Exp})_i-(\varepsilon_{xx}^{Num}(\mathbf{A}))_i\right)^2+\left((\varepsilon_{yy}^{Exp})_i-(\varepsilon_{yy}^{Num}(\mathbf{A}))_i\right)^2+\left((\varepsilon_{xy}^{Exp})_i-(\varepsilon_{xy}^{Num}(\mathbf{A}))_i\right)^2\right]\right\}^{\frac{1}{2}}, \quad (3.15)$$

where $(\varepsilon^{Exp})_i$ and $(\varepsilon^{Num}(\mathbf{A}))_i$ are the experimentally determined and numerical values of the strain components ε_{xx}, ε_{yy} and ε_{xy} at point i, respectively, n is the total number of measuring points and $\mathbf{A}$ is the vector of the six parameters to be identified: parameters F, H and N of the Hill'48 criterion and K, ε_0 and n of the Swift law; the condition $G+H=1$ is assumed and 2D numerical simulations are performed. The initial estimate of parameters of the yield criterion corresponds to isotropy and the initial values of Swift hardening law parameters are chosen according to those typical of mild steel. The minimisation of the cost-function is performed with the Gauss-Newton algorithm, and stopped when the greatest update value, within all parameters, is less than 0.5% of the previous value of the each parameter, which occurs after 5 iterations.

The results from the inverse identification were compared with those obtained using classical homogeneous tests using two distinct strategies [32]. In one of them, herein referred to as "Classical_A", the Hill'48 parameters are identified from the anisotropy coefficients obtained with three tensile tests (in directions RD, TD, and making 45° with the RD), as traditionally. The other strategy, referred to as "Classical_B", is based on stress-state fitting of the initial yield surface making use of 8 experimental tests (3 tensile, 3 plane strain and 2 shear tests). In both strategies, the hardening parameters are determined by using uniaxial tensile tests at different angles with respect to RD (0°, 45°, and 90°). Table 3.1 shows the identified parameters of the Hill'48 criterion and the Swift law, by the inverse and classical identification strategies. According to the authors, the results from the inverse strategy are similar to those from the two classical strategies, except for the parameter ε_0. The similarities in the yield parameters are more evident for the inverse strategy and "Classical B", since both use a wider range of data than the "Classical A". Nevertheless, the discrepancy in the value of ε_0, determined by inverse and classical strategies, leads to clearly different yield stress values and hardening behaviour. For better comparing the results of the three identification strategies, Figures 3.12 (a) and (b) show the results of the equivalent stress-strain curves and the yield surfaces (not shown by the authors), respectively, which were constructed from the values of the parameters shown in Table 3.1. The authors attribute the discrepancy of ε_0 results to the use of a cost function based on strain field results from loading steps that neglect the beginning of the test, as shown in Figure 3.11 (b). They suggest performing the inverse identification using additional strain fields from loading steps located near the onset of plastic deformation. In our opinion, a simpler alternative, from the experimental point of view, would be to use a cost function that includes the load-displacement curves for both axes of the cruciform sample.

Table 3.1. Constitutive parameters of the Hill'48 criterion and the Swift law identified from the inverse identification strategy ("Inverse") and classical identification strategies ("Classical_A" and "Classical_B") [25].

Strategy	Hill'48 anisotropy parameters			Swift hardening law parameters		
	F	H	N	ε_0	K [MPa]	n
Inverse	0.405	0.633	1.438	0.00253	493	0.257
Classical_A	0.260	0.665	1.270	0.0063	500	0.250
Classical_B	0.495	0.505	1.520	0.0063	500	0.250

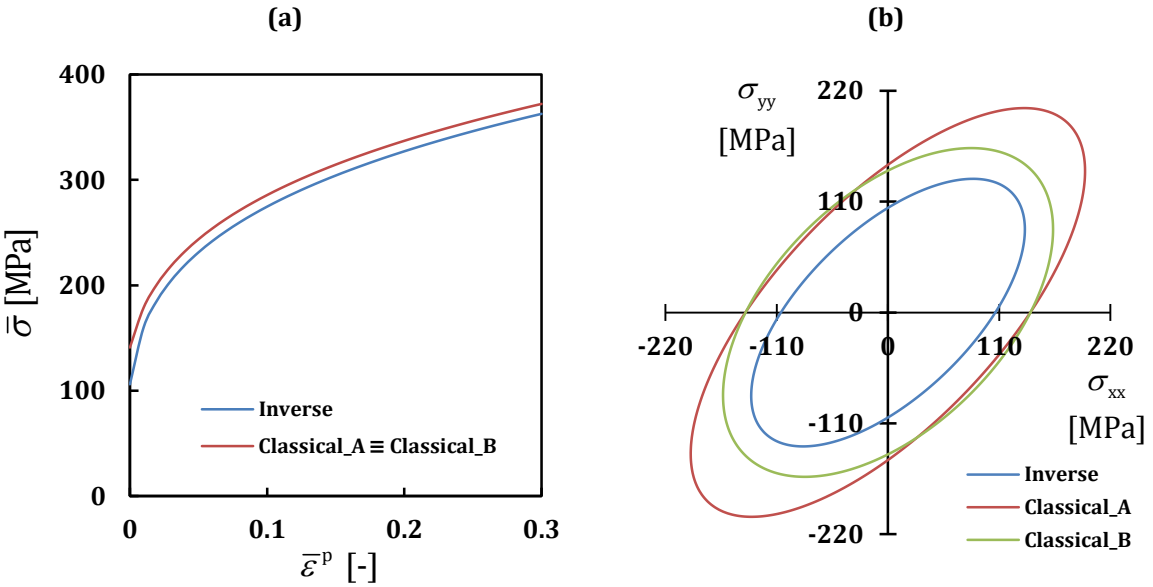

Figure 3.12. Comparison between the results of the inverse identification strategy (Inverse) and those of the classical identification of the constitutive parameters ("Classical_A" and "Classical_B"): (a) equivalent stress *vs.* equivalent plastic strain curves and (b) initial yield surface in the plane (σ_{xx}; σ_{yy}).

3.3.4. Eggertsen & Mattiasson [9]

Eggertsen & Mattiasson [9] were focused on the identification of the hardening law with the main concern of the accurate prediction of springback. The goal was to select the hardening model able to accurately describe kinematic hardening features, such as the early re-yielding, transient behaviour, work-hardening stagnation and permanent softening (see Figure 2.7 in Chapter 2), taking in account also the complexity on the evaluation of its parameters. In this context, three-point bending tests (see Figure 3.13) on four typical materials from car manufacturing industry, were performed: two dual-phase steels (TKS-DP600HF and SSAB-DP600), from different suppliers and with different thicknesses, a mild steel (Voest-DX56D) and an interstitial-free steel (TKS-220IF).

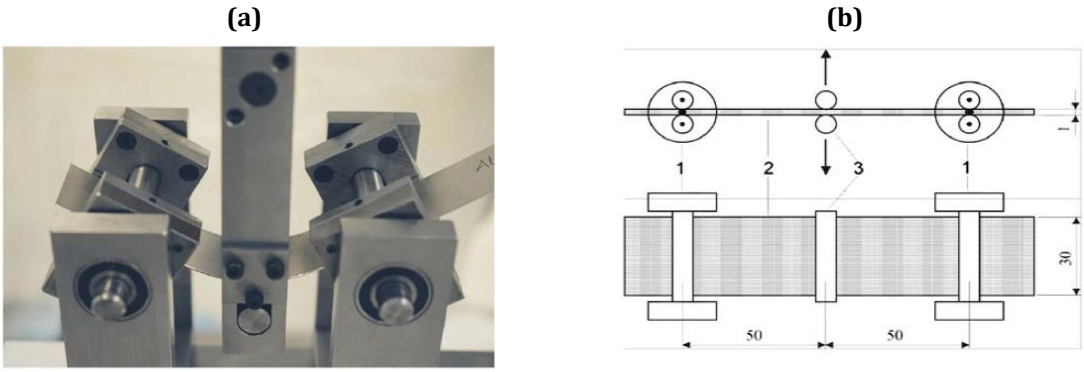

Figure 3.13. Device for three-point bending test [9]: (a), experimental set-up and (b) schematic representation of horizontal and vertical views.

Five different hardening models were considered: (i) a pure isotropic hardening law, used as comparative reference; (ii) a mixed isotropic-kinematic law, based on the works of Hodge [33] and Crisfield [34]; (iii) the Armstrong-Frederick model [35]; (iv) the Geng-Wagoner hardening law [36] and (v) the Yoshida-Uemori hardening law [37]. These models present increasing complexity, by adding one, two, three and four parameters to the pure isotropic hardening law, respectively. The hardening parameters of all models were determined by inverse analysis, where the difference between the experimentally and numerically generated load-displacement curves of the three-point bending test is minimised, through the following least-squares cost function:

$$F(\mathbf{A}) = \frac{1}{n}\sum_{i=1}^{n} w_i \left(\frac{P_i^{\mathrm{Num}}(\mathbf{A}) - P_i^{\mathrm{Exp}}}{s_i} \right)^2, \tag{3.16}$$

where $P_i^{\mathrm{Num}}(\mathbf{A})$ represent the calculated values of the punch load as a function of the vector of hardening parameters $\mathbf{A}$, and P_i^{Exp} represents the measured values of the punch load; s_i is the residual scale factor and w_i is the weight applied to each component of the cost function. Both s_i and w_i were set equal to 1. The inverse identification of the material parameters was performed using the LS-OPT® software package, resorting to Response Surface Methodology (RSM).

Firstly, a classical identification strategy was performed on all materials to determine the parameters of three yield criteria: Hill'48 [38], Barlat-Lian [39] and Banabic/Aretz [40, 41] criteria. Hill'48 and Barlat-Lian yield parameters were identified from the results of three tensile tests: the yield stress value in the RD and three anisotropy coefficients from tensile tests performed at 0°, 45° and 90° with the RD. Banabic/Aretz yield parameters were identified additionally using the values of equibiaxial yield stress and anisotropy coefficient from a viscous bulge test [42].

The authors performed a study concerning the influence of the yield criterion on the accuracy of the numerical prediction of the three-point bending test results. This study was only performed for TKS-DP600HF steel with the previously identified parameters of Hill'48, Barlat-Lian and Banabic/Aretz yield criteria. For all yield criteria, the Yoshida-Uemori hardening law parameters were identified. The accuracy of the results was evaluated based on the value of $F(\mathbf{A})$ (Eq. (3.16)). All yield criteria had quite similar values of $F(\mathbf{A})$, and the authors concluded that the selected yield criterion has a minor impact on the accuracy of the results. Moreover, they suggest that the yield criterion can have a major influence on springback prediction only for parts with pronounced biaxial stress states, which is not the case for the three-point bending test.

The inverse identification of the hardening parameters was performed for all models and materials using Banabic/Aretz yield criterion. The authors selected the results of only two bending cycles (bending-unbending-bending) as typically

observed in complex forming operations. Figure 3.14 shows the results for all hardening models, in case of TKS-DP600HF steel. The authors conclude that Yoshida–Uemori model provides the best result for all materials, while the isotropic hardening model gives the worst result. However, when taking into account the accuracy and the complexity of the hardening model, the authors indicate that Geng-Wagoner law corresponds to a better compromise. In fact, the authors state that about 30 simulations are needed to optimise the parameters of the mixed isotropic-kinematic hardening law, while up to 170 simulations are required to optimise the parameters of Yoshida-Uemori hardening law.

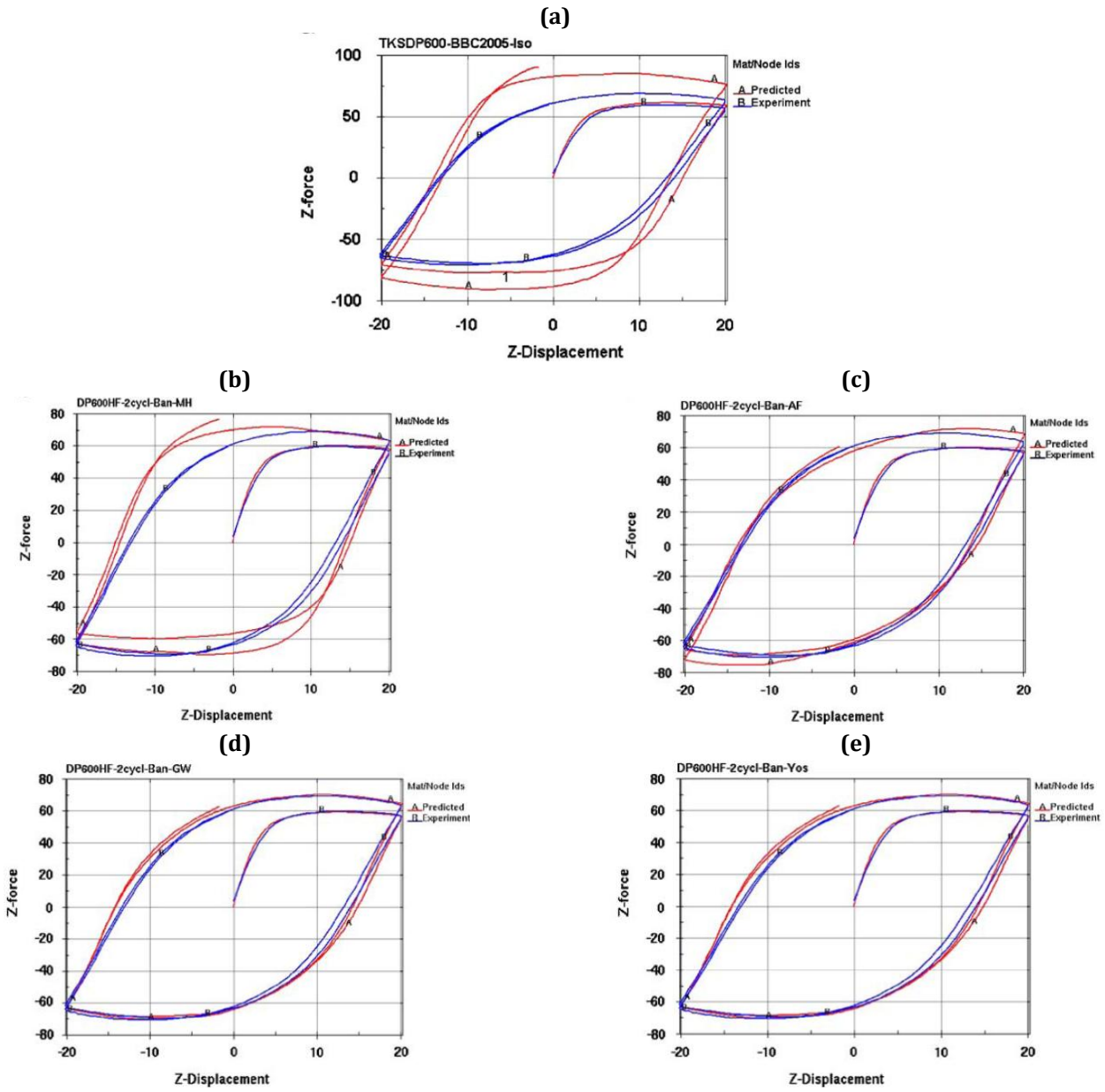

Figure 3.14. Comparison between numerical and experimental load *vs.* displacement results for the TKS-DP600HF steel [9], concerning: (a) Isotropic hardening; (b) mixed isotropic-kinematic hardening; (c) Armstrong-Frederick hardening; (d) Geng-Wagoner hardening and (e) Yoshida-Uemori hardening.

Finally, the identified hardening parameters were validated, by comparing the numerical with the experimental springback results, for the U-bend benchmark problem from the NUMISHEET'93 conference, as shown in Figure 3.15. The authors also performed numerical simulations taking into account the elastic stiffness degradation effect due to plastic straining. As main conclusion, the authors state that it is pointless to perform springback simulations without including the elastic stiffness degradation effect, since its influence on the accurate springback prediction is even larger than that of the hardening model.

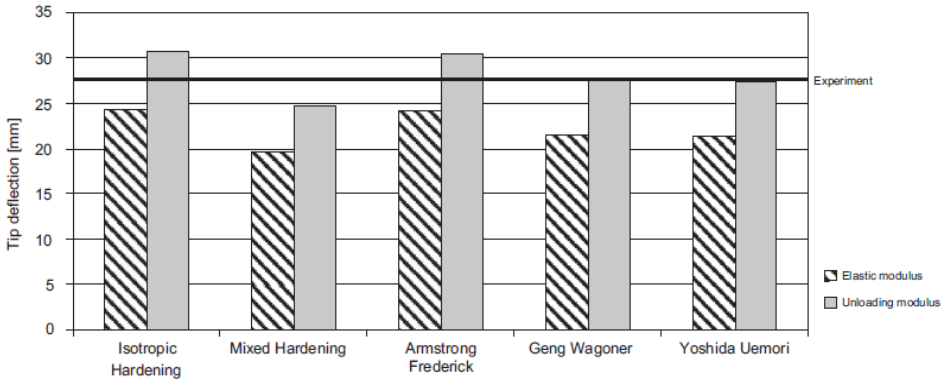

Figure 3.15. Numerical and experimental tip deflection results of U-bend test, for a constant elastic modulus ("Elastic modulus") and for elastic stiffness degradation effect ("Unloading modulus") [9].

In a more recent work [10], the same authors proposed the improvement of this identification strategy. In this case, the cost function is formulated with the computed and experimental bending moment results, at the mid-section of the sheet. This strategy allows a drastic reduction in the number of FE simulations and, consequently, in the computational time when compared to the original strategy. With the new strategy, the number of FE simulations required to optimise the parameters for the mixed isotropic-kinematic hardening law and for the Yoshida-Uemori hardening law is reduced to 4 and 13, respectively. Moreover, the results present an excellent correspondence with the parameters identified by the original strategy.

3.4. Final Remarks

This overview shows that the identification strategies, including the sample design, loading conditions and optimisation procedure, have had recent developments in order to make the identification of parameters easier and more accurate. The current trend is to develop strategies that allow the identification of all or the largest number of parameters of constitutive laws with the smallest possible number of tests. In this context, the four examples of the literature review are significant in the framework of this thesis.

References

[1] Cao J, Lin J (2008) A study on formulation of objective functions for determining material models, International Journal of Mechanical Sciences, 50, 193–204.

[2] Andrade-Campos A, de-Carvalho R, Valente RAF (2012) Novel criteria for determination of material model parameters. International Journal of Mechanical Sciences, 54, 294–305.

[3] Pottier T, Toussaint F, Vacher P (2011) Contribution of heterogeneous strain field measurements and boundary conditions modelling in inverse identification of material parameters. European Journal of Mechanics A/Solids, 30, 373–382.

[4] Ponthot J-P, Kleinermann J-P (2006) A cascade optimization methodology for automatic parameter identification and shape/process optimization in metal forming simulation. Computer Methods in Applied Mechanics and Engineering, 195, 5472–5508.

[5] Chaparro BM, Thuillier S, Menezes LF, Manach PY, Fernandes JV (2008) Material parameters identification: Gradient-based, genetic and hybrid optimization algorithms. Computational Materials Science, 44, 339–346.

[6] Meuwissen M (1998) An Inverse Method for the Mechanical Characterisation of Metals. PhD Thesis, Technische Universiteit Eindhoven.

[7] Cooreman S (2008) Identification of the plastic material behaviour through full-field displacement measurements and inverse methods. PhD Thesis, Vrije Universiteit Brussel.

[8] D.W. Marquardt DW (1963) An algorithm for least-squares estimation of nonlinear parameters. Journal of the Society for Industrial and Applied Mathematics, 11, 431–441.

[9] Eggertsen P-A, Mattiasson K (2009) On the modelling of the bending–unbending behaviour for accurate springback predictions. International Journal of Mechanical Sciences, 51, 547–563.

[10] Eggertsen P-A, Mattiasson K (2010) An efficient inverse approach for material hardening parameter identification from a three-point bending test. Engineering with Computers, 26, 159–170.

[11] Kuwabara T (2007) Advances in experiments on metal sheets and tubes in support of constitutive modeling and forming simulations. International Journal of Plasticity, 23, 385–419.

[12] Rabahallah M, Balan T, Bouvier S, Bacroix B, Barlat F, Chung K, Teodosiu C

(2009) Parameter identification of advanced plastic strain rate potentials and impact on plastic anisotropy prediction. International Journal of Plasticity, 25, 491–512.

[13] Güner A, Soyarslan C, Brosius A, Tekkaya AE (2012) Characterization of anisotropy of sheet metals employing inhomogeneous strain fields for Yld2000-2D yield function. International Journal of Solids and Structures, 49, 3517–3527.

[14] Güner A, Zillmann B, Lampke T, Tekkaya AE (2014) In-situ measurement of loading stresses with x-ray diffraction for yield locus determination. International Journal of Automotive Technology, 15, 303–316.

[15] Avril S, Bonnet M, Bretelle A-S, Grédiac M, Hild F, Ienny P, Latourte F, Lemosse D, Pagano S, Pagnacco E, Pierron F (2008) Overview of Identification Methods of Mechanical Parameters Based on Full-field Measurements. Experimental Mechanics, 48, 381–402.

[16] Xiao-qiang LI, De-hua HE (2013) Identification of material parameters from punch stretch test, Transactions of Nonferrous Metals Society of China, 23, 1435–1441.

[17] Chamekh A, Bel Hadj Salah H, Hambli R (2009) Inverse technique identification of material parameters using finite element and neural network computation. International Journal of Advanced Manufacturing Technology, 44, 173–179.

[18] Oliveira MC, Alves JL, Chaparro BM, Menezes, LF (2007) Study on the influence of work-hardening modeling in springback prediction. International Journal of Plasticity, 23, 516–543.

[19] Kajberg J, Lindkvist G (2004) Characterisation of materials subjected to large strains by inverse modelling based on in-plane displacement fields. International Journal of Solids and Structures, 41, 3439–3459.

[20] Pottier T, Toussaint F, Vacher P (2011) Contribution of heterogeneous strain field measurements and boundary conditions modelling in inverse identification of material parameters. European Journal of Mechanics A/Solids, 30, 373–382.

[21] Pottier T, Vacher P, Toussaint F, Louche H, Coudert T (2012) Out-of-plane Testing Procedure for Inverse Identification Purpose: Application in Sheet Metal Plasticity. Experimental Mechanics, 52, 951–963.

[22] Robert L, Velay V, Decultot N, Ramde S (2012) Identification of hardening parameters using finite element models and full-field measurements: some case studies. Journal of Strain Analysis for Engineering Design, 47, 3–17.

[23] Haddadi H, Belhabib S (2012) Improving the characterization of a hardening law using digital image correlation over an enhanced heterogeneous tensile test. International Journal of Mechanical Sciences, 62, 47–56.

[24] Schmaltz S, Willner K (2014) Comparison of Different Biaxial Tests for the Inverse Identification of Sheet Steel Material Parameters. Strain, 1–15.

[25] Cooreman S, Lecompte D, Sol H, Vantomme J, Debruyne D (2008) Identification of Mechanical Material Behavior Through Inverse Modeling and DIC. Experimental Mechanics 48, 421–433.

[26] Zhang S, Leotoing L, Guines D, Thuillier S, Zang S (2014) Calibration of anisotropic yield criterion with conventional tests or biaxial test. International Journal of Mechanical Sciences, 85, 142–151.

[27] Pierron F, Avril S, The Tran V (2010) Extension of the virtual fields method to elasto-plastic material identification with cyclic loads and kinematic hardening. International Journal of Solids and Structures, 47, 2993–3010.

[28] Pannier Y, Avril S, Rotinat R, Pierron F (2006) Identification of Elasto-Plastic Constitutive Parameters from Statically Undetermined Tests Using the Virtual Fields Method. Experimental Mechanics, 46, 735–755.

[29] Kim J-H, Barlat F, Pierron F, Lee M-G (2014) Determination of Anisotropic Plastic Constitutive Parameters Using the Virtual Fields Method. Experimental Mechanics, 54, 1189–1204.

[30] Pottier T (2010) Identification paramétrique par recalage de modèles éléments finis couplée à des mesures de champs cinématiques et thermiques. PhD Thesis, University of Savoie.

[31] Bouvier S, Teodosiu C, Maier C, Banu M, Tabacaru V (2001) Selection and identification of elastoplastic models for the materials used in the benchmarks, WP3, Task 1, 18-Months progress report of the Digital Die Design Systems (3DS), IMS 1999 000051.

[32] Flores P (2005) Development of experimental equipment and identification procedures for sheet metal constitutive laws. PhD thesis, Université de Liège.

[33] Hodge PG (1957) A new method of analyzing stresses and strains in work hardening solids. Transactions of ASME, Journal of Applied Mechanics, 24, 482–3.

[34] Crisfield MA (2001) More plasticity and other material non-linearity-II. Non-linear finite element analysis of solids and structures, vol. 2. Chichester, UK: Wiley, 158–64.

[35] Armstrong PJ, Frederick CO (1966) A mathematical representation of the multiaxial Bauschinger effect. GEGB Report RD/B/N 731.

[36] Geng L, Shen Y, Wagoner R H (2002) Anisotropic hardening equations derived from reverse-bend testing. International Journal of Plasticity, 18, 743–67.

[37] Yoshida F, Uemori T (2002) A model of large-strain cyclic plasticity describing the Bauschinger effect and workhardening stagnation. International Journal of Plasticity, 18, 661–686.

[38] Hill R (1948) A theory of yielding and plastic flow of anisotropic metals. Proc. R. Soc. London, 193, 281–297.

[39] Barlat F, Lian J. (1989) Plastic behaviour and stretchability of sheet metals. Part I: a yield function for orthotropic sheets under plane stress condition. Interna-

tional Journal of Plasticity, 5, 51–66.

[40] Banabic D, Aretz H, Comsa DS, Paraianu L (2005) An improved analytical description of orthotropy in metallic sheets. International Journal of Plasticity, 21, 493–512.

[41] Aretz H. (2005) A non-quadratic plane stress yield function for orthotropic sheet metals. Journal of Material Processing Technology, 168, 1–9.

[42] Sigvant M, Mattiasson, Vegter H, Thilderkvist P (2009) A viscous pressure bulge test for the determination of a plastic hardening curve and equibiaxial material data. International Journal of Material Forming, 2, 235–242.

(Page intentionally left blank)

Chapter 4

Contribution to the Development of Inverse Identification Strategies

This chapter presents the contributions of this research in the framework of inverse strategies for constitutive parameters identification. It consists of an introductory subchapter that summarises and contextualises the developed work, highlighting the contrast with former methodologies detailed in Chapter 3. The remaining subchapters correspond to the collection of publications that represent the innovative work.

(Page intentionally left blank)

4.1. General Framework

Firstly, a general methodology for equivalence between sets of plastic constitutive parameters is established. Besides the intrinsic interest of this equivalence, this methodology has favoured the study and development of the inverse strategies for the constitutive parameters identification.

Afterwards, two strategies for simultaneously identifying the parameters of the anisotropic yield criteria and isotropic hardening law of sheet metals are proposed. The well-known biaxial tensile test of a cruciform sample was chosen, and its geometry was selected by means of a numerical study in order to allow a wide range of strain paths in the measured region of the sample and to maximise the sensitivity of the test results to the values of the constitutive parameters (see Appendix for details).

The work was initially addressed for the identification of the parameters of the Hill'48 yield criterion and the Swift hardening law. A simple optimisation procedure was used, i.e. without resorting to traditional cost functions. Afterwards, a general inverse identification strategy that sequentially uses three distinct cost functions was developed. This strategy allows the identification of parameters of numerous yield criteria and hardening laws. It can be applied directly for a given criteria or, sequentially, starting from the Hill'48 criterion and then using the Hill'48 solution as an initial estimate for identifying the parameters of other criteria, on the condition that they can be converted into the Hill'48 criterion for particular values of the parameters.

Finally, an inverse analysis methodology for identifying the parameters of the kinematic law is outlined. This strategy suggests the use of a modified shear sample with a cylindrical notch along the axis of the sample (details on the study of the notch geometry are found in [1]), in order to confine the plastic deformation within the entire gauge section, which is not always the case of the classical shear samples with constant thickness.

It is also important to mention the approach chosen to support the performance analysis of the strategies that uses computer generated results instead of the commonly used experimental results. In fact, the use of experimental results to assess the performance of the identification methodologies is always unsatisfactory and problematic. Unsatisfactory, when the comparison between experimental and identified results is performed using simple classical tests, which are not representative of the whole plastic behaviour, even if in a large number. Problematic, when using the approach commonly adopted that consists on the direct comparison

between the assessed results with those obtained with other identification strategies. This allows comparing strategies, but does not assess the extent to which each model and strategy is efficiently able to represent the mechanical behaviour of the material. In general, none constitutive model and identification strategy allow perfectly describing the behaviour of a given material. Finally, it should also be noted that the use of complex deep-drawing tests for assessing the performance of the identification is sensitive to process parameters. In summary, the comparison with experimental results leads to difficulties hardly surmountable when wanting to fully evaluate the capability of the strategy under study. The use of computer-generated results allows conducting a more successful analysis, since it allows the directly comparison of the identified constitutive models with those used as input.

In order to contextualise the work undertaken in this thesis, Table 4.1 shows an overview of the inverse identification strategies addressed in this chapter and the case studies from literature detailed in Chapter 3. Chapter 5 emphasizes the main enhancements of the present work.

Table 4.1. Comparative overview of inverse identification strategies, including the addressed in the current Chapter

Author	Type of test	Strain paths	Strain path reversal	Constitutive model	Optimisation Steps	Number of cost functions	Analysed Results	Measuring instants
Pottier et al. [2]	Out-of-plane test	Shear to Biaxial stretching	No	Hill'48 Criterion + Ludwick isotropic law	One	One	Load + Displacement field (3D)	Various (6)
Schmaltz & Willner [3]	Cruciform biaxial tensile test	Shear to Biaxial stretching (but depending on the test geometry)	No	Hill'48 criterion + Hockett-Sherby isotropic law (only 2/4 parameters identified)	Two steps using the same cost function	One	Displacement field (2D)	One
Cooreman et al. [4]	Cruciform biaxial tensile test	Tension to Biaxial stretching	No	Hill'48 criterion + Swift isotropic law	One	One	Strain field (2D)	Various (7)
Eggertsen & Mattiasson [5]	Three-point bending test	Tension - Compression	Yes	Various kinematic laws (4)	One	One	Load	During the test
Prates et al. [6]	Cruciform biaxial tensile test	Tension to Biaxial stretching	No	Hill'48 criterion + Swift isotropic law	Five steps using four cost functions	Four	Load + Equivalent strain field (1D)	During the test One
Prates et al. [7]	Cruciform biaxial tensile test	Tension to Biaxial stretching	No	Various criteria (4) + Swift and Voce isotropic laws	Two (Hill'48 criterion) or Three (other criteria)	Two or Three	Load + Equivalent strain field (1D) + Strain path field (1D)	During the test One One
Pereira et al. [8]	Shear test	Shear with reversal	Yes	Lemaître -Chaboche kinematic law	One	One	Load	During the test

Note: 1D - in one direction in the sheet plane; 2D on the surface of the sheet plane; 3D - three-dimensional

References

[1] Pereira AFG (2013) Novos Métodos para a Determinação da Lei de Encruamento Cinemático em Chapas Metálicas. MSc thesis, University of Coimbra.

[2] Pottier T, Vacher P, Toussaint F, Louche H, Coudert T (2012) Out-of-plane Testing Procedure for Inverse Identification Purpose: Application in Sheet Metal Plasticity. Experimental Mechanics, 52, 951–963.

[3] Schmaltz S, Willner K (2014) Comparison of Different Biaxial Tests for the Inverse Identification of Sheet Steel Material Parameters. Strain, 1–15.

[4] Cooreman S, Lecompte D, Sol H, Vantomme J, Debruyne D (2008) Identification of Mechanical Material Behavior Through Inverse Modeling and DIC. Experimental Mechanics 48, 421–433.

[5] Eggertsen P-A, Mattiasson K (2009) On the modelling of the bending–unbending behaviour for accurate springback predictions. International Journal of Mechanical Sciences, 51, 547–563.

[6] Prates PA, Oliveira MC, Fernandes JV (2014) A new strategy for the simultaneous identification of constitutive laws parameters of metal sheets using a single test. Computational Materials Science, 85, 102–120.

[7] Prates PA, Oliveira MC, Fernandes JV (2014) Sequential inverse identification of constitutive parameters in metal sheets under a single biaxial tensile test. International Journal of Mechanical Sciences (Submitted).

[8] Pereira AFG, Prates PA, Sakharova NA, Oliveira MC, Fernandes JV (2014) On the identification of kinematic hardening with reverse shear test. Engineering with Computers, 1–10.

4.2. On the equivalence between sets of parameters of the yield criterion and the isotropic and kinematic hardening laws

This subchapter contains the paper "On the equivalence between sets of parameters of the yield criterion and the isotropic and kinematic hardening laws", published in International Journal of Material Forming. This work allows the proper comparison of full sets of constitutive parameters, which for a given material depends of assumptions implemented in the identification strategy. It shows that distinct sets of parameters can describe the same material behaviour.

(Page intentionally left blank)

Int J Mater Form
DOI 10.1007/s12289-014-1173-z

THEMATIC ISSUE: ADVANCED MODELING AND INNOVATIVE PROCESSES

On the equivalence between sets of parameters of the yield criterion and the isotropic and kinematic hardening laws

P. A. Prates · M. C. Oliveira · J. V. Fernandes

Received: 23 December 2013 / Accepted: 14 April 2014

Abstract The identification of the material parameters of a given constitutive model can follow diverse methodologies and use distinct sets of experimental data. In order to easily compare different sets of material parameters, it is necessary to know how to establish the equivalence between identification results. This work explores the correlation between sets of parameters of constitutive models concerning the yield criterion and the isotropic and kinematic hardening laws. It is shown that distinct sets of parameters for a given constitutive model (yield criterion and isotropic and kinematic hardening laws) can describe the same material behavior, and a rule for matching the sets is established.

Keywords Constitutive law parameters · Yield criteria · Isotropic hardening law · Kinematic hardening law

Introduction

The numerical simulation of sheet metal forming processes has proven to be efficient and suitable to be used in a wide range of industries. Nevertheless, efforts are being made to improve the numerical simulation accuracy by developing improved constitutive material or friction models, or ameliorating the numerical methods employed. In fact, the accuracy of the numerical simulation results of sheet metal forming processes depends on the selected constitutive material model (e.g. [1–12]) but also on the procedure adopted to perform its parameters identification (e.g. [13–16]). In general, the identification strategies proposed are essentially optimisation problems, where the cost function quantifies dissimilarities between experimental and numerically generated results (i.e. obtained through the manipulation of the constitutive parameters), for each type of experimental test. Different algorithms have been adopted for this purpose (e.g. [14, 17, 18]). Regardless of the strategy used for the constitutive parameters identification, the results obtained by different authors and research centres may seem inconsistent and, moreover, not directly comparable to each other, even if they concern the same constitutive model. Furthermore, the parameters associated with the out-of-plane shear stress components are generally not identified due to experimental difficulties. Thus, their values are assumed "as in isotropy" (for example, $L = M = 1.5$ for Hill'48 criterion [19]) in the numerical model.

In this work, a general methodology for equivalence between sets of constitutive parameters is proposed, which can be applied to a wide range of yield criteria and isotropic and kinematic hardening laws. The meaning and consequences of the assumption "as in isotropy" for the parameters associated with the out-of-plane shear stresses, is also analysed.

Constitutive modelling

In plasticity, the constitutive model establishes a relation between the stress and plastic strain states of the deformable body. The full constitutive model describing the behavior of metal sheets is typically defined by a yield criterion, a hardening law and an associated flow rule. The yield criterion and the hardening law describe the yield surface of the material

P. A. Prates (✉) · M. C. Oliveira · J. V. Fernandes
CEMUC, Department of Mechanical Engineering, University of Coimbra, Pinhal de Marrocos, 3030-788 Coimbra, Portugal
e-mail: pedro.prates@dem.uc.pt

M. C. Oliveira
e-mail: marta.oliveira@dem.uc.pt

J. V. Fernandes
e-mail: valdemar.fernandes@dem.uc.pt

Published online: 04 June 2014

and its evolution during plastic deformation, which can be modelled through $\mathcal{F}$, such that

$$\mathcal{F}\left(\boldsymbol{\sigma}'-\mathbf{X}', \bar{\varepsilon}^{\mathrm{p}}\right) = \bar{\sigma}(\boldsymbol{\sigma}'-\mathbf{X}')-Y\left(\bar{\varepsilon}^{\mathrm{p}}\right)\leq 0, \tag{1}$$

where $\bar{\sigma}(\boldsymbol{\sigma}'-\mathbf{X}')$ is the equivalent stress, which is expressed according to a given yield criterion, and $Y(\bar{\varepsilon}^{\mathrm{p}})$ is the yield stress, respectively; the yield criterion defines the equivalent stress, $\bar{\sigma}(\boldsymbol{\sigma}'-\mathbf{X}') = \bar{\sigma}$, as a function of the effective stress tensor $(\boldsymbol{\sigma}'-\mathbf{X}')$ ($\boldsymbol{\sigma}'$ and $\mathbf{X}'$ are the deviatoric Cauchy stress and the deviatoric back-stress tensors, respectively); the hardening law represents the evolution of the yield stress, $Y(\bar{\varepsilon}^{\mathrm{p}}) = Y$, as a function of the equivalent plastic strain, $\bar{\varepsilon}^{\mathrm{p}}$.

When $\bar{\sigma} < Y$ the stress state of the material remains on the interior of the yield surface and only elastic deformation occurs. The condition $\bar{\sigma} = Y$ is related to the plastic state governed by the associated flow rule, which can be expressed

$$\mathrm{d}\boldsymbol{\varepsilon}^{\mathrm{p}} = \mathrm{d}\lambda \frac{\partial \bar{\sigma}(\boldsymbol{\sigma}'-\mathbf{X}')}{\partial(\boldsymbol{\sigma}'-\mathbf{X}')}, \tag{2}$$

where $\mathrm{d}\boldsymbol{\varepsilon}^{\mathrm{p}}$ is the increment of the plastic strain tensor, $\mathrm{d}\lambda$ is a scalar multiplier that depends on the value of the equivalent stress defined by a given yield criterion function, and $\bar{\sigma}(\boldsymbol{\sigma}'-\mathbf{X}')$ is the equivalent stress function, representing herein the plastic potential.

Equivalent sets of constitutive parameters

This section shows that different sets of constitutive law parameters can be selected without changing the description of the plastic behavior of a given material, by establishing an equivalence criterion between sets of parameters (each set containing parameters of the yield criterion, the hardening and kinematic laws). This applies not only to the Hill'48 criterion, but also to other anisotropic criteria, commonly used. In this work, Drucker's yield criterion extended to anisotropy by means of a linear transformation (Drucker + L) [20] and the generalisation of Drucker's yield criterion to anisotropy (CB2001) are also used as examples [20]. The following section examines various hypotheses for the standardisation of the set of parameters of the yield criterion, providing the framework of the subsequent analysis concerning the equivalence between sets of constitutive parameters.

Yield criterion parameters

In literature, the experimental identification of the material parameters for a given constitutive model, particularly the set of parameters of the yield criterion, does not follow any standardisation, which makes the comparison between sets of constitutive parameters of a given material, obtained by different research teams, often problematic.

For example, Hill'48 criterion can be comprehensively written with a multiplicative factor, K, inserted into the second member of the equation (as any other criterion), as follows:

$$F\left(\sigma_{\mathrm{yy}}-\sigma_{\mathrm{zz}}\right)^2 + G(\sigma_{\mathrm{zz}}-\sigma_{\mathrm{xx}})^2 + H\left(\sigma_{\mathrm{xx}}-\sigma_{\mathrm{yy}}\right)^2 + 2L\tau_{\mathrm{yz}}^2 + 2M\tau_{\mathrm{xz}}^2 + 2N\tau_{\mathrm{xy}}^2 = KY^2. \tag{3}$$

where F, G, H, L, M and N are the set of anisotropy parameters to be identified, and $\sigma_{\mathrm{xx}}, \sigma_{\mathrm{yy}}, \sigma_{\mathrm{zz}}, \tau_{\mathrm{yz}}, \tau_{\mathrm{xz}}, \tau_{\mathrm{xy}}$ are the components of Cauchy stress tensor $(\boldsymbol{\sigma})$ in the orthotropic frame, 0xyz.

The condition of isotropy applied to the Hill'48 criterion is fulfilled when the relationship between the anisotropy parameters is: $F=G=H=L/3=M/3=N/3=0.5$ if $K = 1$. The most appropriate way to standardise the set of parameters of Hill'48 criterion is demanding that Hill'48 criterion directly agrees with the isotropic von Mises criterion, written usually as:

$$0.5\left(\sigma_{\mathrm{yy}}-\sigma_{\mathrm{zz}}\right)^2 + 0.5(\sigma_{\mathrm{zz}}-\sigma_{\mathrm{xx}})^2 + 0.5\left(\sigma_{\mathrm{xx}}-\sigma_{\mathrm{yy}}\right)^2 + 3\tau_{\mathrm{yz}}^2 + 3\tau_{\mathrm{xz}}^2 + 3\tau_{\mathrm{xy}}^2 = Y^2. \tag{4}$$

Based on the comprehensive Hill'48 criterion formulation (Eq. (3)), it is possible to write:

$$\begin{cases} \sigma_{\mathrm{xx}}^2(G+H) = KY^2 & \text{(for tensile test in the 0x direction)} \\ \sigma_{\mathrm{yy}}^2(F+H) = KY^2 & \text{(for tensile test in the 0y direction)} \\ \sigma_{\mathrm{zz}}^2(F+G) = KY^2 & \text{(for tensile test in the 0z direction)} \\ 2L\tau_{\mathrm{yz}}^2 = KY^2 & \text{(for shear test in the 0yz plane)} \\ 2M\tau_{\mathrm{xz}}^2 = KY^2 & \text{(for shear test in the 0xz plane)} \\ 2N\tau_{\mathrm{xy}}^2 = KY^2 & \text{(for shear test in the 0xy plane)} \end{cases}. \tag{5}$$

Considering that in isotropy $\sigma_{\mathrm{xx}} = \sigma_{\mathrm{yy}} = \sigma_{\mathrm{zz}} = \sqrt{3}\tau_{\mathrm{yz}} = \sqrt{3}\tau_{\mathrm{xz}} = \sqrt{3}\tau_{\mathrm{xy}} = \sigma = Y$ (from Eq. (4)), where σ is the yield stress in tension, the following K values can be achieved:

$$\begin{cases} K = G + H \\ K = (F+G+H)/1.5 \\ K = \left[F+G+H+{}^{1}\!/_{3}(L+M+N)\right]/3 \end{cases}. \tag{6}$$

These equations are obtained considering, respectively: (i) only the first of Eqs. (5) (for tensile test in the 0x direction); (ii) the first three of Eqs. (5) and (iii) all Eqs. (5). Other considerations could be made to get K.

Under conditions such as in Eqs. (6), to have K=1 in Eq. (3), the set of parameters of Hill'48 criterion must obey the following relationships , as assumed by Bouvier et al. [21], Yamashita [22] and Prates et al. [23], respectively

$$\begin{cases} G+H=1 \\ F+G+H=1.5 \\ F+G+H+{}^{1}\!/_{3}(L+M+N)=3 \end{cases}. \tag{7}$$

But, most of the times, none of these conditions is assumed (e.g. [24]) for identifying the constitutive parameters, although K is usually taken equal to 1. Nevertheless, for a given material which behavior is fully described by Hill'48 criterion, the values of the parameters of the hardening law ($Y = Y(\bar{\varepsilon}^{p})$) depend on the condition for K, whether or not explicitly assumed, as discussed in the next section.

The same kind of analysis can be applied to any other yield criteria. Given the impossibility to address all criteria, we choose Drucker + L and CB2001 anisotropic yield criteria, as further examples.

Drucker + L criterion is an extension of Drucker isotropic criterion [25] to anisotropy, using the linear transformation **L**. In the general case (i.e. similarly to Eq. (3), for Hill'48 criterion), Drucker + L criterion is usually expressed:

$$\left\{\left[\frac{1}{2}\mathrm{tr}\left(\mathbf{s}^{2}\right)\right]^{3}-c\left[\frac{1}{3}\mathrm{tr}\left(\mathbf{s}^{3}\right)\right]^{2}\right\}^{1/3}=\frac{K}{3}Y^{2}, \tag{8}$$

where tr (**s**) is the trace of the matrix **s**; **s** is the stress tensor resulting from the linear transformation of Cauchy stress tensor and c is an isotropic parameter, ranging between –27/8 and 9/4 in order to ensure the convexity of the yield surface [20, 25]. When c is equal to zero, Drucker + L criterion coincides with Hill'48 yield criterion. The **s** stress tensor is given by.

$$\mathbf{s}=\mathbf{L}:\boldsymbol{\sigma}, \tag{9}$$

where **L** is the linear transformation operator, written as follows

$$\mathbf{L}=\begin{bmatrix} (C_2+C_3)/3 & -C_3/3 & -C_2/3 & 0 & 0 & 0 \\ -C_3/3 & (C_3+C_1)/3 & -C_1/3 & 0 & 0 & 0 \\ -C_2/3 & -C_1/3 & (C_1+C_2)/3 & 0 & 0 & 0 \\ 0 & 0 & 0 & C_4 & 0 & 0 \\ 0 & 0 & 0 & 0 & C_5 & 0 \\ 0 & 0 & 0 & 0 & 0 & C_6 \end{bmatrix}, \tag{10}$$

where C_k, (k=1 to 6) are anisotropy parameters. When the anisotropy parameters C_k are equal to each other, then the condition of isotropy for Drucker + L criterion is accomplished. If C_k are equal to each other and c=0, then von Mises criterion is recovered.

Different strategies can be adopted for defining K. For instance, an approach similar to the one used for Hill'48 criterion (based on three tensile tests and three shear tests (Eqs. (5)), but using Drucker + L anisotropic and Drucker isotropic criteria, leads to a complex equation for K which depends on the anisotropic parameters, C_k, and also on the isotropic parameter c. For keeping the simplicity, it is preferable to choose K as defined in Eqs. (6), which leads to K factors independent of c. This approach consists on using Drucker + L anisotropic criterion, with the condition c=0 (i.e. equivalent to Hill'48 criterion), and von Mises yield criterion as reference. Whatever the strategy, the K values are certainly not quite different. For the latter approach, the value of K can be determined according to Eqs. (6), and using the equations that relate the parameters of both criteria (with c=0) as follows:

$$\begin{cases} F=\left(2C_1^2+C_1C_2+C_1C_3-C_2C_3\right)/6 \\ G=\left(2C_2^2+C_1C_2+C_2C_3-C_1C_3\right)/6 \\ H=\left(2C_3^2+C_1C_3+C_2C_3-C_1C_2\right)/6 \\ L={}^{3}\!/_{2}C_4^2; M={}^{3}\!/_{2}C_5^2; N={}^{3}\!/_{2}C_6^2 \end{cases}. \tag{11}$$

The CB2001 criterion is a generalisation of the Drucker's isotropic criterion to anisotropy, and is written as follows:

$$\left(J_2{}^3-cJ_3{}^2\right)^{1/3}=\frac{K}{3}Y^{2}, \tag{12}$$

where J_2 and J_3 are, respectively, the second and third generalised invariants of the Cauchy stress tensor:

$$\begin{aligned} J_2 &= \frac{a_1}{6}(\sigma_{xx}-\sigma_{yy})^2+\frac{a_2}{6}(\sigma_{yy}-\sigma_{zz})^2+\frac{a_3}{6}(\sigma_{xx}-\sigma_{zz})^2+a_4\tau_{xy}^2 \\ &\quad +a_5\tau_{xz}^2+a_6\tau_{yz}^2 \\ J_3 &= \frac{1}{27}(b_1+b_2)\sigma_{xx}^3+\frac{1}{27}(b_3+b_4)\sigma_{yy}^3+\frac{1}{27}[2(b_1+b_4)-b_2-b_3]\sigma_{zz}^3 \\ &\quad -\frac{1}{9}(b_1\sigma_{yy}+b_2\sigma_{zz})\sigma_{xx}^2-\frac{1}{9}(b_3\sigma_{zz}+b_4\sigma_{xx})\sigma_{yy}^2 \\ &\quad -\frac{1}{9}[(b_1-b_2+b_4)\sigma_{xx}+(b_1-b_3+b_4)\sigma_{yy}]\sigma_{zz}^2 \\ &\quad +\frac{2}{9}(b_1+b_4)\sigma_{xx}\sigma_{yy}\sigma_{zz}-\frac{\tau_{xz}^2}{3}[2b_9\sigma_{yy}-b_8\sigma_{zz}-(2b_9-b_8)\sigma_{xx}] \\ &\quad -\frac{\tau_{xy}^2}{3}[2b_{10}\sigma_{zz}-b_5\sigma_{yy}-(2b_{10}-b_5)\sigma_{xx}] \\ &\quad -\frac{\tau_{yz}^2}{3}[(b_6+b_7)\sigma_{xx}-b_6\sigma_{yy}-b_7\sigma_{zz}]+2b_{11}\tau_{xy}\tau_{yz}\tau_{xz} \end{aligned}, \tag{13}$$

Coefficients a_k (k=1 to 6) and b_k (k=1 to 11) are the anisotropy parameters of the yield criterion (a_k and b_k are equal to 1 for the isotropy condition). As for Drucker + L criterion, the value of K for CB2001 criterion can be determined according to Eqs. (6), using the equations that relate its

parameters with the ones from Hill'48 criterion (with c=0) as follows:

$$F=\frac{1}{2}a_2;G=\frac{1}{2}a_3;H=\frac{1}{2}a_1;L=\frac{3}{2}a_6;M=\frac{3}{2}a_5;N=\frac{3}{2}a_4. \tag{14}$$

Nevertheless, also for this criterion, any other strategy can be used for defining K.

Yield criterion and isotropic hardening law

The identification of a set of parameters of the yield criterion and the isotropic hardening law usually follows Eqs. (3), (8) and (12), with K=1. In case of Hill'48 criterion, this corresponds to:

$$F\left(\sigma_{yy}-\sigma_{zz}\right)^2+G(\sigma_{zz}-\sigma_{xx})^2+H\left(\sigma_{xx}-\sigma_{yy}\right)^2+2L\tau_{yz}^2 +2M\tau_{xz}^2+2N\tau_{xy}^2=Y^2, \tag{15}$$

The identified parameters of the yield criterion can or cannot conform to conditions such as any of Eqs. (7). Whatever the condition, in view of establishing a methodology for equivalence between sets of constitutive parameters, Eq. (15) can be written as follows:

$$F^*\left(\sigma_{yy}-\sigma_{zz}\right)^2+G^*(\sigma_{zz}-\sigma_{xx})^2+H^*\left(\sigma_{xx}-\sigma_{yy}\right)^2+2L^*\tau_{yz}^2 +2M^*\tau_{xz}^2+2N^*\tau_{xy}^2=Y^{*2}, \tag{16}$$

where the first member of Eq. (15) is divided by K, which corresponds to consider:

$$F^*=F/K;G^*=G/K;H^*=H/K;L^*=L/K; M^*=M/K \text{ and } N^*=N/K. \tag{17}$$

The relationship between the right members of Eqs. (15) and (16) cannot be handled as simply as the left side, and so $Y=Y(\bar{\varepsilon}^{\mathrm{p}})$, in Eq.(15), is replaced by $Y^*=Y^*(\bar{\varepsilon}^{\mathrm{p}*})$, in Eq. (16).

Applying a similar procedure to the first member of Drucker + L criterion, the following relationship between parameters is obtained:

$$C_{\mathrm{k}}^*=C_{\mathrm{k}}/K^{1/2},c^*=c, \tag{18}$$

where C_{k} (C_{k}^*) represents the parameters C_1 (C_1^*) to C_6 (C_6^*).

In the case of the CB2001 criterion, the procedure leads to:

$$a_{\mathrm{k}}^*=a_{\mathrm{k}}/K,b_{\mathrm{k}}^*=b_{\mathrm{k}}/K^{3/2},c^*=c, \tag{19}$$

where a_{k} (a_{k}^*) and b_{k} (b_{k}^*) represent, respectively, the parameters a_1 (a_1^*) to a_6 (a_6^*) and b_1 (b_1^*) to b_{11} (b_{11}^*).

In the general case, the relationship between parameters (*) and ( ) are identical to Eqs. (17), (18) and (19), where K is raised to a power equal to the inverse of the power of the parameter appearing in the yield function, provided that the criterion is written such that the power of $Y=Y(\bar{\varepsilon}^{\mathrm{p}})$, in the second member, is equal to 2 (such as in Eqs. (3), (8) and (12)).

In order to relate the right members of the equations of the yield criterion (respectively $Y=Y(\bar{\varepsilon}^{\mathrm{p}})$ and $Y^*=Y^*(\bar{\varepsilon}^{\mathrm{p}*})$ in Eqs. (15) and (16), for the case of Hill'48 criterion), we make use of the definition of plastic work, which must be equal for both situations, at any moment of the deformation:

$$\mathrm{d}W=\bar{\sigma}\mathrm{d}\bar{\varepsilon}^{\mathrm{p}}=\bar{\sigma}^*\mathrm{d}\bar{\varepsilon}^{\mathrm{p}*} \tag{20}$$

In fact, knowing that the first member of Eq. (15), $\bar{\sigma}^2$, is related with the first member of Eq. (16), $\bar{\sigma}^{*2}$, through the K value by the equation $\bar{\sigma}^{*2}=\bar{\sigma}^2/K$ (i.e. $\bar{\sigma}^*=\bar{\sigma}/\sqrt{K}$), as long as the condition in Eq. (20) is fulfilled, the relationship $\mathrm{d}\bar{\varepsilon}^{\mathrm{p}*}=\sqrt{K}\mathrm{d}\bar{\varepsilon}^{\mathrm{p}}$ and so $\bar{\varepsilon}^{\mathrm{p}*}=\sqrt{K}\bar{\varepsilon}^{\mathrm{p}}$ is accomplished. In summary:

$$\begin{cases}\bar{\sigma}^*=\bar{\sigma}/\sqrt{K}\\ \bar{\varepsilon}^{\mathrm{p}*}=\sqrt{K}\bar{\varepsilon}^{\mathrm{p}}\end{cases}. \tag{21}$$

The accumulated plastic work, W, up to a given moment of the deformation, can be determined by integrating Eq. (20), where $\bar{\sigma}$ and $\bar{\sigma}^*$ were respectively replaced by $Y=Y(\bar{\varepsilon}^{\mathrm{p}})$ and $Y^*=Y^*(\bar{\varepsilon}^{\mathrm{p}*})$, satisfying the following condition:

$$W=\int_0^{\bar{\varepsilon}}Yd\bar{\varepsilon}^{\mathrm{p}}=\int_0^{\bar{\varepsilon}^*}Y^*d\bar{\varepsilon}^{\mathrm{p}*}. \tag{22}$$

Figure 1 illustrates the equality of plastic work expressed by Eq. (22), showing two cases of evolution of the yield stress vs. equivalent plastic strain, up to A (curve $Y=Y(\bar{\varepsilon}^{\mathrm{p}})$) and B (curve $Y^*=Y^*(\bar{\varepsilon}^{\mathrm{p}*})$).

The most commonly used functions for describing the hardening are Swift [26] and Voce [27] laws. For both

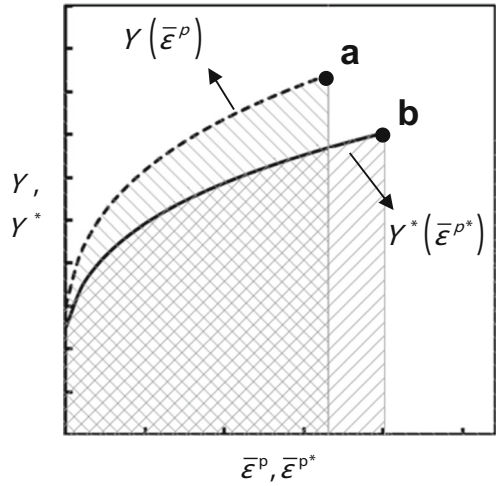

Fig. 1 Evolution of the yield stress with the equivalent plastic strain, up to **a** (curve $Y = Y(\bar{\varepsilon}^{p})$) and **b** (curve $Y^* = Y^*(\bar{\varepsilon}^{p*})$), which correspond to an equal plastic work value

situations of Fig. 1, obeying to Eq. (22), these functions can be written as follows, respectively:

$$Y = C\left(\bar{\varepsilon}^{p} + \varepsilon_0\right)^{n}; \quad Y^* = C^*\left(\bar{\varepsilon}^{p*} + \varepsilon_0^*\right)^{n^*}, \tag{23}$$

$$\begin{aligned} Y &= Y_0 + R_{Sat}\left[1-\exp\left(-C_Y\bar{\varepsilon}^{p}\right)\right];\\ Y^* &= Y_0^* + R_{Sat}^*\left[1-\exp\left(-C_Y^*\bar{\varepsilon}^{p*}\right)\right], \end{aligned} \tag{24}$$

where C (C^*), ε_0 (ε_0^*) and n (n^*) are the parameters of Swift law ($Y_0 = C(\varepsilon_0)^n$ and $Y_0^* = C^*\left(\varepsilon_0^*\right)^{n^*}$ are the initial yield stress); and Y_0 (Y_0^*), R_{Sat} (R_{Sat}^*) and C_Y (C_Y^*) are the parameters of Voce law.

The equality expressed in Eq. (20) (or Eq. (22)) allows us to find the relationships between the parameters for each law. For the case of Swift law (Eqs. (23)),

$$\begin{cases} n^* = n \\ C^* = C/\left(\sqrt{K}\right)^{n+1} \\ \varepsilon_0^* = \sqrt{K}\varepsilon_0 \\ Y_0^* = Y_0/\sqrt{K} \end{cases}. \tag{25}$$

For the case of Voce law (Eqs. (24)),

$$\begin{cases} Y_0^* = Y_0/\sqrt{K} \\ R_{Sat}^* = R_{Sat}/\sqrt{K} \\ C_Y^* = C_Y/\sqrt{K} \end{cases} \tag{26}$$

Kinematic hardening law

If the hardening behavior is not purely isotropic, i.e. for materials with non-negligible Bauschinger effect, a kinematic hardening component must be considered. This component is expressed by $\dot{\mathbf{X}}'$, the translational velocity of the yield surface centre. The yield surface centre, represented in the deviatoric stress space, is usually designated as back-stress tensor, $\mathbf{X}'$. When the kinematic hardening is taken into account, the Cauchy stress tensor should be replaced with the effective stress tensor ($\boldsymbol{\sigma}'-\mathbf{X}'$) in the yield criterion. The kinematic hardening taken as example is the Lemaître and Chaboche model [28]:

$$\dot{\mathbf{X}}' = C_X\left[X_{Sat}\frac{(\boldsymbol{\sigma}'-\mathbf{X}')}{\bar{\sigma}} - \mathbf{X}'\right]\dot{\bar{\varepsilon}}^{p}. \tag{27}$$

where $\dot{\bar{\varepsilon}}^{p}$ is the equivalent plastic strain rate and C_X and X_{Sat} are the set of kinematic hardening parameters; X_{Sat} is the saturation value for the equivalent back stress and C_X defines the rate of saturation.

The values of $\dot{\mathbf{X}}'$ and $\dot{\mathbf{X}}'^*$ (corresponding to both situations analysed in the last section) must be equal, at a given moment of the deformation. Since $\dot{\bar{\varepsilon}}^{p*} = \sqrt{K}\dot{\bar{\varepsilon}}^{p}$ (from Eq. (21)), it can be easily concluded that:

$$\begin{cases} X_{Sat}^* = \dfrac{X_{Sat}}{\sqrt{K}} \\ C_X^* = \dfrac{C_X}{\sqrt{K}} \end{cases}. \tag{28}$$

The same conclusion can be obtained by integrating Eq. (27). In fact, given that $[(\boldsymbol{\sigma}'-\mathbf{X}')/\bar{\sigma}]$ is kept constant during deformation, the integration leads to the following equation:

$$\mathbf{X}' = X_{Sat}\frac{\boldsymbol{\sigma}'-\mathbf{X}'}{\bar{\sigma}}\left[1-\exp\left(-C_X\bar{\varepsilon}^{p}\right)\right]. \tag{29}$$

Considering that

$$\frac{\mathbf{X}'}{\bar{X}} = \frac{\boldsymbol{\sigma}'-\mathbf{X}'}{\bar{\sigma}}, \tag{30}$$

where $\bar{X}$ is the equivalent back stress, $\bar{X} = \bar{X}(\bar{\varepsilon}^{p})$, determined using the same function (yield criterion) as for $\bar{\sigma}$, it is possible to conclude:

$$\bar{X} = X_{Sat}\left[1-\exp\left(-C_X\bar{\varepsilon}^{p}\right)\right]. \tag{31}$$

Now, following an approach similar to the one used for the isotropic hardening law, Eqs. (28) can be easily obtained.

Numerical tests

Numerical simulations of the deep drawing process of a cross-shaped cup were performed, in order to corroborate the equivalence between sets of parameters of the yield criterion, the isotropic and the kinematic hardening laws. Also, numerical simulations of a Bauschinger shear test were performed to support the specific case of equivalency between sets, with regard to the parameters of the kinematic hardening law. It will be also emphasised the consequences of the usual assumption "as in isotropy", for the parameters associated with the out-of-plane stress components (for example, $L = M = 1.5$ for Hill'48 criterion) regardless the value of K. The numerical simulations were carried out with the DD3IMP in-house finite element code, developed and optimised to simulate sheet metal forming processes [29]. Tri-linear 8-node hexahedral solid elements associated to a selective reduced integration are used in both examples, always considering two layers through-thickness.

The deep drawing process of the cross-shaped cup was simulated taking into account the tool geometry, which includes a closed die and a punch displacement of 45 mm. Due to geometric and material symmetries, only one quarter of the cup geometry was considered. The blank, with initial dimensions 125x125x1 mm^3, is discretised with an average in-plane size of 2.0 mm. The blank holder applies a constant force of 290 kN and the frictional contact between surfaces is modelled by Coulomb criterion, with a constant coefficient of friction equal to 0.03 [30].

For the numerical simulation of Bauschinger shear test, inversions were performed after amounts of 20 % and 40 % of shear strain (γ_{xy}); the sample geometry is rectangular, with a length of 60 mm, a width of 3 mm and 1 mm of thickness [31], and it is discretised with an average in-plane size of 0.3 mm. A null displacement in all directions is imposed on one side of the sample, while on the other side a displacement is imposed along the length direction, with a null displacement along the remaining directions.

Numerical simulations were performed for three different materials (HSLA340, AA6016-T4 and DC06) whose sets of constitutive parameters (A, B and C) have been

Table 1 Sets of parameters of the materials from Groups 1, 2 and 3

Group 1			Group 2			Group 3		
Constitutive Model	A [31]	A*	Constitutive Model	B [31]	B*	Constitutive Model	C [31]	C*
Hill'48 parameters			Drucker + L parameters			CB2001 parameters		
F	0.4140	0.8280	C_1	1.1704	1.6552	a_1	1.4076	2.8152
G	0.5580	1.1160	C_2	1.1535	1.6313	a_2	1.6795	3.3590
H	0.4420	0.8840	C_3	0.9489	1.3419	a_3	0.5007	1.0014
$L=M$	1.5	3	$C_4=C_5$	1	1.4142	a_4	1.0784	2.1568
N	1.5200	3.0400	C_6	0.9766	1.3811	$a_5=a_6$	1	2
			c	0.2954	0.2954	b_1	−1.524	−4.3105
						b_2	0.7165	2.0266
						b_3	6.0672	17.1606
						b_4	3.3440	9.4583
						b_5	3.0156	8.5294
						b_{10}	1.4879	4.2084
						$b_6=b_7=b_8=b_9=b_{11}$	1	2.8284
						c	0.8202	0.8202
Swift law parameters			Voce law parameters			Swift law parameters		
Y_0[MPa]	367.70	520.01	Y_0[MPa]	124.20	175.65	Y_0[MPa]	122.20	172.82
C [MPa]	530.90	787.86	R_{Sat} [MPa]	167.00	236.17	C [MPa]	435.00	663.69
n	0.139	0.139	C_Y	9.50	13.44	n	0.219	0.219
L&C law parameters			L&C law parameters			L&C law parameters		
C_X	20.7	29.27	C_X	146.50	207.18	C_X	1.45	2.05
X_{Sat}[MPa]	98.00	138.59	X_{Sat}[MPa]	34.90	49.36	X_{Sat}[MPa]	116.7	165.04

previously identified, using in each case a different constitutive model [32]. For each material, a set of equivalent parameters (A^*, B^* and C^*) was also considered according to the analysis presented in the previous section, with K=0.5. Table 1 shows: (i) Group 1 of parameters concerning a high-strength steel HSLA340, which parameters were identified for Hill'48 yield criterion and Swift law combined with Lemaître and Chaboche (L&C) kinematic law; (ii) Group 2 concerning an aluminium alloy AA6016-T4, which parameters were identified for Drucker + L yield criterion and Voce law combined with L&C kinematic law; and (iii) Group 3 concerning a mild steel DC06, which parameters were identified for CB2001 yield criterion and Swift law combined with L&C kinematic law. The isotropic elastic behaviour considers a Young modulus E equal to 210 GPa for the steels and 70 GPa for the aluminium, and a Poisson ratio ν= 0.3, for all materials.

Figure 2a shows the yield surface in the plane (σ_{xx}; σ_{yy}), for the materials in study. Fig. 2b and c show the evolution of the yield stress, Y, and of the equivalent back stress, $\overline{X}$, respectively, both as a function of the equivalent plastic strain, $\overline{\varepsilon}^p$. For the last two figures, the evolutions are shown up to the same amount of plastic work for the two equivalent sets of parameters of each material.

Figure 3 concerns the results of the numerical simulation of the cross-shaped cup. Figure 3a displays an example of the deformed shape projected on the 0xy plane, after a punch displacement of 45 mm (Group 1 of parameters) and Fig. 3b compares the draw-in (s) of the flange in function of α, defined as the angle with the rolling direction of the sheet, for all cases. Figure 3c compares the load (P) evolution as a function of the displacement of the punch (Δl), also for all cases. Figure 3 d, e and f compare the same cases, plotting the thickness t vs. the distance measured from the cup's centre, d, along the 0x, 0x=0y and 0y axes, respectively. Figure 4 shows the shear stress (τ_{xy}) vs. shear strain (γ_{xy}) curves obtained for the Bauschinger shear test, for all cases in Table 1. Within each group of parameters, the results in Fig. 3 and 4 are entirely identical, which confirms the equivalence between the sets of parameters A and A^*, B and B^*, and C and C^*, in agreement with the analysis of the previous section.

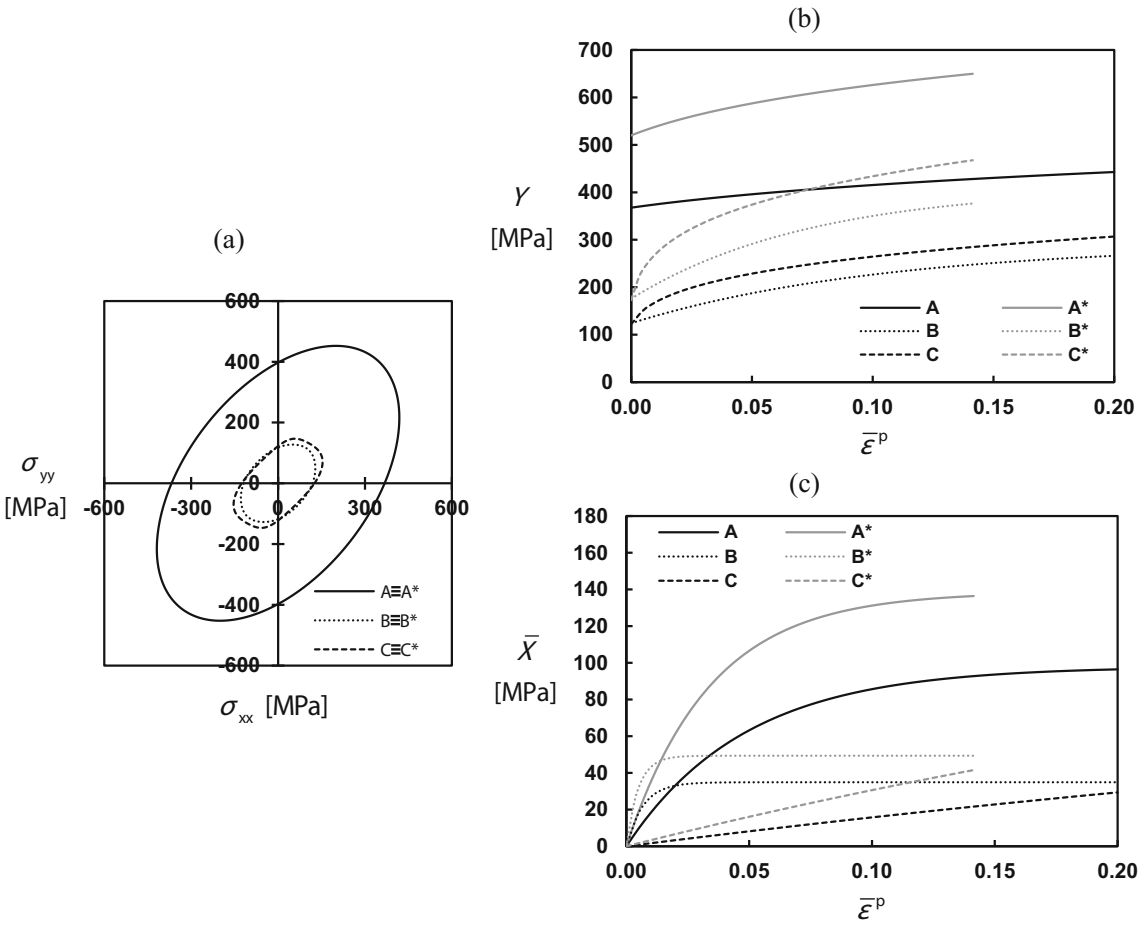

Fig. 2 **a** Yield surfaces in the (σ_{xx}; σ_{yy}) plane; **b** Yield stress, Y, and **c** equivalent back stress, $\overline{X}$, both as a function of the equivalent plastic strain, $\overline{\varepsilon}^p$, for the sets of parameters studied

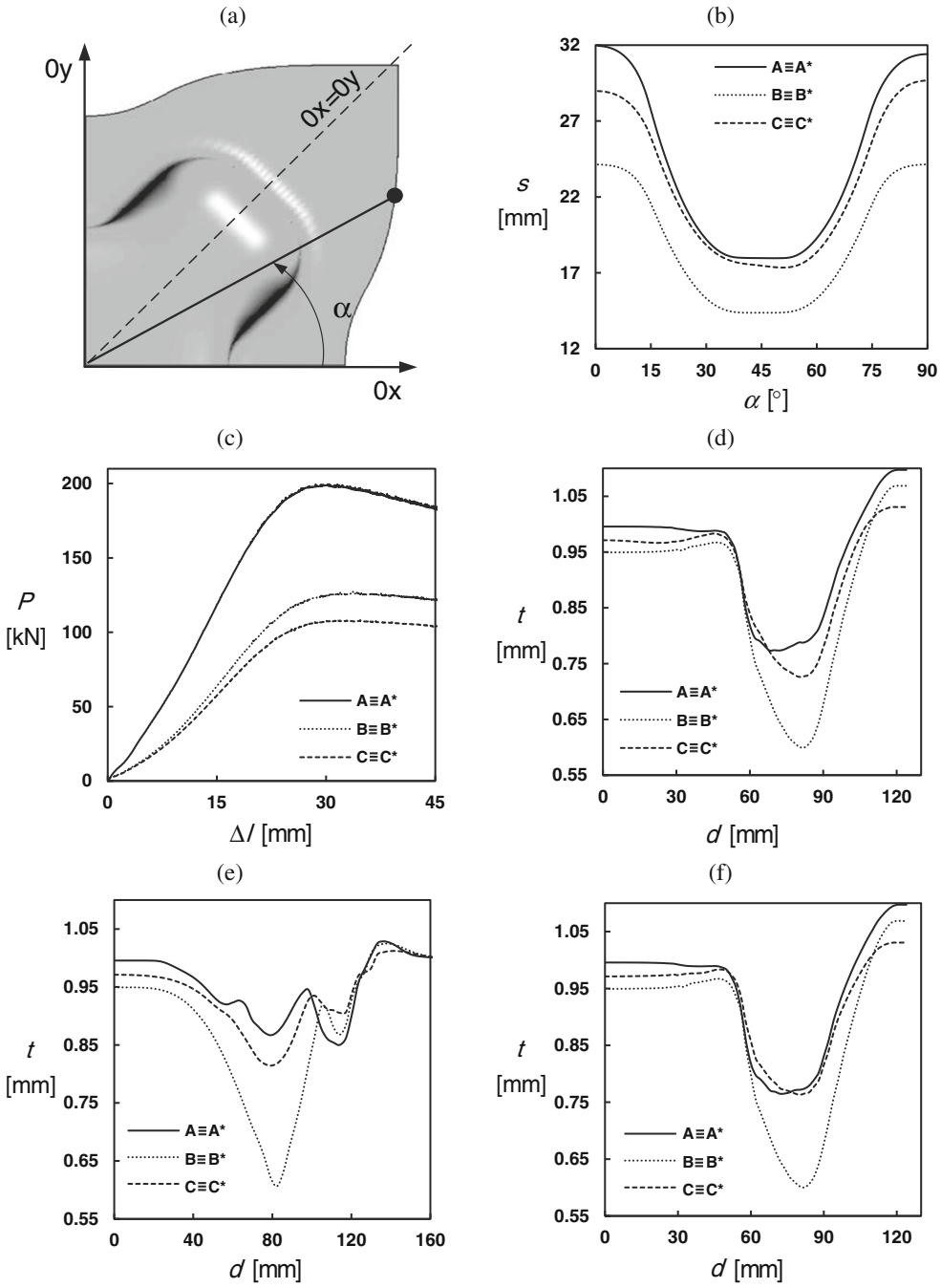

Fig. 3 Results of the deep-drawing test for all cases in study, concerning: **a** Deformed shape (1/4), projected on the 0xy plane; **b** flange draw-in (s) as a function of α; **c** P vs. Δl; **d**, **e** and **f** t vs. d, along the 0x, 0x=0y and 0y axes, respectively

In this context, the experimental identification of the material parameters for a given constitutive model can lead to apparently different but equivalent sets of constitutive parameters, which raises the question about the physical meaning of the parameters. Generally, the set of identified parameters follows or is close to one of the relations (7), for the case of the Hill'48 criterion, or similar relations in case of other criteria. Under this conditions, the identified hardening law will be relatively close to the tensile stress–strain curves of the material in the sheet plane (for example, if $G+H=1$, the pure isotropic hardening law is coincident with the tensile stress–strain curve in the 0x direction), and so the values of the constitutive parameters are more in line with its experimental significance. Otherwise, the level of the identified hardening law can move away substantially from the level of the tensile stress–strain curves in the sheet plane and so the equivalent stress (and equivalent strain) at a given amount of plastic work loses its usual physical meaning (see Fig. 1 and Figs. 2b and 2c).

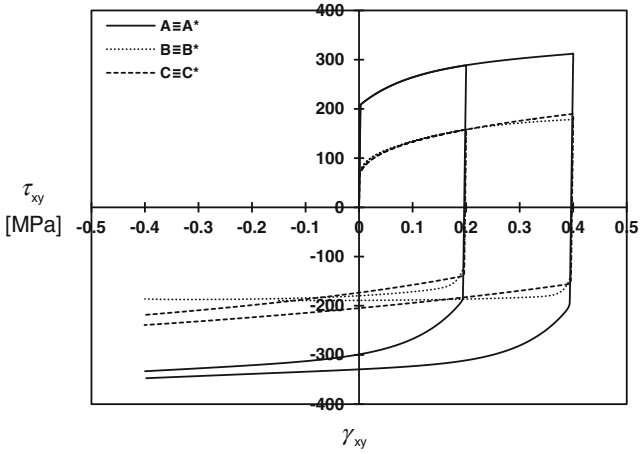

Fig. 4 Results of the Bauschinger shear test, showing coincidence within each group of parameters for the τ_{xy} vs. γ_{xy} curves, before and after inversion of loading direction at γ_{xy} equal to 20 % and 40 %

Numerical simulations were also performed with the set of parameters A', B' and C' identical to A*, B* and C*, but assuming: (i) $L=M=1.5$ for A'; (ii) $C_4=C_5=1$, for B' and (iii) $a_5=a_6=b_6=b_7=b_8=b_9=b_{11}=1$ for C'. In other words, the set of parameters A', B' and C' are respectively obtained from A, B and C by applying the factor $K=0.5$ only to the remaining parameters. This example allows to evaluate the importance of assuming the usually "as in isotropy" condition for the parameters associated with the out-of-plane shear stresses, independently of the values of the other parameters.

Figure 5 a and b show the yield surfaces in the planes (τ_{xz}; τ_{yz}) and (σ_{zz}; τ_{yz} or τ_{xz}), respectively, for the sets of parameters A, B, C and A', B', C'. The yield surface in plane (σ_{xx}; σ_{yy}), is identical between sets of parameters A and A', B and B' and C and C' (see Fig. 2 a). The isotropic and kinematic hardening laws for A', B' and C' are identical to A*, B* and C*, respectively (see Fig. 2 b and c). The results of the numerical simulations of the cross-shaped cup are shown in Fig. 6, which shows the same kind of results of Fig. 3, but for the sets of parameters A, B, C and A', B', C'. The results in Fig. 6 show differences between A' and A, B' and B and C' and C, namely perceptible differences for the punch load evolution (see Fig. 6 b), and for the thickness distribution with the distance from the cup's centre, along the 0x=0y and 0y axes (see Fig. 6 d and e, respectively).

Due to experimental difficulties, the parameters associated with the out-of-plane shear stress components are generally not identified and their values are usually assumed "as in isotropy" (i.e. $L=M=1.5$, in case of Hill'48 criterion; $C_4=C_5=1$ in case of Drucker + L yield criterion and $a_5=a_6=b_6=b_7=b_8=b_9=b_{11}=1$, for the case of CB2001, or the corresponding conditions for any other criterion), independently of the K value. The assumption of this isotropy condition, for sets of parameters with different values of K, leads to distinct geometries of the yield surfaces, namely near the axes τ_{xz} and τ_{yz} (see Fig. 5 a and b). Consequently, the numerical results such as those reported in Fig. 6 depend on the occurrence of significant values of the out-of-plane shear strain (and stress) components, for a given deep-drawing process. Nevertheless, the differences (between A and A'; B and B'; C and C') are not pronounced for the case of Fig. 6, which is already an extreme overemphasis case with $K=0.5$.

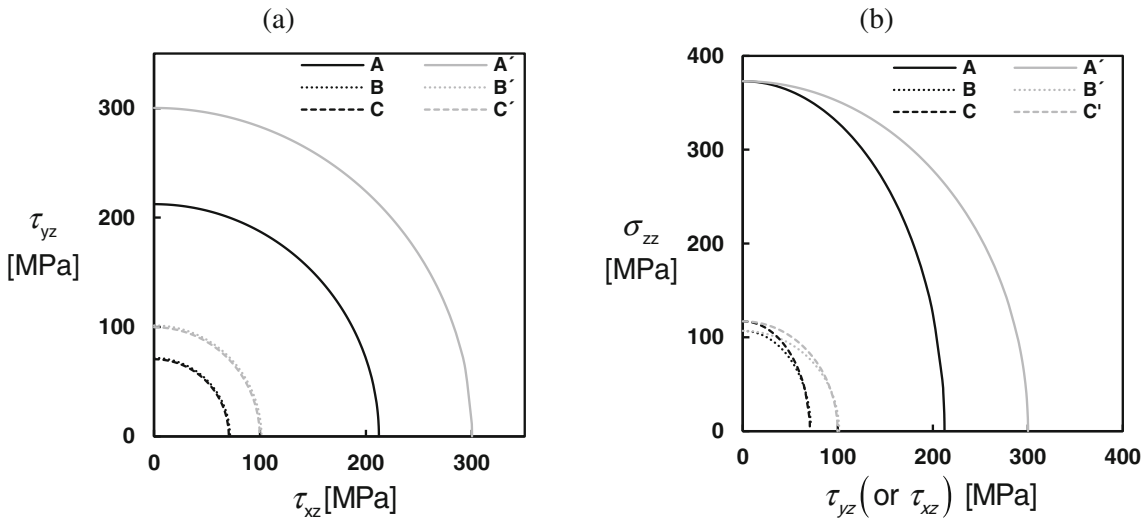

Fig. 5 **a** and **b** Yield surfaces in the (τ_{xz}; τ_{yz}) and (τ_{yz} or τ_{xz}; σ_{zz}) planes, respectively, for the sets of parameters A, B, C and A', B', C'

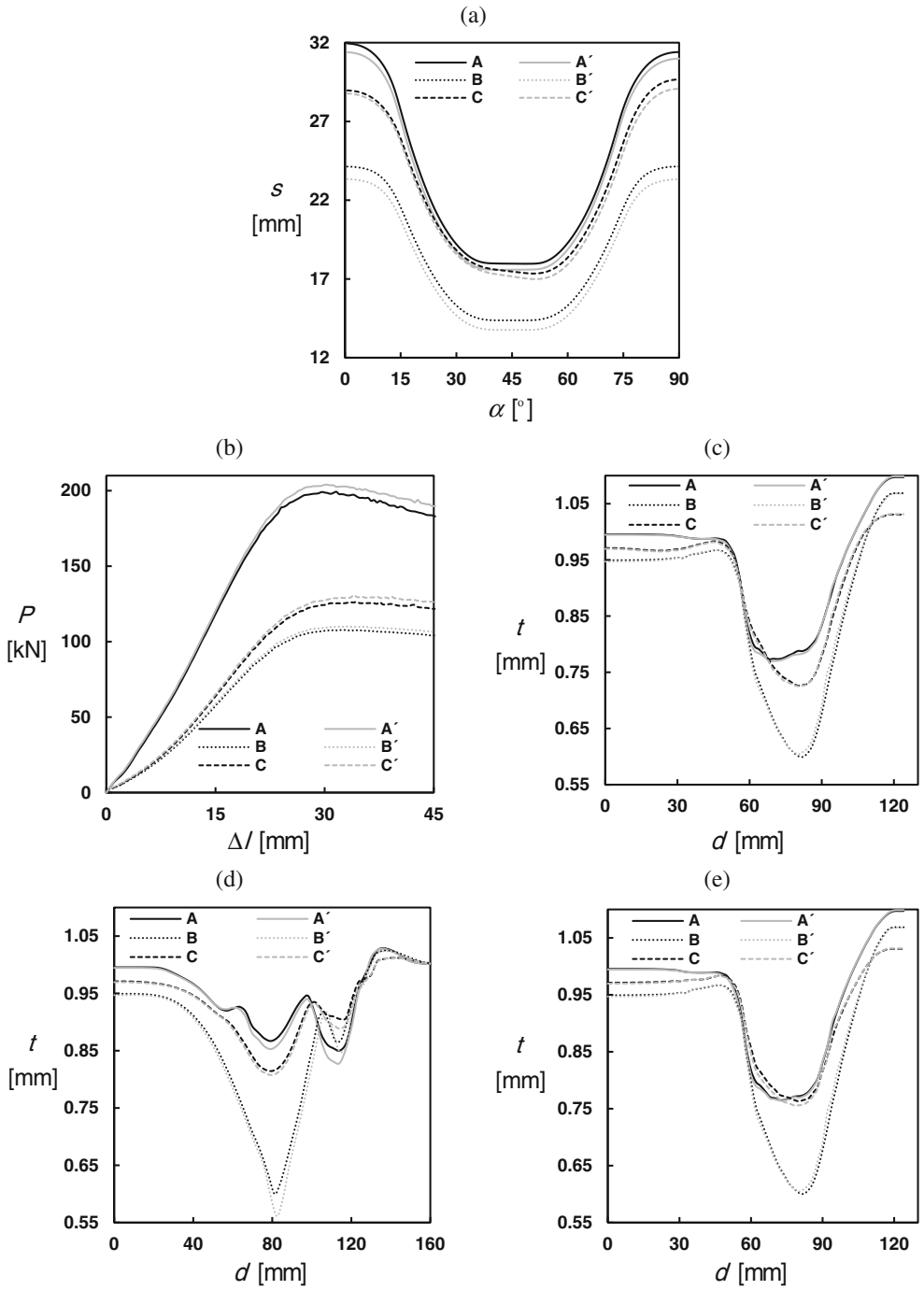

Fig. 6 Results of the deep-drawing test for the sets of parameters A, B, C and A', B', C', concerning: **a** flange draw-in (s) as a function of α; **b** P vs. Δl; **c**, **d** and **e** t vs. d, along the 0**x**, 0**x**=0y and 0y axes, respectively

In summary, different sets of constitutive parameters, comprising the yield criterion and the isotropic and kinematic hardening laws, can describe the same plastic behavior, as highlighted by the current numerical simulation results. Moreover, the assumption for the values of the parameters associated with the out-of-plane stress components "as in isotropy" independently of the K value, leads to different numerical results although its importance is not necessarily significant.

Conclusions

In this work, a general methodology for equivalence between sets of plastic constitutive parameters is established. This allows the proper comparison of the parameters obtained using different identification strategies. The methodology was applied to constitutive models comprising Hill'48, Drucker + L and CB2001 anisotropic yield criteria, Swift and Voce isotropic hardening laws and Lemaître and

Chaboche kinematic hardening law. However, it can also be applied to any other yield criteria and isotropic and kinematic hardening laws. Finally, numerical simulation results of the deep drawing process of a cross-shaped cup and of a Bauschinger shear test were shown, for different sets of constitutive parameters, in order to support the proposed methodology.

Acknowledgements This research work is sponsored by national funds from the Portuguese Foundation for Science and Technology (FCT) via the projects PTDC/EME–TME/113410/2009 and PEst-C/EME/UI0285/2013 and by FEDER funds through the program COMPETE – Programa Operacional Factores de Competitividade, under the project CENTRO–07–0224 -FEDER -002001 (MT4MOBI). One of the authors, P.A. Prates, was supported by a grant for scientific research from the Portuguese Foundation for Science and Technology. All supports are gratefully acknowledged.

References

1. Aretz H, Barlat F (2013) New convex yield functions for orthotropic metal plasticity. Int J Non-Linear Mech 51:97–111
2. Bron F, Besson J (2004) A yield function for anisotropic materials. Application to aluminium alloys. Int J Plast 20:937–963
3. Cazacu O, Barlat F (2004) A criterion for description of anisotropy and yield differential effects in pressure-insensitive metals. Int J Plast 20:2027–2045
4. Cazacu O, Plunkett B, Barlat F (2006) Orthotropic yield criterion for hexagonal closed packed metals. Int J Plast 22:1171–1194
5. Chaboche JL (2008) A review of some plasticity and viscoplasticity constitutive theories. Int J Plast 24:1642–1693
6. Fernandes JV, Rodrigues DM, Menezes LF, Vieira MF (1998) A modified Swift law for prestrained materials. Int J Plast 14:537–550
7. Geng LM, Shen Y, Wagoner RH (2002) Role of plastic anisotropy and its evolution on springback. Int J Mech Sci 44:123–148
8. Plunkett B, Cazacu O, Barlat F (2008) Orthotropic yield criteria for description of the anisotropy in tension and compression of sheet metals. Int J Plast 24:847–866
9. Teodosiu C, Hu Z (1995) Evolution of the intragranular microstructure at moderate and large strains: Modelling and computational significance. In Proc of the 5th International Conference on Numerical Methods in Industrial Forming Processes (NUMIFORM '95), Eds. Shan-Fu Shen, P. R. Dawson, pp 173–182
10. Teodosiu C, Hu Z (1998) Microstructure in the continuum modelling of plastic anisotropy. In Proc of the 19th Riso International Symposium on Materials Science: Modelling of Structures and Mechanics from Microscale to Products, Riso National Laboratory, pp 149–168
11. Yoshida F, Uemori T (2002) A model of large-strain cyclic plasticity describing the Bauschinger effect and workhardening stagnation. Int J Plast 18:661–686
12. Yoshida F, Hamasaki H, Uemori T (2013) A user-friendly 3D yield function to describe anisotropy of steel sheets. Int J Plast 45:119–139
13. Aguir H, Alves JL, Oliveira MC, Menezes LF, BelHadjSalah H (2012) Cazacu and Barlat Criterion Identification Using the Cylindrical Cup Deep Drawing Test and the Coupled Artificial Neural Networks – Genetic Algorithm Method. Key Eng Mater 504–506:637–642
14. Chaparro BM, Thuillier S, Menezes LF, Manach PY, Fernandes JV (2008) Material parameters identification: Gradient-based, genetic and hybrid optimization algorithms. Comput Mater Sci 44:339–346
15. Oliveira MC, Alves JL, Chaparro BM, Menezes LF (2007) Study on the influence of work-hardening modeling in springback prediction. Int J Plast 23:516–543
16. Prates PA, Oliveira MC, Fernandes JV (2014) A new strategy for the simultaneous identification of constitutive laws parameters of metal sheets using a single test. Comp Mater Sci 85:102–120
17. Rossi M, Pierron F (2012) Identification of plastic constitutive parameters at large deformations from three dimensional displacement fields. Comput Mech 49:53–71
18. Güner A, Soyarslan C, Brosius A, Tekkaya AE (2012) Characterization of anisotropy of sheet metals employing inhomogeneous strain fields for Yld 2000–2D yield function. Int J Solids Struct 49:3517–3527
19. Hill R (1948) A theory of yielding and plastic flow of anisotropic metals. Proc R Soc Lond 193:281–297
20. Cazacu O, Barlat F (2001) Generalization of Drucker's yield criterion to orthotropy. Math Mech Solids 6:613–630
21. Bouvier S, Teodosiu C, Maier C, Banu M, Tabacaru V (2001) Selection and identification of elastoplastic models for the materials used in the benchmarks. WP3, Task 1, 18-Months progress report of the Digital Die Design Systems (3DS), IMS 1999 000051
22. Yamashita T (1996) Analysis of anisotropic material. Ohio University, Dissertation
23. Prates PA, Oliveira MC, Sakharova NA, Fernandes JV (2013) How to combine the parameters of the yield criteria and the hardening law. Key Eng Mater 554–557:1195–1202
24. Rabahallah M, Balan T, Bouvier S, Bacroix B, Barlat F, Chung K, Teodosiu C (2009) Parameter identification of advanced plastic strain rate potentials and impact on plastic anisotropy prediction. Int J Plast 25:491–512
25. Drucker DC (1949) Relation of experiments to mathematical theories of plasticity. J Appl Mech Tran ASME 16:349–357
26. Swift HW (1952) Plastic instability under plane stress. J Mech Phys Solids 1:1–18
27. Voce E (1948) The relationship between stress and strain for homogeneous deformation. J Inst Met 74:537–562
28. Chaboche JL (1989) Constitutive equations for cyclic plasticity and cyclic viscoplasticity. Int J Plast 5:247–302
29. Oliveira MC, Alves JL, Menezes LF (2008) Algorithms and strategies for treatment of large deformation frictional contact in the numerical simulation of deep drawing process. Arch Comput Method Eng 15:113–162
30. Resende TC, Balan T, AbedMeraim F, Bouvier S, Sablin SS (2010) Application of a dislocation based model for Interstitial Free (IF) steels to typical stamping simulations. In Proc. of the 10th International Conference on Numerical Methods in Industrial Forming Processes Dedicated to Professor O. C. Zienkiewicz (1921–2009), 1252:1339–1346
31. Coër J, Manach PY, Laurent H, Oliveira MC, Menezes LF (2013) Piobert–Lüders plateau and Portevin–Le Chatelier effect in an Al–Mg alloy in simple shear. Mech Res Commun 48:1–7
32. Alves JL (2003) Simulação numérica do processo de estampagem de chapas metálicas - modelação mecânica e métodos numéricos. University of Minho, Dissertation

(Page intentionally left blank)

4.3. A new strategy for the simultaneous identification of constitutive laws parameters of metal sheets using a single test

This subchapter presents the paper "A new strategy for the simultaneous identification of constitutive laws parameters of metal sheets using a single test", published in Computational Materials Science. This work proposes an inverse analysis methodology for the simultaneous identification of Hill'48 yield criterion and Swift hardening law parameters, based on an exploratory step-by-step optimisation procedure of the results of a single biaxial tensile test of a cruciform sample.

(Page intentionally left blank)

Computational Materials Science 85 (2014) 102–120

Contents lists available at ScienceDirect

Computational Materials Science

journal homepage: www.elsevier.com/locate/commatsci

A new strategy for the simultaneous identification of constitutive laws parameters of metal sheets using a single test

P.A. Prates *, M.C. Oliveira, J.V. Fernandes

CEMUC, Department of Mechanical Engineering, University of Coimbra, Rua Luís Reis Santos, Pinhal de Marrocos, 3030-788 Coimbra, Portugal

ARTICLE INFO

Article history:
Received 5 July 2013
Received in revised form 10 December 2013
Accepted 19 December 2013

Keywords:
Constitutive law parameters
Inverse analysis
Cruciform biaxial tensile test
Finite element method

ABSTRACT

An inverse analysis methodology for determining the parameters of plastic constitutive models is proposed. This involves the identification of the yield criterion and work-hardening law parameters, which best describe the results of the biaxial tensile test on cruciform samples of metal sheets. The influence and sensitivity of the constitutive parameters on the biaxial tensile test results is studied following a forward analysis, based on finite element simulations. Afterwards, the inverse analysis methodology is established, by evaluating the relative difference between numerical and experimental results of the biaxial tensile test, namely the load evolution in function of the displacements of the grips and the equivalent strain distribution, at a given moment of the test, along the axes of the sample. This methodology is compared with a classical identification strategy and proves to be an efficient alternative, allowing to avoid time-consuming tests, some of them hard to analyse and liable to uncertainties.

1. Introduction

The accuracy of the numerical simulation results in sheet metal forming depends on the selected constitutive model and the strategy used for the parameters identification [1–4]. Several phenomenological yield criteria (e.g. [5–10]) and hardening laws (e.g. [11–16]) have been proposed in order to improve the description of the plastic behaviour of metal sheets. Increasing the flexibility of the constitutive models is often associated with a larger number of parameters to identify. This requires a wide set of experimental tests and complex identification strategies. The constitutive parameters are usually identified from linear strain path tests (namely tensile, bulge and shear tests) with homogeneous deformation in the measuring region, using classical methodologies. As the rolling process makes the metal sheets anisotropic, different mechanical behaviours are expected for different loading directions and conditions. However, sheet metal forming processes are carried out with inhomogeneous deformation and under multiaxial strain paths. Therefore, limiting the characterization of the mechanical behaviour of metal sheets to a restricted number of tests with linear strain paths and homogeneous deformation can lead to a somewhat incomplete characterization of the overall plastic behaviour of the material [17].

From mechanical tests with heterogeneous strain fields it is possible to obtain a larger amount of information than the one found in case of tests with homogeneous strain fields. Therefore, heterogeneous strain fields can more suitably describe the influence of the strain path on the plastic behaviour of metals than homogeneous strain fields [18]. Material parameters obtained from homogeneous strain path tests are more appropriate for describing the material behaviour for one particular strain path, but can be unsuitable for other strain paths. To overcome this problem, it is necessary to develop tests allowing heterogeneous stress and strain fields and, eventually, strain path changes. The material parameters obtained through these tests will describe the overall mechanical behaviour of the material, taking into account the mutual influence of the various strain paths occurring in the sample, even if they are not fully appropriate for describing each particular strain path [18–20]. The material parameters obtained through such tests will be also suitable for describing the plastic behaviour of metal sheets during complex forming operations, in view of the heterogeneous nature of the deformation.

The increasing development of optical full-field measurement techniques for analysing heterogeneous strain fields, such as the digital image correlation (DIC) technique, has led to the development of new tests and methodologies for characterising the plastic behaviour of materials [21]. One possible approach consists on using inverse analysis methodologies, which are based on the determination of the material parameters that minimise the gap between numerically predicted and experimental test results [22]. These methodologies have been recently explored in the literature for the parameters identification of constitutive laws, by combining DIC measurements on the test samples with numerical simulation results of the test [18–20,23–25]. In this context, several works in literature, which propose the coupling of optical

* Corresponding author. Tel.: +351 239790700; fax: +351 239790701.
E-mail address: pedro.prates@dem.uc.pt (P.A. Prates).

0927-0256/$ - see front matter © 2013 Elsevier B.V. All rights reserved.
http://dx.doi.org/10.1016/j.commatsci.2013.12.043

measurement results and inverse analysis methodologies together with numerical simulations results for the identification of constitutive laws parameters, are highlighted in the following.

Güner et al. [23] proposed an inverse analysis procedure for the identification of the Yld2000-2d yield criterion parameters corresponding to the initial yield locus of representative materials. This study, strictly numeric, uses a notched specimen submitted to a uniaxial tensile test, enabling strain paths near uniaxial tension. The required data for the inverse identification of the yield criterion parameters are variables such as the major and minor principal strains in the sheet plane, the tool force, and the equibiaxial yield stress value (which is assumed known *a priori*). The objective function is a combination of principal strain, tool force (at selected tool displacements) and equibiaxial yield stress differences between numerically generated and experimental reference values, and is minimised using the Levenberg–Marquardt algorithm. Different alternative orientations of the specimen with the rolling direction (0°, 45°, 90°) and configurations of the objective function (setting the strain, or tool force, components to zero) were considered to test the inverse procedure. The authors highlight the importance of including strain information on the objective function, which leads to an improvement on its minimisation.

Pottier et al. [18] developed a testing procedure based on the out-of-plane deformation of a sample, using stereo image correlation, for the simultaneous identification of the constitutive parameters of Hill'48 yield criterion and Ludwick work-hardening law of a pure titanium sheet. The identification procedure consists of a finite element update inverse method and the parameters are determined using Levenberg–Marquardt minimisation strategy, where the gap between experimental and finite element simulation results of the surface displacement fields and the global force is minimised. The authors highlight the importance of increasing the strain field heterogeneity for a better assessment of the material behaviour.

In another work, an inverse analysis methodology based on a least-squares formulation along with Gauss–Newton minimisation strategy was developed in order to simultaneously determine the constitutive parameters for Hill'48 yield criterion and Swift work-hardening law of a stainless steel [20]. In this case, the parameter identification is performed from the results of three different complex tests, all of them comprising heterogeneous strain fields: a uniaxial tensile test on a perforated tensile specimen, a uniaxial tensile test on a complex shaped specimen and a biaxial tensile test of a perforated cruciform specimen. Furthermore, the sets of parameters obtained from each test are applied to simulate the three complex tests previously described. This allowed concluding that a good practice is to develop the mechanical test in accordance with the sheet metal forming process in study [20]. This methodology was also adopted for performing the identification of Hill'48 yield criterion and Swift work-hardening law parameters of a mild steel, from the results of a biaxial tensile test of a perforated cruciform specimen [19]. This strategy allowed the determination of averaged parameters of the yield criterion and hardening law, which are better suited for the simulation of real sheet metal forming processes than the ones obtained from classical identification strategies [19].

The idea of testing cruciform specimens dates back to the 1960s [26]. Such tests show potential for application in characterising the plastic behaviour of materials, i.e. for estimating the parameters of the anisotropic yield criterion and the work-hardening law, namely: (i) strain paths ranging from uniaxial tension (in the arms region of the specimen) to biaxial tension (in the central region of the specimen), (ii) high strain gradients, from the central region of the specimen to the extremity of the arms and (iii) no sliding contact occurs with tools, avoiding friction. Also, by changing the load and/or the displacement ratio between the two perpendicular loading axes, it is possible to obtain different biaxial strain and stress states, in the central region of the specimen [27]. However, this test allows only attaining low values of equivalent plastic strain (close to those obtained in uniaxial tension) before instability occurs and no occurrence of out-of-plane shear stress is observed (which prevents the determination of the constitutive parameters associated with out-of-plane stress components, as usually occurs when using classical methodologies). The aim of this work consists in developing and evaluating the performance of an inverse analysis methodology for the identification of the plastic constitutive parameters (anisotropic yield criterion and work-hardening law), which describe the plastic behaviour of metal sheets, from a single biaxial tensile test of a cruciform specimen. The current approach aims to be simple, from an experimental point of view, and for this purpose one just analyses the load evolution during the test and the equivalent strain distribution along the axes of the specimen, at a given moment of deformation, as an alternative to follow the strain fields on the specimen surface during the test, as previously performed by other authors [19].

2. Numerical model

The geometry of the cruciform specimen was studied using finite element method results in order to reproduce, as far as possible, inhomogeneous deformation with the occurrence of strain paths that are commonly observed in sheet metal forming processes [28]. An overview of the optimisation procedure for the sample geometry is presented in Appendix A. Fig. 1 shows the selected geometry and the relevant dimensions of the cruciform specimen in the sheet plane. The 0*x* and the 0*y* axes coincide with the rolling direction (RD) and the transverse direction (TD) of the sheet, respectively. The cruciform specimen is submitted to equal displacements in both 0*x* and 0*y* directions, applied by the grips, as indicated in Fig. 1. The displacements along the 0*x* and 0*y* axes are measured at points A and B, respectively. The sheet thickness considered in this study is 1.0 mm.

The material is considered orthotropic. Due to geometrical and material symmetries, only one eight of the specimen was considered in the numerical simulation model. The specimen was discretised with tri-linear 8-node hexahedral solid elements with an average in-plane size of 0.5 mm and two layers through-thickness. Numerical simulations were carried out with DD3IMP in-house

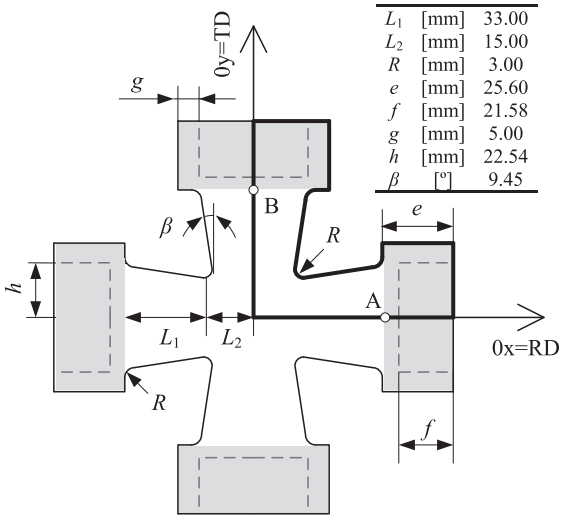

Fig. 1. Geometry and dimensions of the cruciform specimen. The grips, represented in grey, hold the specimen by grabbing it along the dashed grey lines. A and B represent the points for measuring the displacements, Δl.

finite element code, developed and optimised to simulate sheet metal forming processes [29].

The constitutive model adopted in developing of the proposed methodology considers Hill'48 yield criterion [30] with the associated flow rule and Swift work-hardening law [31]. The Hill'48 yield criterion describes the yield surface for the case of an orthotropic material as follows:

$$F(\sigma_{yy}-\sigma_{zz})^2+G(\sigma_{zz}-\sigma_{xx})^2+H(\sigma_{xx}-\sigma_{yy})^2+2L\tau_{yz}^2+2M\tau_{xz}^2+2N\tau_{xy}^2=Y^2 \quad (1)$$

where σ_{xx}, σ_{yy}, σ_{zz}, τ_{xy}, τ_{xz} and τ_{yz} are the components of the effective Cauchy stress tensor ($\boldsymbol{\sigma}$) defined in the system of axes of orthotropy of the metal sheet; F, G, H, L, M and N are the anisotropy parameters to be identified and Y is the yield stress, which evolution is defined by the work-hardening law. In this study, it is assumed the condition $G + H = 1$ and so the work-hardening law is represented by the uniaxial tensile stress along the RD. The work-hardening is described by Swift law as follows:

$$Y = C(\varepsilon_0+\bar{\varepsilon}^p)^n \quad (2)$$

where $\bar{\varepsilon}^p$ is the equivalent plastic strain and C, ε_0 and n are the material parameters. The yield stress can also be written as a function of C, n and Y_0, where $Y_0 = C(\varepsilon_0)^n$. The elastic behaviour is considered isotropic and is described by the generalised Hooke's law.

3. Identification strategy

The proposed identification strategy consists on the simultaneous determination of the constitutive parameters of Hill'48 criterion and Swift law, using results of the biaxial tensile test on the cruciform sample. The first step of this work consists on a forward analysis using finite element simulation results of this test, in order to study the sensitivity of the results to variations of the values of the constitutive models parameters, revealed by the evolution and/or distribution of variables such as the ones shown in Fig. 2. This forward study allowed the developing of an inverse analysis methodology, for identifying the constitutive laws parameters.

3.1. Forward analysis

In this forward study, the analysis is focused on:

(i) The evolutions of the load, P, with the specimen boundaries displacement, Δl, during the test, for the axes 0x and 0y; Δl is measured for points A and B in Fig. 1.

(ii) The distributions of the equivalent strain, $\bar{\varepsilon}_{vM}$, along the axes of the sample (i.e. $\bar{\varepsilon}_{vM}$ as a function of the distance to the centre of the sample, d), for a given boundaries displacement, Δl, preceding and close to the displacement at the maximum load; the equivalent strain is determined using von Mises definition:

$$\bar{\varepsilon}_{vM}=2\left[(\varepsilon_1^2+\varepsilon_2^2+\varepsilon_1\varepsilon_2)/3\right]^{1/2} \quad (3)$$

where ε_1 and ε_2 are respectively the major and the minor principal strains, in the sheet plane. The principal strain axes are parallel to the axes of the specimen (in case of the 0x axis, ε_1 is equal to ε_{xx} and ε_2 is equal to ε_{yy}, and in case of the 0y axis, ε_1 is equal to ε_{yy} and ε_2 is equal to ε_{xx} – see Fig. 1).

(iii) The distributions of the strain path ratio, defined by $\varepsilon_2/\varepsilon_1$, along the axes 0$x$ and 0y, for the same boundaries displacement, Δl, as previously stated in (ii); observations performed during the test, at different values of Δl, showed that the strain paths are quite linear.

It is worth noting that the strain variables, ε_1 and ε_2, can be experimentally measured, using DIC technique [32], or even the classical Circle Grid Strain analysis [33], which allows establishing a correspondence between the numerical and experimental results for developing the inverse analysis strategy.

Table 1 summarises the mechanical properties of the illustrative cases of materials used in the forward study. A material with isotropic behaviour, described by von Mises yield criterion, is denoted as "reference". The remaining materials diverge from the reference one due to the value of one parameter that was increased by 50%, compared to the reference one. The following designations are adopted: "Y0_300" and "n_0.300", for materials presenting also isotropic behaviour, but with different yield stress and work-hardening exponent values, respectively; "F_0.75", "H_0.75" and "N_2.25", for materials with the same hardening behaviour as the "reference" material, but with different Hill'48 anisotropy parameters. The condition $G + H = 1$ is assumed for all cases; consequently, in case of the material "H_0.75", the G value is equal to 0.25. Also, this condition implies that $Y_0 = \sigma_0$ and $(F + H)^{1/2} = \sigma_0/\sigma_{90}$ where σ_0 and σ_{90} are the tensile stresses along the rolling and transverse directions, respectively. In all simulations, the L and M anisotropic parameters are kept equal to 1.5, since the results of the biaxial cruciform test are not sensitive to these parameters. ε_0 is assumed fixed with a small value as for most materials not subjected to pre-strain [12], in this case of 0.005. The elastic behaviour considers a Young modulus (E) equal to 210 GPa and a Poisson ratio (ν) equal to 0.3.

The forward analysis is performed by comparing the numerical simulation results obtained for the last five materials presented in Table 1 with the results of the "reference" material (see Fig. 2), in terms of relative difference. In this context, δ_P is defined as the relative difference between the load for a given material, P, and the load for the reference one, P_{ref}, at a certain Δl value, i.e. $\delta_P = (P - P_{ref})/P_{ref}$; $\delta_{\bar{\varepsilon}_{vM}}$ is the relative difference between von Mises equivalent strain of a given material, $\bar{\varepsilon}_{vM}$, and the reference one, $\bar{\varepsilon}_{vM_{ref}}$, at a given d value, i.e. $\delta_{\bar{\varepsilon}_{vM}} = (\bar{\varepsilon}_{vM} - \bar{\varepsilon}_{vM_{ref}})/\bar{\varepsilon}_{vM_{ref}}$. The strain paths can also be analysed in terms of the relative difference of the ratio $\varepsilon_2/\varepsilon_1$, at a given d value. However, a more intuitive parameter is adopted to define the dissimilarity of the strain paths, $\cos(\varphi)$, which is the cosine of the angle φ that corresponds to the angular difference between the two vectors representing the strain tensors, such that:

$$\cos(\varphi) = (\boldsymbol{\varepsilon}\cdot\boldsymbol{\varepsilon}_{ref})/(\|\boldsymbol{\varepsilon}\|\|\boldsymbol{\varepsilon}_{ref}\|) \quad (4)$$

where $\boldsymbol{\varepsilon}$ and $\boldsymbol{\varepsilon}_{ref}$ are the vectors representing the strain tensors, for a given material and the "reference" case, respectively; $\|\boldsymbol{\varepsilon}\|$ and $\|\boldsymbol{\varepsilon}_{ref}\|$ are the norm of both vectors. In this context, the similarity between strain paths for a given material and for the "reference" case is full when $\cos(\varphi) = 1$ and the strain paths deviate from each other when $\cos(\varphi)$ moves away from 1. In order to correctly calculate the relative differences for a certain value of d and Δl, the numerical and reference variables, shown in Fig. 2, were obtained for the same value of d and Δl. This is achieved by performing linear interpolations of the results.

Fig. 2 shows the effects of an increase of 50% in each parameter (Y_0, n, F, H and N), relatively to the reference material. The results presented are P vs. Δl and δ_P vs. Δl (Fig. 2(a and b), respectively), $\bar{\varepsilon}_{vM}$ vs. d and $\delta_{\bar{\varepsilon}_{vM}}$ vs. d (Fig. 2(c and d), respectively) and $\varepsilon_2/\varepsilon_1$ vs. d and $\cos(\varphi)$ vs. d (Fig. 2(e and f), respectively). The results in Fig. 2 concern both the 0x and 0y axes. The results in Fig. 2(c–f) are plotted for $\Delta l = 4$ mm, equal for both 0x and 0y axes. This results concern the distance, d, from the centre of the cruciform specimen ($d = 0$ mm) up to a distance corresponding to the minimum value of $\varepsilon_2/\varepsilon_1$ (see Fig. 2(e), where this minimum occurs for a d value slightly less than 40 mm; after such d value, $\varepsilon_2/\varepsilon_1$

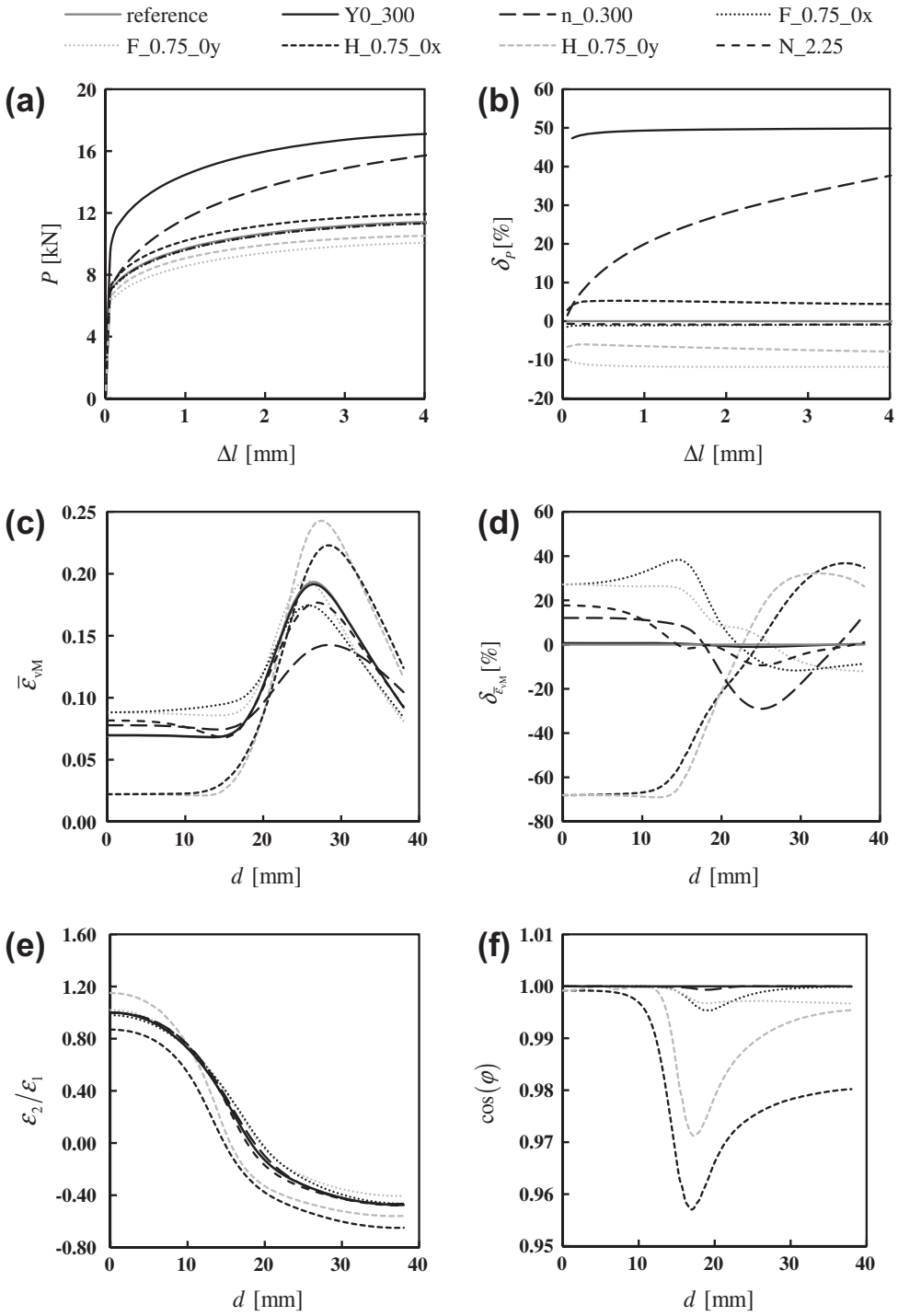

Fig. 2. Numerical simulation results for the materials presented in Table 1: (a) P vs. Δl; (c) $\bar{\varepsilon}_{vM}$ vs. d; (e) $\varepsilon_2/\varepsilon_1$ vs. d. Relative differences with respect to the "reference" material: (b) δ_P vs. Δl; (d) $\delta_{\bar{\varepsilon}_{vM}}$ vs. d and (f) $\cos(\varphi)$ vs. d distributions. The results are shown for both 0x and 0y axes (in the legend, the absence of a label, 0x or 0y, means that the results are equal for both axes).

Table 1
Constitutive parameters of the materials used in the forward analysis.

Material	Hill'48 Anisotropy Parameters				Swift Law Parameters			$(F+H)^{1/2}(=\sigma_0/\sigma_{90})$
	F	G	H	N	Y_0 [MPa]	C [MPa]	n	
Reference	0.5000	0.5000	0.5000	1.5000	200.00	577.08	0.200	1.000
Y0_300	0.5000	0.5000	0.5000	1.5000	300.00	865.62	0.200	1.000
n_0.300	0.5000	0.5000	0.5000	1.5000	200.00	980.25	0.300	1.000
F_0.75	0.7500	0.5000	0.5000	1.5000	200.00	577.08	0.200	1.100
H_0.75	0.5000	0.2500	0.7500	1.5000	200.00	577.08	0.200	1.100
N_2.25	0.5000	0.5000	0.5000	2.2500	200.00	577.08	0.200	1.000

increases approaching zero – not shown in the figure). The choice of this range for the d values intends to avoid: (i) considering two points with the same strain path (the strain paths that occur for d values between about 20 and 40 mm are repeated between the latter d value and the end of the arms of the specimen) and (ii) measuring the variables $\bar{\varepsilon}_{vM}$ and $\cos(\varphi)$ close to the heads of the sample, where the comparison between experimental and numerical results can be influenced by the boundary conditions, if the experimental boundary conditions are not properly reproduced numerically. In the following, the results will be always considered within this range of d values.

The results shown in Fig. 2 enable performing the study of the trends required to develop the inverse analysis strategy for the identification of the constitutive parameters. The influence of an increase of 50% on the value of each of the parameters Y_0, n, F, H and N in the results of the cruciform test can be summarised as follows:

(i) The increase of Y_0 increases the level of the P vs. Δl curves (Fig. 2(a)), so that the corresponding δ_P value is constant during the test (Fig. 2(b)). However, the distribution of the equivalent strain (Fig. 2(c)) and the strain paths (Fig. 2(e)), along the axes of the sample, are not changed (see also Fig. 2(d and f)).

(ii) The increase of the work-hardening exponent, n, increases the slope of the P vs. Δl curves (Fig. 2(a)), without changing the P value at the beginning of the plastic deformation. Consequently, the δ_P value increases during the test (see Fig. 2(b)). The distributions of the equivalent strain, along the axes of the sample, show noticeably complex changes (Fig. 2(c)): the $\delta_{\bar{\varepsilon}_{vM}}$ value is positive for d between 0 and 18 mm and negative for the remaining region of the arms (see also Fig. 2(d)). The strain paths, along the axes of the sample, are almost coincident with the reference material results (see Fig. 2(e and f)).

(iii) The increase of F and H, separately, leads to dissimilarities between 0x and 0y results. Concerning the load evolution during the test, the increase of F leads to an imperceptible decrease of the P vs. Δl evolution for the 0x axis and to a decrease of the level of the P vs. Δl curve for the 0y axis (see Fig. 2(a and b)). The increase of H leads to an increase of the P vs. Δl evolution for the 0x axis and to a decrease of the level of the P vs. Δl curve for the 0y axis (see Fig. 2(a and b)). Moreover, it is worth noting that the dissimilarity between the 0x and 0y axes for the P vs. Δl results is nearly the same whatever the parameter increased, F or H (see Fig. 2(b)). This is certainly related with the fact that the value of $(F+H)^{1/2}$, which represents σ_0/σ_{90}, is equal to 1.1 for both materials "F_0.75" and "H_0.75" (see Table 1). Concerning the equivalent strain distribution along the axes of the specimen, the increase of F leads to positive values of $\delta_{\bar{\varepsilon}_{vM}}$ in the central region of the cruciform specimen (d between 0 and at about 25 mm) and negative values of $\delta_{\bar{\varepsilon}_{vM}}$ in the remaining region of the arms (see Fig. 2(c and d)). The increase of H leads to the opposite effect of the increase of F (i. e. negative values of $\delta_{\bar{\varepsilon}_{vM}}$ in the central region of the cruciform specimen (d between 0 and at about 25 mm) and positive values of $\delta_{\bar{\varepsilon}_{vM}}$ in the remaining region of the arms (see Fig. 2(c) and d)). Concerning the strain path distribution along the axes of the specimen, the increase of F leads to small changes in the ratio $\varepsilon_2/\varepsilon_1$ and in the $\cos(\varphi)$ values, along both 0x and 0y axes (see Fig. 2(e and f)). The increase of H leads to noticeable changes in the ratio $\varepsilon_2/\varepsilon_1$, also clearly perceptible in terms of $\cos(\varphi)$, for both 0x and 0y axes (see Fig. 2(e and f)).

(iv) The increase of N leads to an imperceptible decrease of the P vs. Δl results along both axes (see Fig. 2(a and b)). The $\bar{\varepsilon}_{vM}$ vs. d results show noticeable complex changes with N (Fig. 2(c)): the $\delta_{\bar{\varepsilon}_{vM}}$ value is positive at d between 0 and 15 mm and negative for the remaining region of the arms. The strain paths, along the axes of the sample, are almost coincident with the reference material results (see Fig. 2(e and f)).

In summary, it can be concluded from Fig. 2(a and b) that the load evolution during the test is mainly influenced by variations in the values of the work-hardening law parameters, Y_0 and n, and in the value of $(F+H)^{1/2}$. The equivalent strain distribution is not influenced by changes in the Y_0 parameter. Variations in the values of the remaining parameters (n, F, H and N) present a complex effect on the equivalent strain distributions. Fig. 2(f) shows that the $\cos(\varphi)$ value is close to 1 in the entire measurement region, not being enough sensitive to variations in the parameters, except the H parameter. Thus, the dissimilarity of the strain paths is not suitable for estimating the constitutive parameters. In this context, the δ_P vs. Δl results will be used for estimating the work-hardening law parameters and the $(F+H)^{1/2}$ value, while the $\delta_{\bar{\varepsilon}_{vM}}$ vs. d results will be only used for estimating Hill'48 parameters. The dissimilarity of the strain paths ($\varepsilon_2/\varepsilon_1$ and $\cos(\varphi)$) will not be used in the optimisation procedure.

3.2. Inverse analysis algorithm

The forward analysis previously presented allowed the development of an inverse analysis methodology, with the following assumptions: (i) the experimental results under the cruciform biaxial test, concerning the evolutions of P vs. Δl and $\bar{\varepsilon}_{vM}$ vs. d, are determined in advance and (ii) the elastic properties of the material are known. In order to illustrate the proposed inverse analysis strategy, the "experimental" results are computer generated using a material, which behaviour is described by Drucker's yield criterion extended to anisotropy by means of a linear transformation (Drucker + L) and Swift isotropic work-hardening law. The constitutive models parameters to be identified concern Hill'48 yield criterion and Swift work-hardening law. The Hill'48 anisotropy parameters L and M are set equal to 1.5.

The use of computer generated results instead of experimental ones is a simple and efficient way to test the inverse analysis methodology, since the behaviour of the tested material is properly defined, without the errors generally associated with experimental measurements. The disadvantage of this approach is that parameters identification is known to be sensitive to experimental noise, although experimental full-field strain measurements, with noise in the range of DIC admissible uncertainties, allow obtaining parameters dispersion that remains in narrow and acceptable ranges (e.g. [18]). However, the use of computer generated results allows the suitable comparison between inverse analysis and "experimental" results, concerning the yield surface and the work-hardening functions that, for real experimental cases, can only be accessed with resource to other methodologies such as the classical ones, using constitutive models that not adequately describe the behaviour of the material. In fact, it is legitimate to consider that any constitutive model cannot perfectly describe the behaviour of a given material.

The proposed inverse analysis methodology consists on determining a primary solution, which can be enhanced using a gradient-based algorithm, i.e. the Levenberg–Marquardt method.

3.2.1. Primary solution

The initial part of the proposed inverse analysis methodology is summarised in Table 2. This methodology is detached in six steps;

Table 2
Summary of the inverse analysis methodology for identifying the parameters of the Hill'48 criterion and the Swift work-hardening law.

Step	Parameters to optimise	Results compared (Numerical – Experimental)	Variables analysed
1.	Initial estimate of the parameters of the Swift work-hardening law and the Hill'48 yield criterion		
2.	n	P vs. Δl	ϕ^{avg}
3.	$(F+H)^{1/2}$ ($=\sigma_0/\sigma_{90}$)	P vs. Δl	$\delta_P^M(0x-0y)$
4.	F, G, H	$\bar{\varepsilon}_{vM}$ vs. d	$\lvert\delta_{\bar{\varepsilon}_{vM}}\rvert^{avg}$
5.	N	$\bar{\varepsilon}_{vM}$ vs. d	$\lvert\delta_{\bar{\varepsilon}_{vM}}\rvert^{avg}$
6.	Y_0	P vs. Δl	δ_P^{avg}

for starting the inverse analysis (Step 1), an initial set of parameters is chosen. In each of the following steps, numerical simulations are performed and the results are compared with the experimental ones, for verifying whether it is necessary to repeat each step of the procedure. Table 2 shows the type of results, numerical and experimental, which are compared at each step of the analysis, along the 0x and 0y axes, as well as the variables analysed from each type of results. The sequence shown in Table 2 does not require returning to previous steps, i.e. the variables analysed in a given step remain stable in the following steps, as it was concluded from a comprehensive study concerning the ordering of steps. The parameters analysed and the objectives of each step are next described.

- Step 1: The initial estimate of the parameters of Hill'48 yield criterion and Swift work-hardening law. A comprehensive study showed that the accuracy of the final results is not influenced by the first estimate, although it may influence the number of iterations. To accomplish this step, it is suggested to determine the initial Hill'48 parameters based on the knowledge of the anisotropy coefficients at angles of 0°, 45° and 90° between the tensile axis and the rolling direction of the sheet, r_0, r_{45} and r_{90}, respectively. The anisotropy coefficient is defined as the width to thickness strains ratio in the uniaxial tensile test. The r_0, r_{45} and r_{90} values can be determined by the traditional method, using tensile tests, for example. Alternatively, the values of r_0 and r_{90} can be estimated from the results of the material under the cruciform biaxial test, through the following equation:

$$r_0, r_{90} = -(\varepsilon_2/\varepsilon_1)/(\varepsilon_2/\varepsilon_1 + 1) \tag{5}$$

  which considers that the values of r_0 and r_{90} are calculated from ε_1 and ε_2, at the 0x and 0y axes, respectively, for a d value such as the ratio $\varepsilon_2/\varepsilon_1$ attains its minimum value, which naturally occurs in the arms of the specimen. For this d value, the strain path is close to uniaxial tension. The first estimate of r_{45} can be assumed, for example, as the arithmetic average between the first estimate of the r_0 and r_{90} values. For Hill'48 yield criterion, the equations which relate Hill'48 anisotropy parameters with the anisotropy coefficients r_0, r_{45} and r_{90} are as follows:

$$r_0 = H/G \quad r_{45} = N/(F+G) - 0.5 \quad r_{90} = H/F \tag{6}$$

  Another alternative for the initial values of Hill'48 parameters is to consider their values as in isotropy, i.e. $F = G = H = 0.5$ and $N = 1.5$.The first estimate of Swift work-hardening law parameters consists on adopting values typical for the material in study. As alternative, the first estimate of Swift work-hardening parameters can be obtained using a tensile test with any axis orientation relatively to the rolling direction of the sheet, or from the cruciform biaxial test following the strain and stress values during loading, at a point in the central region of the arm (along the 0x axis, for example), for which the strain path is close to uniaxial tension.
- Step 2: The estimate of the n value by adjusting the slope of the δ_P vs. Δl results. This slope is defined as $\phi = (1/p)\sum_{i=1}^{p}\left|\lvert\delta_P\rvert - \lvert\delta_P\rvert^M\right|_i$, where $\lvert\delta_P\rvert$ is the absolute value of the relative difference in loading for the measuring loading point i (which corresponds to a certain Δl value - see forward analysis) and $\lvert\delta_P\rvert^M = (1/p)\sum_{i=1}^{p}\lvert\delta_P\rvert_i$ is the average of the absolute values of the relative difference in loading, where p is the total number of measuring loading points. The estimated n value is obtained when the average value, $\phi^{avg} = (\phi(0x) + \phi(0y))/2$, of 0$x$ ($\phi(0x)$) and 0y($\phi(0y)$) axes, reaches a minimum. In other words, for the estimated n value, the experimental and numerical P vs. Δl curves, obtained for the axis 0x (and 0y), can be superimposed, as much as possible, by making a vertical displacement, proportional to the load, of one of them. Moreover, the evolution of δ_P (along both 0x and 0y axes) during the test allows to decide if increments or decrements of n should be performed, in agreement with the forward analysis. If δ_P increases with the increase of Δl, then decrements of n must be performed; otherwise, if δ_P decreases with the increase of Δl, then increments of n must be performed.
- Step 3: The estimate of the $(F+H)^{1/2}$ value by reducing the disagreement of the δ_P vs. Δl results between the 0x and 0y axes. Generally, at the end of the previous step, the values of the relative vertical displacements necessary for superimposing the experimental and numerical P vs. Δl curves are not equal for the two axes, 0x and 0y. The average of the relative difference in loading is evaluated as $\delta_P^M = (1/p)\sum_{i=1}^{p}\delta_{P_i}$, for the 0$x$ ($\delta_P^M(0x)$) and the 0y axes ($\delta_P^M(0y)$), where p is the total number of measuring loading points. The disagreement is quantified by the difference between the 0x and 0y results of δ_P^M, $\delta_P^M(0x-0y) = (\delta_P^M(0x) - \delta_P^M(0y))$. The minimisation of $\delta_P^M(0x-0y)$ is achieved by acting on the $(F+H)^{1/2}$ value (for example, by changing F or H, separately). In this regard, decrements of $(F+H)^{1/2}$ must be performed if $\delta_P^M(0y) < \delta_P^M(0x)$, otherwise, increments of $(F+H)^{1/2}$ should be performed, in agreement with the forward analysis. At the end of this step, an equation $(F+H)^{1/2} = k$ coupling the F and H constitutive parameters is established, in addition to the equation $G + H = 1$.
- Step 4: The estimate of the F, G and H values which minimise the average of the relative differences in von Mises equivalent strain between the 0x and the 0y axes, $\lvert\delta_{\bar{\varepsilon}_{vM}}\rvert^{avg} = (\lvert\delta_{\bar{\varepsilon}_{vM}}\rvert^M(0x) + \lvert\delta_{\bar{\varepsilon}_{vM}}\rvert^M(0y))/2$. This step keeps the $(F+H)^{1/2} = k$ value as adjusted in Step 3 and the condition $G + H = 1$ unchanged. The average relative difference in equivalent strain, defined as $\lvert\delta_{\bar{\varepsilon}_{vM}}\rvert^M = (1/q)\sum_{i=1}^{q}\lvert\delta_{\bar{\varepsilon}_{vM}}\rvert_i$, is evaluated for the 0$x$ $\left(\lvert\delta_{\bar{\varepsilon}_{vM}}\rvert^M(0x)\right)$ and 0y $\left(\lvert\delta_{\bar{\varepsilon}_{vM}}\rvert^M(0y)\right)$ axes, where i is the measuring point of the equivalent strain (which corresponds to a certain d value – see forward analysis) and q is the total number of points for measuring the equivalent strain. The proposed approach consists in performing simulations for different sets of F, G and H. This is performed by changing either F or H, for example. Increments, or decrements, of F (or H) should be performed according to the sign of the value of $\delta_{\bar{\varepsilon}_{vM}}$ in the centre of the cruciform specimen. In fact, according with the forward analysis, if this value is positive, then decrements of F (or increments of H) should be performed; otherwise, if this value is negative, then the opposite should be performed. Moreover, if the $\delta_{\bar{\varepsilon}_{vM}}$ value in the centre of the specimen is close to zero, simulations with both increasing and decreasing values of F (or H) should be performed.
- Step 5: The estimate of the N value which minimises $\lvert\delta_{\bar{\varepsilon}_{vM}}\rvert^{avg}$, while keeping unchanged the F, G and H values previously identified in Step 4. The sign of the value of $\delta_{\bar{\varepsilon}_{vM}}$ in the centre of the

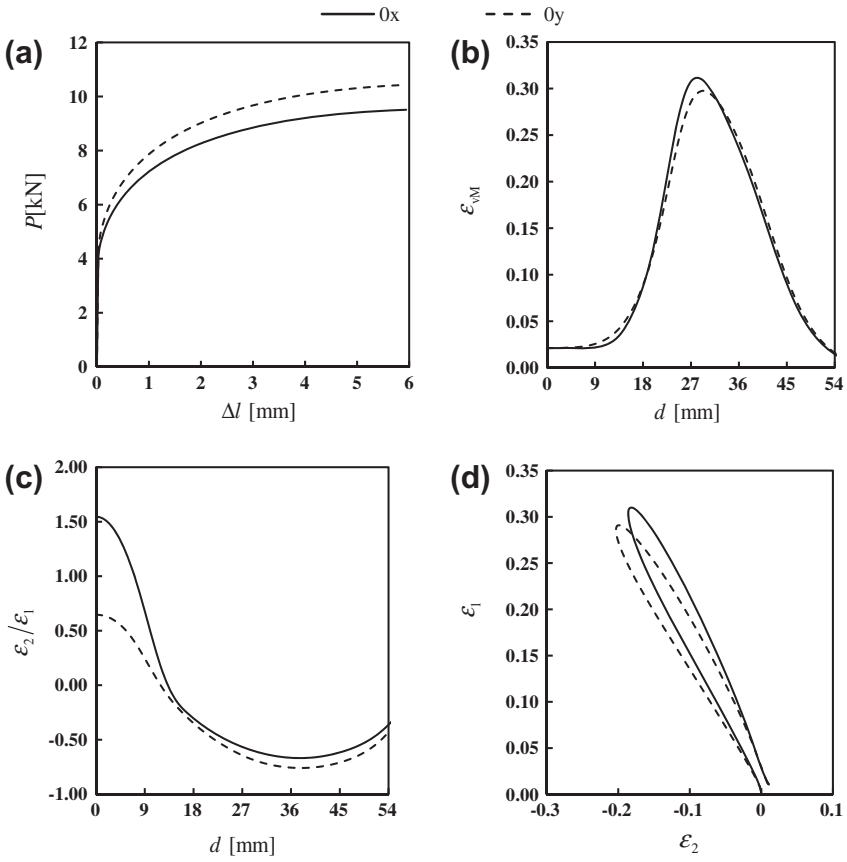

Fig. 3. Cruciform test results concerning the reference material, along the 0*x* and 0*y* axes: (a) *P* vs. Δ*l*; (b) $\bar{\varepsilon}_{vM}$ vs. *d*; (c) $\varepsilon_2/\varepsilon_1$ vs. *d* and (d) ε_1 vs. ε_2 .

cruciform specimen allows deciding if increments, or decrements, of *N* should be performed. If this value is positive, then decrements of *N* should be performed; otherwise, if this value is negative, then the opposite should be performed. Moreover, if the $\delta_{\bar{\varepsilon}_{vM}}$ value in the centre of the specimen is close to zero, then simulations with both increasing and decreasing values of *N* should be performed.

- Step 6: The estimate of Y_0 in such way that the experimental and numerical loading curves coincide as much as possible. In this step, the average of the relative differences in loading between the 0*x* and the 0*y* axes, $\delta_P^{avg} = (\delta_P^M(0x) + \delta_P^M(0y))/2$ is used for adjusting the Y_0 value, which is obtained when minimising δ_P^{avg}. Increments of Y_0 must be performed if δ_P^{avg} is negative; otherwise, decrements of Y_0 must be performed.

Briefly, the variables analysed during this exploratory inverse analysis (see Table 2) allow converting each evolution and distribution, such as in Fig. 2, into a unique value, making the optimisation procedure easier. After the initial estimate of Swift work-hardening law and Hill'48 yield criterion parameters (Step 1), the aim of Step 2 is to make, as much as possible, the overlapping of the numerical and experimental *P* vs. Δ*l*, unless a vertical displacement, proportional to the load, of one of them to the other. In Step 3, the difference in relative difference in loading between the 0*x* and 0*y* axes is minimised. Step 4 and Step 5 concern the minimisation of the numerical and experimental $\bar{\varepsilon}_{vM}$ vs. *d* results, along both axes. The purpose of Step 6 is to overlap the numerical and experimental *P* vs. Δ*l* curves.

The procedure indicated in Table 2 can be extended to other constitutive models provided that the analysed variables and the compared results at each step remain the same. The difference is in the parameter(s) to be optimised in each step of the procedure. That is to say, for a given constitutive model, the parameters to be optimised are the ones associated to: (Step 2) the work-hardening (e.g. for Voce work-hardening law [34], the parameters are the stress saturation rate and the saturation value); (Step 3) the σ_0/σ_{90} ratio; (Step 4) the normal stress components σ_{xx}, σ_{yy}; (Step 5) the shear stress component τ_{xy} and (Step 6) the yield stress value.

Table 3
Initial estimate for the constitutive parameters of the Hill'48 yield criterion and the Swift work-hardening law.

Hill'48 yield parameters				Swift work-hardening parameters		
F	*G*	*H*	*N*	Y_0 (MPa)	*C* (MPa)	*n*
0.5000	0.5000	0.5000	1.5000	100.00	288.54	0.200

3.2.2. Enhanced solution

Afterwards, the gradient-based Levenberg–Marquardt method [35] was adopted to enhance the primary solution, provided by the inverse analysis methodology summarised in Table 2. This method requires an initial solution somewhat close to the final one, otherwise, it may cause convergence problems. In this context, the primary solution can be used as first solution for the minimisation problem, described by the following least squares cost function:

$$F(\mathbf{A}) = \frac{1}{q}\sum_{i=1}^{q}\left(\frac{\bar{\varepsilon}_{vM}^{exp} - \bar{\varepsilon}_{vM}^{num}(\mathbf{A})}{\bar{\varepsilon}_{vM}^{exp}}_i\right)_{0x}^2 + \frac{1}{q}\sum_{i=1}^{q}\left(\frac{\bar{\varepsilon}_{vM}^{exp} - \bar{\varepsilon}_{vM}^{num}(\mathbf{A})}{\bar{\varepsilon}_{vM}^{exp}}_i\right)_{0y}^2 + \frac{1}{p}\sum_{i=1}^{p}\left(\frac{P^{exp} - P^{num}(\mathbf{A})}{P^{exp}}_i\right)_{0x}^2 + \frac{1}{p}\sum_{i=1}^{p}\left(\frac{P^{exp} - P^{num}(\mathbf{A})}{P^{exp}}_i\right)_{0y}^2 \quad (7)$$

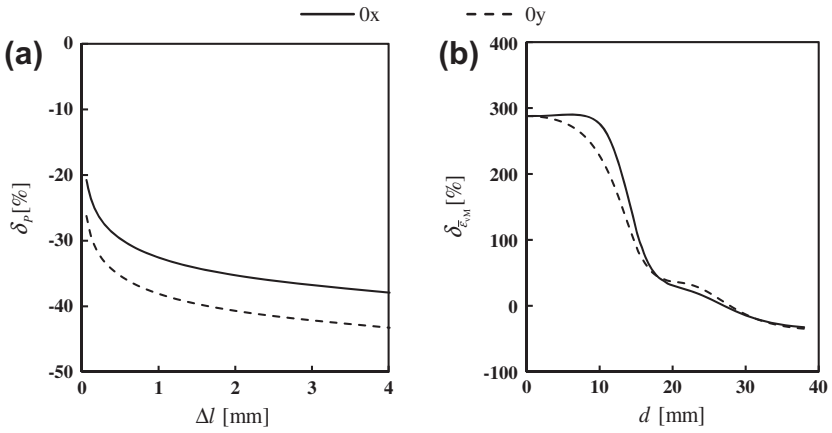

Fig. 4. Relative difference between the first estimate and the reference results, along the 0*x* and 0*y* axes: (a) δ_P vs. Δl and (b) $\delta_{\bar{\varepsilon}_{vM}}$ vs. d.

Table 4
Values of n used in the simulations during the second step of the inverse analysis strategy, and the respective ϕ values. The last line shows the results of ϕ for the estimated n value, at the end of Step 2.

	n	$\phi(0x)$ (%)	$\phi(0y)$ (%)	ϕ^{avg} (%)
Starting point	0.200	2.79	2.70	2.75
Trials	0.220	2.01	1.99	2.00
	0.240	1.23	1.28	1.26
	0.260	0.46	0.56	0.51
	0.280	0.68	0.53	0.61
	0.300	1.59	1.29	1.44
Final estimate	0.268	0.48	0.36	0.42

where $F(\mathbf{A})$ is the cost function; $\mathbf{A}$ is the set of constitutive parameters to be optimised; $\bar{\varepsilon}_{vM}^{exp}$ and $\bar{\varepsilon}_{vM}^{num}$ are the experimental and numerical values of von Mises equivalent strain, respectively, along the 0*x* and 0*y* axes, at an instant previous to maximum load; P^{exp} and P^{num} are the experimental and numerical load values during the test, respectively, along both 0*x* and 0*y* axes. In this work, $\mathbf{A} = [Y_0, n, C, F, G, H, N]^T$ and so the value of ε_0 is left free; also the condition $G + H = 1$ is no longer imposed. The previous cost function is minimised by applying Levenberg–Marquardt method that requires the knowledge of Jacobian matrix, which defines the gradient of the numerically computed measures of equivalent strain and loads with respect to the constitutive parameters. Typically, this matrix is updated at each iteration step k, in order to improve the convergence. However, its calculation in each step requires high computational cost (at least one numerical simulation of the biaxial tensile test per constitutive parameter).

In the case in study, Jacobian matrix is computed using a forward finite differentiation approach. Since the initial values for $\mathbf{A}$ are obtained using the inverse analysis methodology previously mentioned, assuming that they are close to the local minimum, Jacobian matrix was kept unchanged during the optimisation procedure. Also, close to the local minimum, it is preferable to use a small damping factor λ, as it provides near quadratic convergent steps towards the solution. In this work, the recommended value of $\lambda = \|F(\mathbf{A})\|^2$ was used [36].

3.2.3. Final remarks

In summary, the optimisation procedure uses results concerning the loading curve (P vs. Δl) and the evolution of $\bar{\varepsilon}_{vM}$ vs. d; this last evolution is determined at a fixed Δl value, the closer as possible to the one attained at the maximum load. Alternatively, the evolution of $\bar{\varepsilon}_{vM}$ vs. d could be followed and compared at several loading values, during the test, as performed by other authors [19]. However, such a procedure would hinder its practical application and proves to be unnecessary, given the accuracy obtained when using only one Δl value for measuring the strain evolution along the 0*x* and 0*y* axes combined with the loading curves, as we will see later in this study. It will be also shown that the strain measurement on points placed along the 0*x* and 0*y* axes (which can be performed by DIC, but also using other classical measurement procedures) is enough for performing the accurate identification of the constitutive parameters, without requiring the measuring of the whole strain field of the specimen (see e.g. [19,20]), which is a relatively complex procedure. Moreover, when comparing with the classical methodologies, the currently developed inverse analysis strategy only requires the measuring of the load curves and strain evolutions along both axes, avoiding the hard and fastidious analysis of tensile, bulge and shear tests (for example), for determining the yield stresses, anisotropy coefficients and stress–strain curve.

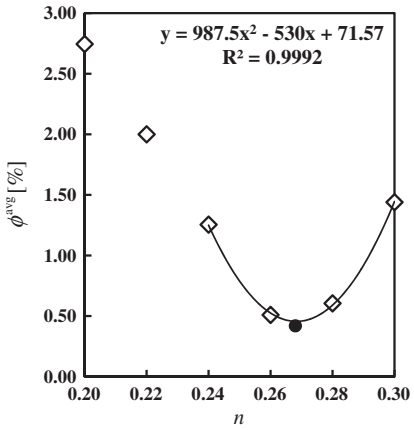

Fig. 5. Polynomial fitting of the results in Table 4, concerning ϕ^{avg} as a function of n (open symbols); the solid symbol represents the estimated value.

3.3. Inverse analysis: case study

In order to exemplify the above described inverse analysis strategy, results of the cruciform biaxial test were computer generated for a material with a plastic behaviour described by Drucker + L criterion and Swift work-hardening law.

Drucker + L is a criterion for orthotropy, given by the equation [37]:

$$[(1/2)\mathrm{tr}(\mathbf{s}^2)]^3 - c[(1/3)\mathrm{tr}(\mathbf{s}^3)]^2 = 27(Y/3)^6 \quad (8)$$

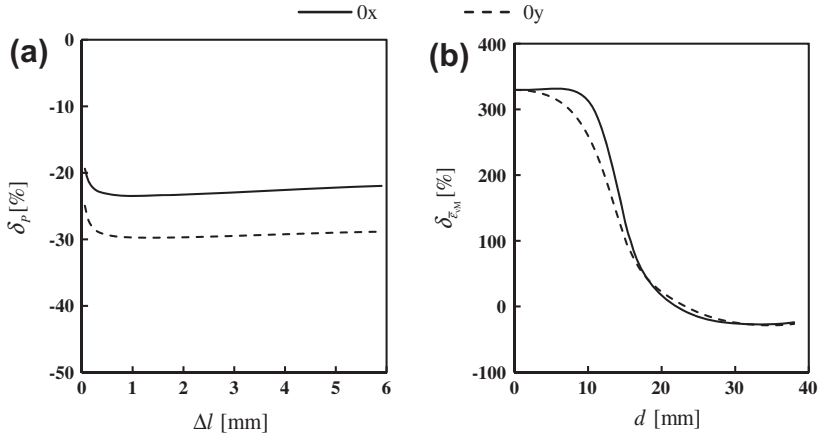

Fig. 6. Relative difference results concerning the second estimate: (a) δ_P vs. Δl and (b) $\delta_{\bar{\varepsilon}_{vM}}$ vs. d.

Table 5
Values of $(F+H)^{1/2}$ used in the simulations during the third step of the inverse analysis strategy, and the respective δ_P^M values. The last line shows the estimated $(F+H)^{1/2}$ value for each approach (F or H approaches, in square brackets) and the corresponding δ_P^M results.

		F				H			
	$(F+H)^{1/2}$	$\delta_P^M(0x)$ (%)	$\delta_P^M(0y)$ (%)	$\delta_P^M(0x-0y)$ (%)	ϕ^{avg} (%)	$\delta_P^M(0x)$ (%)	$\delta_P^M(0y)$ (%)	$\delta_P^M(0x-0y)$ (%)	ϕ^{avg} (%)
Starting point	1.0000	−22.75	−29.26	6.51	0.42	−22.75	−29.26	6.51	0.42
Trials	0.9747	−22.55	−26.72	4.17	0.41	−23.76	−27.89	4.13	0.49
	0.9487	−22.33	−23.93	1.60	0.39	−25.60	−27.20	1.60	1.40
	0.9220	−22.11	−20.87	−1.24	0.37	−26.74	−25.74	−1.00	1.50
	0.8944	−21.88	−17.47	−4.41	0.35	−28.05	−24.37	−3.68	0.50
Final estimate	0.9358 [F approach]	−22.23	−22.48	0.25	0.38				
	0.9329 [H approach]					−25.52	−25.60	0.08	0.56

where tr(**s**) is the trace of the stress tensor **s**, resulting from the linear transformation of the effective Cauchy stress tensor, **σ**, and c is a weight parameter, ranging between −27/8 and 9/4, to ensure the convexity of the yield surface. When c equals zero, this criterion coincides with Hill'48 yield criterion. The **s** stress tensor is given by:

$$\mathbf{s} = \mathbf{L} : \boldsymbol{\sigma} \tag{9}$$

where **L** is the linear transformation operator, written as follows:

$$\mathbf{L} = \begin{bmatrix} (C_2+C_3)/3 & -C_3/3 & -C_2/3 & 0 & 0 & 0 \\ -C_3/3 & (C_3+C_1)/3 & -C_1/3 & 0 & 0 & 0 \\ -C_2/3 & -C_1/3 & (C_1+C_2)/3 & 0 & 0 & 0 \\ 0 & 0 & 0 & C_4 & 0 & 0 \\ 0 & 0 & 0 & 0 & C_5 & 0 \\ 0 & 0 & 0 & 0 & 0 & C_6 \end{bmatrix} \tag{10}$$

where C_i, with $i = 1,\ldots,6$, are the anisotropy parameters. This yield criterion includes one more parameter, the parameter c, than Hill'48 yield criterion, thus being more flexible. So, when the parameter c is not zero, Hill'48 criterion cannot fully describe the behaviour of a material that follows Drucker + L criterion.

The purpose of this case study is to find the set of parameters for Hill'48 yield criterion and Swift work-hardening law, which best describe the reference results of the cruciform test, considered as experimental. In order to obtain these results, the anisotropy parameters considered for Drucker + L criterion are $C_1 = 0.6681$, $C_2 = 0.8158$, $C_3 = 1.2394$, $C_4 = C_5 = 1.0000$, $C_6 = 0.9440$, $c = 1.4265$ and Swift law parameters are $Y_0 = 118.63$ MPa, $C = 502.61$ MPa and $n = 0.268$. The elastic properties are: Young's modulus, $E = 210$ GPa and Poisson ratio, $\nu = 0.3$. Fig. 3 shows the numerically generated results of the cruciform test, along both axes. Fig. 3(a) shows the P vs. Δl evolution; Fig. 3(b) shows the $\bar{\varepsilon}_{vM}$ vs. d distribution; Fig. 3(c) present the $\varepsilon_2/\varepsilon_1$ vs. d distribution and Fig. 3(d) the ε_1 vs. ε_2 distribution. The results in Fig. 3(b–d) were obtained after displacements of the specimen boundaries Δl equal to 6 mm, preceding the maximum load along the 0x and 0y axes. In order to compare material results with the ones obtained at the different steps of the inverse analysis, the number of points used to evaluate the loading evolution and the equivalent strain distribution, p and q, respectively, are equal to 100 for each axis.

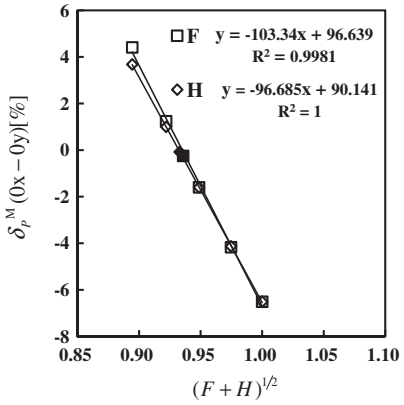

Fig. 7. Linear fitting of the results in Table 5, concerning $\delta_P^M(0x-0y)$ as a function of $(F+H)^{1/2}$, regarding the F or H approaches (open symbols); the solid symbols represent the estimated values for each case.

Table 3 shows the parameters of Hill'48 criterion (as for isotropy), as well as Swift work-hardening parameters, which were estimated based on values typical for the material in study (which is somewhat identical to a mild-steel), used as initial estimate of

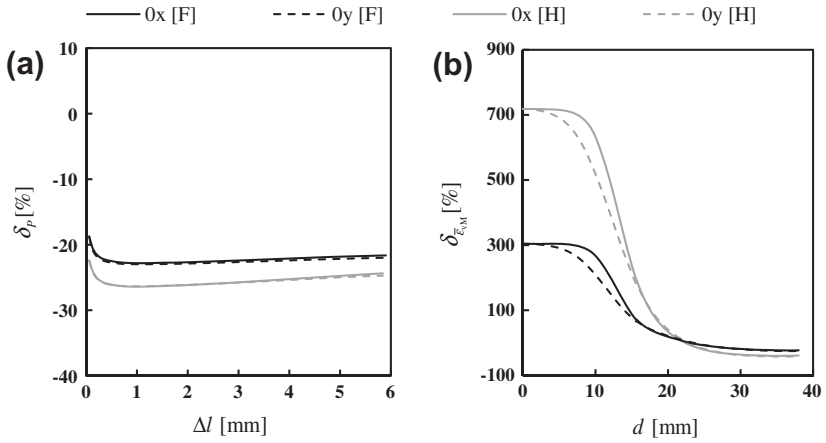

Fig. 8. Relative difference results concerning the third estimate, along both 0x and 0y axes, for each approach (F and H approaches, in square brackets): (a) δ_P vs. Δl and (b) $\delta_{\bar{\varepsilon}_{vM}}$ vs. d.

Table 6
Estimate of F from the fourth step of the inverse analysis strategy (the value of $(F+H)^{1/2}$ is kept unchanged and the condition $G+H=1$ is preserved).

	F	$\lvert\delta_{\bar{\varepsilon}_{vM}}\rvert^{M}(0x)$ (%)	$\lvert\delta_{\bar{\varepsilon}_{vM}}\rvert^{M}(0y)$ (%)	$\lvert\delta_{\bar{\varepsilon}_{vM}}\rvert^{avg}$ (%)	$\delta_P^M(0x-0y)$ (%)	ϕ^{avg} (%)
Starting point	0.3757	116.48	106.36	111.42	0.25	0.38
Trials	0.3000	55.54	50.31	52.93	0.14	0.23
	0.2500	24.65	21.95	23.30	0.05	0.17
	0.2000	4.80	4.65	4.73	−0.07	0.23
	0.1500	19.52	18.51	19.02	−0.20	0.25
	0.1000	33.78	31.82	32.80	−0.36	0.38
Final estimate	0.1967	4.44	4.44	4.44	−0.07	0.24

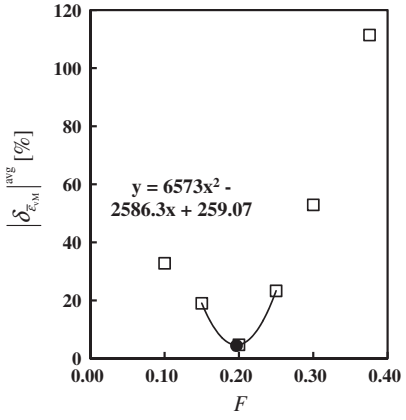

Fig. 9. Polynomial fitting of the results $|\delta_{\bar{\varepsilon}_{vM}}|^{avg}$ as a function of F (open symbols). The solid symbol represents the estimated F value and the obtained $|\delta_{\bar{\varepsilon}_{vM}}|^{avg}$ value.

the inverse analysis procedure (Step 1). In Table 3, the parameter ε_0, of Swift law, is equal to 0.005, which is kept unchanged during the inverse analysis, until determination of the primary solution.

According to Table 2, steps 2, 3 and 6 are focused on the analysis on the δ_P vs. Δl evolution while steps 4 and 5 use the $\delta_{\bar{\varepsilon}_{vM}}$ vs. d distribution. Nevertheless, to make it easy to understand the progression of the optimisation procedure, both types of results are shown in all steps.

The second step of the inverse analysis strategy (see Table 2) started by performing a numerical simulation, considering the initial estimate of the constitutive parameters presented in Table 3, and comparing the results with the experimental ones. Fig. 4 shows the results of the relative difference of the loading evolutions (Fig. 4(a)) and von Mises equivalent strain distributions (Fig. 4(b)), along both 0x and 0y axes. Results in Fig. 4(a) are displayed up to a tool displacement $\Delta l = 4$ mm, since the maximum load value obtained for the initial estimate occurs for a displacement value much less than 6 mm, observed for the experimental results (see Fig. 3(a)); consequently, Fig. 4(b) was plotted for $\Delta l = 4$ mm.

Fig. 4(a) shows a gradual increase on the negative side of the relative difference throughout the test, corresponding to a value of 2.74 for $\phi(0x)$ and 2.66 for $\phi(0y)$ slopes. The forward analysis revealed that an increase of n is related with a gradual increase on the positive side of the evolution of the relative load difference, during the test. Therefore, in Step 2, five trial simulations were performed in parallel, considering increasing values of n, while keeping the remaining parameters unchanged. Table 4 shows the results of $\phi(0x)$, $\phi(0y)$ and ϕ^{avg}, for these simulations (i.e. with increasing work-hardening exponent values). A 2nd order polynomial fit of the results of ϕ^{avg} as a function of n was performed, as shown in Fig. 5; a work-hardening exponent of $n = 0.268$ was estimated from the minimum value of this fit. A new numerical simulation was performed using this n value, in order to determine the respective values of $\phi(0x)$ and $\phi(0y)$ (see Table 4 and Fig. 5). The results obtained were compared with the experimental ones, as shown in Fig. 6(a) for the relative difference results in loading and in Fig. 6(b) for von Mises equivalent strain, along both 0x and 0y axes. Results in Fig. 6(a) are displayed up to a load value prior to the maximum, i.e. for a tool displacement of 6 mm (the maximum load appears after this displacement value for both the numerical and experimental results); consequently, Fig. 6(b) was obtained for $\Delta l = 6$ mm. In general, Fig. 6(a) results display a steady value for the relative difference in loading, during the test, as a result of the improved estimation of n. Therefore, the obtained ϕ^{avg} value equal to 0.42 was considered small enough to proceed to the next step.

The third step of the inverse analysis strategy (see Table 2) consists in performing trial numerical simulations with different values of $(F+H)^{1/2}$, by either changing F or H, in order to find the $(F+H)^{1/2}$ value that minimises $\delta_P^M(0x-0y)$, i.e. minimises the disagreement between the average relative difference in loading results for both axes. Forward analysis showed that when $(F+H)^{1/2}$ increases, the relative difference of the loading results along the 0y axis becomes located below to the results obtained for the 0x axis, i.e. $\delta_P^M(0y) < \delta_P^M(0x)$ (see Fig. 2(b)). Therefore, trial simulations with decreasing values of $(F+H)^{1/2}$ were performed

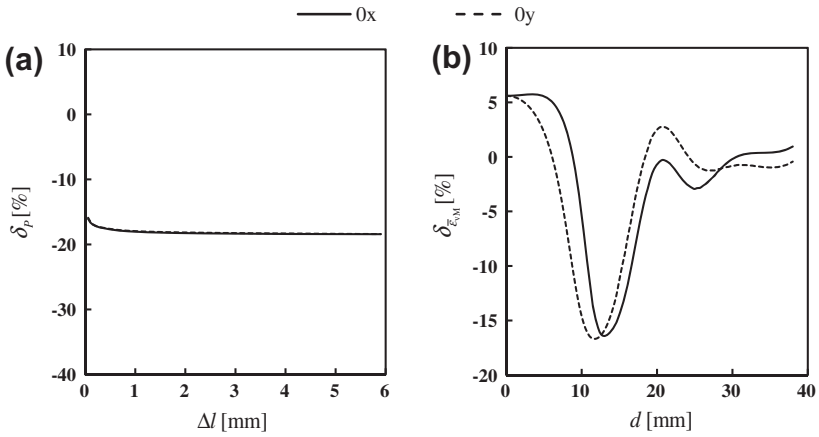

Fig. 10. Relative difference results concerning the fourth estimate: (a) δ_P vs. Δl and (b) $\delta_{\bar{\varepsilon}_{vM}}$ vs. d.

Table 7
Estimate of N from the fifth step of the inverse analysis strategy.

	N	$\lvert\delta_{\bar{\varepsilon}_{vM}}\rvert^{M}(0x)$ (%)	$\lvert\delta_{\bar{\varepsilon}_{vM}}\rvert^{M}(0y)$ (%)	$\lvert\delta_{\bar{\varepsilon}_{vM}}\rvert^{avg}$ (%)	$\delta_P^M(0x-0y)$ (%)	ϕ^{avg} (%)
Starting point	1.5000	4.44	4.44	4.44	−0.07	0.24
Trials	1.7000	5.93	5.93	5.93	−0.02	0.24
	1.6000	5.00	5.10	5.05	−0.05	0.24
	1.4000	4.55	4.51	4.53	−0.09	0.24
	1.3000	6.26	6.43	6.35	−0.12	0.25
Final estimate	1.4620	4.42	4.28	4.35	−0.08	0.24

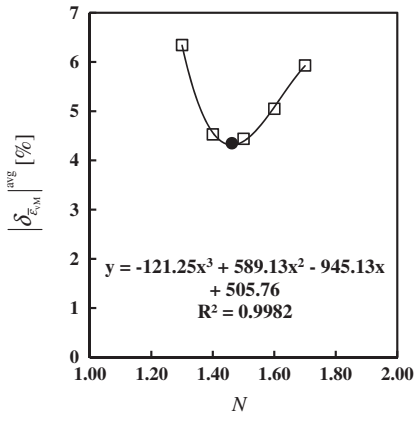

Fig. 11. Polynomial fitting of the results of $\lvert\delta_{\bar{\varepsilon}_{vM}}\rvert^{avg}$ as a function of N (open symbols). The solid symbol represents the estimated N value and the obtained $\lvert\delta_{\bar{\varepsilon}_{vM}}\rvert^{avg}$ value.

in parallel, during this step. Table 5 shows the results of $\delta_P^M(0x)$, $\delta_P^M(0y)$ and $\delta_P^M(0x-0y)$ obtained from two possible approaches, i.e. by either decreasing of F or H. Fig. 7 shows the estimated $(F+H)^{1/2}$ value based on these two approaches by using a linear fitting. Both approaches lead to quite similar estimations of the $(F+H)^{1/2}$ value (0.9358, when acting on F, or 0.9329, when acting on H).

Two numerical simulations were performed using both final estimations of the $(F+H)^{1/2}$ value, in order to determine the respective values of $\delta_P^M(0x-0y)$ (see Table 5 and Fig. 7). The results obtained for δ_P vs. Δl and $\delta_{\bar{\varepsilon}_{vM}}$ vs. d are shown in Fig. 8(a and b), respectively, along both $0x$ and $0y$ axes. Results in Fig. 8(a) are displayed up to a load value prior to the maximum, i.e. for a tool displacement of 6 mm; Fig. 8(b) was obtained for $\Delta l = 6$ mm. In general, for each final estimation, Fig. 8(a) displays an overlapping of δ_P vs. Δl for the $0x$ and $0y$ axes, as a result of the improved estimation of $(F+H)^{1/2}$, for both approaches. The values of $\delta_P^M(0x-0y)$ obtained from the linear fittings of Fig. 7 are 0.25 and 0.08, for the approaches with F and H, respectively. During this step, the variables studied in the previous step (ϕ^{avg}) almost not change its value ($\phi^{avg} = 0.38$ (for the F approach) and $\phi^{avg} = 0.56$ (for the H approach), in contrast with $\phi^{avg} = 0.42$ for the starting point in Table 5).

In the fourth step of the inverse analysis strategy (see Table 2) simulations with different F, G and H sets are carried out, while keeping constant the $(F+H)^{1/2}$ value found in Step 3 and the condition $G+H=1$ unchanged. This step uses as starting point the final estimate of the parameters corresponding to $(F+H)^{1/2} = 0.9358$ (F approach in Table 5). The $\delta_{\bar{\varepsilon}_{vM}}$ value in the centre of the specimen is positive (see Fig. 8(b)), therefore, five trial simulations with decreasing values of F were performed in parallel during this step. Table 6 shows the results of $\lvert\delta_{\bar{\varepsilon}_{vM}}\rvert^{M}$ obtained for the different F values, emphasising the value $F = 0.1967$, retained from a 2nd order polynomial fit on $\lvert\delta_{\bar{\varepsilon}_{vM}}\rvert^{avg}$ vs. F, as shown in Fig. 9. The value of $\lvert\delta_{\bar{\varepsilon}_{vM}}\rvert^{avg}$ obtained from the polynomial fitting of Fig. 9 is equal to 4.44%. Also, the variables studied in the previous steps ($\delta_P^M(0x-0y)$, ϕ^{avg}) are not significantly affected with the changing of the F parameter. The numerical simulation results obtained with the improved value of F are compared with the experimental ones in Fig. 10, which show the relative differences in loading (Fig. 10(a)) and in von Mises equivalent strain (Fig. 10(b)), for both axes. Fig. 10(b) display a global shifting of the $\delta_{\bar{\varepsilon}_{vM}}$ values towards 0%, when compared with the third estimate (see Fig. 8(b)), resulting from the improved estimation of the F parameter. Fig. 10(a) shows a slight positive vertical displacement of the δ_P values, when compared with the third estimate corresponding to the approach of decreasing F (see Fig. 8(a)).

The fifth step of the inverse analysis strategy (see Table 2) consists in performing trial numerical simulations with different N values, while keeping the other parameters unchanged, in order to find the value that minimises the overall relative difference in von Mises equivalent strain distribution, $\lvert\delta_{\bar{\varepsilon}_{vM}}\rvert^{avg}$. Starting from the estimate in Step 4, the $\delta_{\bar{\varepsilon}_{vM}}$ value in the centre of the specimen is positive, although not far from zero (5% – see Fig. 10(b)); therefore, four trial simulations, two of which with increasing and the other two with decreasing values of N are considered in this step. From Table 7 it is shown that the $\lvert\delta_{\bar{\varepsilon}_{vM}}\rvert^{M}$ values obtained for the different N values are at the vicinity of the minimum, namely the

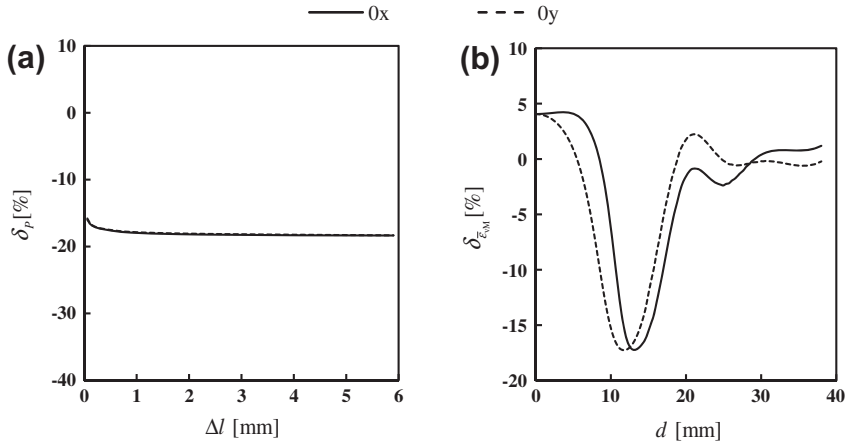

Fig. 12. Relative difference results concerning the fifth estimate: (a) δ_P vs. Δl and (b) $\delta_{\bar{\varepsilon}_{vM}}$ vs. d.

Table 8
Estimate of Y_0 from the sixth step of the inverse analysis strategy.

	Y_0 (MPa)	$\delta_P^M(0x)$ (%)	$\delta_P^M(0y)$ (%)	δ_P^{avg} (%)	$\lvert\delta_{\bar{\varepsilon}_{vM}}\rvert^{avg}$	$\delta_P^M(0x-0y)$ (%)	ϕ^{avg} (%)
Starting point	100.00	−18.12	−18.04	−18.08	4.35	−0.08	0.24
Trials	110.00	−9.98	−9.90	−9.94	4.39	−0.08	0.23
	120.00	−1.85	−1.77	−1.81	4.44	−0.08	0.21
	130.00	6.28	6.36	6.32	4.49	−0.08	0.18
	140.00	14.40	14.47	14.44	4.55	−0.07	0.16
Final estimate	122.23	−0.03	0.05	0.01	4.45	−0.08	0.13

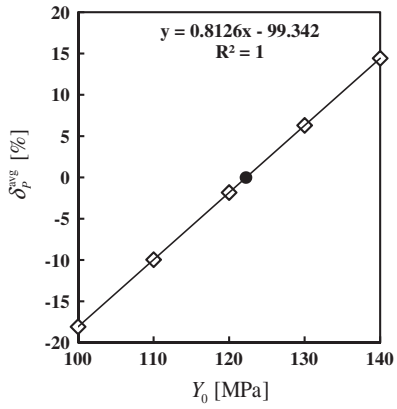

Fig. 13. Linear fitting of the results of δ_P^{avg} vs. Y_0 (open symbols). The solid symbol represents the estimated Y_0 value and the obtained δ_P^{avg} value.

starting point value ($N = 1.5000$). The value of $N = 1.4620$ was retained from the polynomial fitting on the results of $|\delta_{\bar{\varepsilon}_{vM}}|^{avg}$ vs. N, as shown in Fig. 11. The value of $|\delta_{\bar{\varepsilon}_{vM}}|^{avg}$ obtained from the polynomial fitting of Fig. 11 is equal to 4.35%. Also, the variables studied in the previous steps ($\delta_P^M(0x-0y)$ and ϕ^{avg}) are not significantly affected with the changing of N value. The numerical simulation results obtained with the improved value of N are compared with the experimental ones in Fig. 12, which show the relative differences in loading (Fig. 12(a)) and von Mises equivalent strain (Fig. 12(b)), for both axes. Fig. 12(b) display a slight improvement of the $|\delta_{\bar{\varepsilon}_{vM}}|^{avg}$ values when compared with the fourth estimate (see Fig. 10(b)), due to an improvement of the N parameter estimation. Fig. 12(a) shows no changes of the relative difference in loading, when compared with the fourth estimate (see Fig. 10(a)).

The sixth step of the inverse analysis strategy (see Table 2) consists in performing numerical simulations with different values of Y_0, in order to minimise the overall relative difference in load, δ_P^{avg}. In the forward analysis it was shown that an increase of Y_0 is related with an increase of δ_P^{avg}. Therefore, in this step, and taking the estimate results of the fifth step as reference, four trial simulations were performed with increasing values of Y_0, while keeping the remaining parameters unchanged. Table 8 shows the results obtained for δ_P^M as a function of Y_0, for all these simulations, including the estimate from step five. Table 8 also shows the variables analysed in the previous steps, in order to show that the respective differences are not significantly affected when changing the Y_0 value. The yield stress equal to 122.23 MPa was estimated from a linear fitting of the δ_P^{avg} vs. Y_0 results, as shown in Fig. 13. The value of δ_P^{avg} obtained from the linear fitting of Fig. 13 is equal to 0.01%. Also, the variables studied in the previous steps ($|\delta\bar{\varepsilon}_{vM}|^{avg}$, $\delta_P(0x-0y)$, ϕ^{avg}) indicate enough accuracy, at the end of this step. The results obtained with the improved estimation of Y_0 were compared with the experimental ones and are shown in Fig. 14: (a) the relative difference in loading and (b) von Mises equivalent strain, along both 0x and 0y axes. Fig. 14(a) displays values for the relative difference in loading close to 0%, i.e. the numerical and material P vs. Δl curves become similar.

The inverse analysis methodology previously presented allowed the determination of a primary solution for the constitutive parameters (with a total of 28 simulations). This primary solution was used as first solution for the error minimisation problem defined in Eq. (7), using Levenberg–Marquardt optimisation method. This method has converged to a solution with a cost function value 20% lower than the one obtained at the end of Step 6, after three iterations (with a total of 10 simulations). Otherwise, using Levenberg–Marquardt algorithm for the parameter identification, starting from the initial estimate in Table 3 (Full-LM identification), a similar value of the cost function was reached after 5 iterations, but in this case it was necessary to update Jacobian matrix in each iteration (with a total of 41 simulations). Fig. 15 compares the relative difference in loading (Fig. 15(a)) and von Mises equivalent strain (Fig. 15(b)), along both 0x and 0y axes, at the end of Step 6 (PS), after applying Levenberg–Marquardt optimisation strategy (LM) and for full Levenberg–Marquardt optimisation (Full-LM). Table 9 allows comparing the identified constitutive parameters for all cases in Fig. 15, showing the corresponding cost function values and the values for $|\delta_{\bar{\varepsilon}_{vM}}|^{avg}$, δ_P^{avg}, $\delta_P^M(0x-0y)$ and ϕ^{avg}. In addition, the cost function was also evaluated for the results from Step 1 of the inverse analysis (Initial estimate). The major reduction of $F(\mathbf{A})$ and of both δ_P^M and $|\delta_{\bar{\varepsilon}_{vM}}|^M$ occur during the inverse analysis strategy.

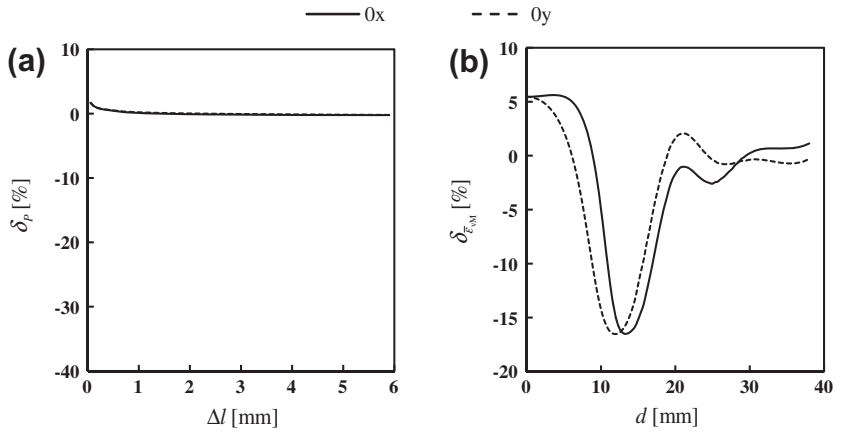

Fig. 14. Relative difference results concerning the sixth estimate: (a) δ_P vs. Δl and (b) $\delta_{\bar{\varepsilon}_{vM}}$ vs. d.

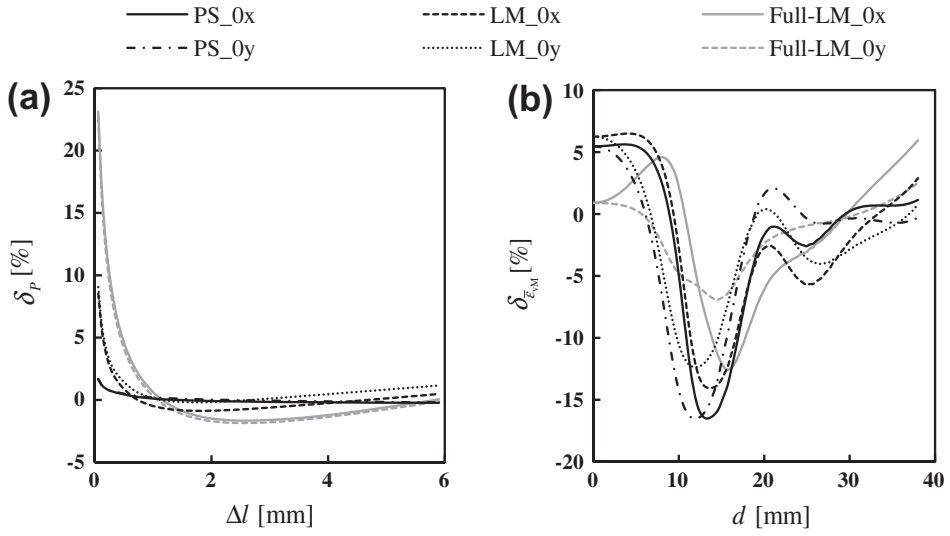

Fig. 15. Relative difference results at the end of Step 6 (PS), after applying the Levenberg–Marquardt strategy (LM) to the primary solution and for the complete Levenberg–Marquardt optimisation (Full-LM), along both 0x and 0y axes: (a) δ_P vs. Δl and (b) $\delta_{\bar{\varepsilon}_{vM}}$ vs. d.

Table 9
Cost function values, $|\delta_{\bar{\varepsilon}_{vM}}|^{avg}$, δ_P^{avg}, $\delta_P^M(0x-0y)$ and ϕ^{avg} values and constitutive parameters for the inverse analysis at Step 1 (Initial Estimate), at the end of the Step 6 (PS), at the end of the Levenberg–Marquardt optimisation strategy (LM) and for the full Levenberg–Marquardt optimisation (Full-LM).

	$F(\mathbf{A})$	$\lvert\delta_{\bar{\varepsilon}_{vM}}\rvert^{avg}$ (%)	δ_P^{avg} (%)	$\delta_P^M(0x-0y)$ (%)	ϕ^{avg} (%)	Hill'48 Anisotropy Parameters				Swift Law Parameters		
						F	G	H	N	Y_0 [MPa]	C [MPa]	n
Initial estimate	5.3022	116.11	−36.84	−5.45	2.75	0.5000	0.5000	0.5000	1.5000	100.00	288.54	0.200
PS	0.0090	4.45	0.01	−0.08	0.13	0.1967	0.3210	0.6790	1.4620	122.23	505.65	0.268
LM	0.0075	4.71	0.71	−0.02	0.56	0.1901	0.3213	0.6787	1.3811	134.60	527.12	0.296
Full-LM	0.0067	3.24	1.99	0.24	1.54	0.2201	0.3431	0.6569	1.0014	156.82	547.61	0.344

According to the cost function used for this optimisation method (see Eq. (7)), the results for "LM" and "Full-LM" cases are slightly better than the results for "PS". However, in the perspective of the exploratory inverse analysis methodology, the $|\delta_{\bar{\varepsilon}_{vM}}|^{avg}$, $\delta_P^{avg}$and ϕ^{avg} variables (evaluated during Step 2) are lower for "PS" than for "LM", and only the value of the variable $|\delta_{\bar{\varepsilon}_{vM}}|^{avg}$ is improved for the "Full-LM" solution, having increased the values of the variables δ_P^{avg}, $\delta_P^M(0x-0y)$, and ϕ^{avg}. That is, for the case of the "Full-LM" solution, the gain in variable $|\delta_{\bar{\varepsilon}_{vM}}|^{avg}$ is compensated by a loss in the remaining variables. In conclusion, the quality of the results obtained by the different optimisation strategies (using variables such as $|\delta_{\bar{\varepsilon}_{vM}}|^{avg}$, δ_P^{avg}, $\delta_P^M(0x-0y)$, and ϕ^{avg}, for the "PS", or cost function, for the gradient-based optimisation strategy) cannot be directly compared, as the quantities minimised in the optimisation strategies are distinct.

4. Classical identification strategy

In this section, the results obtained by the inverse analysis strategy previously presented are compared with the results obtained by a classical methodology. For this case, Hill'48 anisotropy parameters are identified from computer generated results of the following linear strain path tests: tensile and shear tests, with an angle α at 0°, 15°, 30°, 45°, 60°, 75° and 90° with the rolling direction, for which were determined the yield stress and anisot-

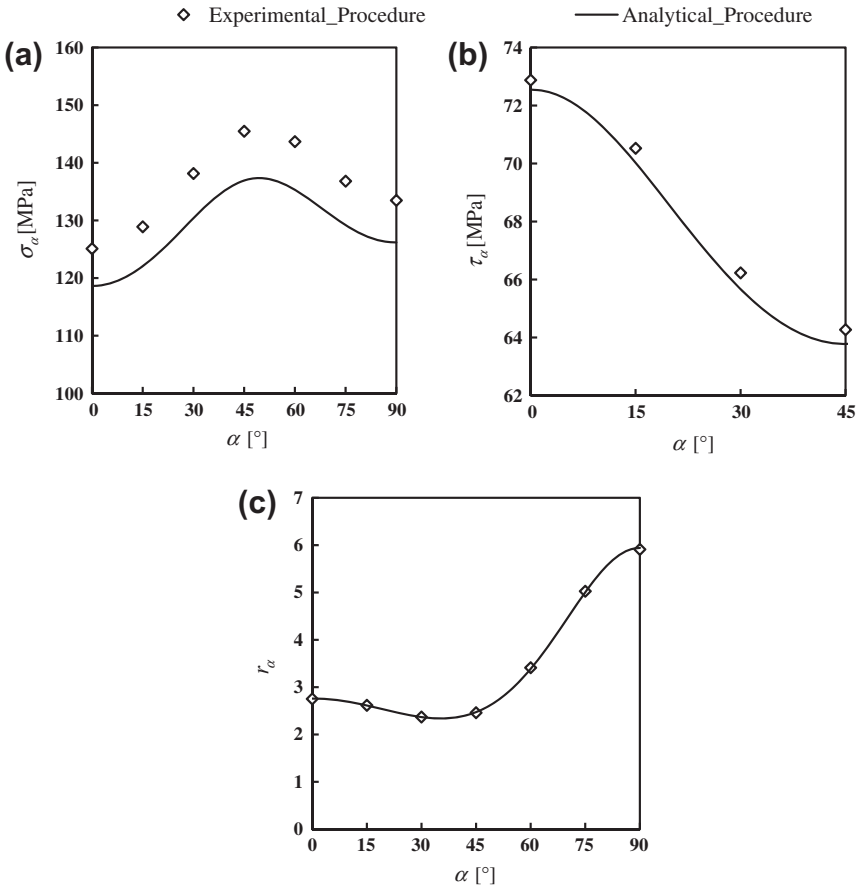

Fig. 16. Comparison between the evolutions of the measured variables with α, according to the experimental and the analytical procedures: (a) initial yield stress in tension and (b) in shear, (c) anisotropy coefficient.

Table 10
Constitutive parameters identified from inverse analysis, i.e. primary solution (PS) and after Levenberg–Marquardt optimisation (LM), from the full Levenberg–Marquardt optimisation (Full-LM) and using the classical methodology with both procedures, i.e. like experimental and analytical.

	Hill'48 anisotropy parameters				Swift law parameters		
	F	G	H	N	Y_0 (MPa)	C (MPa)	n
PS	0.1967	0.3210	0.6790	1.4620	122.23	505.65	0.268
LM	0.1901	0.3213	0.6787	1.3811	134.60	527.12	0.296
Full-LM	0.2201	0.3431	0.6569	1.0014	156.82	547.61	0.344
CM_E	0.1819	0.3877	1.0329	1.6725	135.70	553.89	0.268
CM_A	0.1597	0.3397	0.9258	1.4935	128.38	555.80	0.268

ropy coefficient evolutions in the sheet plane, σ_α and r_α, and the yield stress in shear, τ_α; circular bulge and compression tests, for determining the biaxial yield stress, σ_b, and the biaxial anisotropy coefficient, r_b, respectively. These variables were determined following the same assumptions used in experimental analyses: the values of the yield stresses σ_α, τ_α, and σ_b were obtained from the corresponding stress–strain curves at a plastic strain value of 0.1% [38]; the r_α anisotropy coefficients were determined using strain values from 0.5% up to the onset of necking [38]. As usually, the biaxial stress–strain curve was determined from the bulge test results assuming that the material is isotropic and with resource to the membrane theory [39]. The r_b value, defined by $r_b = \varepsilon_2/\varepsilon_1$, was determined using strain values between 0.5% and 50%.

The parameters of Hill'48 criterion and Swift work-hardening law were also directly identified from the equations describing the behaviour of the material, in order to check the influence of the uncertainties of the experimental analysis on the classical identification results. Concomitantly, this allows to check the influence of assumptions generally taken in the analysis of the experimental data (for example: the yield stress defined at 0.1% of plastic strain; the isotropy condition imposed for determining the equivalent stress–strain curve) on the results of the parameter identification. Fig. 16 shows the comparison between the measured variables according to the experimental and the analytical procedures, namely the yield stress in tension and shear and the anisotropy coefficient as a function of the angle, α, between the tensile and shear directions and the rolling direction (Fig. 16(a), (b) and (c), respectively). The classical experimental procedure used in this section leads to different results when compared with the analytical ones, concerning the yield stresses values (Fig. 16(a and b)). However, the distribution of the anisotropy coefficient, obtained from the experimental procedure (Fig. 16(c)), shows similar results to the analytical solution. The biaxial yield stress values obtained from the experimental procedure and analytically are 131.75 MPa and 165.85 MPa, respectively. The biaxial anisotropy coefficient obtained from the experimental procedure is 0.483 and the analytical value is 0.476.

Subsequently, the classical identification of the parameters is performed from the results obtained from both procedures, like experimental and analytical. For both cases, the difference between the results and the optimisation approach is used to define the cost function with the following formulation [40]:

$$F(\mathbf{A}) = \sum w_i(\sigma_\alpha/\sigma_\alpha^{\exp} - 1)^2 + \sum w_i(r_\alpha/r_\alpha^{\exp} - 1)^2 + \sum w_i(\tau_\alpha/\tau_\alpha^{\exp} - 1)^2 + \sum w_i(\sigma_b/\sigma_b^{\exp} - 1)^2 + \sum w_i(r_b/r_b^{\exp} - 1)^2 \quad (11)$$

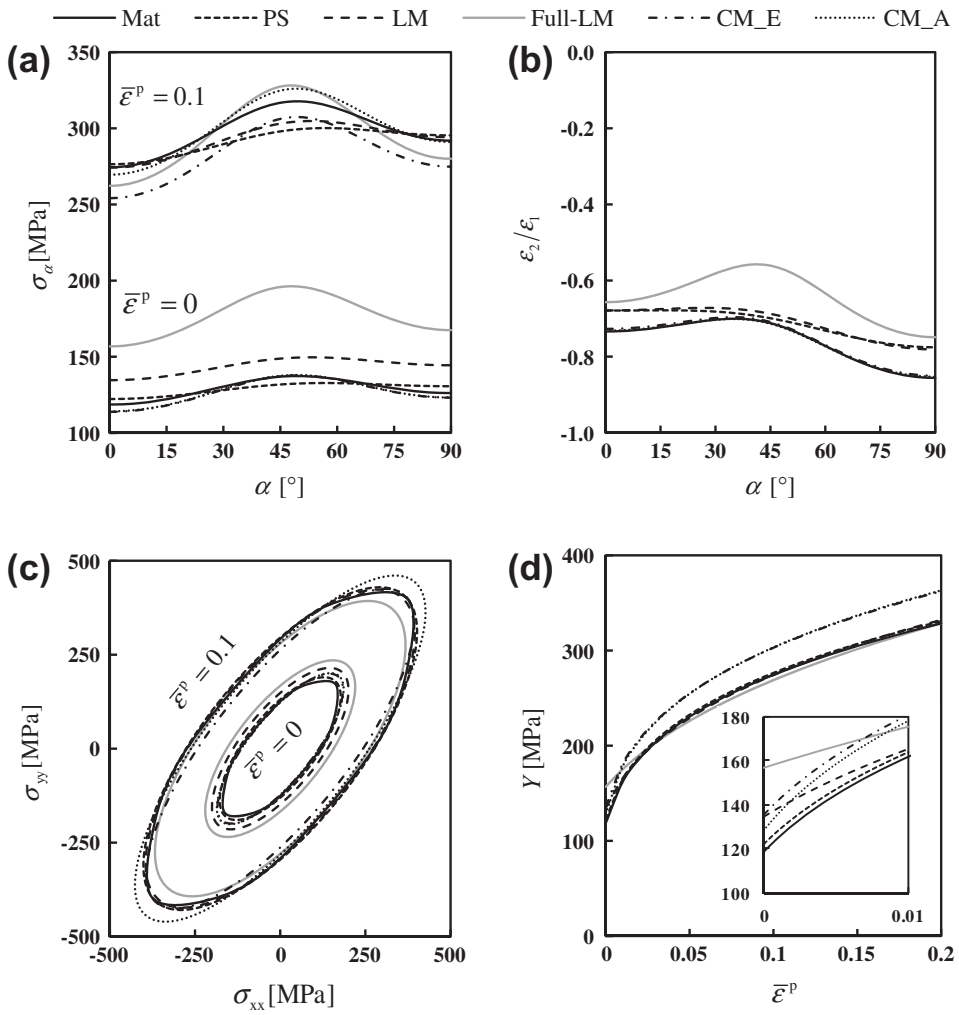

Fig. 17. Comparison between the material (Mat) and identified results: (a) yield stress in tension as a function of α, for $\bar{\varepsilon}^p = 0$ (lower curves) and $\bar{\varepsilon}^p = 0.1$ (upper curves); (b) tensile strain path, distributions as a function of α; (c) the yield surfaces, for $\bar{\varepsilon}^p = 0$ (inner curves) and $\bar{\varepsilon}^p = 0.1$ (outer curves) and (d) equivalent stress–strain curves. The identified results concern the primary solution (PS), after applying the Levenberg–Marquardt optimisation to the primary solution (LM), the complete Levenberg–Marquardt optimisation (Full-LM) and for the classical identification methodologies, with both procedures, like experimental (CM_E) and analytical (CM_A).

A represents the set of anisotropy parameters for the yield criterion, σ_α^{exp}, r_α^{exp}, τ_α^{exp}, σ_b^{exp} and r_b^{exp} are the experimental values, σ_α, r_α, τ_α, σ_b and r_b are the corresponding values predicted by the constitutive equations and w_i are weighting factors (in this study, w_i is equal to 1 for all the performed tests). This objective function was minimised using the downhill simplex method [40]. Swift law parameters were identified assuming that the equivalent work-hardening curve is the average of the seven stress–strain curves in tension, plotted in agreement with von Mises definition of stress and strain [38].

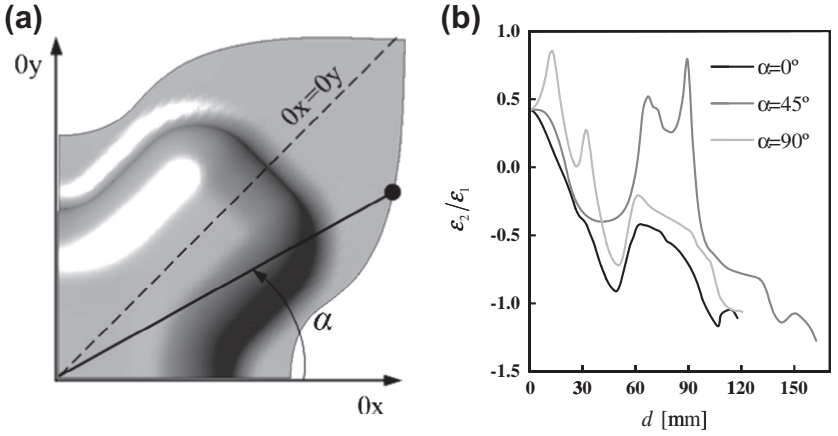

Fig. 18. (a) Projection of the deformed shape (1/4), on the 0xy plane; (b) $\varepsilon_2/\varepsilon_1$ vs. d for the material case, along the 0x ($\alpha = 0°$), 0x = 0y ($\alpha = 45°$) and 0y ($\alpha = 90°$) axes (ε_2 and ε_1 are the minor and major strains in the sheet plane).

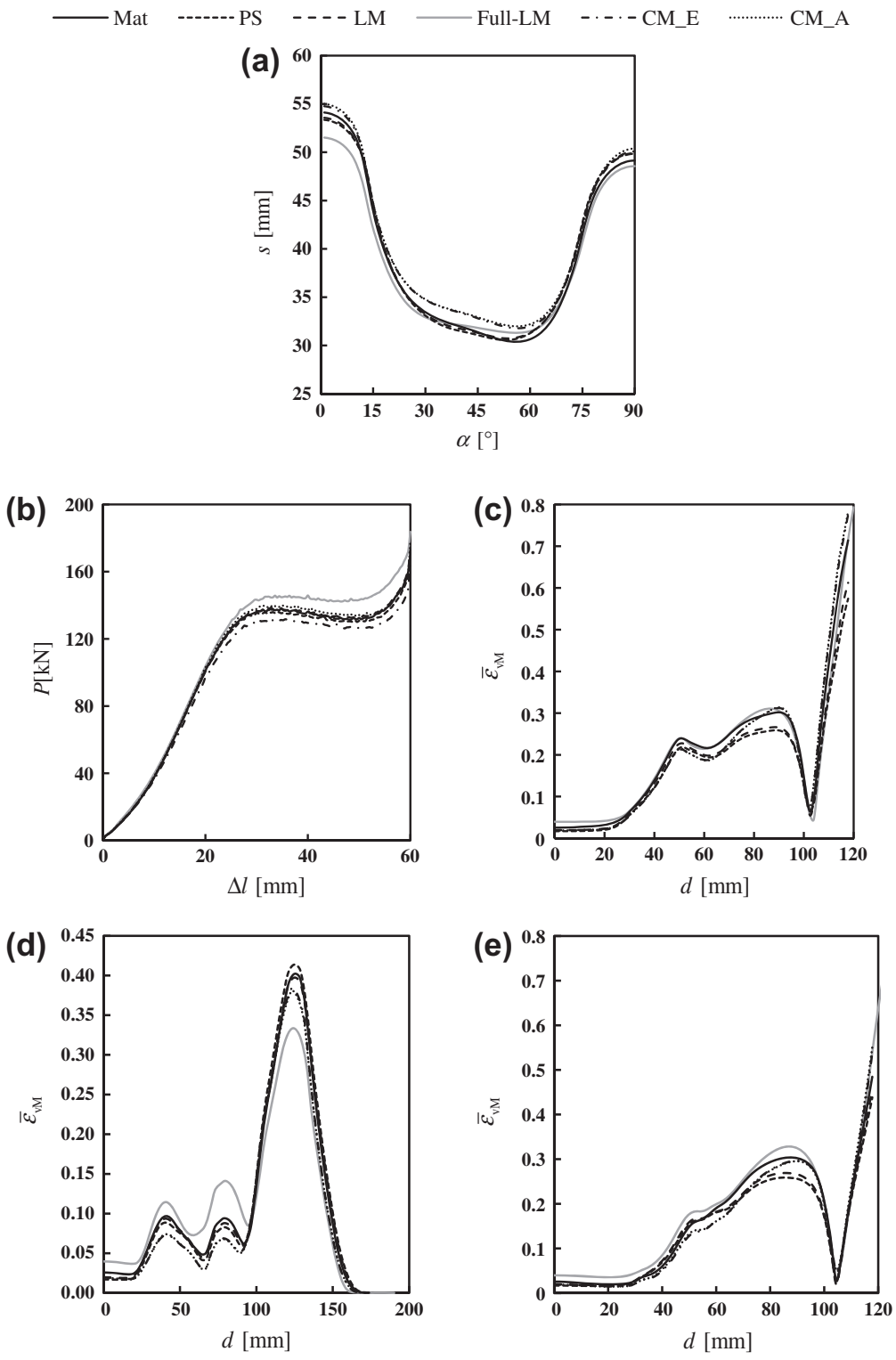

Fig. 19. Cross-shaped cup deep-drawing results: (a) flange draw-in (s) as a function of α, (b) P vs. Δl, (c), (d) and (e) $\bar{\varepsilon}_{vM}$ vs. d, along the 0x, 0x = 0y and 0y axes, respectively, for the material case (Mat), primary solution of the inverse analysis (PS), inverse analysis after the Levenberg–Marquardt optimisation (LM), complete Levenberg–Marquardt optimisation (Full-LM) and classical identification methodology, like experimental and analytical (CM_E and CM_A, respectively).

The sets of parameters identified by inverse analysis with and without using Levenberg–Marquardt optimisation and by both procedures using the classical identification strategy are presented in Table 10. Fig. 17 shows the yield stress (initial, i.e. for $\bar{\varepsilon}^p = 0$, and after a certain amount of equivalent plastic strain, $\bar{\varepsilon}^p = 0.1$) and the strain path in tension, defined by the ratio $\varepsilon_2/\varepsilon_1$, with α (Fig. 17(a and b), respectively), the yield surfaces, for $\bar{\varepsilon}^p = 0$ and for $\bar{\varepsilon}^p = 0.1$, in the $\sigma_{xx} - \sigma_{yy}$ plane (Fig. 17(c)), and the equivalent stress–strain curves, with a detail of the beginning of plastic deformation (Fig. 17(d)). These results are shown for the material (Mat), for the identifications obtained by inverse analysis strategy, i.e. the primary solution (PS) and after Levenberg–Marquardt optimisation

Table 11
Average relative difference results ($|\delta_P|^M$, $|\delta_{\bar{\varepsilon}_{eM}}|^M$ and $|\delta_s|^M$) obtained for the primary solution (PS), after the Levenberg–Marquardt optimisation (LM), for the full Levenberg–Marquardt optimisation (Full-LM) and classical methodology, like experimental (CM_E) and analytical (CM_A) data sets.

Strategy	$\lvert\delta_P\rvert^M$ (%)	$\lvert\delta_{\bar{\varepsilon}_{eM}}\rvert^M$ (%)			$\lvert\delta_s\rvert^M$ (%)
		0x	0x = 0y	0y	
PS	0.84	18.01	16.06	13.54	1.43
LM	0.79	13.31	7.89	11.20	1.19
Full-LM	6.62	13.11	35.64	28.95	2.25
CM_E	4.07	13.76	21.10	13.31	2.95
CM_A	1.60	14.39	20.86	13.74	3.40

Table A1
Examples of geometries considered for the cruciform specimen optimisation design.

Geometry	R (mm)	L_1/L_2 (L_2 = 15 mm)	β (°)
A	1	1.0	0.00
B	3	1.0	0.00
C	3	2.2	0.00
D	3	2.2	9.46

strategy (LM), for full Levenberg–Marquardt optimisation (Full-LM) and for the identifications based on the classical methodology, as experimentally (CM_E) and analytically (CM_A).

When comparing the results from the identified sets of parameters to the material ones, the following is observed: (i) for $\bar{\varepsilon}^p = 0$, the yield stress distribution with α (Fig. 17(a)) is best described by both classical identifications and for the primary solution of the inverse analysis, and is overestimated for both cases identifications, "LM" and "Full-LM"; moreover, for $\bar{\varepsilon}^p = 0.1$, the experimental results are best described by "PS", "LM", "Full-LM" and "CM_A" cases; (ii) the distribution of the tensile strain path with α (Fig. 17(b)) is better described by both classical identifications than by "PS", "LM" and "Full-LM"; (iii) the yield surfaces (see Fig. 17(c)) obtained from both classical identifications (with experimental and analytical analysis) and the primary solution of the inverse analysis identification seem to better describe the material initial yield surface than both identifications using Levenberg–Marquardt algorithm; for $\bar{\varepsilon}^p = 0.1$, the yield surfaces obtained from both inverse analysis identifications (primary solution, "PS", and after Levenberg–Marquardt optimisation, "LM") well fit the material yield surface (these results are in agreement with the results of the yield stress distribution in the sheet plane (Fig. 17(a))), and (iv) the equivalent stress–strain curve obtained from the inverse analysis identification for the primary solution has an overall good description of the material curve; in contrast, the cases "LM" and "Full-LM" overestimate the material curve only until 1% and 2.5% of deformation, respectively, and both classical identification strategies overestimate the entire material curve. In conclusion, cases "PS", "LM" and "Full-LM" allows closely describing the work-hardening behaviour (Fig. 17(a), (c) and (d)), at least for strain values larger than 1% (LM) and 2.5% (Full-LM), whereas the classical strategies mainly describe the distributions of the tensile strain path, in the sheet plane (Fig. 17(b)).

5. Deep-drawing of a cross-shaped cup

The deep drawing of a cross-shaped cup (see Fig. 18(a)) is used to support the proposed inverse analysis strategy, since this process exhibit high plastic strain values and deformation heterogeneity, with a wide range of strain paths, as shown in Fig. 18(b). In this section, the numerical simulations performed use the parameters: (i) of the material, (ii) obtained by the proposed inverse analysis strategy, with and without the final optimisation, (iii) obtained by a full Levenberg–Marquardt optimisation and (iv) obtained by a classical identification strategy with both sets of like experimental and analytical data. The deep drawing process was simulated taking into account the tool geometry, which includes a closed die and a total punch displacement of 60 mm. Due to geometric and material symmetries, only one quarter of the cup geometry was considered. The blank, with initial dimensions $125 \times 125 \times 1$ mm^3, was discretised with tri-linear 8-node hexahedral solid elements with an average in-plane size of 2.0 mm and two layers through-thickness. The blank holder applies a total force of 290 kN and the frictional contact between the sheet and the tools is modelled by Coulomb law, with a friction coefficient equal to 0.03 [41].

Fig. 18(a) displays the deformed shape of the simulated part after the deep-drawing test for the material (Mat) on the initial plane of the sheet, 0xy; Fig. 18(b) shows the complex strain path distribution along the 0x ($\alpha = 0°$), 0x = 0y ($\alpha = 45°$) and 0y ($\alpha = 90°$) axes for the material case.

Fig. 19(a) allows comparing the results of the draw-in (s) of the flange as a function of α (as shown in Fig. 18(a)) for the material with the ones obtained by inverse analysis, corresponding to the primary solution (PS) and after applying Levenberg–Marquardt optimisation (LM), by the full Levenberg–Marquardt optimisation

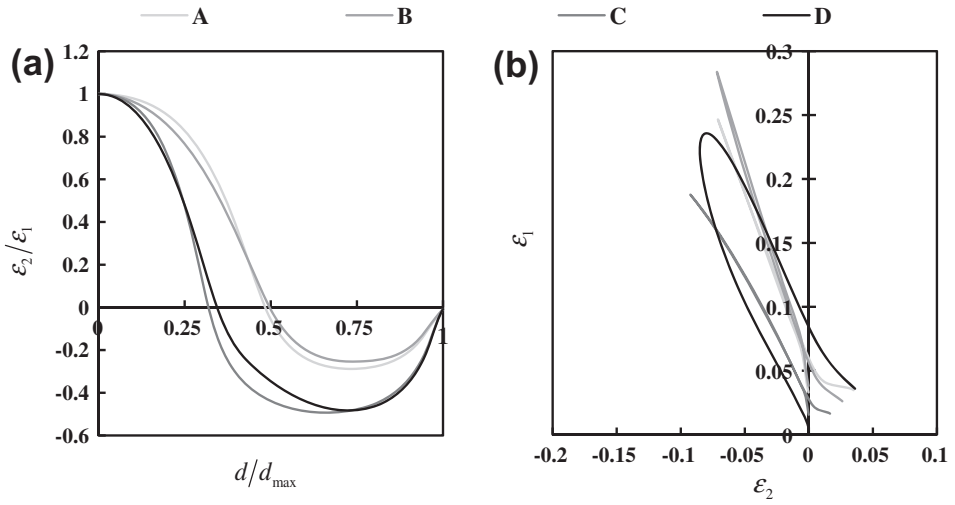

Fig. A1. Influence of the geometric parameters on the results of the cruciform test along the axes of the specimen: (a) $\varepsilon_2/\varepsilon_1$ vs. d/d_{max} and (b) ε_1 vs. ε_2, for the geometries indicated in Table A1: for case A to case B, the fillet radius, R, increases; from B to C, the L_1/L_2 value increases; and from C to D, the opening angle of the arms, β, increases.

(Full-LM) and by the classical identification methodology, with like experimental and analytical procedures (CM_E and CM_A, respectively), for the punch displacement of 60 mm. Also, Fig. 19(b) compares the results of the load evolution as a function of the punch displacement and Fig. 19(c–e) compares the plots $\bar{\varepsilon}_{vM}$ vs. d, along the 0x, 0x = 0y and 0y axes, respectively. The relative difference results of the load (δ_P) and flange draw-in ($\delta_s = (s - s_{ref})/s_{ref}$) were determined for all identification procedures, relatively to the material under study. Table 11 shows the δ_P^M and $|\delta_{\bar{\varepsilon}_{vM}}|^M$ results and the average absolute relative difference of the sliding, $|\delta_s|^M = (1/m)\sum_{i=1}^{m}|\delta_s|_i$, between the experimental results and the ones obtained using identification methodologies. The total number of points in study for the cross tool results are $p = 150$, for δ_P^M, $q = 63$ for $|\delta_{\bar{\varepsilon}_{vM}}|^M$ and $m = 180$, for $|\delta_s|^M$.

For the cross-shaped cup test results, the main conclusions are (see the summary of the results in Table 11 and Fig. 19): (i) globally, the draw-in of the flange, quantified by $|\delta_s|^M$ variable, is better described by the inverse analysis methodology, whatever the case "PS" or "LM"; (ii) both inverse analysis identification strategies, i.e. the primary solution (PS) and after Levenberg–Marquardt optimisation (LM) describe more conveniently the load evolution results than the classical identification strategies and the full Levenberg–Marquardt optimisation (Full-LM); the worst results concern the like experimental procedure (CM_E) and the full Levenberg–Marquardt optimisation (Full-LM); (iii) the equivalent strain distributions show similar or better performance for both inverse methodologies than for both classical identification procedures, except for the case of $|\delta_{\bar{\varepsilon}_{vM}}|^M$ (0x), for the "PS" case, and for the $|\delta_{\bar{\varepsilon}_{vM}}|^M$ (0x = 0y) and $|\delta_{\bar{\varepsilon}_{vM}}|^M$ (0y) values, in the "Full-LM" case; (iv) concerning the comparison between the two inverse analyses procedures, the relative difference results $|\delta_P|^M$ and $|\delta_s|^M$ show better performance after Levenberg–Marquardt optimisation; this better performance is not noticeable with regard to the results of the cruciform test (see Table 9), which means that identifications with different results, though with similar accuracy, can lead to a different degree of accuracy when applied to a specific test (see e.g. Debruyne et al. [20]).

6. Conclusions

This work allowed developing an inverse analysis strategy for simultaneously determining the constitutive parameters of Hill'48 yield criterion and Swift isotropic work-hardening law, from a single test, the biaxial tensile test of a cruciform sample. The sample geometry has been designed in order to guarantee strain heterogeneity, exhibiting strain paths from uniaxial up to equibiaxial tension. The inverse strategy consists on determining a primary solution, based on an optimisation methodology that compares the experimental and numerical results, the latter obtained by making variations of the constitutive parameters from an initial solution, according to an algorithm previously built up from a irect analysis study. Optionally, a gradient-based algorithm, Levenberg–Marquardt method can be used, for enhancing the primary solution. The proposed identification approach leading to the primary solution was shown to be competitive with classical strategies. The classical strategies make use of a large number of linear strain-path tests and are time consuming and expensive, as well as require complex and sensitive analysis of the results. The proposed inverse analysis strategy only requires the measuring of the load evolutions during the biaxial tensile test of the cruciform specimen and the evaluations of the equivalent strain distribution along the axes of the specimen, at a given moment of the test. This simplicity coupled with the wide range of strain paths allowed by the design of experiments, and also the circumstance that is not mandatory the use of an optimisation algorithm, such as Levenberg–Marquardt, represent advantage over identification strategies previously proposed, related to the use of full-field measurement methods. Additional studies will focus on experimental identifications and on extending the presented methodology for identifying parameters of more complex plastic models, i.e. with high number of parameters to be identified.

Acknowledgements

This research work is sponsored by national funds from the Portuguese Foundation for Science and Technology (FCT) via the projects PTDC/EME–TME/113410/2009 and PEst-C/EME/UI0285/2013 and by FEDER funds through the program COMPETE – Programa Operacional Factores de Competitividade, under the project CENTRO -07-0224 -FEDER -002001 (MT4MOBI). One of the authors, P.A. Prates, was supported by a grant for scientific research from the Portuguese Foundation for Science and Technology. All supports are gratefully acknowledged.

Appendix A. Cruciform specimen geometry optimisation

The cruciform specimen geometry was studied based on the following geometric parameters [28]: (i) fillet radius, R, (ii) L_1/L_2 ratio and (iii) the opening angle of the arms, β (see Fig. 1).

The design of experiments was performed for an isotropic material and a wide set of geometries, which include the four geometries exemplified in Table A1. The aim was to select: (i) the value for the L_1/L_2 ratio in order to cover as much as possible strain paths that commonly occur in sheet metal forming processes, from uniaxial to biaxial tension (L_1 and L_2 define the dimension of the arms and the dimension of the square central region of the specimen, respectively); (ii) the value of R that maximises the strain value attained in the centre of the specimen, while minimising the stress concentration effect in the fillet region; and (iii) the value of β that guarantees a smooth gradient of the ratio between the maximum and minimum principal strains along the arms of the specimen, so that the relative representation of all strain paths between uniaxial and biaxial tension is balanced, whilst ensuring a relatively high strain value in the centre of the specimen. Fig. A1 shows the strain paths, at points placed along the axes of the sample, for the geometries indicated in Table A1: (i) in Fig. A1(a), the strain path is defined by the ratio $\varepsilon_2/\varepsilon_1$ as a function of the relative distance to the centre of the sample, $d/d_{\max}$, where $d_{\max}$ is the distance of A and B points to the centre of the sample (see Fig. 1); and (ii) in Fig. A1 (b) the strain path is represented by the ε_1 vs. ε_2 distributions. The chosen geometry, D (shown in Fig. 1) (i) covers a relatively wide range of strain paths (from biaxial tension to uniaxial tension), with (ii) a relatively high strain value in the centre of the specimen, and (iii) a relative smooth gradient of the maximum and minimum principal strains along the arms of the specimen.

References

[1] M.C. Oliveira, J.L. Alves, B.M. Chaparro, L.F. Menezes, Int. J. Plast 23 (2007) 516–543.
[2] B.M. Chaparro, S. Thuillier, L.F. Menezes, P.Y. Manach, J.V. Fernandes, Comput. Mater. Sci. 44 (2008) 339–346.
[3] P.A. Prates, J.V. Fernandes, M.C. Oliveira, N.A. Sakharova, L.F. Menezes, IOP Conf. Series: Mater. Sci. Eng. 10 (2010) 012142.
[4] H. Aguir, J.L. Alves, M.C. Oliveira, L.F. Menezes, H. BelHadjSalah, Key Eng. Mater. 504–506 (2012) 637–642.
[5] F. Bron, J. Besson, Int. J. Plast 20 (2004) 937–963.
[6] O. Cazacu, F. Barlat, Int. J. Plast. 20 (2004) 2027–2045.
[7] O. Cazacu, B. Plunkett, F. Barlat, Int. J. Plast 22 (2006) 1171–1194.
[8] B. Plunkett, O. Cazacu, F. Barlat, Int. J. Plast 24 (2008) 847–866.
[9] H. Aretz, F. Barlat, Int. J. Non-Linear Mech. 51 (2013) 97–111.
[10] F. Yoshida, H. Hamasaki, T. Uemori, Int. J. Plast 45 (2013) 119–139.
[11] C. Teodosiu, Z. Hu, Evolution of the intragranular microstructure at moderate and large strains: Modelling and computational significance, in: S.F. Shen, P.R.

Dawson (Eds.), Proceedings of the 5th International Conference on Numerical Methods in Industrial Forming Processes (NUMIFORM '95), New York, 1995, pp. 173–182.
[12] J.V. Fernandes, D.M. Rodrigues, L.F. Menezes, M.F. Vieira, Int. J. Plast 14 (1998) 537–550.
[13] C. Teodosiu, Z. Hu, Microstructure in the continuum modelling of plastic anisotropy, in: Proceedings of the 19th Riso International Symposium on Materials Science: Modelling of Structures and Mechanics from Microscale to Products, Roskilde, 1998, pp. 149–168.
[14] L.M. Geng, Y. Shen, R.H. Wagoner, Int. J. Mech. Sci. 44 (2002) 123–148.
[15] F. Yoshida, T. Uemori, Int. J. Plast 18 (2002) 661–686.
[16] J.L. Chaboche, Int. J. Plast 24 (2008) 1642–1693.
[17] I. Zidane, D. Guiness, L. Léotoing, E. Ragneau, Meas. Sci. Technol. 21 (2010) 1–11.
[18] T. Pottier, F. Toussaint, P. Vacher, Eur. J. Mech. A/Solid 30 (2011) 373–382.
[19] S. Cooreman, D. Lecompte, H. Sol, J. Vantomme, D. Debruyne, Exp. Mech. 48 (2008) 421–433.
[20] D. Debruyne, S. Cooreman, P. Lava, S. Coppieters, Identification of the plastic material behaviour through inverse modelling and DIC: influence of the specimen's geometry, in: Proceedings of the SEM Annual Conference, Albuquerque, New Mexico, USA, 2009.
[21] S. Avril, F. Pierron, Y. Pannier, R. Rotinat, Exp. Mech. 48 (2008) 403–419.
[22] M. Teaca, I. Charpentier, M. Martiny, G. Ferron, Int. J. Mech. Sci. 52 (2010) 572–580.
[23] A. Güner, Q. Yin, C. Soyarslan, A. Brosius, A. Tekkaya, Int. J. Mater. Form. 4 (2011) 121–128.
[24] M. Rossi, F. Pierron, Comput. Mech. 49 (2012) 53–71.
[25] S. Zhang, L. Leotoing, D. Guines, S. Thuillier, Key Eng. Mater. 554–557 (2013) 2111–2117.
[26] E. Mönch, D. Galster, Br. J. Appl. Phys. 14 (1963) 810–812.
[27] A. Hannon, P. Tiernan, J. Mater. Process. Technol. 198 (2008) 1–13.
[28] P.A. Prates, Metodologia de análise inversa para determinação simultânea dos parâmetros de leis constitutivas, com recurso a um provete cruciforme, MSc Dissertation, University of Coimbra, 2010.
[29] M.C. Oliveira, J.L. Alves, L.F. Menezes, Arch. Comput. Method Eng. 15 (2008) 113–162.
[30] R. Hill, Proc. Roy. Soc. London 193 (1948) 281–297.
[31] H.W. Swift, J. Mech. Phys. Solids 1 (1952) 1–18.
[32] T.C. Chu, W.F. Ranson, M.A. Sutton, W.H. Peters, Exp. Mech. 25 (1985) 232–244.
[33] S. Dinda, K.F. Jarnes, S.P. Keeler, P.A. Stine, How to Use Circle Grid Analysis for Die Tryout, ASM International, USA, 1981.
[34] E. Voce, J. Inst. Metals 74 (1948) 537–562.
[35] D.W. Marquardt, J. Soc. Ind. Appl. Math. 11 (1963) 431–441.
[36] J. Fan, Y. Yuan, Computing 74 (2005) 23–39.
[37] O. Cazacu, F. Barlat, Math. Mech. Solids 6 (2001) 613–630.
[38] S. Bouvier, C. Teodosiu, C. Maier, M. Banu, V. Tabacaru, IMS 1999 (2001) 000051.
[39] L.C. Reis, C.A. Rodrigues, M.C. Oliveira, N.A. Sakharova, J.V. Fernandes, Characterization of the plastic behaviour of sheet metal using the hydraulic bulge test, in: A. Andrade-Campos, N. Lopes, R.A.F. Valente, H. Varum (Eds.), First ECCOMAS Young Investigators Conference on Computational Methods in Applied Sciences, Aveiro, 2012, pp. 67.
[40] J.L. Alves, M.C. Oliveira, L.F. Menezes, Mater. Sci. Forum 455–456 (2004) 732–737.
[41] T.C. Resende, T. Balan, F. AbedMeraim, S. Bouvier, S.S. Sablin, Application of a dislocation based model for Interstitial Free (IF) steels to typical stamping simulations, in: NUMIFORM 2010: Proceedings of the 10th International Conference on Numerical Methods in Industrial Forming Processes Dedicated to Professor O.C. Zienkiewicz (1921–2009), Pohang, 2010, pp. 1339–1346.

(Page intentionally left blank)

4.4. Sequential inverse identification of constitutive parameters in metal sheets under a single biaxial tensile test

This subchapter contains the paper "Sequential inverse identification of constitutive parameters in metal sheets under a single biaxial tensile test", submitted for publication. This work proposes a sequential inverse analysis methodology for the simultaneous identification of a number of constitutive laws, based on the successive optimisation of three cost functions, each one focusing on a specific type of results extracted from a single biaxial tensile test of a cruciform sample.

(Page intentionally left blank)

Sequential inverse identification of constitutive parameters in metal sheets under a single biaxial tensile test

P.A. Prates*, M.C. Oliveira, J.V. Fernandes

CEMUC — Department of Mechanical Engineering, University of Coimbra, Rua Luís Reis Santos, Pinhal de Marrocos, 3030-788 Coimbra, Portugal

*Corresponding author: pedro.prates@dem.uc.pt

Abstract

An inverse analysis methodology for the simultaneous identification of the parameters of anisotropic yield criteria and isotropic work-hardening laws of metal sheets is proposed. This identification makes use of results of the cruciform biaxial test, i.e. the evolution of the force during the test, for the two axes of the sample, and the major and minor strain distributions along both axes, at a given moment during the test. Based on a study of the sensitivity of the constitutive parameters to the biaxial tensile test results, the inverse identification consists on a procedure that sequentially minimises the gap between experimental and numerical results. Each step of the sequence uses a distinct cost function according to the type of results to be minimised, using a gradient-based optimisation algorithm, the Levenberg-Marquardt method. The inverse methodology allows the identification of constitutive parameters of complex constitutive models. This sequential identification strategy is compared to a strategy based on a single cost function, involving all parameters and type of results, which has lower performance.

Highlights

- Inverse identification strategy based on a single cruciform tensile test.
- Simultaneous identification of yield criterion and work-hardening law parameters.
- Sequential parameter identification procedure, using distinct cost functions.
- Load evolution and principal strains at a single load step, for both axes are used.

Keywords

Constitutive parameter identification; Biaxial tensile test; Inverse analysis; Optimisation algorithm; Finite element method.

1. Introduction

The accurate modelling of the plastic behaviour of metal sheets is a fundamental aspect to be considered in numerical simulation of sheet metal forming processes. The non-linear nature of the plastic behaviour of metal sheets makes their characterisation quite complex, depending on factors such as: (i) the constitutive model used to describe the material hardening and anisotropic behaviour; (ii) the experimental tests, comprising the sample geometries and testing conditions and (iii) the strategy for identification of the constitutive parameters. Until now, there is no standard approach for performing the constitutive parameters identification, although several models for describing the yielding [1–9] and hardening [10–16] behaviours, and identification strategies [17–26] have been suggested. The use of deep-drawn components with increasingly elaborate geometries, together with the emergence of new metals and alloys in the sheet metal forming industry, has stimulated the development of sophisticated

constitutive models, whose increased flexibility for describing the material plastic behaviour is associated with a larger number of parameters to identify. In contrast, relatively little emphasis has been given to the development of new strategies for constitutive parameters identification, and the classical strategies are predominantly used. In this context, the parameters identification is usually performed using sets of simple mechanical tests that promote linear strain paths and homogeneous deformation in the measuring region, like uniaxial tension, plane strain, shear and biaxial tests. As sheet metal forming processes are carried out under multi-axial strain paths and heterogeneous deformation, the use of these conventional tests is certainly not the most appropriate option to characterise the material plastic behaviour. Therefore, efficient inverse identification procedures are being developed as an alternative to the classical identification strategies. These procedures make use of one mechanical test unlike the classical strategies, for which the number of tests increases with the number of parameters to be identified. In general, this issue does not arise in inverse identifications, provided that the experimental results are sensitive to the parameters to be identified.

The use of optical full-field measurement techniques for analysing heterogeneous strain fields, such as digital image correlation (DIC), has motivated the development of inverse methods for identification of constitutive parameters. These methods are based on the minimisation of the gap between the numerical and experimental results of one mechanical test. A comprehensive overview on this topic can be found in [27]. Approaches for the inverse parameters identification have been conducted using the biaxial tensile testing of cruciform specimens (see e.g. [28–32]). For example, in a recent work by Zhang et al. [32], the parameters identification of Hill'48 [1] and Bron and Besson [5] yield criteria was performed for AA5086 aluminium sheet, using two methods: (i) a classical one, using conventional homogeneous tests, and (ii) an inverse analysis, from only one biaxial tensile test of a cruciform sample. The inverse analysis methodology consists of minimising the gap between the experimental and numerical distributions of the major and minor strains along the diagonal direction of the sample central area, at an instant immediately before rupture, using a SIMPLEX optimisation algorithm. The authors conclude that both methods provide similar yield contours, and so a single biaxial tensile test is adequate to obtain all the material parameters of the yield criterion for the AA5086 sheet. This and other cases have shown the capability to identify parameters of the constitutive laws from tests inducing heterogeneous deformation in the samples, as the biaxial cruciform test adopted in the current work.

It turns out, however, that the evaluation of the performance of inverse methodologies is a sensitive issue. Generally, this assessment is performed using the following procedures. One of them consists on the comparison between experimental and identified results from simple classical tests (e.g. [31]; [33–34]), which are not representative of the whole plastic behaviour, even if in a large number. Also, the direct comparison between the assessed results with those obtained with other identification strategies is used (e.g. [29]; [32]; [35–36]). This allows comparing strategies, but does not assess the efficiency of the strategy to represent the mechanical behaviour of the material. In general, none constitutive model and identification strategy allows to perfectly describe the behaviour of a material. Finally, the use of deep-drawing tests for assessing the performance of the identification (e.g. [21], [24]; [35]; [37–38]) is sensitive not only to the constitutive parameters but also to process parameters.

The authors of the current work have previously developed an inverse analysis methodology for the simultaneous identification of the parameters of Hill'48 yield criterion and Swift work-hardening law [11], from results of a single biaxial tensile test on a cruciform specimen [30]. The inverse identification procedure consists on determining a solution for the constitutive parameters, according to an algorithm built from a forward analysis study. The algorithm comprises a sequence of six steps, each one referring to the optimisation of distinct parameters. The proposed identification strategy only requires the measurement of the load evolutions during the biaxial tensile test of the cruciform specimen and the evaluations of the major and the minor principal strains along the axes of the specimen, at a given moment of the test. This simplicity, coupled with the wide range of strain paths occurring in the cruciform specimen during the biaxial test, is an advantage over identification strategies previously proposed, related to the use of full-field measurement methods (e.g. [29]). This methodology also proved to be an alternative to classical identification using conventional tests with homogeneous deformation, which is time-consuming, hard to analyse and liable to uncertainties. Following this work, it is now established an inverse methodology that allows parameters identification of complex constitutive models describing the

plastic behaviour of metal sheets, from a single biaxial tensile test of a cruciform specimen. The simultaneous identification of the constitutive parameters (yield criteria and isotropic work-hardening law) is performed with resource to an optimisation procedure using a gradient-based optimisation algorithm, the Levenberg-Marquardt method [39], and distinct cost functions in a pre-specified sequence, depending on the type of result that is minimised.

In order to develop the proposed strategy, computer generated results are used. This allows the proper design of the identification strategy, enabling the direct comparison of the identified constitutive model with that used as input (see e.g. [40]). In contrast, the use of experimental results leads to difficulties in assessing the extent to which the material behaviour is described by the identified constitutive model.

2. Numerical model

The geometry selected for the cruciform specimen was previously designed and optimised, in order to ensure the occurrence of strain paths that are commonly observed in sheet metal forming processes, i.e. strain paths ranging from uniaxial tension (in the arms region of the specimen) to biaxial tension (in the central region of the specimen) [30]. Fig. 1 shows the geometry and the dimensions of the cruciform specimen in the sheet plane. The 0x and the 0y axes coincide with the rolling direction (RD) and the transverse direction (TD) of the sheet, respectively. The cruciform specimen is submitted to equal displacements in both 0x and 0y directions. The displacements along the 0x and 0y axes are measured at points A and B, respectively. The sheet thickness is equal to 1.0 mm.

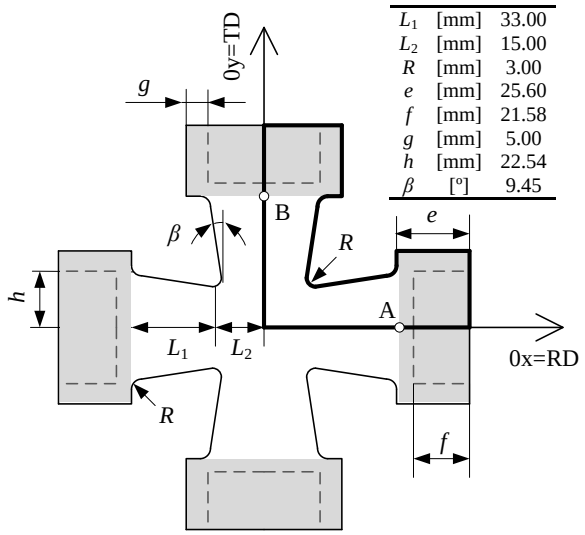

L_1	[mm]	33.00
L_2	[mm]	15.00
R	[mm]	3.00
e	[mm]	25.60
f	[mm]	21.58
g	[mm]	5.00
h	[mm]	22.54
β	[º]	9.45

Fig. 1. Geometry and dimensions of the cruciform specimen. The grips, represented in grey, hold the specimen by grabbing it along the dashed lines. A and B represent the points for measuring the displacements, Δl [30].

Due to geometrical and material (orthotropic) symmetries, the numerical simulation model only considers one eight of the specimen. The specimen is discretised with tri-linear 8-node hexahedral solid elements associated to a selective reduced integration, with an average in-plane size of 0.5 mm and one layer through-thickness. Numerical simulations were carried out with DD3IMP in-house finite element code, developed and optimised to simulate sheet metal forming processes [41].

3. Constitutive Model

A constitutive model establishes a relationship between the stress and plastic strain states of the deformable body. In case of metal sheets, the full constitutive model is typically defined by: (i) an anisotropic yield function; (ii) a hardening law and (iii) an associated flow rule. The yield function and hardening law allow describing the initial yield surface of the material and its subsequent evolution during plastic deformation. The associated flow rule states that the increment of plastic strain remains normal to the yield surface, for any arbitrary stress increment driven towards the outside of the yield surface.

In this paper, material parameters identification is performed for the following anisotropic yield functions: (i) Hill'48 [1]; (ii) Barlat'91 - below denoted as Yld'91 [2]; (iii) Karafillis & Boyce - below denoted as KB'93 [3] and (iv) Drucker+L [4]. The last three yield functions contain a number of parameters greater than the Hill'48 criterion, namely the so-called isotropic parameters that provide flexibility to the shape of the yield surface of anisotropic materials. Moreover, these criteria can be converted to Hill'48 criterion for predefined values of its parameters.

Hill'48 yield criterion describes the yield surface for orthotropic materials as follows:

$$F(\sigma_{yy}-\sigma_{zz})^2+G(\sigma_{zz}-\sigma_{xx})^2+H(\sigma_{xx}-\sigma_{yy})^2+2L\tau_{yz}^2+2M\tau_{xz}^2+2N\tau_{xy}^2=Y^2 \tag{1}$$

where σ_{xx}, σ_{yy}, σ_{zz}, τ_{xy}, τ_{xz} and τ_{yz} are the components of the effective Cauchy stress tensor (**σ**) in the orthotropic axes system of the metal sheet; *F*, *G*, *H*, *L*, *M* and *N* are the anisotropy parameters to be identified and *Y* is the yield stress, which evolution during deformation is defined by the work-hardening law.

The criteria Yld'91, KB'93 and Drucker+L are described through a stress tensor, **s**, obtained by a linear transformation of the effective Cauchy stress tensor, **σ**:

$$\mathbf{s} = \mathbf{L} : \boldsymbol{\sigma} \tag{2}$$

where **L** is the linear transformation operator proposed by Barlat et al. [2]:

$$\mathbf{L}=\begin{bmatrix} (C_2+C_3)/3 & -C_3/3 & -C_2/3 & 0 & 0 & 0 \\ -C_3/3 & (C_3+C_1)/3 & -C_1/3 & 0 & 0 & 0 \\ -C_2/3 & -C_1/3 & (C_1+C_2)/3 & 0 & 0 & 0 \\ 0 & 0 & 0 & C_4 & 0 & 0 \\ 0 & 0 & 0 & 0 & C_5 & 0 \\ 0 & 0 & 0 & 0 & 0 & C_6 \end{bmatrix} \tag{3}$$

in which C_i represents the anisotropy parameters, with i = 1,…,6; C_i is equal to 1 for the isotropy condition.

The Yld'91 yield criterion is an extension to anisotropy of the isotropic yield criterion of Hosford [42]:

$$|s_1-s_2|^m+|s_2-s_3|^m+|s_3-s_1|^m=2Y^m \tag{4}$$

where s_1, s_2 and s_3 are the principal components of the stress tensor **s**; *m* is an isotropic parameter that can assume any positive and real value greater than 1. Hosford [42] proposes values of *m* depending on the crystallographic structure of the material: *m* is equal to 6 and 8, for metals with BCC (body centred cubic) and FCC (face centred cubic) structure, respectively. As a more general alternative, *m* can be optimised in the context of constitutive parameter identification, as in the current work.

Karafillis & Boyce yield criterion describes the anisotropy as follows:

$$(1-a)\Phi_1 + a\frac{3^{2k}}{2^{2k-1}+1}\Phi_2 = 2Y^{2k}, \tag{5}$$

where a is an isotropic weighting parameter, ranging between 0 and 1; $2k$ is an isotropic exponential parameter, with k integer and positive to ensure the convexity of the yield surface, and Φ_1 and Φ_2 are defined as:

$$\Phi_1 = (s_1 - s_2)^{2k} + (s_2 - s_3)^{2k} + (s_3 - s_1)^{2k}, \tag{6}$$

$$\Phi_2 = s_1^{2k} + s_2^{2k} + s_3^{2k}. \tag{7}$$

Any yield surface described by Eq. (5) lies between the lower bound of the Φ_1 function (a = 0) (the lower bound of this function occurs for k = +∞ - Tresca yield surface - and the upper bound for k = 1 - von Mises yield surface) and the upper bound of Φ_2 function (a = 1) (the lower bound of this function occurs for k = 1 - von Mises yield surface - and the upper bound for k = +∞ - outside von Mises yield surface). Karafillis & Boyce proposed to set k fixed and equal to a high enough value (k = 15), which enables approximately describing any surface between the lower bound and the upper bound of Eq. (5), varying only the value of the weighting factor a [3], as in this work.

Drucker+L is an extension of Drucker isotropic criterion [43] to anisotropy:

$$\left[1/2\,\mathrm{tr}(\mathbf{s}^2)\right]^3 - c\left[1/3\,\mathrm{tr}(\mathbf{s}^3)\right]^2 = 27\left(Y/3\right)^6 \tag{8}$$

where tr(**s**) is the trace of the stress tensor **s** and c is a weighting isotropic parameter, ranging between -27/8 and 9/4, to ensure the convexity of the yield surface.

It is worth highlighting that Hill'48 criterion is a special case of the yield functions described above, under the following conditions: (i) m = 2, for Yld'91 criterion; (ii) a = 0 and k = 1, for KB'93 criterion and (iii) c = 0, for Drucker+L criterion. In all these cases, the equations that relate the Hill'48 yield parameters with those of Yld'91, KB'93 and Drucker+L yield criteria are [44]:

$$\begin{cases} F = (2C_1^2 + C_1C_2 + C_1C_3 - C_2C_3)/6 \\ G = (2C_2^2 + C_1C_2 + C_2C_3 - C_1C_3)/6 \\ H = (2C_3^2 + C_1C_3 + C_2C_3 - C_1C_2)/6 \\ L = 3/2\,C_4^2; M = 3/2\,C_5^2; N = 3/2\,C_6^2 \end{cases} \tag{9}$$

The Swift [11] and Voce [10] laws are used for identifying the isotropic hardening. They are written, respectively:

$$Y = C(\varepsilon_0 + \bar{\varepsilon}^{\mathrm{p}})^n \tag{10}$$

$$Y = Y_0 + (Y_{\mathrm{Sat}} - Y_0)\left[1 - \exp(-C_{\mathrm{Y}}\bar{\varepsilon}^{\mathrm{p}})\right] \tag{11}$$

where $\bar{\varepsilon}^{\mathrm{p}}$ is the equivalent plastic strain and C, ε_0 and n are the material parameters of Swift law ($Y_0 = C\varepsilon_0^{\,n}$ is the initial yield stress) and Y_0, Y_{Sat} and C_{Y} are the material parameters of Voce law. For simplicity, it is assumed that the work-hardening law is represented by the uniaxial tensile curve along the rolling direction, which means that the parameters of the yield criteria must fulfil the following equations:

Hill'48:

$$G + H = 1 \tag{12}$$

Yld'91:

$$\frac{1}{2\times 3^m}\left(\left|2C_2 + C_3\right|^m + \left|C_3 - C_2\right|^m + \left|C_2 + 2C_3\right|^m\right) = 1 \tag{13}$$

KB’93:

$$\frac{1-a}{2\times 3^{2k}}\left[\left(2C_2+C_3\right)^{2k}+\left(C_3-C_2\right)^{2k}+\left(-C_2-2C_3\right)^{2k}\right]+ \\ \frac{a}{2\times\left(1+2^{2k-1}\right)}\left[\left(C_2+C_3\right)^{2k}+\left(-C_2\right)^{2k}+\left(-C_3\right)^{2k}\right]=1 \tag{14}$$

Drucker+L:

$$3\left[\frac{1}{8\times 9^3}\left[\left(C_2+C_3\right)^2+C_3^{\,2}+C_2^{\,2}\right]^3-\frac{c}{9^4}\left[\left(C_2+C_3\right)^3+\left(-C_3\right)^3+\left(-C_2\right)^3\right]^2\right]^{\frac{1}{3}}=1 \tag{15}$$

In this study, the anisotropic parameters associated to the out-of-plane shear stress are kept as in isotropy (i.e. $L = M = 1.5$, for Hill’48 yield criterion and $C_4 = C_5 = 1$, for Yld’91, KB’93 and Drucker+L yield criteria), since the results of the biaxial cruciform test are not sensitive to these parameters [30]. This approach is generally adopted in the constitutive parameters identification of metal sheets. Moreover, the elastic behaviour is considered isotropic and is described by the generalised Hooke's law.

4. Inverse parameter identification

A potential approach for solving the problem of constitutive parameters identification consists on performing successive numerical simulations of the physical experiment using the finite element method, for example, and obtaining the set of parameters by minimising the gap between the experimental and the numerical results. This is known as inverse identification strategy, where the gap to minimise is described by a cost function that depends on the variables to be analysed.

The inverse identification strategy developed in this work is based on a previous one, proposed by the authors, which allows identifying the parameters of Hill’48 yield criterion and Swift work-hardening law [30], using the results of a unique test, the cruciform biaxial tensile test. Now, the strategy is extended to a wider range of constitutive models. Hill’48 and three other criteria that can be converted to Hill’48 criterion for predefined values of its parameters were used, although the procedure can be naturally extended to any other criterion. The Swift and Voce work-hardening laws were used. The simultaneous identification of the constitutive parameters (yield surface and work-hardening laws) is performed with resource to a sequential optimisation procedure using a gradient-based optimisation algorithm, the Levenberg-Marquardt method. The results of the biaxial cruciform test required for implementing the proposed inverse identification strategy are:

(i) the evolutions of the load, P, with the specimen boundaries displacement, Δl, during the test, for the axes 0x and 0y; Δl is measured at A and B in Fig. 1.

(ii) the distributions of the equivalent strain, $\bar{\varepsilon}$, along the axes 0x and 0y of the sample (i.e. $\bar{\varepsilon}$ as a function of the distance, d, to the centre of the sample), for a given boundaries displacement, Δl, preceding and close to the value of the displacement at maximum load; the equivalent strain is determined using von Mises definition:

$$\bar{\varepsilon}=2\left[\left(\varepsilon_1^{\,2}+\varepsilon_2^{\,2}+\varepsilon_1\varepsilon_2\right)/3\right]^{1/2}. \tag{16}$$

where ε_1 and ε_2 are respectively the major and the minor principal strains, in the sheet plane. The principal strain axes are parallel to the axes of the specimen (in case of the 0x axis, ε_1 is equal to ε_{xx} and ε_2 is equal to ε_{yy}, and in case of the 0y axis, ε_1 is equal to ε_{yy} and ε_2 is equal to ε_{xx} - see Fig. 1).

(iii) the distributions of the strain path ratio, defined by $\rho=\varepsilon_2/\varepsilon_1$, along the axes 0x and 0y of the sample (i.e. ρ as a function of the distance, d, to the centre of the sample), for the boundaries displacement, Δl, as stated above in (ii).

The strain variables ε_1 and ε_2 can be experimentally determined using DIC technique or even the classical circle grid strain analysis. In order to correctly calculate the differences for a certain value of *d* and Δl, the numerical and reference variables were obtained for the same value of *d* and Δl. This is achieved by performing linear interpolations of the results.

A forward analysis previously performed by the authors [30] led to the following conclusions concerning the sensitivity of the cruciform test results to the variation of the constitutive parameters values:

(i) the load evolution during the test (*P* vs. Δl), for the 0x and 0y axes, is almost only influenced by the work-hardening law parameters (i.e. the initial yield stress, Y_0, and the parameters that define the work-hardening: *n*, in case of Swift law, and R_{Sat} (=Y_{Sat} - Y_0) and C_Y, in case of Voce law) and by an amount, *K*, that depends on the parameters of the yield criterion (e.g. for the case of Hill'48 criterion this amount, *K*, is equal to the value of $(F+H)^{1/2}$, when $G + H = 1$ (Eq.(12))). In fact, when altering this amount, the σ_0/σ_{90} ratio (where σ_0 and σ_{90} are the tensile yield stresses along the rolling and transverse direction, respectively) is changed, and consequently the relative level of the load evolutions between the 0x and 0y axes, is also altered. The following equations summarise how to estimate the value of *K* for all yield criteria studied in this work, assuming that Eqs. (12) to (15) are observed:

Hill'48:

$$K = (F+H)^{1/2} \ (=\sigma_0/\sigma_{90}) \tag{17}$$

Yld'91:

$$K = \left[\frac{1}{2\times 3^m}\left(\left|C_1 - C_3\right|^m + \left|2C_1 + C_3\right|^m + \left|2C_3 + C_1\right|^m\right)\right]^{\frac{1}{m}} \ (=\sigma_0/\sigma_{90}) \tag{18}$$

KB'93:

$$K = \left[\frac{1-a}{2\times 3^{2k}}\left[\left(-C_3 - C_1\right)^{2k} + \left(-C_3\right)^{2k} + \left(2C_3 + C_1\right)^{2k}\right] + \frac{a}{2\times\left(2^{2k-1}+1\right)}\left[\left(-C_3\right)^{2k} + \left(-C_1\right)^{2k} + \left(C_1 + C_3\right)^{2k}\right]\right]^{\frac{1}{2k}} \tag{19}$$

$(=\sigma_0/\sigma_{90})$

Drucker+L:

$$K = \frac{1}{3}\left[\frac{1}{8}\left[C_3^{\,2} + \left(C_1 + C_3\right)^2 + C_1^{\,2}\right]^3 - \frac{c}{9}\left[\left(-C_3\right)^3 + \left(C_1 + C_3\right)^3 + \left(-C_1\right)^3\right]^2\right]^{\frac{1}{3}} \ (=\sigma_0/\sigma_{90}) \tag{20}$$

(ii) the equivalent strain distribution ($\bar{\varepsilon}$ vs. *d*), evaluated nearly before the maximum load, is influenced by the anisotropy parameters and by the parameters that define the work-hardening (for example *n*, in case of Swift law);

(iii) the strain path ratio distribution (ρ vs. *d*), evaluated nearly before the maximum load, is almost not influenced by the parameters of the work-hardening law;

A complementary forward study is now performed in order to analyse the sensitivity of the cruciform test results to variations of the value of the isotropic parameter of each criterion, which defines the shape of the yield surface. The illustrative cases shown below concern the Swift work-hardening law (with Y_0 = 100 MPa; *C* = 288.54 MPa and *n* = 0.2) and the values of the parameters of the yield criteria are as in the isotropy condition. The von Mises yield criterion is used as reference. The behaviours under comparison are described by Yld'91 (with *m* = 6), KB'93 (with *a* = 0.90, for *k* = 15) and Drucker+L (*c* = 2) criteria; it should be noted that: (i) Yld'91 becomes von Mises for *m* = 2; (ii) KB'93 with *k* = 15 approaches von Mises criterion when *a* is close to 0.97; and (iii) Drucker+L becomes von Mises for *c* = 0. Fig. 2 (a) shows the yield surfaces of these materials on the plane (σ_{xx} - σ_{yy}) for $\bar{\varepsilon}^p$ = 0 (i.e. at the onset of plastic deformation). The results of the forward analysis are summarised in Fig. 2 (b) to (d), showing the effects of varying the isotropic parameters relatively to the von Mises yield criterion. These results concern: *P* vs. Δl (Fig. 2 (b)); $\bar{\varepsilon}$ vs. *d* (Fig. 2 (c)) and ρ vs. *d* (Fig. 2 (d)), which are equal for 0x and 0y

axes (isotropic materials). The results in Fig. 2 (c) and (d) are plotted for Δl = 3 mm, with d measured from the centre of the cruciform specimen up to a distance corresponding to the minimum value of ρ (see Fig. 2 (d); this minimum occurs for a d value near 38 mm after which ρ increases approaching zero - not shown in the figure). The choice of this range of d values to be used in the inverse analysis intends to avoid: (i) considering two points with the same strain path (the strain paths that occur for d values between about 20 and 38 mm are repeated between this latter d value and the end of the arms of the specimen) and (ii) measuring the variables $\bar{\varepsilon}$ and ρ close to the heads of the sample, where the comparison between experimental and numerical results can be influenced by the boundary conditions, if they are not properly reproduced numerically.

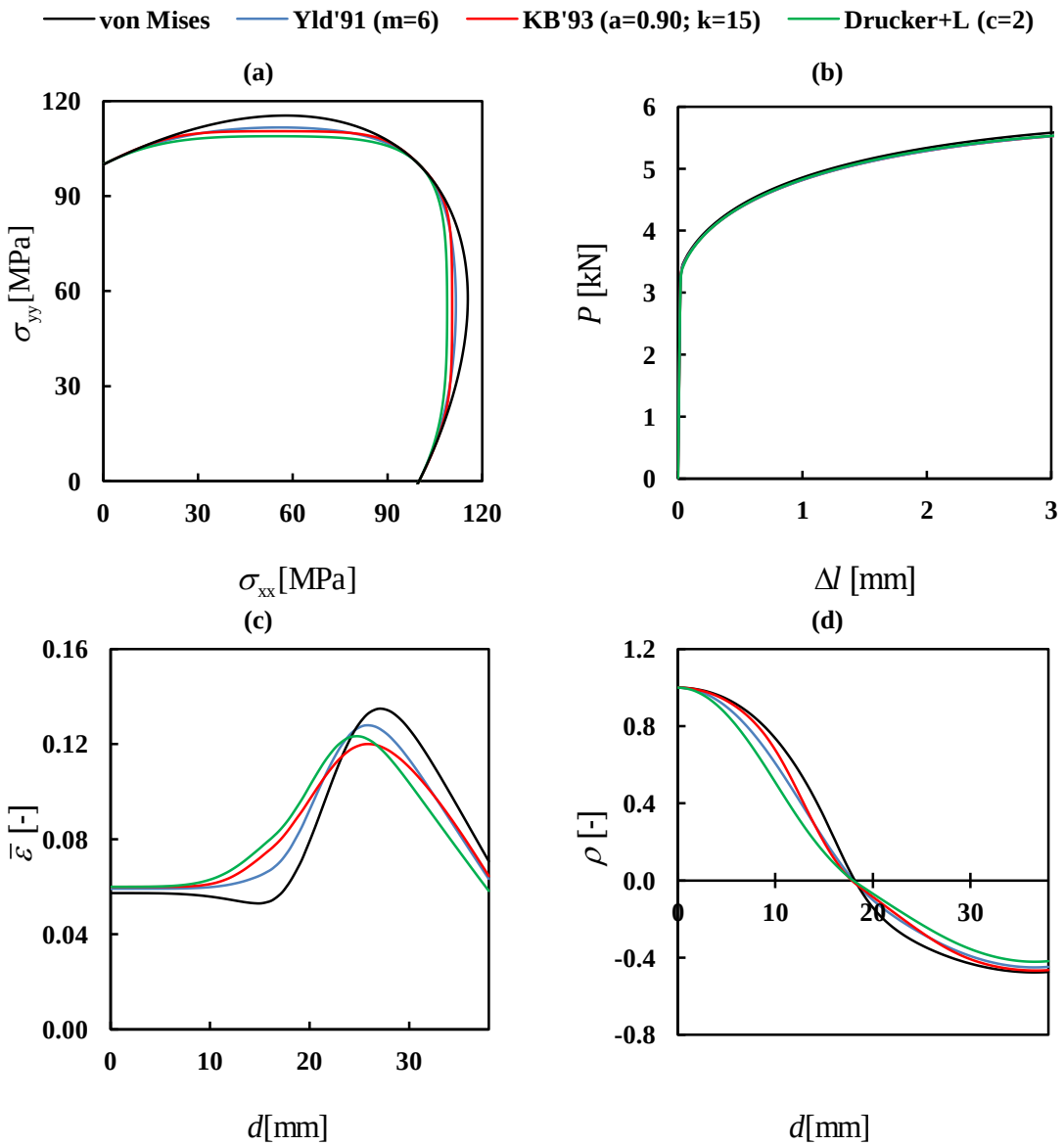

Fig. 2. Materials behaviour studied in the forward analysis: (a) yield surfaces in the plane (σ_{xx} - σ_{yy}), for $\bar{\varepsilon}^p$ = 0; numerical simulation results of the cruciform test concerning (b) P vs. Δl; (c) $\bar{\varepsilon}$ vs. d; (d) ρ vs. d. The results in figures (b) to (d) are equal for the 0x and 0y axes (isotropic materials).

The sensitivity of the cruciform test results to the variation of the values of the isotropic parameters in the studied range, can be summarised as follows: (i) the load evolution during the test (P vs. Δl), for the 0x and 0y axes, is almost not influenced by the isotropic parameters; in contrast, (ii) the equivalent strain

($\bar{\varepsilon}$ vs. d) and the strain path ratio (ρ vs. d) distributions are influenced by the isotropic parameters, showing noticeably complex changes.

The forward analysis conclusions allowed developing an inverse strategy for parameters identification, with the following assumptions: (i) the experimental results under the cruciform biaxial test, concerning the evolutions of P vs. Δl, $\bar{\varepsilon}$ vs. d and ρ vs. d are determined in advance and (ii) the elastic properties of the material are known.

The proposed inverse parameters identification strategy is detached in two stages. The first stage consists on the simultaneous identification of Hill'48 and work-hardening law parameters, using the results of P vs. Δl and $\bar{\varepsilon}$ vs. d. The work-hardening parameters must be separately identified for Swift and Voce laws and the law (Swift or Voce) that best describes the results of the cruciform test may be selected to proceed to the next stage of identification. The second stage allows extending the parameters identification procedure to more complex yield functions (Yld'91, KB'93 and Drucker+L, in the current work), whenever the identification carried out during the first stage proves to be insufficient to describe the experimental results of the cruciform test, namely the ρ vs. d results, not analysed in the first stage.

4.1. First stage of the identification strategy

The first stage of the inverse identification strategy consists on the identification of the Hill'48 parameters, concurrently with the Swift law parameters, by one side, and with the Voce law parameters, by other side. This stage is detached in three steps: firstly, an initial set of parameters is chosen (Step 1) and then the Levenberg-Marquardt optimisation algorithm is applied, in the next two steps (Steps 2 and 3). These steps sequentially minimise the gap between the following numerical and experimental results of the test: (i) P vs. Δl results, along the 0x and 0y axes, are minimised in Step 2 for identifying the parameters of the work-hardening law and the $(F+H)^{1/2}$ value; and (ii) $\bar{\varepsilon}$ vs. d results, along the 0x and 0y axes, are minimised in Step 3, for identifying the values of the Hill'48 criterion parameters. The choice of this sequence is derived from the forward analysis, which allowed concluding that the variables analysed in Step 2 (P vs. Δl results) remain quite stable during Step 3. Moreover, it should be noted that the simultaneous minimisation of both P vs. Δl and $\bar{\varepsilon}$ vs. d results in a unique step could lead to somewhat unbalanced identifications, resulting in a less adequate combination of the parameters of the yield criterion and hardening law, as it was concluded from a comprehensive study in a previous work [30].

Step 1: Initial estimate of the parameters of Hill'48 yield criterion and Swift and/or Voce work-hardening laws. The initial values of Hill'48 parameters can be set equal to the isotropic material, i.e. $F = G = H =$ 0.5 and $L = M = N = 1.5$, as in the current work; alternatively, the initial estimate of the parameters can be determined, for example, from the Lankford coefficients values at various directions in the sheet plane (r_0, r_{45} and r_{90}, for example), if available. For the first estimate of the parameters of the work-hardening laws, typical values of the material can be used, as in the current work; the parameters obtained by fitting a tensile curve for any strain path, such as tension along the rolling direction, can also be used. A comprehensive study showed that the accuracy of the final results is not influenced (i.e. the material behaviour is similarly accurately described) by the first estimate, although it can influence the number of iterations.

Step 2: Optimisation of the work-hardening parameters (Y_0, C and n, in case of Swift law, and Y_0, Y_{Sat} and C_Y, in case of Voce law) and of the value of $K=(F+H)^{1/2}$, by modifying F or H values, for example. The optimisation is carried out by minimising the gap between the numerical and experimental P vs. Δl results, along the 0x and 0y axes, through the following least-squares cost function:

$$F_1(\mathbf{A}) = \frac{1}{Q_1}\sum_{i=1}^{Q_1}{\delta_{P_i}}^2_{0x} + \frac{1}{Q_2}\sum_{i=1}^{Q_2}{\delta_{P_i}}^2_{0y} \tag{21}$$

where δ_p is defined as the relative difference between the numerical, $P^{\text{num}}(\mathbf{A})$, and the experimental reference load values, P^{exp}, during the test, $\delta_P = (P^{\text{num}}(\mathbf{A}) - P^{\text{exp}})/P^{\text{exp}}$, along the 0x and 0y axes; **A** is the set of parameters to be optimised, *i* is the measuring point of load (which corresponds to a certain Δl value) and Q_1 and Q_2 are the total number of load measuring points, in the 0x and 0y axes respectively. The total number of load measuring points should be equal for both axes. The condition $G + H = 1$ can be kept unchanged during this step, as in the current study.

Step 3: Optimisation of the values of *F*, *G*, *H* and *N* anisotropy parameters of the Hill'48 criterion. This is performed by minimising the gap between the numerical and experimental $\bar{\varepsilon}$ vs. *d* results along the 0x and 0y axes, through the following least-squares cost function:

$$F_2(\mathbf{B}) = \frac{1}{R_1}\sum_{i=1}^{R_1}{\delta_{\bar{\varepsilon}_i}}^2_{0x} + \frac{1}{R_2}\sum_{i=1}^{R_2}{\delta_{\bar{\varepsilon}_i}}^2_{0y} \tag{22}$$

Where $\delta_{\bar{\varepsilon}}$ is defined as the relative difference between the numerical, $\bar{\varepsilon}^{\text{num}}(\mathbf{B})$, and the experimental reference von Mises equivalent strain, $\bar{\varepsilon}^{\text{exp}}$, distributions, $\delta_{\bar{\varepsilon}} = (\bar{\varepsilon}^{\text{num}}(\mathbf{B}) - \bar{\varepsilon}^{\text{exp}})/\bar{\varepsilon}^{\text{exp}}$, along the 0x and 0y axes; **B** is the set of constitutive parameters to be optimised, *i* is the measuring point of the equivalent strain (which corresponds to a certain *d* value) and R_1 and R_2 are the total number of equivalent strain measuring points in the 0x and 0y axes, respectively. The total number of measuring points should be equal for both axes. This step keeps the work-hardening parameters and the $K = (F + H)^{1/2}$ value as identified in Step 2 and also, by choice, the condition $G + H = 1$ unchanged; therefore, only *N* and one of the parameters, *F*, *H*, and *G* are updated in **B**.

The optimisation procedure for both F_1 and F_2 stops when the relative difference between a given set of parameters and the next one is less than a user predefined tolerance, for each of the constitutive model parameters. It is inappropriate to predefine a tolerance for the minimum values of the cost functions, because it depends on how the selected constitutive model describes the behaviour of the material. Generally the parameters are properly identified after Step 3. However, in some cases, especially for severe anisotropy, it is advisable to repeat Steps 2 and 3, although one cycle is usually sufficient. The need to repeat steps 2 and 3 can be evaluated by computing the value of the cost function F_1 after Step 3 and comparing its value with that obtained at the end of Step 2. No updating is needed if the order of magnitude of F_1 remains unchanged.

4.2. Second stage of the identification strategy

The second stage of the inverse identification strategy consists on extending the parameter identification to other yield functions, starting from the solution of the parameters of Hill'48 criterion, as previous identified in the first stage. Yield functions, like Yld'91, KB'93 and Drucker+L criteria, contain more parameters than Hill'48 criterion, making them more flexible to describe the experimental reference results. Typically, such yield functions contain the so-called isotropic parameters, which affect the shape of the yield surface and therefore mainly influence the strain path ratio distribution, along the 0x and 0y axes. It is worth mentioning that, at the end of Step 3 of the first stage, the gap between numerical and experimental *P* vs. Δl and $\bar{\varepsilon}$ vs. *d* results, along the 0x and 0y axes, is minimised. But if the experimental ρ vs. *d* results, along these axes, are far from those numerically obtained, this indicates that the Hill'48 criterion does not conveniently describes the material behaviour. Therefore, at the end of Step 3, it is required to check if the strain path distributions along both axes are well predicted by the numerical simulation, to decide whether to stop or proceed with the optimisation procedure. In the first case, it is accepted that Hill'48 criterion properly describes the behaviour of the material; in the second case, this behaviour is not adequately described and the optimisation can proceed selecting other criteria that eventually describes it better.

Step 4: Evaluation of the requirement to expand the identification to other yield criteria. This evaluation can be performed using a function, characterising the gap between the numerical and experimental strain path distributions, along the 0x and 0y axes, defined as

$$F_3(\mathbf{B}) = \frac{1}{S_1}\sum_{i=1}^{S_1}\Delta\rho_i^{\,2}{}_{0x} + \frac{1}{S_2}\sum_{i=1}^{S_2}\Delta\rho_i^{\,2}{}_{0y} \tag{23}$$

where $\Delta\rho$ is defined as the difference between the numerical, $\rho^{\text{num}}(\mathbf{B})$, and the experimental reference strain path ratios, ρ^{exp}, i.e. $\Delta\rho = \rho^{\text{num}}(\mathbf{B}) - \rho^{\text{exp}}$, along the 0x and 0y axes; **B** is the set of constitutive parameters determined at the end of Step 3, i is the measuring point of the strain path ratio (which corresponds to a certain d value) and S_1 and S_2 are the total number of strain path ratio measuring points, in the 0x and 0y axes, respectively. The total number of measuring points should be equal for both axes.

It is up to the decision maker to choose the degree to which the correspondence between numerical and experimental results is acceptable. If proceeding to the second stage of the identification strategy, the parameters to continue optimisation must be obtained from the set of Hill'48 yield criterion parameters optimised during the first stage, which must be converted into the set of anisotropic parameters of one of the Yld'91, KB'93 or Drucker+L yield criteria, using Eqs. (9) and assuming that the isotropic parameters are as follows: m = 2 for Yld'91; a about 0.97 when fixing k = 15 for KB'93; and c = 0 for Drucker+L. The following step (Step 5) consists on optimising the isotropic parameter of the yield criterion, keeping the anisotropic parameters and the work-hardening law unchanged.

Step 5: Optimisation of the isotropic parameters of the yield criterion (m, a and c, for Yld'91, KB'93 and Drucker+L criteria, respectively). This consists on minimising the numerical and the experimental reference $\Delta\rho$ vs. d results along both 0x and 0y axes, through the least-squares cost function $F_3(\mathbf{C})$, defined as in Eq. (23), where **C** represents the isotropic parameter to be optimised. The total number of measuring points should also be equal for both axes. As for F_1 and F_2, the optimisation procedure stops when the relative difference between a given value of the parameter and the next one is less than the user predefined tolerance.

It is important to point out that the change of the isotropic parameter, occurring during this optimisation step, modifies the shape of the yield surface and also alters its size. In fact, when changing the isotropic parameter, keeping fixed the anisotropic ones, Eqs. (13), (14) and (15) are no longer observed, i.e. the size of yield surface will change. However, even changing the isotropic parameter, the size of the surface can be maintained, as much as possible, by acting on the anisotropic parameters. This should be done by multiplying all the anisotropic parameters by the same amount, such that the full set of parameters obeys to Eqs. (13), (14) and (15). This allows keeping the parameters of the work-hardening law unchanged during this step.

Step 6: Evaluation of the requirement for cycling. At the end of Step 5 it should be checked if the numerical results concerning the evolutions of the load during the test, for both axes, and the distributions of equivalent strain along these axes are not changed. This can be done computing the values of the cost functions F_1 and F_2, after Step 5 and comparing their values with those obtained at the end of Step 3. No updating is needed if the order of magnitude of both cost functions remains unchanged. Generally, the numerical results concerning the load evolution are not significantly changed, unless the isotropic parameter of the yield criterion is far from the value that takes for the Hill'48 criterion (i.e. m = 2, for Yld'91; a about 0.97, for the k value used (equal to 15), for KB'93, and c = 0, for Drucker+L). If significant changes are observed, then Step 2 (first stage) must be performed again (minimisation of F_1). Even without the need to minimise F_1, the numerical $\bar{\varepsilon}$ vs. d results are sensitive to the transition from Hill'48 to other criteria and, consequently, the cost function F_2 must be minimised again after Step 5. Thus, generally it is necessary to perform a step similar to Step 3 of the first stage, to optimise the values of C_1, C_2, C_3 and C_6, i.e. the anisotropy parameters of the criterion. As in Step 3 for the Hill'48 criterion,

where the value of $K = (F + H)^{1/2}$ is kept fixed, the equivalent condition on the parameters of the other yield criteria, defined by the K value (Eqs. (18), (19) and (20)), is also kept unchanged; also the condition defined by one of the equations (13), (14) and (15), depending on the criterion, can be kept unchanged. Therefore, only C_6 and one of the parameters C_1, C_2, and C_3 need to be updated. At this point, it is advisable to repeat Step 5 and again check the orders of magnitude of functions F_1 and F_2. Usually, it is sufficient to perform only one cycle.

4.3. Final remarks

Table 1 summarises the proposed inverse identification strategy, showing the type of results, numerical and experimental, which are compared at each step, as well as the cost functions evaluated at each step. The proposed strategy recommends that the optimisation begins with the Hill'48 criterion, using results concerning the loading curve (P vs. Δl) and the distribution $\bar{\varepsilon}$ vs. d, along the axes 0x and 0y. The optimisation of the loading curve allows realizing which law is most suitable for describing the work-hardening behaviour of the material, regardless of the criteria, and so to make the choice between Swift and Voce laws. The optimisation of the strain distribution allows understanding to what extent the material behaviour is described by the Hill'48 criterion. Furthermore, the comparison between the numerical and experimental distributions of the strain path ratios, ρ vs. d (not optimised until this moment) makes an important additional contribution in this analysis (the distribution $\bar{\varepsilon}$ vs. d, can be satisfactory, but the strain path ratios may not be adequately described by Hill'48). In cases where it is deemed appropriate extending the identification to other criteria, the isotropic parameter of the selected yield criterion must be optimised, using the distributions of the strain path ratios, ρ vs. d. The procedure can continue by repeating the steps of the first stage using the selected yield criterion, and restarting with the second or third step. The latter case occurs when the parameters of the work hardening law does not need to be optimised.

This procedure allows the parameter identification problem to be addressed using autonomous cost functions for each step, which are evaluated one after the other in a pre-specified sequence, as an alternative to perform the parameter identification by minimising a single cost function comprising all material parameters and results of different types, as commonly performed by other authors (e.g. [21, [23], 24, 29]). As it will be shown in the next chapter, the use of a single cost function can lead to a somewhat inadequate description of the plastic behaviour of the material, namely the work-hardening. The currently proposed strategy also has the advantage that, first of all, it allows perceiving to what extent the Hill'48 criterion describes the material behaviour, whose usage is always desirable because of its simplicity. If the Hill'48 criterion does not conveniently describes the material behaviour, the identification results for this criterion provide an initial solution which enables the extension of the inverse analysis to other criteria.

This inverse identification can be applied directly to any of the above-mentioned criteria or further criteria, without going through Hill'48 criterion. The proposal of starting the identification procedure with Hill'48 criterion has the advantage of providing a solution that can be used as initial estimate for parameter identification of more flexible yield criteria. In this context, it should be noted that it is not possible to know *a priori* which is the most convenient constitutive model to describe the experimental results.

Finally, it should be mentioned that, when the parameter identification is performed by minimising a unique weighted cost function comprising all material parameters and different types of experimental results, as classically used, the solution is influenced by the pre-selected weights for each portion of the function. In the methodology proposed herein, the question of the relative weight of each type of result is solved by establishing the sequence of steps for identifying the parameters of the constitutive model. This has the advantage of not requiring user defined weighting factors to consider the influence of each type of result in the identification.

Table 1. Inverse analysis algorithm for the sequential identification of constitutive parameters (yield criterion and isotropic work-hardening law).

0	Generate the reference results of the biaxial tensile test: P vs. Δl $\bar{\varepsilon}$ vs. d ρ vs. d
1	Initial estimate of the parameters of the Hill'48 criterion and the Swift and/or Voce work-hardening laws
2	Minimise $F_1(\mathbf{A}) = \frac{1}{Q_1}\sum_{i=1}^{Q_1}\delta_{P_i}{}^2{}_{0x} + \frac{1}{Q_2}\sum_{i=1}^{Q_2}\delta_{P_i}{}^2{}_{0y}$ Results compared: P vs. Δl Identification of: work-hardening law parameters and K value
3	Minimise $F_2(\mathbf{B}) = \frac{1}{R_1}\sum_{i=1}^{R_1}\delta_{\bar{\varepsilon}_i}{}^2{}_{0x} + \frac{1}{R_1}\sum_{i=1}^{R_1}\delta_{\bar{\varepsilon}_i}{}^2{}_{0y}$ Results compared: $\bar{\varepsilon}$ vs. d Identification of: anisotropic parameters of the yield criterion Note: Check requirement to return to Step 2, by comparing the order of magnitude of values of the function F_1 at the end of Step 3 with that at the end of Step 2
4	Proceed to other criteria? Evaluation taking into consideration, for example, the function $F_3(\mathbf{B}) = \frac{1}{S_1}\sum_{i=1}^{S_1}\Delta\rho_i^2{}_{0x} + \frac{1}{S_2}\sum_{i=1}^{S_2}\Delta\rho_i^2{}_{0y}$ No - End of the optimisation Yes - Obtain an initial solution to proceed with the optimisation for more complex yield criteria
5	Minimise $F_3(\mathbf{C}) = \frac{1}{S_1}\sum_{i=1}^{S_1}\Delta\rho_i^2{}_{0x} + \frac{1}{S_2}\sum_{i=1}^{S_2}\Delta\rho_i^2{}_{0y}$ Results compared: ρ vs. d Identification of: isotropic parameter(s) of the yield criterion
6	Cycling? Evaluation: Comparison of the order of magnitude of F_1 and F_2 at the end of Step 5 with those at the end of Step 3 No - End of the optimisation. Yes - Proceed to Step 2 or 3, depending on the results to be optimised

5. Inverse analysis: Case studies

To illustrate the above described inverse identification strategy, two case studies are considered in the next sections. In each case, computer generated results of the cruciform tensile test were used as "experimental" results. Computer generated results allows the suitable comparison between inverse analysis and "experimental" results, concerning the yield surface and the work-hardening functions. As mentioned in the Introduction, the use of real experimental cases leads to difficulties in assessing the extent to which the material behaviour is described by the identified constitutive model. In Case Study 1, the material plastic behaviour follows Drucker+L criterion and Swift work-hardening law, while in Case Study 2, the material follows CB2001 yield criterion [4] and a Voce work-hardening law.

The purpose of both case studies is to show how to identify the set of parameters of Hill'48 (first stage), Yld'91, KB'93 and Drucker+L (second stage) yield criteria, simultaneously with the work-hardening law parameters. The main objective of Case Study 1 is to illustrate in a simple way how to perform the proposed strategy and only the parameters of Swift law are identified. In Case Study 2, the set of parameters is identified for both work-hardening laws, Swift and Voce, in order to illustrate how to

decide which is the more suitable hardening law for describing the material behaviour. The minimisation procedure adopted for the cost functions F_1, F_2 and F_3 stops when the relative difference between a given set of parameters and the next one is less than 5%, for each of the constitutive model parameters.

5.1. Case Study 1

In this case study, the material anisotropic behaviour is described by Drucker+L criterion and the work-hardening behaviour is described by Swift law, which parameters are shown in Table 2 [30]. The elastic properties are: Young's modulus, E = 210 GPa and Poisson ratio, ν = 0.3. The number of measured points used to evaluate the cost functions F_1, F_2 and F_3, is equal to 100 ($Q_1 = Q_2 = R_1 = R_2 = S_1 = S_2 =$ 100).

Table 2. Constitutive parameters of the reference material of the Case Study 1, described by Drucker+L yield criterion and Swift work-hardening law.

Drucker+L criterion parameters						Swift law parameters		
C_1	C_2	C_3	$C_4 = C_5$	C_6	C	Y_0 [MPa]	C [MPa]	n
0.6681	0.8158	1.2394	1.0000	0.9440	1.4265	118.63	502.61	0.268

The identification is carried out for Hill'48 (first stage), Yld'91, KB'93 and Drucker+L (second stage) yield criteria simultaneously with Swift work-hardening law (Voce's law was not used). Table 3 shows Hill'48 yield criterion (as for isotropy) and Swift isotropic work-hardening parameters used as first estimate for the inverse identifications, as well as the ones resulting from the identified parameters of Hill'48 yield criterion and Swift isotropic work-hardening law, by the proposed inverse identification. The first stage of the identification procedure involved two returns to Step 2, after Step 3. Table 3 also shows the identified parameters of the Yld'91, KB'93 and Drucker+L criteria, together with the Swift law parameters (second stage). The second stage of the identification procedure involved two returns to Step 3, after Step 6, for Yld'91 and Drucker+L criteria, while for KB'93 criterion it involved only one return to Step 3.

Table 3. Cost functions and sequentially identified constitutive parameters (Final), at the end of the stages 1 (Hill'48 yield parameters) and 2 (Yld'91, KB'93 and Drucker+L yield parameters) of the Case Study 1 (Swift law). The initial estimate of the parameters and the correspondent cost functions (Step 1) are also shown.

	Cost functions			**Hill'48 yield parameters**						Swift law parameters		
	F_1	F_2	F_3	F	G	H	$L=M$	N		Y_0 [MPa]	C [MPa]	n
Step 1	7.9×10^{-2}	9.2×10^{0}	2.6×10^{-1}	0.5000	0.5000	0.5000	1.5	1.5000		100.00	490.13	0.300
Final	1.3×10^{-6}	8.6×10^{-3}	3.2×10^{-2}	0.1965	0.3196	0.6804	1.5	1.5026		119.53	507.52	0.268
	Cost functions			**Yld'91 yield parameters**						Swift law parameters		
	F_1	F_2	F_3	C_1	C_2	C_3	$C_4=C_5$	C_6	m	Y_0 [MPa]	C [MPa]	n
Final	6.5×10^{-7}	2.5×10^{-4}	9.4×10^{-4}	0.6454	0.7853	1.1920	1	0.9160	6	118.74	503.76	0.268
	Cost functions			**KB'93 yield parameters (with k = 15)**						Swift law parameters		
	F_1	F_2	F_3	C_1	C_2	C_3	$C_4=C_5$	C_6	a	Y_0 [MPa]	C [MPa]	n
Final	7.5×10^{-5}	2.8×10^{-3}	1.4×10^{-3}	0.6318	0.7732	1.1997	1	0.9144	0.836	119.01	504.76	0.268
	Cost functions			**Drucker+L yield parameters**						Swift law parameters		
	F_1	F_2	F_3	C_1	C_2	C_3	$C_4=C_5$	C_6	c	Y_0 [MPa]	C [MPa]	n
Final	1.2×10^{-7}	2.2×10^{-6}	3.3×10^{-8}	0.6680	0.8155	1.2390	1	0.9442	1.4297	118.53	502.63	0.268

Fig. 3 compares the reference material results (Mat) of the cruciform test with those obtained in the first stage of the sequential strategy (Hill'48 yield criterion and Swift isotropic work-hardening law - Final), for the 0x and 0y axes. The results concerning the initial estimate (Isotropic) are also shown in Fig.

3 (a), (c) and (e). The results concern P vs. Δl and δ_p vs. Δl (Fig. 3 (a) and (b), respectively); $\bar{\varepsilon}$ vs. d and $\delta_{\bar{\varepsilon}}$ vs. d (Fig. 3 (c) and (d), respectively) and ρ vs. d and $\Delta\rho$ vs. d (Fig. 3 (e) and (f), respectively). The results in Fig. 3 (c to f) are plotted for $\Delta l \approx 6$mm, i.e. the Δl value immediately preceding the maximum load. These results concern the distance, d, from the centre of the cruciform specimen up to a distance corresponding to the minimum value of ρ (see Fig. 3 (e), where the minimum occurs for a d value slightly less than 40 mm; after this d value, ρ increases approaching zero - not shown in the figure). It can be concluded that the proposed inverse identification strategy leads to an accurate description of the load evolution during the test for both axes (absolute relative differences less than 0.12%), although this is not the case for the equivalent strain distribution (absolute maximum relative differences of about 15%) and the strain path ratio distribution results (absolute maximum relative differences of about 30%). In fact, the values of F_1, F_2 and F_3 are 1.3×10^{-6}, 8.6×10^{-3} and 3.2×10^{-2}, respectively (see Table 3).

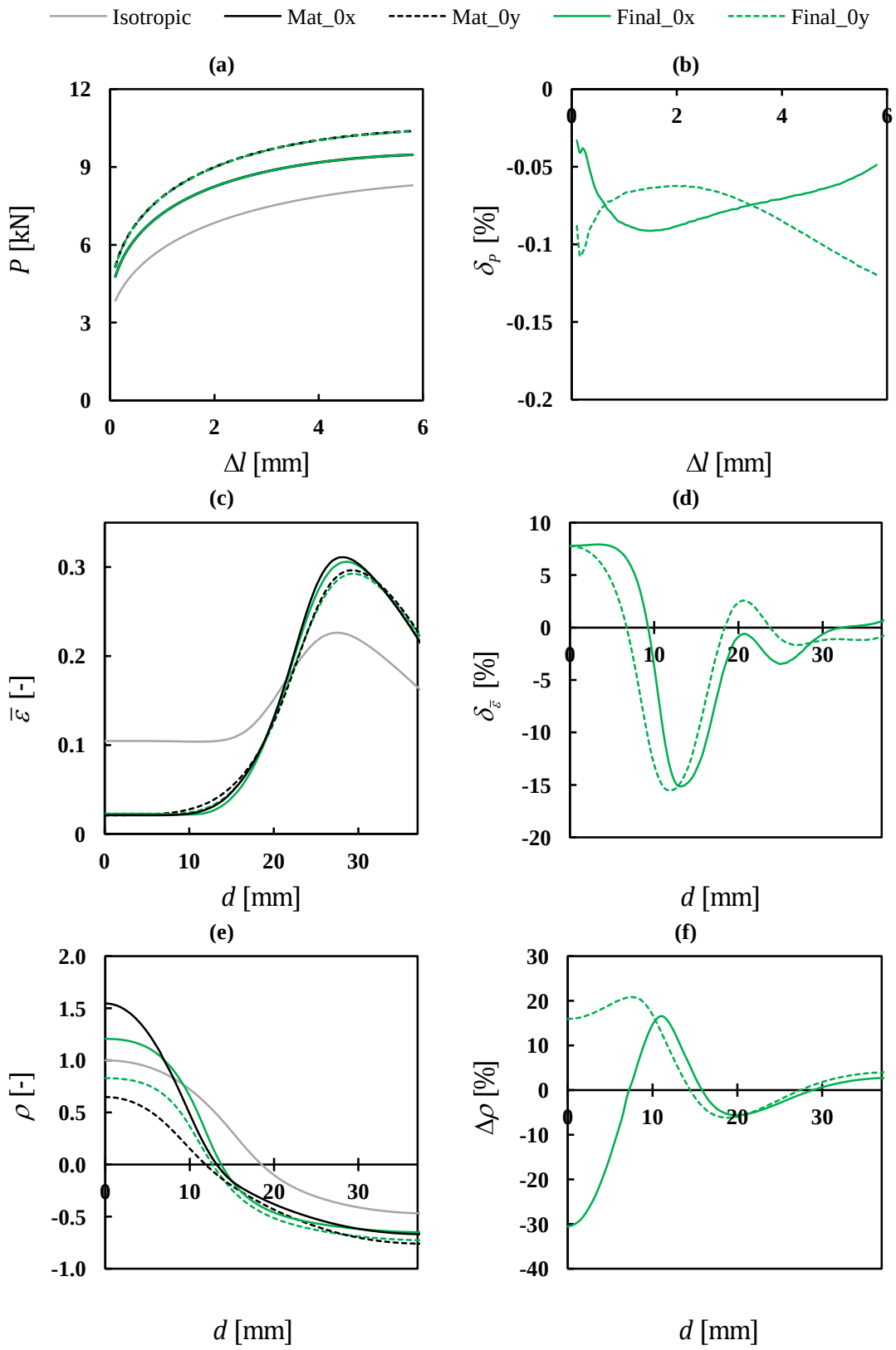

Fig. 3. Comparison between the results of reference material (Mat) and those obtained from the sequential identification of the constitutive parameters of the Swift law and Hill'48 criterion (end of stage 1 - Final), for the Case Study 1: (a) P vs. Δl; (b) δ_P vs. Δl; (c) $\bar{\varepsilon}$ vs. d; (d) $\delta_{\bar{\varepsilon}}$ vs. d; (e) ρ vs. d and (f) $\Delta\rho$ vs. d. In figures 3 (a), (c) and (e), the results labelled "Isotropic" concern the first estimate.

Fig. 4 shows the results corresponding to δ_p vs. Δl (Fig. 4 (a) and (b), for the 0x and 0y axes, respectively), $\delta_{\bar{\varepsilon}}$ vs. d (Fig. 4 (c) and (d), for the 0x and 0y axes, respectively) and $\Delta\rho$ vs. d (Fig. 4 (e) and (f), for the 0x and 0y axes, respectively), allowing the comparison between all criteria studied. These results show that, when compared with the Hill'48 criterion, the accuracy of the load evolution during the test decreases for both axes, in the case of the KB'93 yield criterion, but increases for the Yld'91 and Drucker+L criteria. The accuracy of the equivalent strain and strain path ratio distribution results are substantially increased for the Yld'91 and Drucker+L yield criteria. For the Drucker+L criterion, the comparison of the identified constitutive parameters (Swift law and criterion) with the material parameters (Table 2) shows quasi-absolute coincidence of results, since the Drucker+L criterion allows a fully description of the material behaviour. The above findings are supported by the values of the cost functions shown in Table 3.

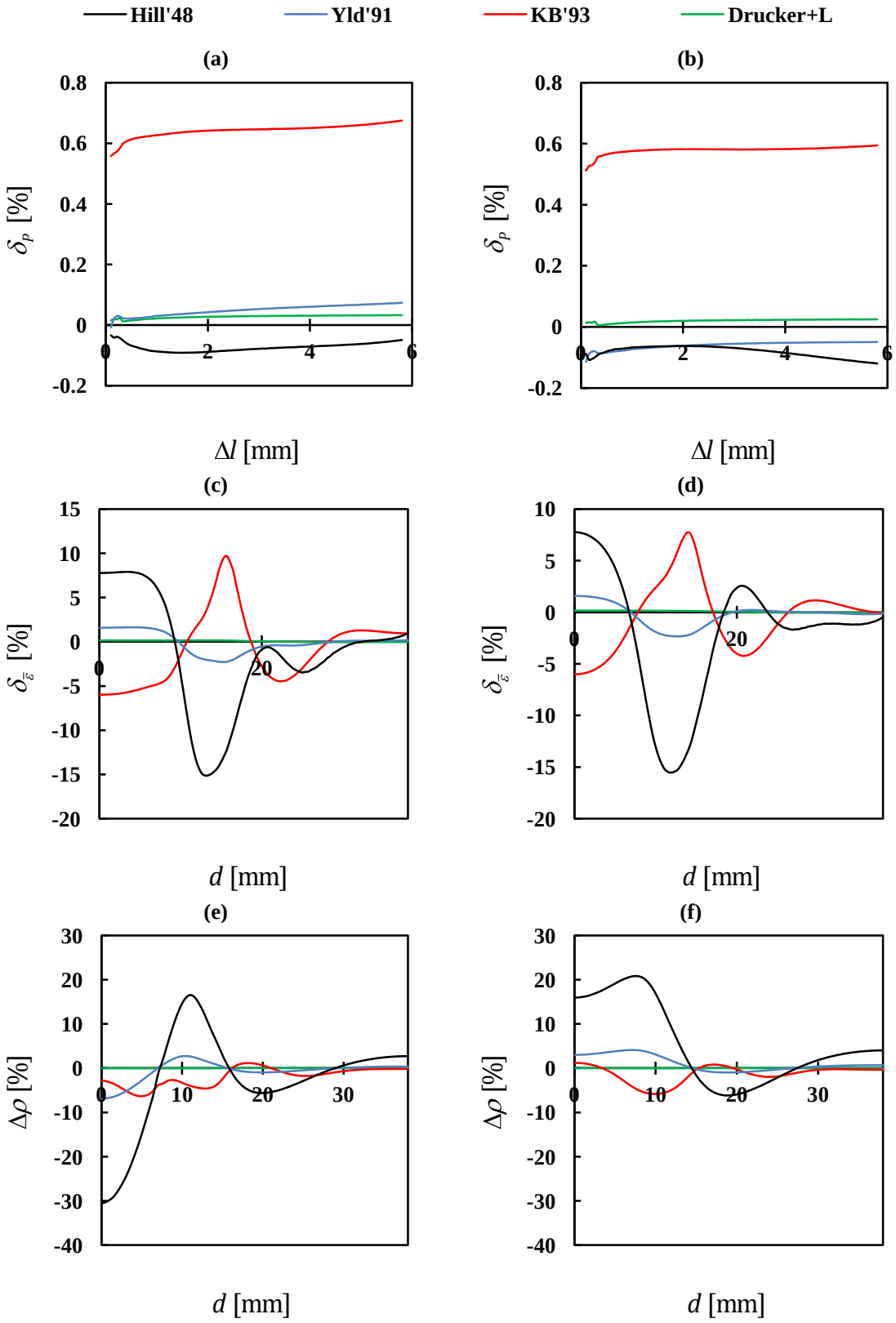

Fig. 4. Comparison between the results obtained from the sequential identification of the constitutive parameters for the Swift law and the Hill'48 criterion (stage 1), Yld'91, KB'93 and Drucker+L criteria (stage 2), for the Case Study 1: (a) and (b) δ_p vs. Δl, for the 0x and 0y axes, respectively; (c) and (d) $\delta_{\bar{\varepsilon}}$ vs. d, for the 0x and 0y axes, respectively; (e) and (f) $\Delta\rho$ vs. d, for the 0x and 0y axes, respectively.

In order to visualise the results of the identification, Fig. 5 shows the equivalent stress-strain curves (Fig. 5 (a)) and the yield surfaces (Fig. 5 (b)), in the plane (σ_{xx}, σ_{yy}), for $\bar{\varepsilon}^p$ = 0.3, close to the maximum value of $\bar{\varepsilon}$ attained during the cruciform test (see Fig. 3 (c), for the material (Mat)) and corresponding to the identifications using Hill'48 criterion (first stage), Yld'91, KB'93 and Drucker+L yield criteria (second stage). When comparing the results obtained from the identified sets of parameters with the material results, the following is observed: (i) the equivalent stress-strain curve obtained from the proposed inverse identification strategy enables an accurate description of the material curve, whatever the yield criteria used; (ii) the Hill'48 criterion does not conveniently describes the material yield surface, unlike the Drucker+L criterion that exactly fits the material yield surface, as would be expected.

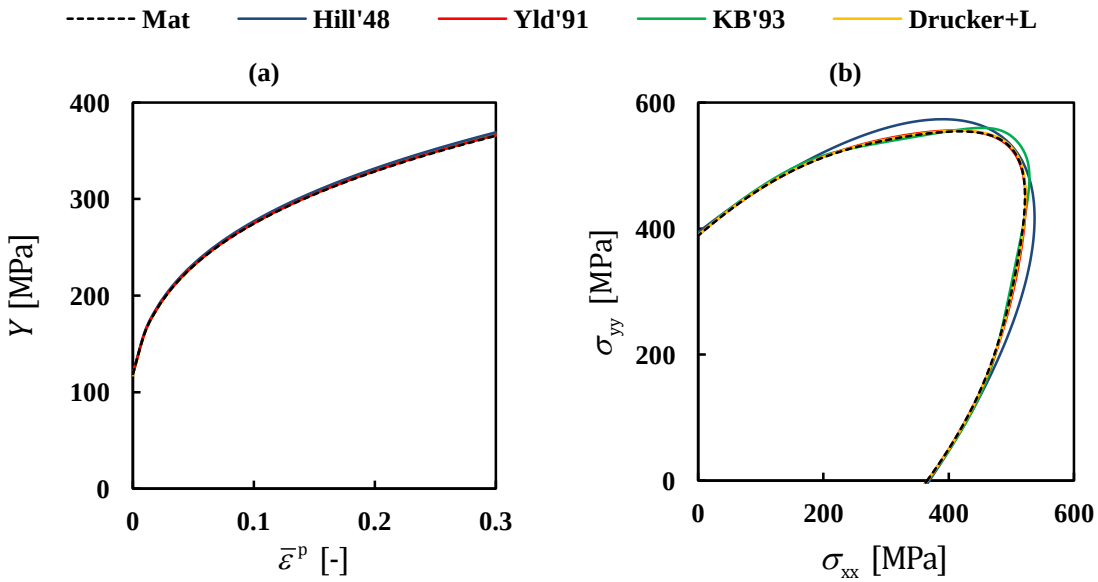

Fig. 5. Comparison between the results of the reference material (Mat) and those obtained from the sequential identification of the constitutive parameters of the Swift law and the Hill'48 (stage 1), Yld'91, KB'93 and Drucker+L (stage 2) criteria, for the Case Study 1: (a) equivalent stress - equivalent plastic strain curves and (b) yield surface, for $\bar{\varepsilon}^p$ = 0.3.

5.2. Case Study 2

In this case study, the mechanical behaviour of the material is described by Voce law and CB2001 yield criterion [4]. The CB2001 criterion is a generalisation of the Drucker's isotropic criterion to anisotropy, and is written as follows:

$$J_2^{\,3} - cJ_3^{\,2} = 27\left(Y/3\right)^6 \tag{24}$$

where J_2 and J_3 are, respectively, the second and third generalised invariants of the Cauchy stress tensor:

$$\begin{aligned}
J_2 &= \frac{a_1}{6}(\sigma_{xx}-\sigma_{yy})^2 + \frac{a_2}{6}(\sigma_{yy}-\sigma_{zz})^2 + \frac{a_3}{6}(\sigma_{xx}-\sigma_{zz})^2 + a_4\tau_{xy}^2 + a_5\tau_{xz}^2 + a_6\tau_{yz}^2 \\
J_3 &= \frac{1}{27}(b_1+b_2)\sigma_{xx}^3 + \frac{1}{27}(b_3+b_4)\sigma_{yy}^3 + \frac{1}{27}\left[2(b_1+b_4)-b_2-b_3\right]\sigma_{zz}^3 \\
&-\frac{1}{9}(b_1\sigma_{yy}+b_2\sigma_{zz})\sigma_{xx}^2 - \frac{1}{9}(b_3\sigma_{zz}+b_4\sigma_{xx})\sigma_{yy}^2 - \frac{1}{9}\left[(b_1-b_2+b_4)\sigma_{xx}+(b_1-b_3+b_4)\sigma_{yy}\right]\sigma_{zz}^2 \\
&+\frac{2}{9}(b_1+b_4)\sigma_{xx}\sigma_{yy}\sigma_{zz} - \frac{\tau_{xz}^2}{3}\left[2b_9\sigma_{yy}-b_8\sigma_{zz}-(2b_9-b_8)\sigma_{xx}\right] \\
&-\frac{\tau_{xy}^2}{3}\left[2b_{10}\sigma_{zz}-b_5\sigma_{yy}-(2b_{10}-b_5)\sigma_{xx}\right] - \frac{\tau_{yz}^2}{3}\left[(b_6+b_7)\sigma_{xx}-b_6\sigma_{yy}-b_7\sigma_{zz}\right] + 2b_{11}\tau_{xy}\tau_{yz}\tau_{xz}
\end{aligned} \tag{25}$$

The coefficients a_k (k = 1 to 6) and b_k (k = 1 to 11) are the anisotropy parameters of the criterion (a_k and b_k are equal to 1 for the isotropy condition) and c is an isotropic parameter.

This yield function holds 18 parameters and so it is more flexible than the criteria used for identification. The material results for Case Study 2 were obtained considering the constitutive parameters, close to ones of aluminium [45], as indicated in Table 4. The elastic properties are: Young's modulus, E = 68.9 GPa and Poisson ratio, ν = 0.33.

Table 4. Constitutive parameters of the reference material of the Case Study 2, described by CB2001 yield criterion and Voce work-hardening law [45].

CB2001 yield parameters							
a_1	a_2	a_3	a_4	a_5=a_6			
1.043	1.416	1.236	0.922	1			
b_1	b_2	b_3	b_4	b_5	b_{10}	b_6=b_7= b_8=b_9=b_{11}	c
1.343	2.436	0.397	0.100	1.015	0.598	1	1.002
Voce work-hardening parameters							
Y_0 [MPa]	Y_{Sat} [MPa]	C_Y					
112.64	318.65	12.99					

Firstly, the proposed inverse identification strategy was performed for the following constitutive models: (i) Hill'48 yield criterion and Swift work-hardening law and (ii) Hill'48 yield criterion and Voce work-hardening law. Table 5 and Table 6 show the identified parameters (Final) and those used as first estimate (Step 1) of the inverse identifications. For comparison, these tables also include the parameters identified with a single cost function strategy (Single), for those constitutive models. Details of this strategy as well as the discussion of its results will be made at the end of this section.

Table 5. Cost functions and constitutive parameters identified by the sequential (Final) and single cost function (Single) strategies, for Voce law, at the end of both stages 1 (Hill'48 yield parameters) and 2 (Yld'91, KB'93 and Drucker+L yield parameters) of the Case Study 2. The initial estimate of the parameters, the correspondent cost functions (Step 1) and the number of simulations are also shown. In cases of Step 1 and Final, $F_4 = F_1 + F_2 + F_3$.

	Cost functions				**Hill'48 yield parameters**					Voce law parameters			Number of simulations
	F_1	F_2	F_3	F_4	F	G	H	$L=M$	N	Y_0 [MPa]	Y_{Sat} [MPa]	C_Y	
Step 1	1.5×10^{-2}	1.1×10^{-1}	4.7×10^{-2}	1.7×10^{-1}	0.5000	0.5000	0.5000	1.5	1.5000	117.05	286.16	8.62	
Final	3.7×10^{-5}	5.8×10^{-3}	1.6×10^{-2}	2.2×10^{-2}	0.7657	0.5596	0.4404	1.5	1.4005	111.05	309.90	13.94	46
Single	3.3×10^{-4}	2.8×10^{-3}	1.6×10^{-2}	1.9×10^{-2}	0.7863	0.5362	0.4638	1.5	1.6213	107.71	296.10	16.59	22
	Cost functions				**Yld'91 yield parameters**					Voce law parameters			Number of simulations
	F_1	F_2	F_3	F_4	C_1	C_2	C_3	$C_4=C_5$	C_6	m	Y_0 [MPa]	Y_{Sat} [MPa]	C_Y	
Final	3.1×10^{-5}	5.7×10^{-3}	1.5×10^{-2}	2.7×10^{-2}	1.2398	1.0489	0.9501	1	1.0325	5	111.03	309.85	13.94	46+10
Single	3.2×10^{-3}	4.0×10^{-3}	8.3×10^{-3}	1.6×10^{-2}	1.3439	1.0174	0.9824	1	1.0295	5	108.01	315.51	15.78	49
	Cost functions				**KB'93 yield parameters (with k = 15)**					Voce law parameters			Number of simulations
	F_1	F_2	F_3	F_4	C_1	C_2	C_3	$C_4=C_5$	C_6	a	Y_0 [MPa]	Y_{Sat} [MPa]	C_Y	
Final	8.9×10^{-6}	1.2×10^{-2}	2.4×10^{-2}	3.6×10^{-2}	1.2364	1.0439	0.9556	1	1.0083	0.9258	111.47	314.81	13.56	46+5
Single	9.8×10^{-5}	9.0×10^{-3}	2.7×10^{-2}	3.6×10^{-2}	1.2356	1.0442	0.9554	1	1.0368	0.9395	108.69	13.81	13.81	25
	Cost functions				**Drucker+L yield parameters**					Voce law parameters			Number of simulations
	F_1	F_2	F_3	F_4	C_1	C_2	C_3	$C_4=C_5$	C_6	c	Y_0 [MPa]	Y_{Sat} [MPa]	C_Y	
Final	2.2×10^{-5}	5.4×10^{-3}	1.4×10^{-2}	1.9×10^{-2}	1.2624	1.0692	0.9566	1	1.0173	0.5255	110.07	311.60	14.13	46+20
Single	2.5×10^{-3}	2.9×10^{-3}	8.9×10^{-3}	1.4×10^{-2}	1.3436	1.0328	0.9896	1	1.0378	0.4406	107.58	314.71	15.68	57

Table 6. Cost functions and constitutive parameters identified by the sequential (Final) and single cost function (Single) strategies, for Swift law, at the end of both stages 1 (Hill'48 yield parameters) and 2 (Yld'91, KB'93 and Drucker+L yield parameters) of the Case Study 2. The initial estimate of the parameters, the correspondent cost functions (Step 1) and the number of simulations are also shown. In cases of Step 1 and Final, $F_4 = F_1 + F_2 + F_3$.

	Cost functions				**Hill'48 yield parameters**					Swift law parameters			Number of simulations
	F_1	F_2	F_3	F_4	F	G	H	$L=M$	N	Y_0 [MPa]	C [MPa]	n	
Step 1	1.2×10^{-2}	1.6×10^{-1}	4.9×10^{-2}	2.2×10^{-1}	0.5000	0.5000	0.5000	1.5	1.5000	100.00	376.06	0.250	
Final	7.3×10^{-5}	1.0×10^{-2}	2.2×10^{-2}	3.2×10^{-2}	0.8051	0.6031	0.3969	1.5	1.4710	108.70	616.06	0.384	32
Single	9.8×10^{-4}	1.8×10^{-2}	1.9×10^{-2}	3.8×10^{-2}	0.7464	0.5475	0.4525	1.5	1.5596	98.78	474.12	0.288	15
	Cost functions				**Yld'91 yield parameters**					Swift law parameters			Number of simulations
	F_1	F_2	F_3	F_4	C_1	C_2	C_3	$C_4=C_5$	C_6	m	Y_0 [MPa]	C [MPa]	n	
Final	1.1×10^{-4}	1.0×10^{-2}	1.9×10^{-2}	2.9×10^{-2}	1.2661	1.0803	0.9166	1	1.0238	5	108.65	615.64	0.384	32+5
Single	2.0×10^{-3}	9.5×10^{-3}	1.6×10^{-2}	2.8×10^{-2}	1.3319	1.0389	0.9602	1	1.0875	6	102.26	568.62	0.331	33
	Cost functions				**KB'93 yield parameters (with k = 15)**					Swift law parameters			Number of simulations
	F_1	F_2	F_3	F_4	C_1	C_2	C_3	$C_4=C_5$	C_6	a	Y_0 [MPa]	C [MPa]	n	
Final	7.2×10^{-5}	1.2×10^{-2}	2.9×10^{-2}	4.1×10^{-2}	1.2535	1.0670	0.9319	1	1.0679	0.9305	108.75	616.40	0.384	32+10
Single	9.3×10^{-4}	1.1×10^{-2}	2.9×10^{-2}	4.1×10^{-2}	1.2002	1.0655	0.9336	1	1.0627	0.9388	97.02	539.64	0.334	25
	Cost functions				**Drucker+L yield parameters**					Swift law parameters			Number of simulations
	F_1	F_2	F_3	F_4	C_1	C_2	C_3	$C_4=C_5$	C_6	c	Y_0 [MPa]	C [MPa]	n	
Final	3.6×10^{-4}	1.0×10^{-2}	1.9×10^{-2}	2.9×10^{-2}	1.2855	1.0978	0.9231	1	1.0227	0.4655	109.97	626.01	0.384	32+11
Single	1.7×10^{-3}	8.8×10^{-3}	1.6×10^{-2}	2.7×10^{-2}	1.3163	1.0566	0.9533	1	1.0757	0.2152	92.45	540.88	0.312	41

The constitutive parameters identified during the first stage of the sequential identification strategy involved one return to Step 2 after Step 3, for both work-hardening laws (Voce or Swift). In case of Voce law, a total of 46 simulations were performed (25 in Step 2 + 21 in Step 3); in case of Swift law, a total of 32 simulations were performed (15 in Step 2 + 18 in Step 3). Table 5 and Table 6 also show the identified parameters of the Voce and Swift laws, respectively, together with the Yld'91, KB'93 and Drucker+L criteria (second stage), whose identification involved always only one return to Step 3, after Step 6. In case of Voce law, the second stage of the identification procedure required the following additional number of simulations: (i) 10, for Yld'91 (4 in Step 5 + 6 in Step 3); (ii) 5, for KB'93 (2 in Step 5 + 3 in Step 3) and (iii) 20, for Drucker+L (17 in Step 5 + 3 in Step 3). In case of Swift law: (i) 5, for Yld'91 (2 in Step 5 + 3 in Step 3); (ii) 10, for KB'93 (4 in Step 5 + 6 simulations in Step 3) and (iii) 11, for Drucker+L (8 in Step 5 + 3 in Step 3).

Figs. 6 and 7 compare the results of the reference material (Mat) of the biaxial cruciform test with those obtained from the parameters identified at the end of the first stage (Step 3) of the proposed inverse strategy (Final), i.e. for the Hill'48 yield criterion, with the Voce and Swift work-hardening laws, respectively. The results presented are P vs. Δl (Figs. 6 and 7 - (a)); $\bar{\varepsilon}$ vs. d (Figs. 6 and 7 - (c)) and ρ vs. d (Figs. 6 and 7 - (e)), for both axes. The comparison is also performed in the form of the differences: δ_p vs. Δl (Figs. 6 and 7 - (b)), $\delta_{\bar{\varepsilon}}$ vs. d (Figs. 6 and 7 - (d)) and $\Delta\rho$ vs. d (Figs. 6 and 7 - (f)), for both axes. The results in Figs. 6 and 7 - (c) to (f) are plotted for Δl = 3.5 mm, equal for both 0x and 0y axes, immediately preceding the maximum load. The results concerning the initial estimate (Isotropic) are also shown in Figs. 6 and 7 - (a), (c) and (e).

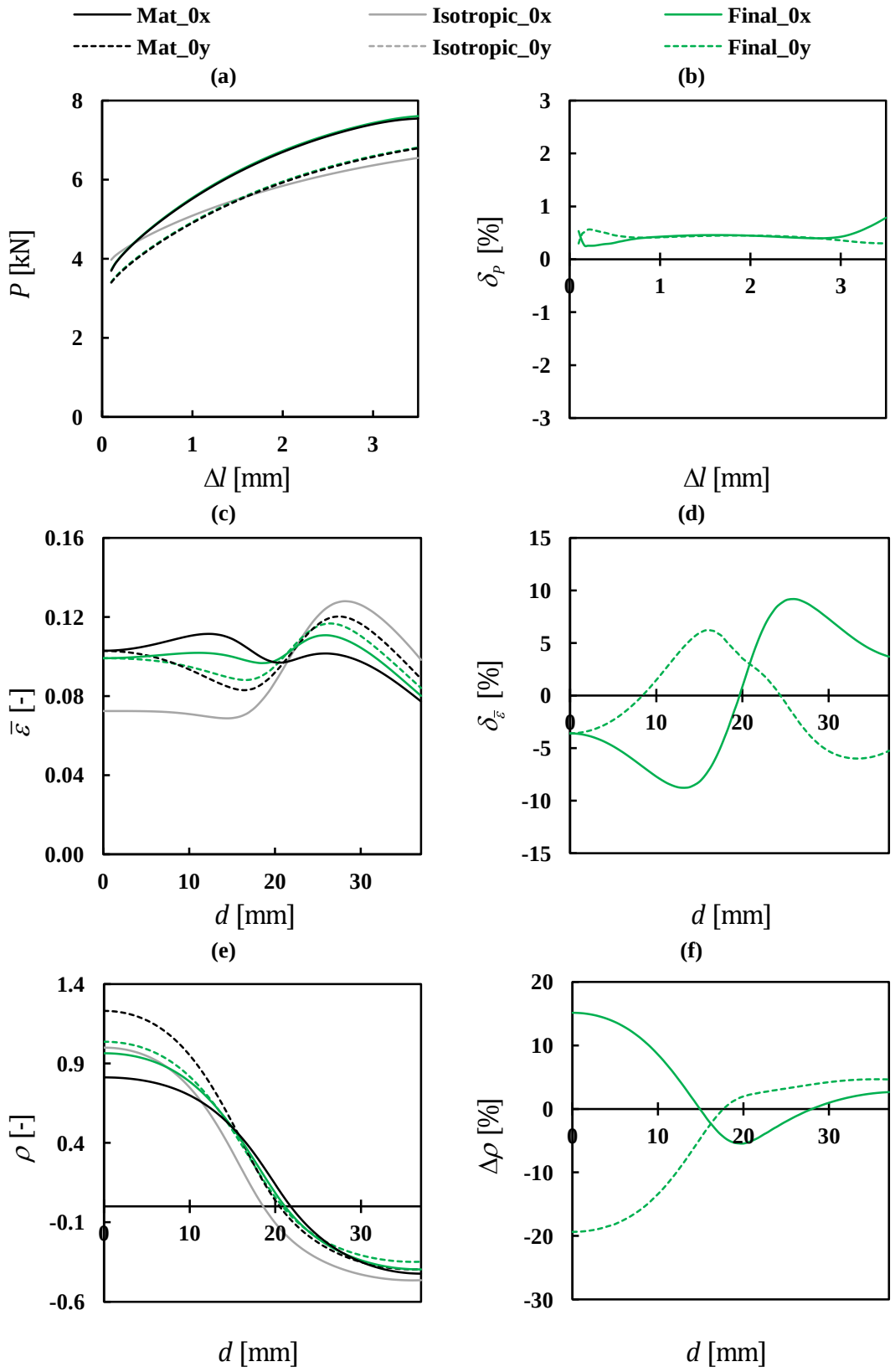

Fig. 6. Comparison between the results of reference material (Mat) and those obtained from the sequential identification of the constitutive parameters of the Voce law and Hill'48 criterion (end of stage 1 - "Final"), for the Case Study 2: (a) P vs. Δl; (b) δ_P vs. Δl; (c) $\bar{\varepsilon}$ vs. d; (d) $\delta_{\bar{\varepsilon}}$ vs. d; (e) ρ vs. d and (f) $\Delta\rho$ vs. d. In figures 6 (a), (c) and (e), the results labelled "Isotropic" concern the first estimate.

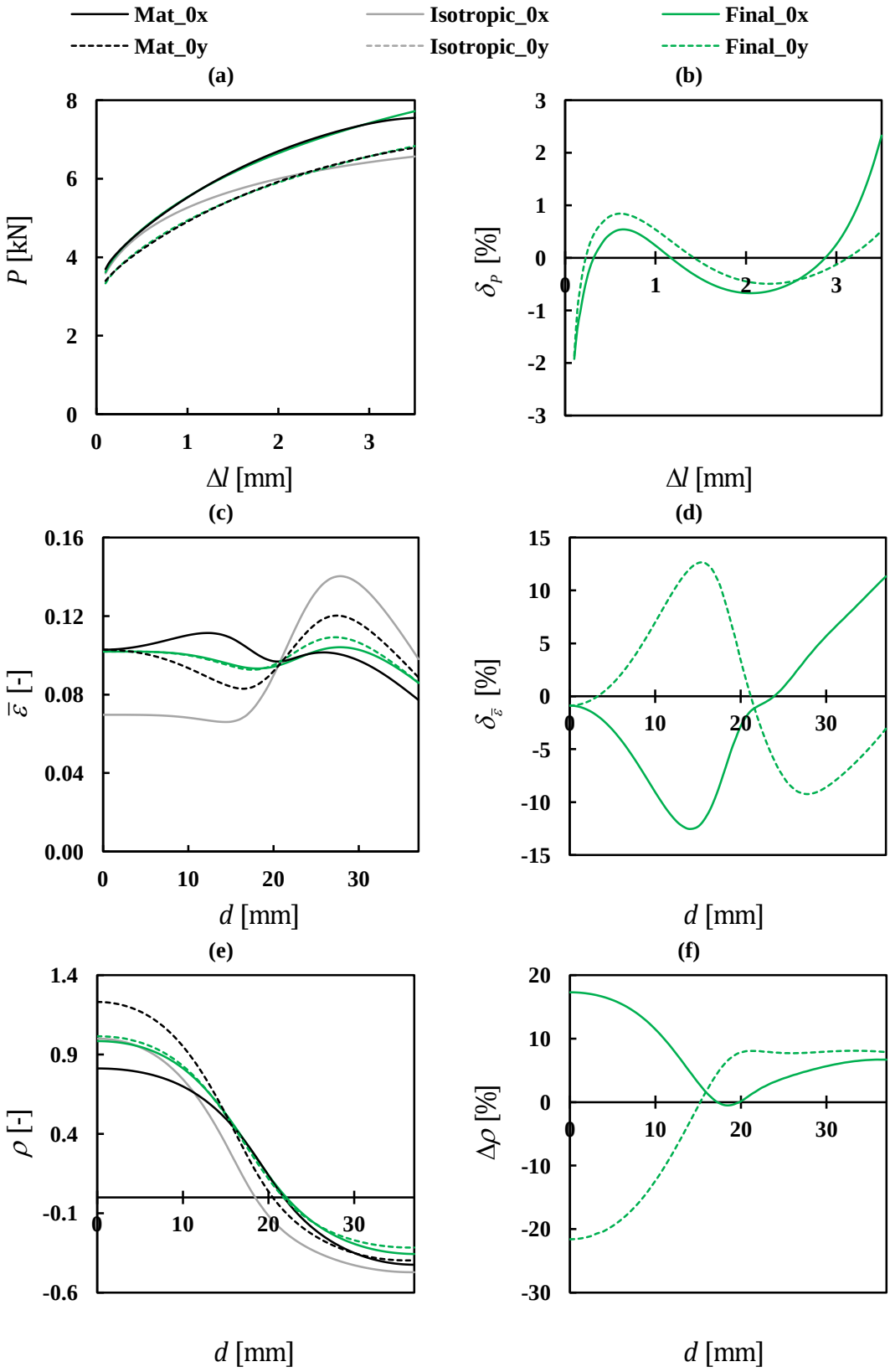

Fig. 7. Comparison between the results of reference material (Mat) and those obtained from the sequential identification of the constitutive parameters of the Swift law and Hill'48 criterion (end of stage 1 - "Final"), for the Case Study 2: (a) P vs. Δl; (b) δ_P vs. Δl; (c) $\bar{\varepsilon}$ vs. d; (d) $\delta_{\bar{\varepsilon}}$ vs. d; (e) ρ vs. d and (f) $\Delta\rho$ vs. d. In figures 7 (a), (c) and (e), the results labelled "Isotropic" concern the first estimate.

To evaluate which work-hardening law (Swift or Voce) best describes the material behaviour, the δ_p vs. Δl results must be analysed. In fact, the parameters of the work hardening law mainly influence the load evolution results [30] and obviously the type of law also influences the load evolution results, as shown in Figs. 6 and 7- (b), for the Voce and Swift laws, respectively. These results show that Voce law leads to a quasi-uniform distribution of δ_p vs. Δl for both axes (with absolute relative differences less than 0.8%) while the Swift law leads to an uneven distribution (with absolute relative differences that reach about 2%). The quasi-uniform distribution obtained with the Voce law means that the work-hardening behaviour of the material is better described by this law than by the Swift law, as expected (the reference material follows the Voce law).

Nevertheless, the Hill'48 criterion poorly describes the material $\bar{\varepsilon}$ vs. d and ρ vs. d distributions whatever the hardening law. The average (0x and 0y axes) of the absolute values of $\delta_{\bar{\varepsilon}}$ are equal to 4.84% (Voce) and 5.97% (Swift), and the F_3 values are equal to 1.6×10^{-2} (Voce) and 2.2×10^{-2} (Swift). Thus, the parameters identification performed for Hill'48 criterion with Voce and Swift laws were extended to other three criteria: Yld'91, KB'93 and Drucker+L.

Figs. 8 and 9 allows comparing the results of the biaxial cruciform test obtained from the parameters identified with the sequential identification strategy for these three criteria with the ones of the reference materials, for Voce and Swift laws, respectively. The results are shown in the form of the differences: δ_p vs. Δl (Figs. 8 and 9 - (a) and (b)), $\delta_{\bar{\varepsilon}}$ vs. d (Figs. 8 and 9 - (c) and (d)) and $\Delta\rho$ vs. d (Figs. 8 and 9 - (e) and (f)). The results in Figs. 8 and 9 - (a), (c) and (e) concern the axis 0x and in Figs. 8 and 9 - (b), (d) and (f) concern the 0y axis. Unlike for Case Study 1, in this case it becomes difficult to realize the improvements attained for each of the three yield criteria used in the second stage, Yld'91, KB'93 and Drucker+L, when compared with the Hill'48 criterion (first stage).

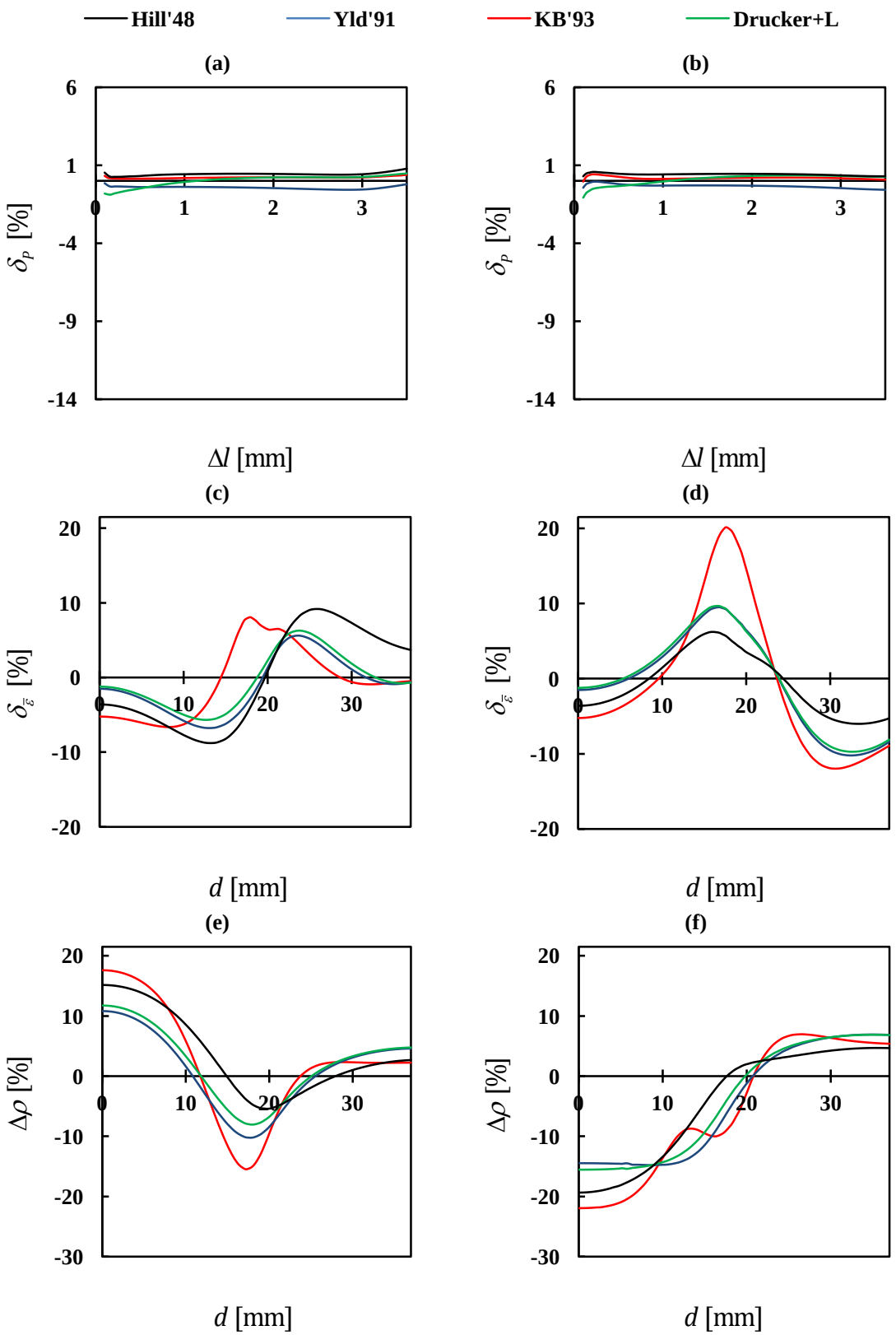

Fig. 8. Comparison between the results obtained from the sequential identification of the constitutive parameters of the Voce law and the Hill'48 criterion (stage 1), Yld'91, KB'93 and Drucker+L criteria (stage 2), for the Case Study 2: (a) and (b) δ_p vs. Δl, for the 0x and 0y axes, respectively; (c) and (d) $\delta_{\bar{\varepsilon}}$ vs. d, for the 0x and 0y axes, respectively; (e) and (f) $\Delta\rho$ vs. d, for the 0x and 0y axes, respectively.

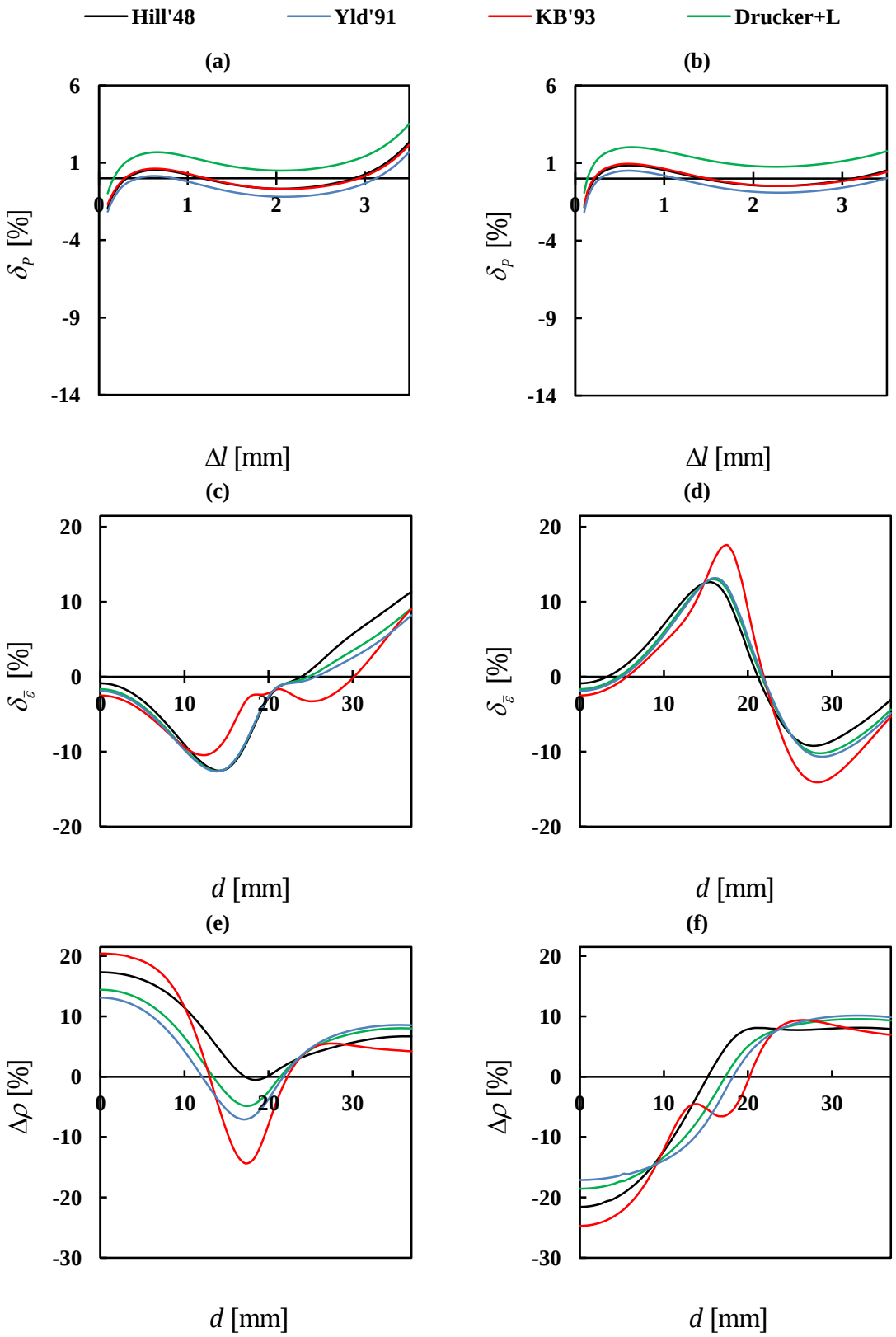

Fig. 9. Comparison between the results obtained from the sequential identification of the constitutive parameters of the Swift law and the Hill'48 (stage 1), Yld'91, KB'93 and Drucker+L criteria (stage 2), for the Case Study 2: (a) and (b) δ_p vs. Δl, for the 0x and 0y axes, respectively; (c) and (d) $\delta_{\bar{\varepsilon}}$ vs. d, for the 0x and 0y axes, respectively; (e) and (f) $\Delta\rho$ vs. d, for the 0x and 0y axes, respectively.

For both work-hardening laws, the results show that the accuracy of the load evolution during the test, for both axes, remains globally the same for the three yield criteria used in the second stage, although it could be argued that for the KB'93 there is a slightly increase of accuracy, in case of the Voce law. Regarding the accuracy of the equivalent strain and strain path ratio distribution results, the KB'93 criterion is the only one that gets worse compared to Hill'48 criterion. The accuracy of the different cases can be better examined from the values of the cost functions in Tables 5 and 6. The small differences between the accuracy of the results are, however, sufficient to highlight the interaction between the work-hardening law and the yield criterion and show that, as expected for this reference material, globally better results are attained with the Voce law, whatever the yield criteria selected. Lastly, it should be mentioned that the Drucker+L criterion together with the Voce law provides slightly better results (lower values of all cost functions: F_1, F_2 and F_3) than other criteria. However, when comparing the results of all criteria, the improvement of accuracy in performing the second stage of the identification is not significant.

In order to visualise the results of the identification, Fig. 10 shows the equivalent stress-strain curves and the yield surfaces, in the plane (σ_{xx}, σ_{yy}), for $\bar{\varepsilon}^p$ = 0.12, close to the maximum value of $\bar{\varepsilon}$ attained during the cruciform test for the reference material (Mat - see Fig. 6 (c)) and the corresponding identifications using Hill'48, Yld'91, KB'93 and Drucker+L yield criteria, combined with Voce law. When comparing the results of the sets of identified parameters with the reference ones, the following is observed: (i) the equivalent stress-strain curves obtained from the sequential inverse identification strategy provides an accurate description of the material, whatever the yield criteria used; (ii) the yield surfaces obtained from the sequential identification strategy are quite similar for all yield criteria and close to the reference yield surface.

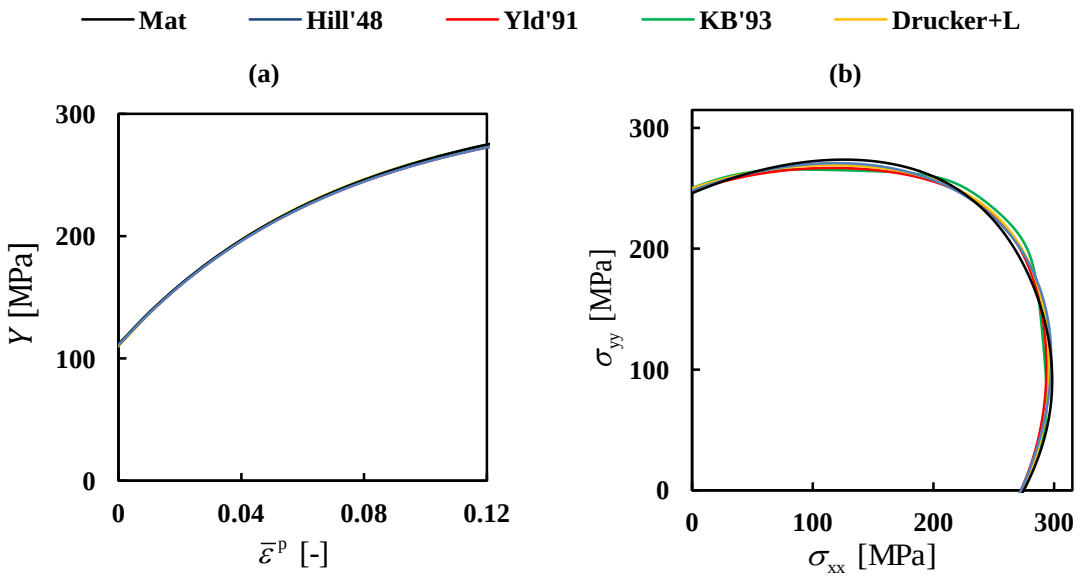

Fig. 10. Comparison between the results of the reference material (Mat) and those obtained from the sequential identification of the constitutive parameters of the Voce law and the Hill'48 (stage 1), Yld'91, KB'93 and Drucker+L (stage 2) criteria, for the Case Study 2: (a) equivalent stress - equivalent plastic strain curves and (b) yield surface, for $\bar{\varepsilon}^p$ = 0.12.

For this case study, the above results from the sequential inverse identification strategy are compared with the results obtained from a single cost function approach, where the parameter identification is performed, as traditionally, by minimising a unique cost function comprising all material parameters and the weighted results of the test:

$$F(\mathbf{D}) = w_1 F_1(\mathbf{D}) + w_2 F_2(\mathbf{D}) + w_3 F_3(\mathbf{D}) \tag{26}$$

where $F_1(\mathbf{D})$, $F_2(\mathbf{D})$ and $F_3(\mathbf{D})$ are the cost functions, whose formulation is equal to Eqs. (21), (22) and (23), respectively, and **D** is the set of constitutive parameters to be optimised, i.e. the parameters of the work-hardening law and yield criterion; each term in the cost function is weighted by a factor, w_i, in order to eventually consider, the influence of each type of result in the identification. For example, in classic identification, Barlat et al. (2005) argue that the weight of each data type should reflect the relative precision with which this can be determined, i.e. more robust results must have higher weight values than those less robust [46]. Also, the weight factors may also be selected according to the preference of the user to favour the minimisation of a type of result over the other. Otherwise, the accurate choice of such values of w_i requires some sort of optimisation procedure, which is always difficult to accomplish concomitantly with the identification process. The difficulty of making a good choice of w_i usually leads to consider all weight factors equal to 1, as in the current work. Similarly to the sequential methodology, the minimisation procedure here adopted for the cost function $F(\mathbf{D})$ stops when the relative difference between a given set of parameters and the next one is less than 5%, for each of the constitutive model parameters.

This single cost function identification strategy was performed for all yield criteria and the Voce and Swift laws, starting with the same initial estimate used in the sequential identification. Figs. 11 and 12 compare the results of the biaxial cruciform test obtained from the parameters identified with the single cost function strategy for all criteria and the Voce and Swift laws, respectively, with those of the reference materials (as in Figs. 8 and 9 for the sequential strategy). Regarding the influence of the type of work-hardening law, whatever the yield criterion used, the single cost function identification approach leads to a less uniform distribution of the δ_p vs. Δl results than the proposed inverse identification, in case of Voce law, although the same kind of non-uniform distributions occurs for the Swift law (compare with Figs. 8 and 9 - (b)). Furthermore, the accuracy of the load evolution during the test is much smaller using the single cost function optimisation procedure than in case of the sequential optimisation. This happens without a visible gain of accuracy in the remaining results (equivalent strain and strain ratio distributions), as we will see in more detail right away.

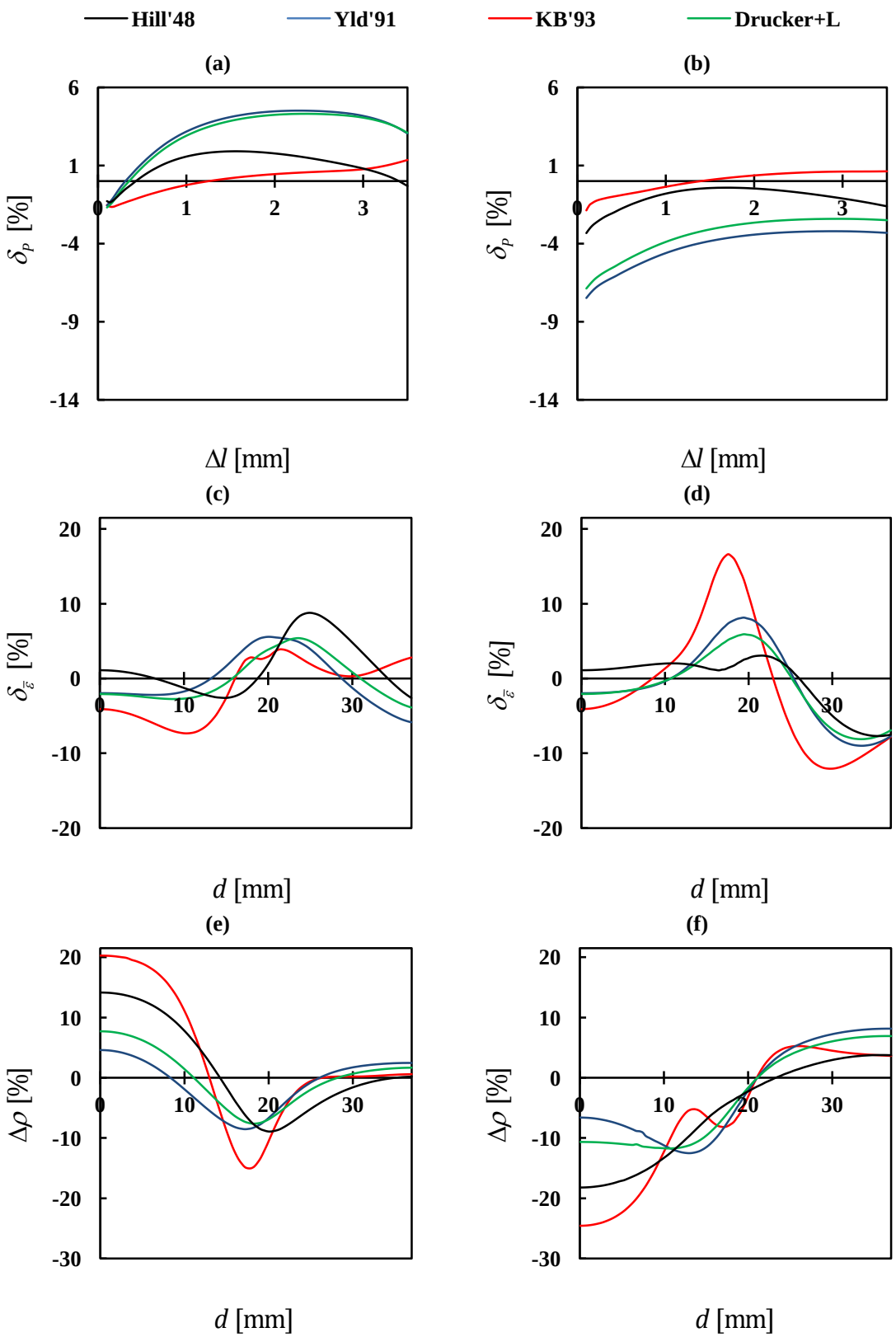

Fig. 11. Comparison between the results obtained from the single cost function identification of the constitutive parameters of the Voce law and the Hill'48, Yld'91, KB'93 and Drucker+L criteria, for the Case Study 2: (a) and (b) δ_p vs. Δl, for the 0x and 0y axes, respectively; (c) and (d) $\delta_{\bar{\varepsilon}}$ vs. d, for the 0x and 0y axes, respectively; (e) and (f) $\Delta\rho$ vs. d, for the 0x and 0y axes, respectively.

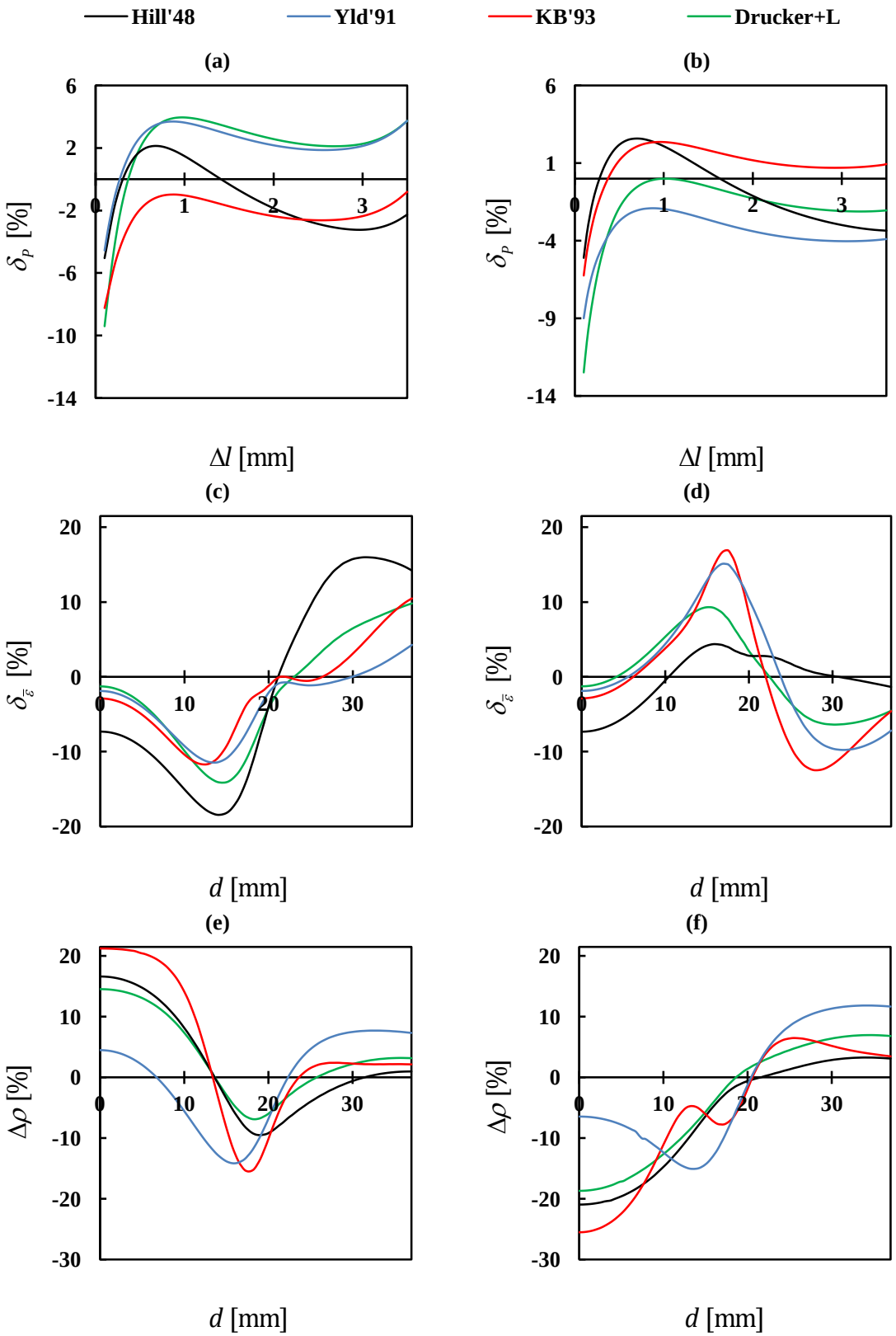

Fig. 12. Comparison between the results obtained from the single cost function identification of the constitutive parameters of the Swift law and the Hill'48, Yld'91, KB'93 and Drucker+L criteria, for the Case Study 2: (a) and (b) δ_p vs. Δl, for the 0x and 0y axes, respectively; (c) and (d) $\delta_{\bar{\varepsilon}}$ vs. d, for the 0x and 0y axes, respectively; (e) and (f) $\Delta\rho$ vs. d, for the 0x and 0y axes, respectively.

The values of the cost function, F_4, which is minimised in the single cost function identification strategy and the identified constitutive parameters are shown in Tables 5 and 6 ("Single" in these tables), for Voce and Swift laws, respectively. These tables also show the values of F_1, F_2 and F_3, for comparison with the sequential identification strategy. The F_4 cost function shows similar values (same order of magnitude) for both identification procedures, although the single cost function identification approach (Single) tends to present slightly smaller values (only in one case – Swift law and Hill'48 criterion - F_4 is slightly greater in the single cost function approach); also, both identification strategies lead to values of cost functions F_2 and F_3 which are of the same order of magnitude. However, the values of F_1 obtained from the sequential identification strategy are about one order of magnitude lower than the ones obtained from the single cost function identification approach. This is the main feature distinguishing both identification strategies. The implications of this distinction can be easily visualised when comparing the equivalent stress-strain curves and the yield surfaces obtained from the sequential inverse identification strategy with those obtained from the single cost function identification approach, as shown in Fig. 13. Fig. 13 (a) shows the equivalent stress-strain curves and Fig. 13 (b) the yield surfaces in the plane (σ_{xx}, σ_{yy}), for $\bar{\varepsilon}^p$ = 0.12, close to the maximum value of $\bar{\varepsilon}$ attained during the cruciform test for the reference material (Mat - see Fig. 6 (c)) and the corresponding identifications using Hill'48, Yld'91, KB'93 and Drucker+L yield criteria, combined with Voce law. When comparing the results from the identified sets of parameters with the reference ones, it can be concluded: (i) the single cost function approach mainly overestimates the entire work-hardening curve; (ii) the yield surfaces obtained from the sequential inverse identification strategy (see Fig. 10) are closer to the reference yield surface than the ones obtained from the single cost function identification approach. The comparison of the total number of simulations required for both strategies, also presented in Tables 5 and 6, shows that the first stage of the sequential strategy is the one requiring more simulations, which in the worst case can be twice the total number required by the "Single" strategy. It should be noted that, after identifying the Hill'48 parameters, the extension to more complex yield criteria requires a relatively low number of simulations.

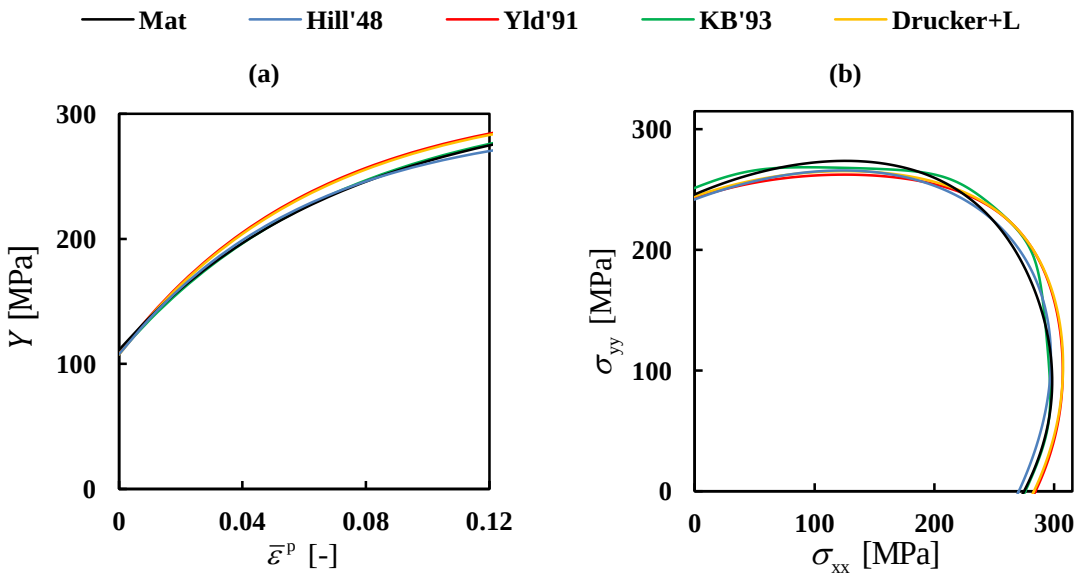

Fig. 13. Comparison between the results of the reference material (Mat) and those obtained from the single cost function identification of the constitutive parameters of the Voce law and the Hill'48, Yld'91, KB'93 and Drucker+L criteria, for the Case Study 2: (a) equivalent stress - equivalent plastic strain curves and (b) yield surface, for $\bar{\varepsilon}^p$ = 0.12.

5.3. Final Remarks

The results from both case studies allow reaching the following conclusions:

(i) The proposed inverse identification procedure (see Table 1) uses three cost functions that are sequentially minimised. Priority is given to the fitting of the P vs. Δl results. The following step concern the minimisation of the gap between numerical and experimental $\bar{\varepsilon}$ vs. d results. The quality of the fitting of the P vs. Δl results can allow choosing which hardening law better describes the material behaviour, if using several laws. The procedure can use of the ρ vs. d results, in order to capture the experimental strain path ratios observed in the specimen. The parameter identification can be more or less accurate depending on the anisotropic material behaviour and on the flexibility of the yield criterion chosen by the user.

(ii) The use of a unique cost function including P vs. Δl, $\bar{\varepsilon}$ vs. d and ρ vs. d results for the inverse identification can lead to inconsistencies regarding the accurate description of the material plastic behaviour. Namely, this identification approach can deteriorate the description of the material P vs. Δl results, and so the parameters and the choice of the hardening law, without improving the description of the $\bar{\varepsilon}$ vs. d and ρ vs. d results.

6. Conclusions

This paper proposes an inverse strategy to simultaneously identify the constitutive parameters of complex constitutive models, i.e. anisotropic yield criteria and work-hardening laws parameters, from the results of biaxial tensile test of a cruciform sample. This strategy makes use of experimental and numerical simulation results of the cruciform biaxial test on metal sheets and a sequential procedure for the parameter identification using a gradient-based method, the Levenberg-Marquardt algorithm. The sequential inverse identification strategy makes use of three distinct cost functions, and their minimisation is performed in a pre-specified sequence. Firstly, the work-hardening law parameters and a quantity that depends on parameters of the yield criterion are identified by minimising the gap between the numerical and experimental load evolution during the test, on both axes of the sample. Thereafter, the anisotropic parameters of the yield criteria are fully identified, by minimising the gap between the numerical and experimental equivalent strain distributions along both axes of the sample, at a given moment of the test close to the maximum load. These two stages can be performed using the Hill'48 or any other criterion. Finally, a third cost function, minimising the gap between the numerical and experimental strain path distributions along both axes of the sample can be used in order to define the most appropriate criterion for describing the material behaviour. This shows to be competitive with typical inverse identification strategies, which make use of a single cost function including all constitutive parameters and different type of results at once.

Acknowledgements

This research work is sponsored by national funds from the Portuguese Foundation for Science and Technology (FCT) via the projects PTDC/EME–TME/113410/2009 and PEst-C/EME/UI0285/2013 and by FEDER funds through the program COMPETE – Programa Operacional Factores de Competitividade, under the project CENTRO -07-0224 -FEDER -002001 (MT4MOBI). One of the authors, P.A. Prates, was supported by a grant for scientific research from the Portuguese Foundation for Science and Technology. All supports are gratefully acknowledged.

References

[1] Hill R. A theory of yielding and plastic flow of anisotropic metals. Proc R Soc London 1948; 193:281–297. doi:10.1098/rspa.1948.0045

[2] Barlat F, Lege DJ, Brem JC. A 6-component yield function for anisotropic materials. Int J Plast 1991; 7:693–712. doi:10.1016/0749-6419(91)90052-Z

[3] Karafillis AP, Boyce MC. A general anisotropic yield criterion using bounds and a transformation weighting tensor. J Mech Phys Solids 1993; 41:1859–1886. doi:10.1016/0022-5096(93)90073-O

[4] Cazacu O, Barlat F. Generalization of Drucker's yield criterion to orthotropy. Math Mech Solids 2001; 6:613–630. doi:10.1177/108128650100600603

[5] Bron F, Besson J. A yield function for anisotropic materials. Application to aluminium alloys. Int J Plast 2004; 20:937–963. doi:10.1016/j.ijplas.2003.06.001

[6] Vegter H, van den Boogaard AH. A plane stress yield function for anisotropic sheet material by interpolation of biaxial stress states. Int J Plast 2006; 22:557–580. doi:10.1016/j.ijplas.2005.04.009

[7] Plunkett B, Cazacu O, Barlat F. Orthotropic yield criteria for description of the anisotropy in tension and compression of sheet metals. Int J Plast 2008; 24:847–866. doi:10.1016/j.ijplas.2007.07.013

[8] Aretz H, Barlat F. New convex yield functions for orthotropic metal plasticity. Int J Non-Linear Mech 2013; 51:97–111. doi:10.1016/j.ijnonlinmec.2012.12.007

[9] Yoshida F, Hamasaki H, Uemori T. A user-friendly 3D yield function to describe anisotropy of steel sheets. Int J Plast 2013;45:119–139. doi:10.1016/j.ijplas.2013.01.010

[10] Voce E. The relationship between stress and strain for homogeneous deformation. J Inst Metals 1948; 74:537–562.

[11] Swift HW. Plastic instability under plane stress. J Mech Phys Solids 1952; 1:1–18. doi:10.1016/0022-5096(52)90002-1

[12] Armstrong PJ, Frederick CO. A mathematical representation of the multiaxial Bauschinger effect. GEGB report RD/B/N 731; 1966.

[13] Geng L, Wagoner RH. Springback analysis with a modified hardening model. SAE paper No. 2000-01-0768 SAE Inc; 2000. doi:10.4271/2000-01-0768.

[14] Chaboche JL. Time-independent constitutive theories for cyclic plasticity. Int J Plast 1986; 2:149–88. doi:10.1016/0749-6419(86)90010-0

[15] Yoshida F, Uemori T. A model of large-strain cyclic plasticity describing the Bauschinger effect and workhardening stagnation. Int J Plast 2002; 18:661–686. doi:10.1016/S0749-6419(01)00050-X

[16] Barlat F, Gracio JJ, Lee MJ, Rauch EF, Vincze G. An alternative to kinematic hardening in classical plasticity. Int J Plast 2011; 27:1309–1327. doi:10.1016/j.ijplas.2011.03.003

[17] Ponthot J-P, Kleinermann J-P. A cascade optimization methodology for automatic parameter identification and shape/process optimization in metal forming simulation. Comput. Methods Appl Mech Engrg 2006; 195:5472–5508. doi:10.1016/j.cma.2005.11.012

[18] Oliveira MC, Alves JL, Chaparro BM, Menezes LF. Study on the influence of work-hardening modeling in springback prediction. Int J Plast 2007; 23:516–543. doi:10.1016/j.ijplas.2006.07.003

[19] Chaparro BM, Thuillier S, Menezes LF, Manach PY, Fernandes JV. Material parameters identification: Gradient-based, genetic and hybrid optimization algorithms. Comput Mater Sci 2008; 44:339–346. doi:10.1016/j.commatsci.2008.03.028

[20] Rabahallah M, Balan T, Bouvier S, Bacroix B, Barlat F, Chung K, Teodosiu C. Parameter identification of advanced plastic strain rate potentials and impact on plastic anisotropy prediction. Int J Plast 2009; 25:491–512. doi:10.1016/j.ijplas.2008.03.006

[21] Pottier T, Toussaint F, Vacher P. Contribution of heterogeneous strain field measurements and boundary conditions modelling in inverse identification of material parameters. Eur J Mech A-Solid 2011; 30:373−382. doi:10.1016/j.euromechsol.2010.10.001.

[22] Andrade-Campos A, de-Carvalho R, Valente RAF. Novel criteria for determination of material model parameters. Int J Mech Sci 2012; 54:294–305. doi:10.1016/j.ijmecsci.2011.11.010

[23] Rossi M, Pierron F. Identification of plastic constitutive parameters at large deformations from three dimensional displacement fields. Comput Mech 2012; 49:53–71. doi:10.1007/s00466-011-0627-0

[24] Pottier T, Vacher P, Toussaint F, Louche H, Coudert T. Out-of-plane testing procedure for inverse identification purpose: application in sheet metal plasticity. Exp Mech 2012; 52:951–963. doi:10.1007/s11340-011-9555-3

[25] Xiao-qiang LI, De-hua HE. Identification of material parameters from punch stretch test. Trans Nonferrous Met Soc China 2013; 23:1435−1441. doi:10.1016/S1003-6326(13)62614-X

[26] Kim J-H, Barlat F, Pierron F, Lee M-G. Determination of anisotropic plastic constitutive parameters using the virtual fields method. Exp Mech 2014; 54:1189–1204. doi:10.1007/s11340-014-9879-x

[27] Avril S, Bonnet M, Bretelle A-S, Grédiac M, Hild F, Ienny P, Latourte F, Lemosse D, Pagano S, Pagnacco E, Pierron F. Overview of identification methods of mechanical parameters based on full-field measurements. Exp Mech 2008; 48:381– 402. doi:10.1007/s11340-008-9148-y

[28] Green DE, Neale KW, MacEwen SR, Makinde A, Perrin R. Experimental investigation of the biaxial behaviour of an aluminum sheet. Int J Plast 2004; 20:1677–1706. doi:10.1016/j.ijplas.2003.11.012

[29] Cooreman S, Lecompte D, Sol H, Vantomme J, Debruyne D. Identification of mechanical material behavior through inverse modeling and DIC. Exp Mech 2008; 48:421–433. doi:10.1007/s11340-007-9094-0

[30] Prates PA, Oliveira MC, Fernandes JV. A new strategy for the simultaneous identification of constitutive laws parameters of metal sheets using a single test. Comp Mater Sci 2014; 85:102–120. doi:10.1016/j.commatsci.2013.12.043

[31] Schmaltz S, Willner K. Comparison of different biaxial tests for the inverse identification of sheet steel material parameters. Strain 2014. doi: 10.1111/str.12080.

[32] Zhang S, Leotoing L, Guines D, Thuillier S, Zang SL. Calibration of anisotropic yield criterion with conventional tests or biaxial test. Int J Mech Sci 2014; 85:142–151. doi:10.1016/j.ijmecsci.2014.05.020.

[33] Khalfallah A, Bel Hadj Salah H, Dogui A. Anisotropic parameter identification using inhomogeneous tensile test. Eur J Mech A-Solid 2002; 21:927–942. doi:10.1016/S0997-7538(02)01246-9

[34] Schmaltz S, Willner K. Material Parameter Identification utilizing Optical Full-Field Strain Measurement and Digital Image Correlation. J Jap Soc Exp Mech 2013; 13:120–125. http://dx.doi.org/10.11395/jjsem.13.s120

[35] Güner A, Soyarslan C, Brosius A, Tekkaya AE. Characterization of anisotropy of sheet metals employing inhomogeneous strain fields for Yld2000-2D yield function. Int J Solids Struct 2012; 49:3517–3527. doi:10.1016/j.ijsolstr.2012.05.001

[36] Kim J-H, Barlat F, Pierron F, Lee M-G. Determination of Anisotropic Plastic Constitutive Parameters Using the Virtual Fields Method. Exp Mech 2014; 54:1189–1204. doi:10.1007/s11340-014-9879-x

[37] Ghouati O, Gelin JC. Identification of material parameters directly from metal forming processes. J Mater Process Technol 1998; 80–81:560–564. doi:10.1016/S0924-0136(98)00159-9

[38] Ghouati O, Gelin JC. A finite element-based identification method for complex metallic material behaviours. Comput Mater Sci 2001; 21:57–68. doi:10.1016/S0927-0256(00)00215-9

[39] Marquardt DW. An algorithm for least squares estimation of non-linear parameters. J Soc Ind Appl Math 1963; 11:431–441. doi:10.1137/0111030

[40] Güner A, Yin Q, Soyarslan C, Brosius A, Tekkaya AE. Inverse method for identification of initial yield locus of sheet metals utilizing inhomogeneous deformation fields. Int J Mater Form 2011; 4:121–128. doi:10.1007/s12289-010-1009-4

[41] Oliveira MC, Alves JL, Menezes LF. Algorithms and strategies for treatment of large deformation frictional contact in the numerical simulation of deep drawing process. Arch Comput Method Eng 2008; 15:113–162. doi:10.1007/s11831-008-9018-x

[42] Hosford WF. A generalized isotropic yield criterion. J Appl Mech -T ASME 1972; 39:607–9. doi:10.1115/1.3422732

[43] Drucker DC. Relation of experiments to mathematical theories of plasticity. J Appl Mech -T

ASME 1949; 16:349–357.
[44] Prates PA, Oliveira MC, Fernandes JV. On the equivalence between sets of parameters of the yield criterion and the isotropic and kinematic hardening laws. Inter J Mater Form 2014; 1–11. doi:10.1007/s12289-014-1173-z
[45] Chaparro BM. Comportamento plástico de materiais metálicos: identificação e optimização de parâmetros. PhD Thesis (in Portuguese). University of Coimbra; 2006.
[46] Barlat F, Aretz H, Yoon JW, Karabin ME, Brem JC, Dick RE. Linear transformation-based anisotropic yield function. Int J Plast 2005; 21:1009–1039. doi:10.1016/j.ijplas.2004.06.004

(Page intentionally left blank)

4.5. On the identification of kinematic hardening with reverse shear test

This subchapter presents the paper "On the identification of kinematic hardening with reverse shear test", published in Engineering with Computers, of which I am the second author. This work outlines an inverse analysis methodology for determining the parameters of the kinematic law of metal sheets, using a reverse shear test. The methodology uses a cost-function based on the load versus displacement curves. A notched sample is proposed in order to allow an easy and suitable numerical representation of the boundary conditions of the shear experimental test, by avoiding plastic deformation under the grips. This strategy can be used to complement the parameters identification retrieved from the single biaxial tensile test of the cruciform sample, which does not allow loading path reversal.

(Page intentionally left blank)

Engineering with Computers
DOI 10.1007/s00366-014-0369-7

ORIGINAL ARTICLE

On the identification of kinematic hardening with reverse shear test

A. F. G. Pereira · P. A. Prates · N. A. Sakharova · M. C. Oliveira · J. V. Fernandes

Received: 24 April 2014 / Accepted: 21 June 2014

Abstract An inverse analysis methodology for determining the parameters of the kinematic law of sheet metals is proposed. The sensitivity of the load versus displacement curves, obtained by reverse shear tests of rectangular and notched specimens, to the kinematic law parameters are studied following a forward analysis, based on finite element simulations. Afterwards, an inverse analysis methodology using a gradient-based Levenberg–Marquardt method is established, by evaluating the relative difference between numerical and experimental results of the shear test, i.e. the load evolution in function of the displacements of the grips. The use of a notched specimen is proposed in order to allow an easy and suitable numerical representation of the boundary conditions of the shear experimental test. This methodology has proven to be appropriate for determining the parameters of the kinematic hardening law.

Keywords Reverse shear test · Kinematic hardening · Inverse analysis · Parameters identification

1 Introduction

The mechanical behaviour of metal sheets is usually described by constitutive equations that allow the approximate representation of experimental tests. This behaviour is often described by a law of elasticity, the generalized Hooke's law, and for the plastic behaviour, by a yield criterion and an isotropic hardening law, which is generally suitable for the deep drawing of components with simple geometries and requirements. The production of components with complex geometries and tight requirements that imposes successive changes of strain path (multi-stage stamping, etc.) requires the accurate characterization of the material behaviour. Under these conditions, additional characterization using a kinematic hardening law, which describes the material behaviour under reverse strain path, is required.

Mechanical tests with reverse strain path are used to identify the parameters of the kinematic law of metal sheets [1–4], which characterizes the Bauschinger effect of the material. The shear test is widely used for this identification [1, 5], since it allows characterizing the behaviour of the material up to large plastic deformations under forward and reverse paths, which cannot be achieved in tensile testing of sheet metals, for example. Different geometries of the shear specimens were suggested [6, 7]. In short, the shear specimens can have a rectangular shape, and be clamped by fixed and moving grips [6], or two symmetrical rectangular shear zones, and be acted by axial and lateral loads through an inner and two outer grips to equilibrate each other [7]. The determination of the shear stress–shear strain curve is not always properly achieved. This is mainly due to the heterogeneity of the strain and stress fields, namely due to the end effects and the occurrence of plastic deformation in the regions of the specimens under the grips [5]. The occurrence of heterogeneous deformation, on a greater or lesser degree, leads to inaccuracies in determining the average shear stress and strain. To overcome some of these problems it is recommended to use specimens with appropriate dimensions and measuring the local shear strain using digital image correlation

A. F. G. Pereira (✉) · P. A. Prates · N. A. Sakharova · M. C. Oliveira · J. V. Fernandes
CEMUC, Department of Mechanical Engineering, University of Coimbra, Polo II, Rua Luís Reis Santos, Pinhal de Marrocos, 3030-788 Coimbra, Portugal
e-mail: andre.pereira@dem.uc.pt

Published online: 18 July 2014

technique, alternatively to the use of the displacement of the moving grip [5].

Traditional methodologies for identifying parameters of constitutive laws make use of stress–strain curves. In case of the kinematic hardening parameters, the required plot of the shear stress–shear strain curves usually brings difficulties related to the lack of deformation homogeneity. In this context, this work tries to overcome the difficulties involved in the analysis of the shear tests. The current approach aims to be simple and accurate, from an experimental point of view, since it uses load–displacement curves instead of stress–strain curves. The method is based in an inverse analysis methodology making use of numerical and experimental results of load–displacement curves for determining the hardening parameters, with emphasis on kinematic hardening. Moreover, a notched shear specimen is suggested as alternative, to ensure that the experimental boundary conditions are well represented numerically, since the plastic deformed region is confined to the notch. On the contrary, the classical specimen has tendency to plastically deform also under the grips [5].

2 Numerical model

Two shear specimen geometries are used, one with a constant thickness as proposed by G'Sell and co-authors [6] referred to herein as classical specimen, and the other with a cylindrical notch along the axis of the specimen, the notched specimen. The initial dimensions of the gauge zone of both specimens are shown in Fig. 1a. The notched specimen allows confining the plastic deformation inside the notch, as show in Fig. 1b, and so the experimental boundary conditions can be well represented numerically. Moreover, as this specimen does not plastically deform near the lateral boundaries (Fig. 1b), it certainly prevents premature rupture near the grips, as mentioned by Bouvier and co-authors [5] for experimental cases of the classical

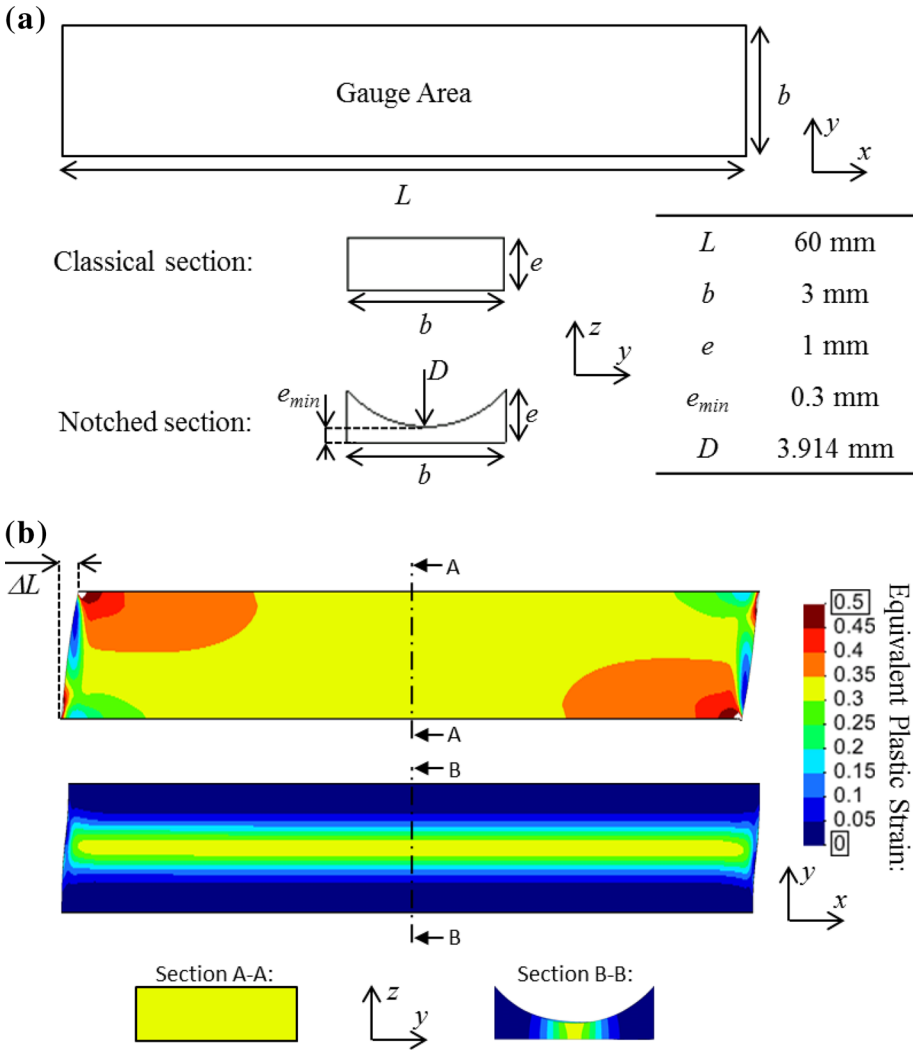

Fig. 1 **a** Schematic representation of the initial geometry and dimensions of the classical and notched specimens: L, b, e, e_{min} and D are the length, width, thickness, minimum thickness and diameter of the cylindrical notch, respectively. **b** Equivalent plastic strain in the specimens for a displacement, ΔL, such that the equivalent plastic deformation in the centre of the specimens is equal to 0.3 [case of an isotropic material with values of yield stress equal to 100 MPa and strain hardening coefficient equal to 0.25 (Swift law)]

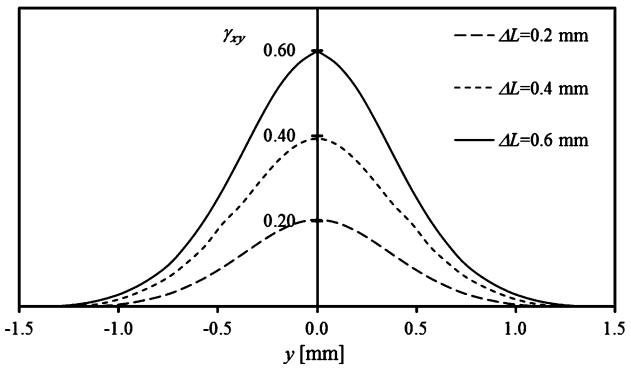

Fig. 2 Shear strain distribution along the 0y axis (Fig. 1), on the curved surface of the notched specimen, during the forward path, for ΔL equal to 0.2, 0.4 and 0.6 mm (isotropic material)

specimen. In this case, plastic deformation occurs along the entire gauge section (Fig. 1b) and, for experimental samples, spreads up to the interior of the clamping region of the specimen [5]. The optimization of the notch geometry was carried out in order to obtain a smooth evolution of the shear strain, γ_{xy}, from the periphery to the centre of the notch. Figure 2 shows examples of the shear strain distribution during the forward path, for the case of an isotropic material with values of yield stress equal to 100 MPa and strain hardening coefficient equal to 0.25 (Swift law).

The numerical model only takes into account the gauge region of the shear specimens, as shown in Fig. 1. The numerical simulations are performed by imposing a null displacement in all directions on one of the lateral surfaces of the specimen while on the other surface a displacement along the length direction (0x in Fig. 1) is imposed, with null displacements along the remaining directions. The simulations were carried out with the finite element implicit program DD3IMP (Deep Drawing 3D Implicit Code) using hexahedral tri-linear solid elements with eight nodes, combined with a selective reduced integration technique [8].

The finite element mesh was optimized in both specimens such that a minimum number of elements can provide accurate representations of the evolution of the strain and the applied load as a function of the displacement, ΔL (Fig. 1). To describe the strain heterogeneities due to the free end effects, the mesh is refined at the extremities of both specimens. Figure 3 shows a schematic representation of the numerical specimens, classical and notched, stating the number of elements (NE) in each distinct region of the specimens.

The constitutive model adopted for the forward and reverse analyses assumes: (1) the isotropic elastic behaviour defined by the generalized Hooke's law; (2) the plastic behaviour described by the orthotropic Hill'48 yield criterion [9]; the mixed hardening model using Swift isotropic [10] and Lemaître and Chaboche [11] kinematic hardening laws.

The Hill'48 yield surface is described by the equation:

$$F\left(\Sigma_{yy}-\Sigma_{zz}\right)^2+G\left(\Sigma_{zz}-\Sigma_{xx}\right)^2+H\left(\Sigma_{xx}-\Sigma_{yy}\right)^2 +2L\Sigma_{yz}^2+2M\Sigma_{xz}^2+2N\Sigma_{xy}^2=Y^2, \quad (1)$$

where F, G, H, L, M and N are the anisotropy parameters; Σ_{xx}, Σ_{yy}, Σ_{zz}, Σ_{xy}, Σ_{xz} and Σ_{yz} are the components of the effective stress tensor, $\boldsymbol{\Sigma}$, defined in the sheet frame of orthotropy and equal to $\boldsymbol{\sigma}' - \mathrm{X}'$ ($\boldsymbol{\sigma}'$ and X' are the deviatoric Cauchy stress tensor and the deviatoric back-stress tensor, respectively); Y represents the yield stress and its evolution during deformation $Y = Y(\bar{\varepsilon}^{\mathrm{p}})$, which is described by Swift isotropic hardening law:

$$Y = C(\varepsilon_0 + \bar{\varepsilon}^{\mathrm{p}})^n, \quad (2)$$

where $\bar{\varepsilon}^{\mathrm{p}}$ is the equivalent plastic strain and C, ε_0 and n are material parameters. The initial yield stress, Y_0, can be written as a function of C, ε_0 and n, as follows $Y_0 = C(\varepsilon_0)^n$.

The translational velocity of the yield surface centre, $\mathbf{X}'$, is defined by the Lemaître and Chaboche kinematic hardening law:

$$\dot{\mathbf{X}}' = C_X\left[X_{\mathrm{Sat}}\frac{\boldsymbol{\sigma}'-\mathbf{X}'}{\overline{\sigma}}-\mathbf{X}'\right]\dot{\bar{\varepsilon}}^{\mathrm{p}}, \quad (3)$$

where $\dot{\bar{\varepsilon}}^{\mathrm{p}}$ is the equivalent plastic strain rate and C_{X} and X_{Sat} are the kinematic hardening parameters, representing,

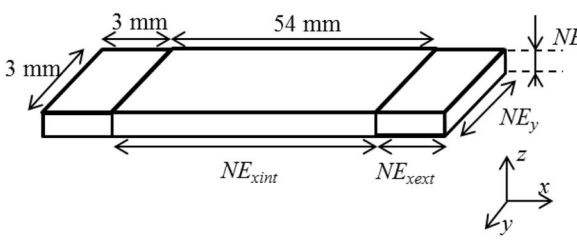

Fig. 3 Schematic representation of the number of elements in different regions and along the 0x, 0y and 0z directions, for both specimens

Specimen	Classical	Notched
NE_{xint} [Elements]	108	2
NE_{xext} [Elements]	18	15
NE_y [Elements]	18	32
NE_z [Elements]	2	5

respectively, the rate of saturation and the saturation value of the equivalent back-stress, $\bar{X}$, which is given by [12]:

$$\bar{X} = X_{Sat}[1 - \exp(-C_X \bar{\varepsilon}^p)]. \quad (4)$$

3 Identification strategy

The proposed methodology for the identification of the hardening parameters consists on using the experimental and numerical load, P, versus displacement, ΔL, curves, and the Levenberg–Marquardt optimization method for minimizing the difference between both curves. The proposed methodology performs the simultaneous identification of the parameters of the hardening laws, although this work is focused on the kinematic hardening parameters. A forward analysis was performed using finite element simulation results of the reverse shear test, in order to study the sensitivity of the results to variations of the hardening laws parameters, revealed by the load evolution during the test. This forward study allowed the developing of an inverse analysis methodology, for identifying the hardening parameters.

3.1 Forward analysis

The forward study is focused on the analysis of the load, P, versus displacement, ΔL, curves after the reverse strain path at several shear strain values, $\gamma_{xy} = 0.20$, 0.40 and 0.60 (in case of the notched specimen, these values correspond to the shear strain at the centre of the specimen). Different sets of parameters of the isotropic and kinematic hardening laws were used, such that the behaviour in the forward strain path is as similar as possible for all sets of parameters, as exemplified in Fig. 4. Table 1 summarizes the parameters of the hardening laws of illustrative cases of materials studied. Since this work is focused on identifying

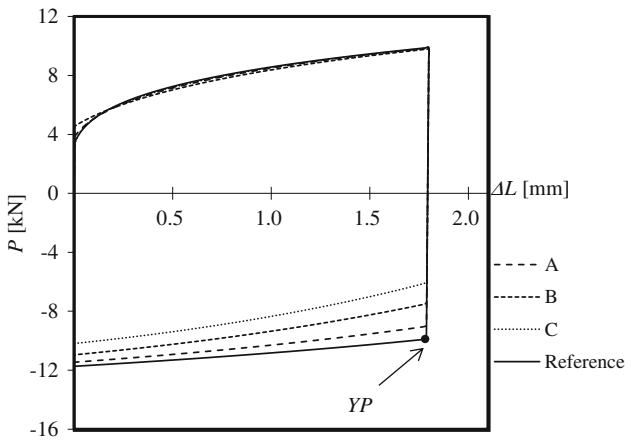

Fig. 4 Example of P versus ΔL curves in forward and reverse strain path, for the classical specimen and for the Reference and Group 1 materials (see Table 1). YP is the yield point after strain path reversal

the kinematical hardening law parameters, a material with pure isotropic hardening is denoted as "Reference". The remaining materials can be separated into two groups: Group 1 with C_X fixed (equal to 3) and X_{Sat} variable and Group 2 with X_{Sat} fixed (equal to 30 MPa) and C_X variable. All materials are isotropic according to von Mises yield criterion and have the Young modulus equal to 210 GPa and the Poisson ratio equal to 0.3.

Figure 5 shows the P versus ΔL curves, after the reversion at a value of shear strain, $\gamma_{xy} = 0.60$, for the materials in Table 1 and both specimens, classical and notched. For C_X fixed and equal to 3 (Fig. 5a, b concerning materials of Group 1 of Table 1), the larger the value of X_{Sat} the lower is the absolute value of the load at the beginning of the plastic deformation under reverse strain path. When the deformation in the reverse path continues, all the curves tend to approach the reference curve. For X_{Sat} fixed and equal to 30 MPa (Fig. 5c, d concerning materials of Group 2 of Table 1), the increase of C_X reduces the absolute value of the load to which the plastic deformation starts, after strain path reversal, and simultaneously increases the rate of approach to the reference material curve. Figure 5 also shows that the curves under reverse strain path are more distinct in the region at the beginning of plastic deformation than at the end of the reverse path ($\Delta L = 0$ mm). This is particularly clear for material G (with high value of C_X) in Fig. 5c, d, whose curves quickly approaches the reference curve.

In order to understand the influence of the strain value at the moment of the strain path reversal, this study was also performed at shear strains reversions of $\gamma_{xy} = 0.20$ and 0.40. The results are systematized in Fig. 6 using two parameters: (1) the relative difference in load at the yield point, YP (see Fig. 4), between the load values under reverse strain path for a given material and the reference material; (2) the relative difference in slope at the beginning of plastic deformation (defined as the linear slope measured between the YP point and the point of the curve under reverse strain path placed at 80 % of the maximum displacement during the forward path), which represents the relative difference between the slope for a given material and the slope for the reference material. Figure 6 shows that the relative differences, in load and slope, increase when the value of the reverse strain increases, and are similar for both specimens, classical and notched. The only exception to this behaviour concerns material G, in case of classical specimen, for which the relative difference in slope decreases for reverse shear strain values, γ_{xy}, from 0.20 to 0.60. Moreover, both relative differences tend to saturate with the increase of the value of reverse shear strain up to 0.60.

The forward analysis enables understanding the trends required for developing the inverse analysis strategy for

Table 1 Parameters of the isotropic and kinematic hardening laws of the materials used in the forward analysis

	Material Reference	Y_0 (MPa) 100.0	ε_0 0.0050	C (MPa) 376.1	n 0.250	C_X 0	X_{Sat} (MPa) 0
Group 1	A	112.4	0.0097	357.8	0.250	3	20
	B	133.1	0.0304	324.5	0.255	3	55
	C	93.8	0.0017	278.7	0.170	3	90
Group 2	D	96.9	0.0037	357.8	0.233	1	30
	E	118.4	0.0133	348.5	0.250	3	30
	F	118.8	0.0206	344.4	0.274	10	30
	G	89.2	0.0074	345.3	0.276	70	30

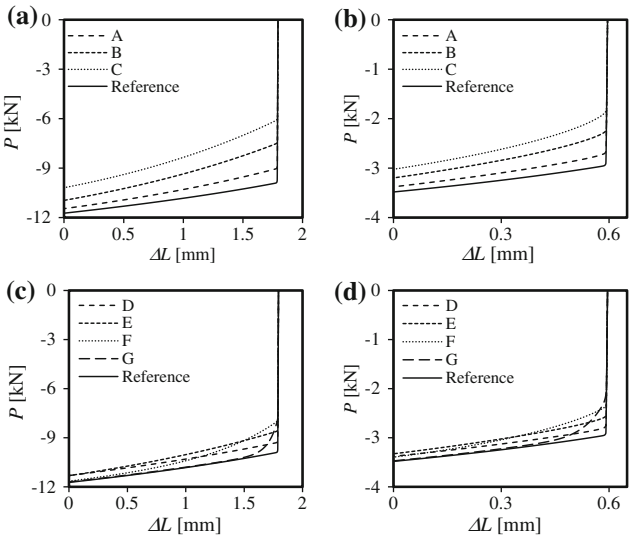

Fig. 5 P versus ΔL curves during the reverse path: (**a**) materials of Group 1 (X_{Sat} variable and $C_X = 3$), classical specimen; (**b**) materials of Group 1 (X_{Sat} variable and $C_X = 3$), notched specimen; (**c**) materials of Group 2 (C_X variable and $X_{Sat} = 30$ MPa), classical specimen; (**d**) materials of Group 2 (C_X variable and $X_{Sat} = 30$ MPa), notched specimen

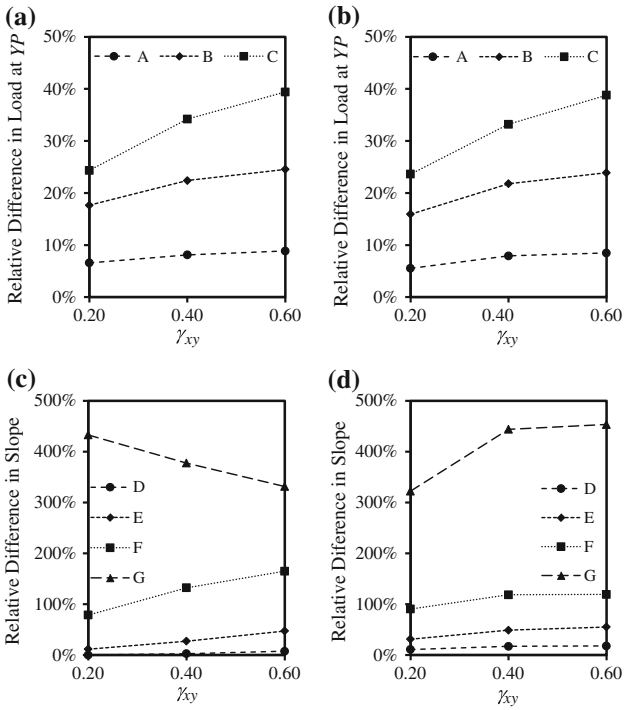

Fig. 6 Sensitivity of X_{Sat} and C_X as a function of reverse shear strain for the materials in Table 1 and both specimens: (**a**) materials of Group 1 (variable X_{Sat}), classical specimen; (**b**) materials of Group 1, notched specimen; (**c**) materials of Group 2 (variable C_X), classical specimen; (**d**) materials of Group 2, notched specimen

identification of the hardening parameters, which allows concluding the following: (1) the sensitivity of the results (P versus ΔL curves) to parameters X_{Sat} and C_X increases with the increase of reverse shear strain, tending to stabilize at shear strain values near 0.60 (only material G with high value of C_X is exception in case of classical specimen); (2) the sensitivity is identical for both types of specimens, classical and notched; (3) in general, the distinguishability of the curves is greater at the beginning of plastic deformation under reverse strain path.

3.2 Inverse analysis strategy

The forward analysis allowed the development of an inverse analysis strategy for identifying simultaneously the parameters of the isotropic and kinematic hardening laws, although the usefulness of this methodology is mainly addressed to the identification parameters of the kinematic hardening law. The following assumptions are taken: (1) the experimental results of the shear test are determined in advanced; (2) the parameters of the anisotropic yield criterion adopted are previously determined; (3) initial estimates of the parameters of the isotropic and kinematic hardening laws are required; (4) the elastic properties of the material are known.

The proposed inverse analysis methodology allows determining the parameters of the Swift isotropic and Lemaître and Chaboche kinematic hardening laws, but certainly can be used for other type of laws. A gradient-based Levenberg–Marquardt method [13] was adopted for

minimizing the difference between numerical and experimental P versus ΔL $F(\mathbf{A})$, is given by:

$$F(\mathbf{A}) = \frac{1}{q}\sum_{i=1}^{q}\left(\frac{P(\Delta L_i)^{\exp} - P(\Delta L_i)^{\text{num}}}{P(\Delta L_i)^{\exp}}\right)^2 + \frac{1}{p}\sum_{i=1}^{p}\left(\frac{P(\Delta L_i)^{\exp} - P(\Delta L_i)^{\text{num}}}{P(\Delta L_i)^{\exp}}\right)^2, \quad (5)$$

where $\mathbf{A} = [X_{\text{Sat}}, C_X, Y_0, C, n]^T$ is the set of parameters to be optimized; q and p are the number of points in the direct and reverse paths, respectively; $P(\Delta L_i)^{\exp}$ and $P(\Delta L_i)^{\text{num}}$ are, respectively, the experimental and numerical values of load for the same displacement ΔL_i. The Levenberg–Marquardt method requires the knowledge of the Jacobian matrix (sensitivity matrix), which is computed after each iteration using a forward finite differentiation approach. A damping factor value is considered and updated inside each iteration [13].

The results of the forward analysis show that the beginning of the curve under reverse strain path is more sensitive to the value of the parameters of the kinematic hardening than the remaining part of the curve. In agreement, the density of points used for the optimization procedure should decrease from the beginning to the end of the reverse path. In the forward path the points can be equally spaced and points within the elastic part are neglected. As it was also mentioned in the forward analysis, the sensitivity of the results (P versus ΔL curves) to parameters X_{Sat} and C_X increases with the increase of reverse shear strain. Accordingly, it is recommended to perform the experimental forward shear test up to high shear strains.

3.3 Inverse analysis: cases study

In order to illustrate the proposed inverse analysis strategy, computer generated P versus ΔL results of four materials were used. These materials have anisotropic behaviour described by Drucker yield criterion extended to orthotropy [14, 15] by means of a linear transformation (Drucker + L), given by:

$$\left[\frac{1}{2}\text{tr}\left((\mathbf{L}:\boldsymbol{\Sigma})^2\right)\right]^3 - c\left[\frac{1}{3}\text{tr}\left((\mathbf{L}:\boldsymbol{\Sigma})^3\right)\right]^2 = 27\left(\frac{Y}{3}\right)^6, \quad (6)$$

where c is a criterion parameter and $\mathbf{L}$ is the linear transformation operator written as:

$$\mathrm{L} = \begin{bmatrix} (C_2+C_3)/3 & -C_3/3 & -C_2/3 & 0 & 0 & 0 \\ -C_3/3 & (C_3+C_1)/3 & -C_1/3 & 0 & 0 & 0 \\ -C_2/3 & -C_1/3 & (C_1+C_2)/3 & 0 & 0 & 0 \\ 0 & 0 & 0 & C_4 & 0 & 0 \\ 0 & 0 & 0 & 0 & C_5 & 0 \\ 0 & 0 & 0 & 0 & 0 & C_6 \end{bmatrix}, \quad (7)$$

where C_1, C_2, C_3, C_4, C_5 and C_6 are the anisotropy parameters. The values of the parameters used are shown in Table 2.

The behaviour of these materials conforms to a mixed hardening model, consisting of Swift isotropic and Lemaître and Chaboche kinematic hardening laws. Table 3 shows the values of the used parameters of the hardening laws, which are such that the behaviour of the four materials is identical under forward strain paths. In this way, it is intended to compare the identification results of materials with identical behaviour in forward strain paths, but with different kinematic hardening.

To make the procedure realistic, the parameters of the Hill'48 yield criterion that best describe the anisotropy of the materials (perfectly described by Drucker + L yield criterion), were identified following the methodology proposed by Prates and co-authors [16] that makes use of a unique cruciform test. The identified parameters of the Hill'48 criterion are shown in Table 4. Simultaneously with the identification of the parameters of the Hill'48 criterion, the parameters of the purely isotropic Swift hardening law, which are herein used as first estimate in the current analysis, were also identified as shown in Table 4. If no identification of the Swift law parameters was previously performed, the first estimate of purely isotropic Swift work-hardening parameters can be obtained adopting typical values for the material under study or using a tensile test with any axis orientation in the sheet plane or even a forward shear test. For all illustrative cases, the initial estimate of the kinematic hardening parameters are X_{Sat} equal to 60 MPa, approximately half of the yield stress of the first estimate of purely isotropic Swift (Table 4), and C_X equal to 10. It was tested that, using different initial sets of parameters, the method converges to similar solutions, i.e. accurately describing the material behaviour. All the materials used in the inverse analysis have the Young modulus equal to 210 GPa and the Poisson ratio equal to 0.3.

Table 2 Parameters of the Drucker + L yield criterion of the materials used in the inverse analysis [16]

c	C_1	C_2	C_3	C_4	C_5	C_6
1.4265	0.6681	0.8158	1.2394	1.0000	1.0000	0.9440

Table 3 Parameters of the isotropic and kinematic hardening laws of the materials used in the inverse analysis

Material	Y_0 (MPa)	ε_0	C (MPa)	n	C_X	X_{Sat} (MPa)
H	106.2	0.0013	413.0	0.205	1.45	116.7
I	121.2	0.0048	473.0	0.255	2.65	30.0
J	138.7	0.0289	440.2	0.326	17.00	60.0
K	105.3	0.0072	465.7	0.301	102.00	38.0

Table 4 Parameters of the Hill'48 yield criterion and the purely isotropic Swift, as previously identified by Prates

F	G	H	L	M	N	Y_0 (MPa)	ε_0	C (MPa)	n
0.1967	0.3210	0.6790	1.5000	1.5000	1.3620	122.2	0.0050	505.7	0.268

As previously mentioned [16], the use of computer generated results instead of experimental ones is a simple and efficient way to test an identification methodology, since the behaviour of the tested material is properly defined, without the errors generally associated with experimental measurements. The disadvantage of this approach is that parameters identification is known to be sensitive to experimental noise, although the load versus displacement results obtained during a shear test are well reproducible and have low sensitivity to noise. Nevertheless, the use of computer generated results allows the suitable comparison between inverse analysis and ''experimental'' results that, for real experimental cases, can only be accessed with resource to other previously proposed methodologies, which are also not free from errors.

The P versus ΔL curves of the four materials are shown in Fig. 7 for both specimens (classical and notched). These curves were obtained for reverse shear strains of approximately 0.30 and 0.60 (in case of notched specimen these values occurs in the centre of the specimen). These strains correspond, respectively, to a maximum displacement of 0.9 and 1.80 mm for the classical specimen, and 0.34 and 0.68 mm for the notched specimen. In case of the classical specimen, the ΔL value that corresponds to a given value of shear strain in the inversion can be estimated as follows: $\Delta L = b\gamma_{xy}$, where b is the specimen's gauge width and γ_{xy} is the shear strain. In case of the notched specimen, the estimate of the ΔL value corresponding to a maximum value of shear strain in the inversion requires another solution, as for example carrying out a numerical simulation of the shear test (using the initial estimate of the constitutive parameters) in the forward path and observe the displacement value for which the desired maximum of the shear strain value occurs.

For minimizing the gap between the material and numerical P versus ΔL curves, using the Levenberg–Marquardt method, 100 points for each of the paths (forward and reverse) are used. The distribution of points along the forward path is uniform along the displacement. For the reverse path, the distribution of points is such that they are almost equally spaced in ΔL values on a logarithmic scale, and so the concentration of points is greater at the beginning of the plastic region. The damping factor is considered equal to 1, for the first simulation and then is divided by 10 inside each iteration, if the cost function value decreases. The minimization procedure stops when the relative difference between a given set of parameters and the next one

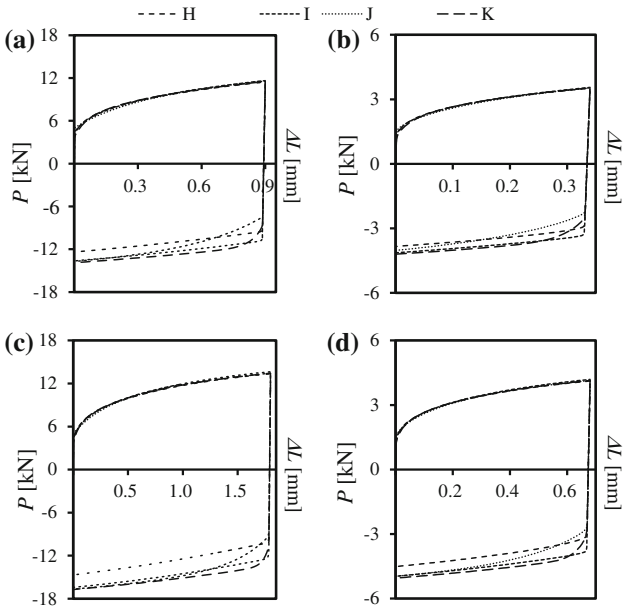

Fig. 7 P versus ΔL curves of the materials in Table 3, for: (**a**) classical specimen and reverse shear strain of 0.30; (**b**) notched specimen and reverse shear strain in the centre of 0.30; (**c**) classical specimen and reverse shear strain of 0.60; (**d**) notched specimen and reverse shear strain in the centre of 0.60

is less than 5 %. In all cases, the final value of the cost function $F(\mathbf{A})$ is less than 4.03×10^{-5} and the last value of the damping factor is close to zero.

The kinematic parameters identified for the different materials with both specimens and for reverse shear strain values of 0.30 and 0.60 are shown in Tables 5, 6, 7 and 8. In order to take a broad understanding of the differences between the material and the identified kinematic hardening laws, Fig. 8 compares both cases, in terms of equivalent back-stress versus the equivalent strain (Eq. 4), for the materials and specimens studied. Based on the results shown in this figure, Fig. 9 plots the absolute error in equivalent back-stress versus the equivalent strain for the identifications with the classical and the notched specimens. It can be concluded that the identifications with both specimens and for the two reverse strain values show quite similar results, with errors always lower than 3 %. For materials with medium/high values of C_X (materials J and K), the absolute error quickly saturates, as show in Fig. 9c, d. For the other materials (materials H and I), the error shows a different trend (see Fig. 9a, b) because the inverse analysis methodology is performed up to reverse strain values that do not attain the back-stress saturation.

Table 5 Identified hardening parameters using the classical specimen and a reverse shear strain value of 0.30

Material	Y_0 (MPa)	ε_0	C (MPa)	n	C_X	X_{Sat} (MPa)	Iterations
H	106.8	0.0013	415.5	0.204	1.82	98.3	7
I	122.2	0.0045	482.9	0.254	3.85	23.7	6
J	140.4	0.0282	444.5	0.323	17.39	61.1	5
K	106.3	0.0073	470.5	0.302	103.66	38.9	7

The number of iterations of the Levenberg–Marquardt method is also indicated

Table 6 Identified hardening parameters using the notched specimen and a reverse shear strain value of 0.30

Material	Y_0 (MPa)	ε_0	C (MPa)	n	C_X	X_{Sat} (MPa)	Iterations
H	107.0	0.0013	415.0	0.203	1.92	92.2	9
I	122.5	0.0045	483.3	0.254	3.75	23.5	7
J	139.6	0.0296	444.3	0.329	17.13	60.7	5
K	106.3	0.0073	471.4	0.303	103.56	38.5	7

The number of iterations of the Levenberg–Marquardt method is also indicated

Table 7 Identified hardening parameters using the classical specimen and a reverse shear strain value of 0.60

Material	Y_0 (MPa)	ε_0	C (MPa)	n	C_X	X_{Sat} (MPa)	Iterations
H	110.0	0.0013	409.9	0.197	1.96	95.4	6
I	121.0	0.0039	480.0	0.248	3.74	27.4	5
J	141.2	0.0309	441.8	0.328	16.99	61.3	4
K	107.3	0.0078	467.0	0.303	103.04	39.8	5

The number of iterations of the Levenberg–Marquardt method is also indicated

Table 8 Identified hardening parameters using the notched specimen and a reverse shear strain value of 0.60

Material	Y_0 (MPa)	ε_0	C (MPa)	n	C_X	X_{Sat} (MPa)	Iterations
H	105.3	0.0012	412.0	0.203	2.14	89.7	6
I	122.0	0.0045	480.3	0.254	4.44	23.2	4
J	141.3	0.0304	442.6	0.327	16.94	60.5	4
K	109.4	0.0079	469.5	0.301	96.99	37.2	5

The number of iterations of the Levenberg–Marquardt method is also indicated

Whatever the case, the use of notched specimens is certainly more suitable for identification, since the boundary conditions of experimental tests can be accurately reproduced numerically. The results also show that a unique shear test with forward and reverse strain path, at a reverse shear strain of about 0.30 or higher, is enough for identifying the kinematic hardening parameters, becoming unnecessary to use several tests at different values of reverse strain as traditionally (see for example [1]). However, since the experimental materials can exhibit dissimilar behaviour along different directions, the use of shear tests is recommend at several angles between the shear direction and the rolling direction (for example: 0, 45 and 90°), but using a unique shear test for each direction.

4 Conclusions

This work allowed the development of an inverse analysis strategy for determining the kinematic hardening parameters, using a unique reverse shear test. The inverse analysis methodology consists of minimizing the gap between experimental and numerical load versus displacement curves by making variations of the constitutive parameters, using the Levenberg–Marquardt method.

The use of the load versus displacement curves instead of stress versus strain curves, as traditionally, avoids the errors in the determination of the stress and strain values that require homogeneity in stress and strain fields in the specimens. Moreover, the use of classical rectangular shear

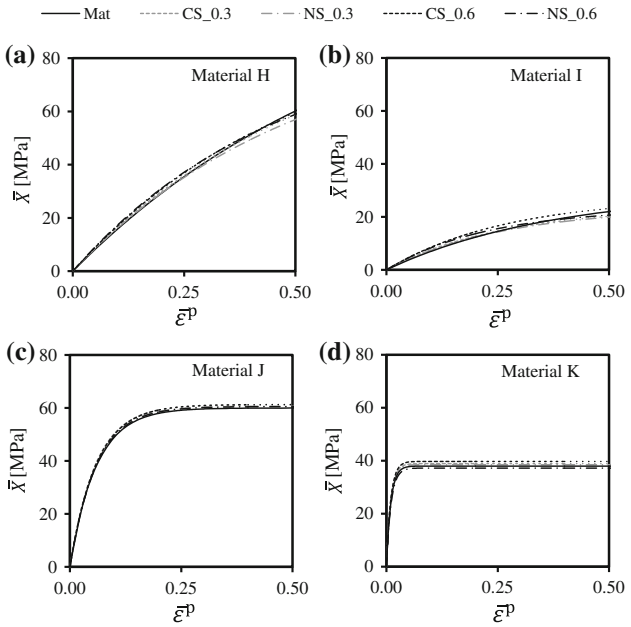

Fig. 8 Equivalent back-stress as a function of the equivalent plastic strain of the studied materials (Mat) and as identified using reverse shear strains of 0.30 and 0.60, with the classical (CS_0.3 and CS_0.6) and notched (NS_0.3 and NS_0.6) specimens, for: (**a**) material H; (**b**) material I; (**c**) material J; (**d**) material K

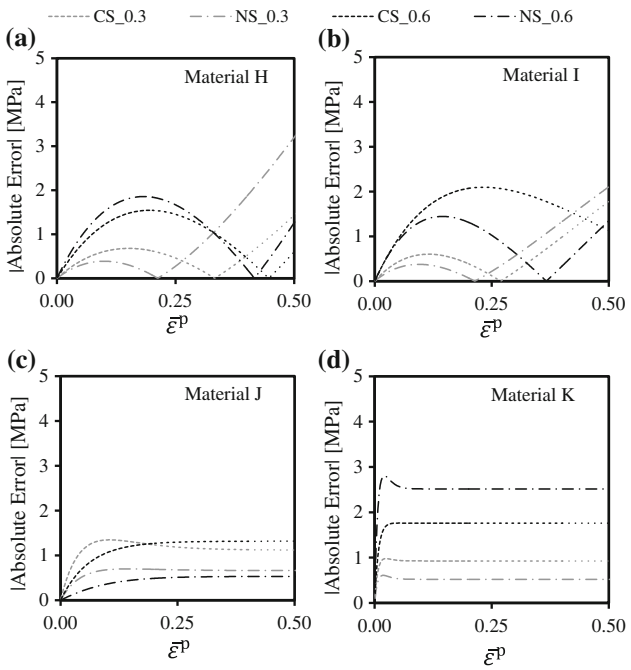

Fig. 9 Absolute error in equivalent back-stress versus equivalent plastic strain, for the identified kinematic hardening laws with a reverse shear strain of 0.30 and 0.60 using the classical (CS_0.3 and CS_0.6) and the notched (NS_0.3 and NS_0.6) specimens, for: (**a**) material H; (**b**) material I; (**c**) material J; (**d**) material K

specimens can induce plastic deformation in the region under the grips, which further prevents the correct determination of load versus displacement curves. In this context, the performances of the rectangular and a new proposed shear specimen, a notched specimen, are compared and it was concluded that in both cases appropriate results were reached. A unique reverse shear test with reversion of 0.30 or higher values of shear strain (maximum shear strain for the notched specimen) are appropriate for the procedure, avoiding the use of several tests at different reverse strain values. Additional studies will focus on experimental validation of the proposed methodology.

Acknowledgments This research work is sponsored by national funds from the Portuguese Foundation for Science and Technology (FCT) via the projects PTDC/EME–TME/113410/2009 and PEst-C/EME/UI0285/2013 and by FEDER—Fundo Europeu de Desenvolvimento Regional funds through the program COMPETE—Programa Operacional Factores de Competitividade, under the project CENTRO-07-0224-FEDER-002001 (MT4MOBI). One of the authors, P.A. Prates, was supported by a grant for scientific research (SFRH/BD/68398/2010) from the FCT. All supports are gratefully acknowledged.

References

1. Chaparro BM, Thuillier S, Menezes LF, Manach PY, Fernandes JV (2008) Material parameters identification: gradient-based, genetic and hybrid optimization algorithms. Comput Mater Sci 44:339–346. doi:10.1016/j.commatsci.2008.03.028
2. Yoshida F, Uemori T, Toropov V (1998) Identification of material parameters in constitutive model for sheet metals from cyclic bending tests. Int J Mech Sci 40:237–249. doi:10.1016/S0020-7403(97)00052-0
3. Yoshida F, Uemori T, Fujiwara K (2002) Elastic–plastic behaviour of steel sheets under in-plane cyclic tension–compression at large strain. Int J Plast 18:633–659. doi:10.1016/S0749-6419(01)00049-3
4. Eggertsen PA, Mattiasson K (2010) An efficient inverse approach for material hardening parameter identification from a three-point bending test. Eng Comp 177:96–103. doi:10.1007/s00366-009-0149-y
5. Bouvier S, Haddadi H, Levée P, Teodosiu C (2006) Simple shear tests: experimental techniques and characterization of the plastic anisotropy of rolled sheets at large strains. J Mater Process Technol 177:96–103. doi:10.1016/j.jmatprotec.2005.09.003
6. G'Sell C, Boni S, Shrivastave S (1983) Application of the plane simple shear test for determination of the plastic behaviour of solid polymers at large strains. J Mater Sci 18:903–918. doi:10.1007/BF00745590
7. Miyauchi K (1984) A proposal of a planar simple shear test in sheet metals. Sci Paper Inst Phys Chem Res 78:27–40
8. Oliveira MC, Alves JL, Menezes LF (2008) Algorithms and strategies for treatment of large deformation frictional contact in the numerical simulation of deep drawing process. Arch Comput Method Eng 15:113–162. doi:10.1007/s11831-008-9018-x
9. Hill R (1948) A theory of yielding and plastic flow of anisotropic metals. Proc R Soc Lond Ser A 193:281–297. doi:10.1098/rspa.1948.0045
10. Swift HW (1952) Plastic instability under plane stress. J Mech Phys Solids 1:1–18. doi:10.1016/0022-5096(52)90002-1

11. Lemaître J, Chaboche J (1990) Mechanics of solid materials. Cambridge University Press, Cambridge
12. Prates PA, Oliveira MC, Fernandes JV (2014) On the equivalence between sets of parameters of the yield criterion and the isotropic and kinematic hardening laws. Inter J Mater Form. doi:10.1007/s12289-014-1173-z
13. Marquardt DW (1963) An algorithm for least-squares estimation of nonlinear parameters. J Soc Ind Appl Math 11:431–441. doi:10.1137/0111030
14. Drucker DC (1949) Relation of experiments to mathematical theories of plasticity. J Appl Mech 16:349–357
15. Cazacu O, Barlat F (2001) Generalization of Drucker's yield criterion to orthotropy. Math Phys Solids 6:613–630. doi:10.1177/108128650100600603
16. Prates PA, Oliveira MC, Fernandes JV (2014) A new strategy for the simultaneous identification of constitutive laws parameters of metal sheets using a single test. Comput Mater Sci 85:102–120. doi:10.1016/j.commatsci.2013.12.043

Chapter 5

Conclusions and Perspectives

This chapter draws the main conclusions from this work as well as the opened perspectives concerning the further refinement and development of inverse strategies for identification of constitutive models parameters of metal sheets.

(Page intentionally left blank)

5.1. Conclusions

This dissertation aims to develop strategies for inverse identification of constitutive models parameters for describing the plastic behaviour of metal sheets. The work was supported by finite element (FE) simulations of two types of tests: the biaxial tensile test of a cruciform sample, for the simultaneous identification of the parameters of yield criteria and of purely isotropic hardening laws, and reverse shear test, for the identifying the parameters of kinematic hardening laws.

The inverse identifications are undertaken by means of successive FE simulations of the experiments and minimisation of the gap between the experimental and numerical results, with resource to sequential or single optimisation procedures. The main stages of this thesis and the main conclusions are next described.

Firstly, a general methodology for equivalence between sets of plastic constitutive parameters is established. This allows the comparison of the parameters obtained using different identification strategies. It is shown that distinct sets of parameters for a given constitutive model can describe the same material behaviour. Besides the intrinsic interest of this equivalence, this methodology has favoured the study and development of the inverse strategies for the constitutive parameters identification.

Two strategies for simultaneously identifying the parameters of the anisotropic yield criteria and isotropic hardening laws of sheet metals are developed. Both strategies aim to be easily implemented of the experimental point of view, simply using results of the load evolution during the test and of the major and minor principal strains distributions, along the axes of the sample, at a given moment of the test. The well-known biaxial tensile test of a cruciform sample was chosen, and the definition of its geometry was performed by means of a numerical study with the purpose of maximising the sensitivity of the test results to the values of the constitutive parameters and for allowing wide range of strain paths, from uniaxial tension to near equibiaxial tension, in the measured region of the sample.

The work was initially addressed for the identification of the parameters of the Hill'48 yield criterion and the Swift hardening law. A simple optimisation procedure was used, i.e. without resorting to the traditional cost functions. The inverse analysis algorithm consists of a sequence of five optimisation steps, each one referring to the optimisation of a unique parameter, in order to obtain a primary solution for the constitutive parameters. This solution can be further enhanced using Levenberg-Marquardt algorithm, for minimising a single cost-function comprising all constitutive parameters and results, i.e. load *versus* displacement and equivalent strain distribution along the axes of the sample at a given moment of the test, although the

primary solution can provide high enough accuracy of the material parameters. The strategy proves to be competitive, when compared with classical strategies. This allowed understanding that a sequential optimisation, once properly elaborated, is clearly advantageous when compared to most commonly inverse identifications, consisting of using a unique cost function including different types of results.

The inverse analysis strategy above mentioned enabled a good understanding of the issues involved, namely concerning to the delineation of the algorithm leading to upper accuracy, which allowed extending the strategy to more complex constitutive models (yield criteria and isotropic hardening laws). Thus, a general inverse identification strategy that sequentially uses three distinct cost functions was developed. It resorts to the Levenberg-Marquardt algorithm for sequential optimisation of the parameters of the yield criteria and isotropic hardening laws. More importantly, this strategy allows the identification of parameters of several yield criteria and hardening laws. It can be used directly for a given criterion or, sequentially, starting from the Hill'48 criterion and then using the Hill'48 solution as an initial estimate for identifying the parameters of other criteria, on the condition that can be converted into the Hill'48 criterion for particular values of the parameters. In the last case, this strategy is detached in two stages and has the advantage of enabling the assessment of the adequacy of a number of constitutive models to describe the experimental results, starting from a simple criterion. The first stage consists of the simultaneous identification of the hardening law (Swift and Voce, in the current work) and Hill'48 yield parameters, using the results of load *versus* displacement and equivalent strain distribution at a given moment of the test. The hardening parameters must be separately identified for the Swift and Voce laws and the one (Swift or Voce) that better describes the results of the cruciform test (if it is possible to distinguish) is selected for further optimisation. The second stage allows extending the parameters identification procedure to more complex yield functions, such as Barlat'91, Karafillis & Boyce and Drucker+L, the cases studied in the current work. This second stage should be performed whenever the identification carried out during the first stage is found not satisfactory enough to capture the experimental strain paths results, along the axes of the sample, which are not considered in minimisation during the first stage. This sequential optimisation procedure is a successful alternative to parameter identification by minimising a single cost function comprising all material parameters and results of different types, as commonly found in the literature. Namely, it is concluded that this last approach can deteriorate the description of the material behaviour, concerning the load *versus* displacement results, and so the parameters and the choice of the hardening law, without apparent improving the description of the results of equivalent strain and strain path distributions.

Finally, an inverse analysis methodology for identifying the parameters of the kinematic hardening law is outlined. This work is complementary to the above

mentioned work. In fact, the full description of plastic behaviour of sheet metals also requires the identification of kinematic hardening parameters. The outlined strategy uses a modified shear sample with a cylindrical notch along the axis of the sample, in order to confine the plastic deformation within the entire gauge section, which is not the case for the classical shear samples with constant thickness. The geometry of the cylindrical notch was defined in order to ensure that all strain values, between the maximum (in the centre of the notch) and the minimum (zero, along the edge of the notch), are equally represented at the moment of the strain path reversing. This geometry allows that the boundary conditions of experimental tests are accurately reproduced numerically and avoids the errors in the determination of the stress *versus* strain curves, used in traditional methodologies, that requires homogeneity in the stress and strain fields of the sample. The inverse analysis methodology consists of minimising the gap between experimental and numerical load *versus* displacement curves by making variations of the constitutive parameters, using the Levenberg-Marquardt algorithm. The forward part of the reverse shear test can also be used for evaluating the information concerning to the parameters of the hardening law of the material obtained from inverse identification based on the biaxial tensile test of the cruciform sample, which does not allow achieving strain values as large as in shear.

5.2. Recommendations and Perspectives

This work contributes to the rise and better definition of few issues that deserve to be further analysed for practical uses and future research. Below, issues that deserve thoughtfulness in the future are suggested.

- The early aim of identifying simultaneously the full set of parameters of constitutive laws from the results of a unique mechanical test, although not a simple task, should not be discarded. Following the results presented in this work, this achievement should be attempted within the context of a test design (sample geometry and loading conditions) that allows strain path changes as close as possible to reversal.
- Regarding the kinematic hardening law, the outlined strategy performs the identification based on the previous knowledge of the parameters of the yield criterion. The joining of the results from the biaxial testing of cruciform samples and reverse shear tests in the same sequence of optimisation should be explored, to improve the results of the full parameters identification; the simultaneous use, in the optimisation procedure, of the results from these two tests allows more adequately considering the high strain values that occur in the shear test.

- The optimisation procedure for the constitutive parameters identification influences the quality of the results, and so it is recommended to give it due attention. In this context, whatever the configuration of the test, it is always important to examine the possibility of resorting to a sequential optimisation procedure.
- The possibility of identifying the parameters of the isotropic hardening law and yield criterion based only on results of load *versus* displacement of the cruciform test should be accomplished. In fact, an exploratory analysis on the influence of the parameters of those laws on the load *versus* displacement results, at three points in the 0x and 0y axes of the sample, promises an adequate identification, at least for simple yield criteria, such as Hill'48.
- In sheet metal forming processes the material flow is governed by the interaction between the plastic behaviour and the friction conditions. In this context, the accurate identification of the plastic behaviour of metal sheets can enable the development of improved identification strategies for friction law parameters, by designing specific tests.
- An accurate robust design approach for characterising the material behaviour of sheet metals and the associated scattering should be envisaged. This will allow the engineer to understand and anticipate problems that may arise in the production line of sheet metal forming components, due to the influence of unavoidable sources of scatter, namely the scatter associated with the material mechanical behaviour.

Appendix

Modelling of the Cruciform Sample

This appendix presents the study of the numerical model of the biaxial tensile test, including the finite element discretisation and geometry of the cruciform sample.

(Page intentionally left blank)

A.1 Introduction

The biaxial tensile test of a cruciform sample was selected to undertake the study on the identification of the parameters of constitutive laws (yield criterion and work-hardening law), allowing multiple strain paths as previously shown [1]. Early in this thesis, the geometry of the cruciform sample was enhanced. Finite Element (FE) simulations were used in order to reproduce, as far as possible: (i) inhomogeneous deformation; (ii) strain paths commonly observed in sheet metal forming processes and (iii) relatively high values of plastic deformation whatever the strain path.

Figure A.1 shows a scheme of the cruciform sample under biaxial tension, exhibiting the geometry with the generic relevant dimensions. The 0x and the 0y axes coincide with the rolling direction (RD) and the transverse direction (TD) of the sheet, respectively. The cruciform sample is submitted to equal displacements in the 0x and 0y directions, applied by the grips, as indicated in Figure A.1 (a); the displacements along the 0x and 0y axes are measured at points A and B, respectively. The relevant dimensions for studying the sample geometry are shown in Figure A.1 (b): (i) L_1 is half of the central area; (ii) L_2 the length of the arms; (iii) R the fillet radius and (iv) β the opening angle of the arms. The sheet thickness considered in this study is equal to 1mm.

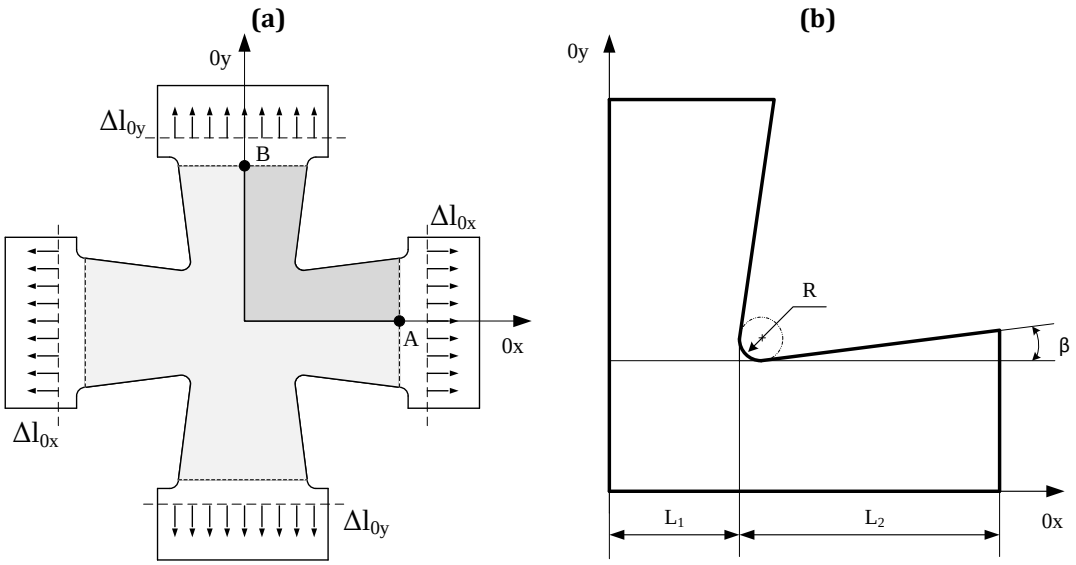

Figure A.1. (a) Schematic representation of the cruciform sample under biaxial tension induced by displacements of the grips, equal for both 0x and 0y axes. It is also shown the gauge area (in grey) and the region of the sample considered for numerical simulation (in dark grey); (b) Geometry and generic dimensions of 1/4 of the cruciform sample.

A.2 FE Discretisation Sensitivity Study

The quality of FE results depends on how truly the numerical model describes the experimental. In the numerical model, the mesh and the type of element define the FE discretisation. This subchapter explores the sensitivity of the numerical model to the FE discretisation. The dimensions of the cruciform sample are: L_1 = 15mm, L_2 = 15mm R = 3mm and β = 0° (Figure A.1 (b)). The model used in the numerical simulations of the biaxial tensile test is only 1/8 of the cruciform sample (as in Figure A.1 (b), but with half-thickness), due to geometrical and material symmetries. The simulations use tri-linear 8-node hexahedral solid elements, with one layer of elements through thickness. In fact, the test is not sensitive to the number of layers through thickness as concluded from a previous study [1]. In order to optimise the finite element size, different discretisations were built taking an average in-plane size of the finite element, e, equal to 1mm, 0.5mm and 0.333mm, designated by Mesh 1, Mesh 0.5 and Mesh 0.333, respectively, as shown in Figure A.2. Table A.1 shows the ratio between the geometric dimensions of the sample and the average in-plane size of the finite element, for the three discretisations.

Table A.2 indicates the material parameters used in this study. The plastic behaviour is described by the Hill'48 yield criterion and the Swift work-hardening law. To simplify, the material is considered isotropic. Three simulations were performed, concerning the discretisations indicated in Table A.1. This study focuses the analysis on:

(i) The evolutions of the load, P, with the sample boundaries displacement, Δl, during the test, for the 0x (or 0y) axis; Δl is measured for points A (or B) in Figure 1;

(ii) The distributions of the equivalent strain, $\bar{\varepsilon}$, along the 0x (or 0y) axis and along the axis at 45° with the rolling direction of the sample (i.e. $\bar{\varepsilon}$ as a function of the distance, d, to the centre of the sample), for a given boundaries displacement, Δl, preceding and close to the displacement at the maximum load; the equivalent strain is determined using the von Mises definition:

$$\bar{\varepsilon} = 2\left[\left(\varepsilon_1^{\,2} + \varepsilon_2^{\,2} + \varepsilon_1\varepsilon_2\right)/3\right]^{1/2}. \tag{A.1}$$

where ε_1 and ε_2 are respectively the major and the minor principal strains, in the sheet plane; ε_1 and ε_2 are parallel and normal to the loading axis under study,

respectively (in the case of the 0x axis, ε_1 is equal to ε_{xx} and ε_2 is equal to ε_{yy}, and in the case of the 0y axis, ε_1 is equal to ε_{yy} and ε_2 is equal to ε_{xx} - see Figure A.1);

(iii) the distributions of the strain path ratio, defined by $\varepsilon_2 / \varepsilon_1$, along the 0x (or 0y) axis for the same value of the boundaries displacement, Δl, as the previously stated in (ii); observations performed during the test, at different values of Δl, showed that the strain paths are quasi strictly linear.

It is worth noting that the strain variables, ε_1 and ε_2, can be experimentally measured, using DIC technique [2], or even the classical Circle Grid Strain analysis [3], which allows establishing the correspondence between the numerical and experimental results for applying the inverse analysis strategy.

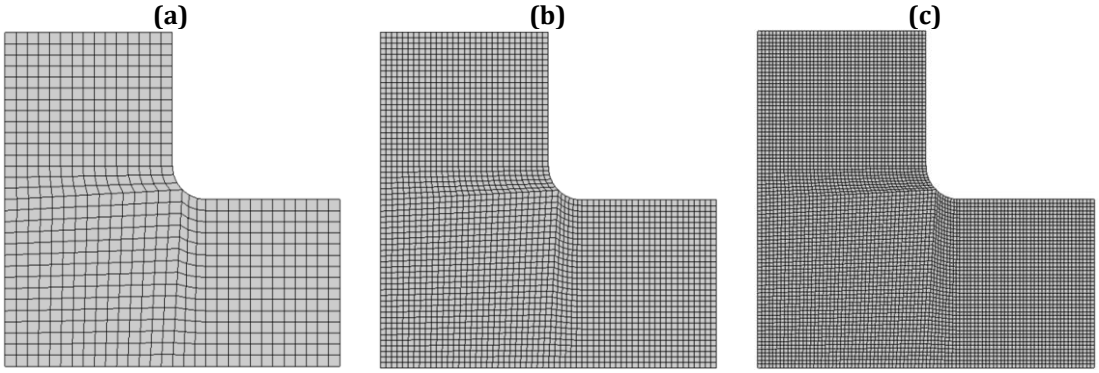

Figure A.2. Finite element discretisations: (a) Mesh 1, (b) Mesh 0.5 and (c) Mesh 0.333.

Table A.1. Ratio between the geometric dimensions of the sample and the average in-plane size of the finite element.

Discretisation	e [mm]	L_1/e	L_2/e	R/e
Mesh 1	1	15	15	3
Mesh 0.5	0.5	30	30	6
Mesh 0.333	0.333	45	45	9

Table A.2. Constitutive parameters used in the numerical simulations for the mesh optimisation of the mechanical model.

Hill'48 Anisotropy Parameters					Swift Hardening Parameters		
F	G	H	$L=M$	N	Y_0 [MPa]	K [MPa]	n
0.5	0.5	0.5	1.5	1.5	100	288.54	0.2

Figure A.3 shows the numerical results for the three discretisations: P *vs.* Δl (Figure A.3 (a)); $\bar{\varepsilon}$ *vs.* d, along the 0x (or 0y) axis (Figure A.3 (b)) and along the axis at 45° with the rolling direction of the sample (Figure A.3 (c)) and $\varepsilon_2 / \varepsilon_1$ *vs.* d, along the

0x (or 0y) axis (Figure A.3 (d)). The results in Figure A.3 (b), (c) and (d) are plotted for Δl = 3mm, i.e. at an instant previous to maximum load. The results concerning the load evolution during the test (Figure A.3 (a)) and the strain path distribution (Figure A.3 (d)) are coincident for the three discretisations, i.e. they do not depend on the finite element size. The equivalent plastic strain distributions are similar for Mesh 0.5 and Mesh 0.333; results from Mesh 1 are also similar to the other discretisations, except in the fillet region, close to d = 22.5mm (Figure A.3 (c)), and in the arms of the sample, for d values near 25mm.

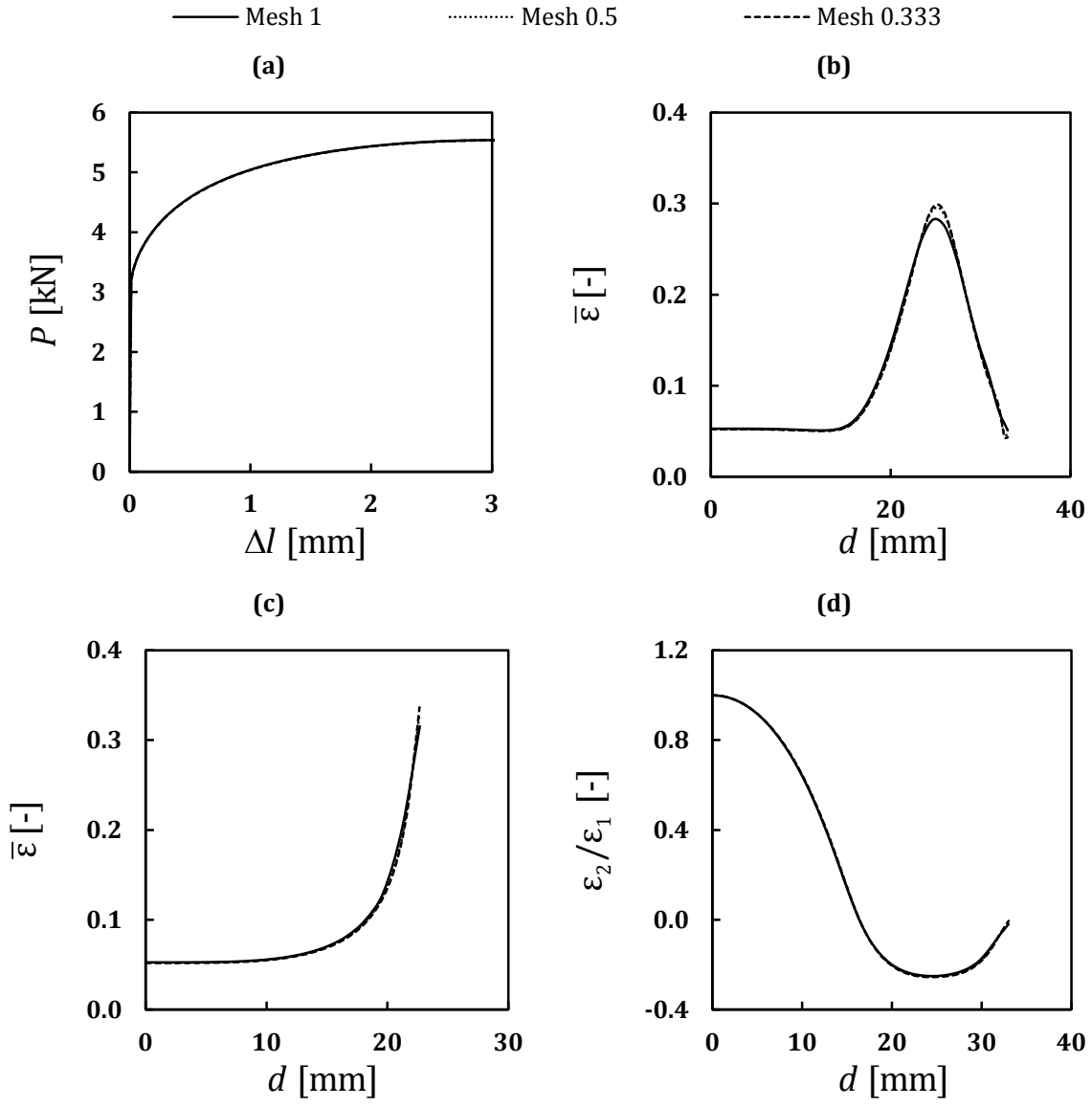

Figure A.3. Numerical simulation results for the discretisations presented in Table A.1: (a) P *vs.* Δl; (b) and (c) $\bar{\varepsilon}$ *vs.* d, along the 0x (or 0y) axis and along the axis at 45° with the rolling direction, respectively, and (d) $\varepsilon_2 / \varepsilon_1$ *vs.* d, along the 0x (or 0y) axis.

Table A.3 shows the computation time and the maximum equivalent strain, in the fillet region and in the arm. The two less refined discretisations (Mesh 1 and Mesh 0.5) display the relative differences (in brackets) with respect to the Mesh 0.333.

Mesh 1 shows the lowest computation time (12 seconds), but is the less accurate in terms of $\overline{\varepsilon}$ values, with relative differences of 6.5% (fillet) and 6.7% (arms) when compared with the most refined mesh (Mesh 0.333), which presents the highest computation time (261 seconds). In this context, Mesh 0.5 was selected for presenting values of $\overline{\varepsilon}$ relatively close to those from Mesh 0.333, with a computation time 79.7% lower than this mesh. Note that the elements in the central region of the Mesh 0.5 are cubic shaped (Figure A.2 (b)).

Table A.3. Computation time and maximum equivalent strain values, in the fillet region and the arms of the sample at Δl = 3mm, for the three meshes.

Discretisation	Computation time (seconds)	$\overline{\varepsilon}$ (maximum in fillet region)	$\overline{\varepsilon}$ (maximum in arm)
Mesh 1	12 (-95.4%)	0.315 (-6.5%)	0.280 (-6.7%)
Mesh 0.5	53 (-79.7%)	0.329 (-2.4%)	0.295 (-1.7%)
Mesh 0.333	261	0.337	0.300

A.3 Geometry Sensitivity Study

This subchapter studies the sensitivity of the cruciform sample geometry to the numerical results of the biaxial tensile test. The ideal geometry for the cruciform sample is that which allows high values of plastic deformation, with the largest deformation gradients and the widest range of strain paths. This study is carried for the geometric parameters: (i) the fillet radius, R, (ii) the L_2/L_1 ratio and (iii) the opening angle of the arms, β (Figure A.1 (b)). Different combinations of these parameters lead to distinct geometries of the cruciform sample and thus distinct results.

A.3.1 Fillet radius

The study on geometry sensitivity is firstly carried out for the fillet radius, R. Three values for the fillet radius were considered: 1mm, 2mm and 3mm; the remaining dimensions of the cruciform sample are L_1 = 15mm, L_2 = 15mm and β = 0°.

Figure A.4 shows the results of the test, for the three values of the fillet radius: P *vs.* Δl (Figure A.4 (a)); $\bar{\varepsilon}$ *vs.* d, along the 0x (or 0y) axis (Figure A.4 (b)) and along the axis at 45° with the rolling direction of the sample (Figure A.4 (c)) and $\varepsilon_2 / \varepsilon_1$ *vs.* d, along the 0x (or 0y) axis (Figure A.4 (d)). Figure A.5 shows the equivalent plastic strain fields on the surface of the cruciform samples. The results in Figures A.4 (b), (c) and (d) and Figure A.5 are plotted for Δl = 3mm, at an instant previous to the maximum load.

The influence of the dimension of the fillet radius on the numerical results of the cruciform test can be summarised:

(i) The load evolution is slightly influenced by the value of fillet radius, since the curves are close to each other (Figure A.4 (a)).

(ii) The equivalent plastic strain values decrease with the increasing of the fillet radius value, for d values between 0mm and 23mm (Figure A.4 (b)). The opposite occurs for d values higher than 23mm.

(iii) A lower fillet radius leads to higher strain values in the fillet region. The further away from the fillet, smaller the difference between the equivalent strain values (Figure A.4 (c)).

(iv) The range of strain paths along the 0x (or 0y) axis are similar for all cases (Figure A.4 (d)), with $\varepsilon_2 / \varepsilon_1$ ranges from 1.0 (at the centre of the cruciform sample) to approximately -0.29, -0.27 and -0.25, in for R = 1mm, 2mm and 3mm, respectively.

(v) The maximum strain value in the arms of the sample is correlated with the maximum strain value achieved in the fillet region: the smaller the latter, the higher is the maximum equivalent strain value on the axis of the sample in the arms region (Figure A.5).

Based on the results shown in Figure A.4 and Figure A.5, the fillet radius equal to 3mm was chosen, since it avoids high strain values in the fillet region. Also the homogeneity of deformation perpendicularly to the axes of the sample, near these axes, encourages this choice.

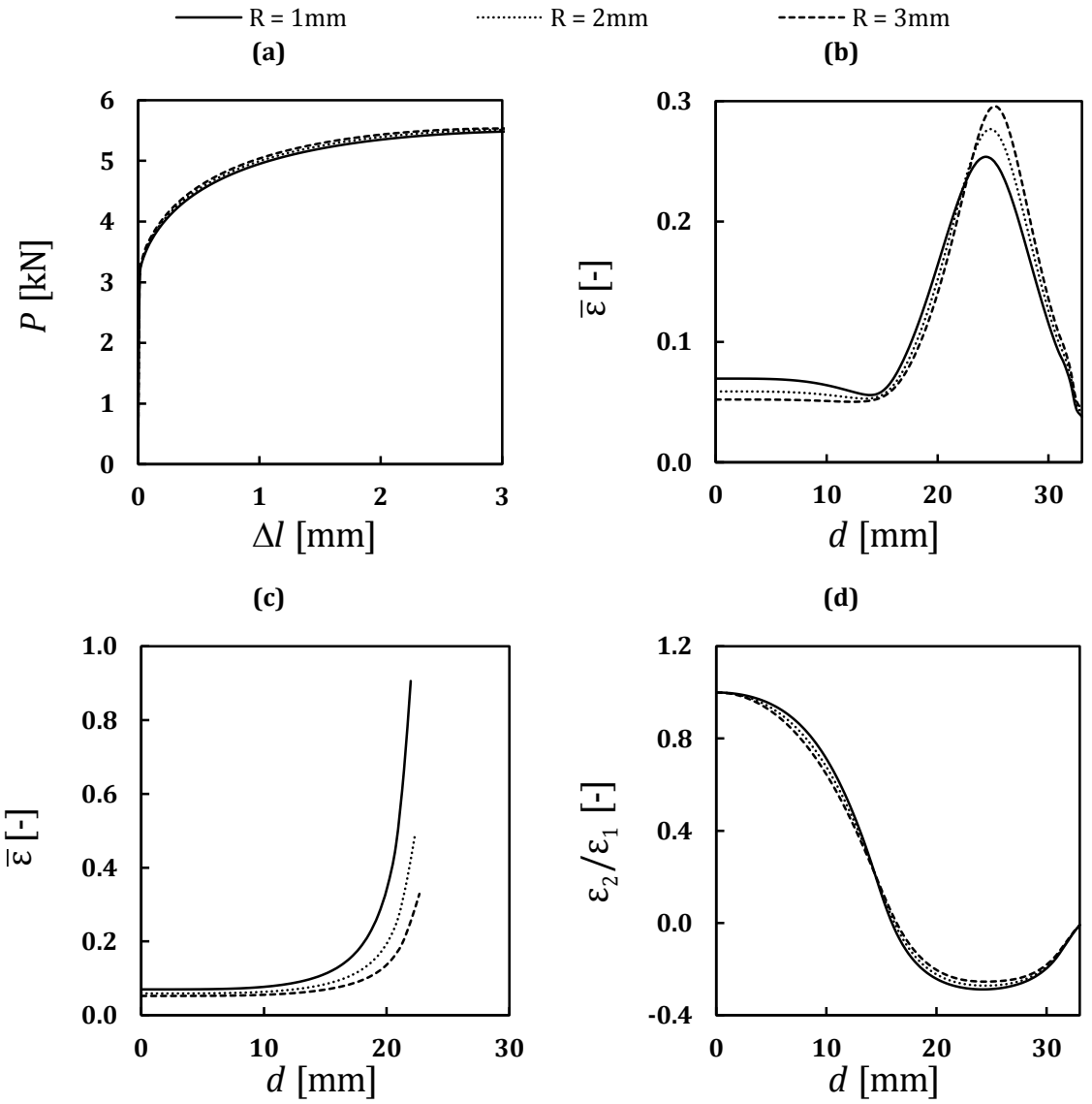

Figure A.4. Numerical simulation results for the fillet radii, R = 1mm, R = 2mm and R = 3mm: (a) P vs. Δl; (b) and (c) $\bar{\varepsilon}$ vs. d, along the 0x (or 0y) axis and along the axis at 45° with the rolling direction, respectively, and (d) $\varepsilon_2 / \varepsilon_1$ vs. d, along the 0x (or 0y) axis.

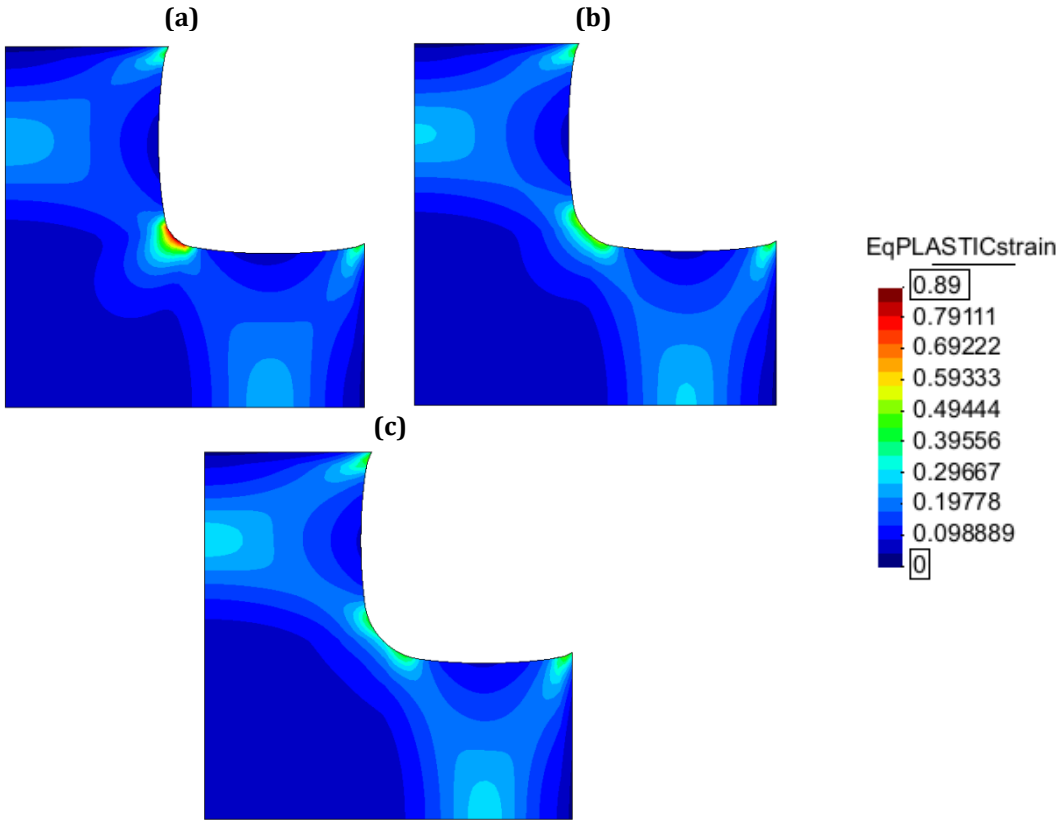

Figure A.5. Equivalent plastic strain fields measured on the surface of the cruciform sample, for the fillet radii: (a) 1mm, (b) 2mm and (c) 3mm.

A.3.2 L_2/L_1 ratio

The geometry sensitivity study is now performed for the L_2/L_1 ratio. In this context, the three values for the L_2/L_1 ratio under study are 1.0, 2.2 and 4.4. The remaining dimensions of the cruciform sample are R = 3mm, L_1 = 15mm, β = 0°, and L_2 = 15mm, 33mm and 66mm, for increasing values of the L_2/L_1 ratio: L_2/L_1 equal to 1.0, 2.2 and 4.4, respectively. Figure A.6 shows the numerical results of the test, for the three values of the L_2/L_1 ratio: P *vs.* Δl (Figure A.6 (a)); $\bar{\varepsilon}$ *vs.* d, along the 0x (or 0y) axis (Figure A.6 (b)) and along the axis at 45° with the rolling direction of the sample (Figure A.6 (c)) and $\varepsilon_2/\varepsilon_1$ *vs.* d, along the 0x (or 0y) axis (Figure A.6 (d)). Figure A.7 shows the equivalent plastic strain fields on the surface of the cruciform sample. The results in Figures A.6 (b), (c) and (d) and Figure A.7 are plotted for an instant immediately before maximum load (Δl = 3mm, 6mm and 11mm, for L_2/L_1 values equal to 1.0, 2.2 and 4.4, respectively).

The influence of L_2/L_1 ratio on the numerical results of the cruciform test can be summarised:

(i) The Δl value corresponding to the maximum load value increases with the increasing of the L_2/L_1 ratio (Figure A.6 (a)). Moreover, the maximum load value decreases with the increasing of the L2/L1 ratio.

(ii) The equivalent strain distribution along the 0x (or 0y) axis becomes smoother with the increase of the L_2/L_1 ratio (Figure A.6 (b) and Figure A.7). The maximum equivalent strain and the equivalent strain values at the centre of the cruciform sample decrease with the increasing of the L_2/L_1 ratio.

(iii) The equivalent strain values near the fillet of the sample are sensitive to changes in the L_2/L_1 ratio, with the lower L_2/L_1 ratio leading to higher values of equivalent strain (Figure A.6 (c) and Figure A.7). The further away from the fillet, the smaller the difference between the equivalent strain values.

(iv) The increase of the L_2/L_1 ratio is related with a wider range of strain paths, from equibiaxial tension to near-uniaxial tension (Figure A.6 (d)). The lowest $\varepsilon_2/\varepsilon_1$ values are -0.25, -0.48 and -0.50, for the cases of L_2/L_1 = 1.0, 2.2 and 3.3, respectively (in isotropy, the $\varepsilon_2/\varepsilon_1$ value in uniaxial tension is -0.5); the largest strain paths difference occurs between the cases L_2/L_1 = 1.0 and L_2/L_1 = 2.2.

Based on the results shown in Figure A.6 and Figure A.7, the L_2/L_1 ratio equal to 2.2 (i.e. L_1 = 15mm and L_2 = 33mm) was selected for the cruciform geometry. It allows: (i) a more convenient evolution of the equivalent strain along the axes of the sample than those from the remaining conditions studied; (ii) strain paths from very close to the uniaxial tension ($\varepsilon_2/\varepsilon_1$ = -0.48) up to biaxial symmetrical ($\varepsilon_2/\varepsilon_1$ = 1); (iii) relatively low strain values in the fillet region; and (iv) homogeneity of deformation perpendicularly to the axes of the sample, near these axes.

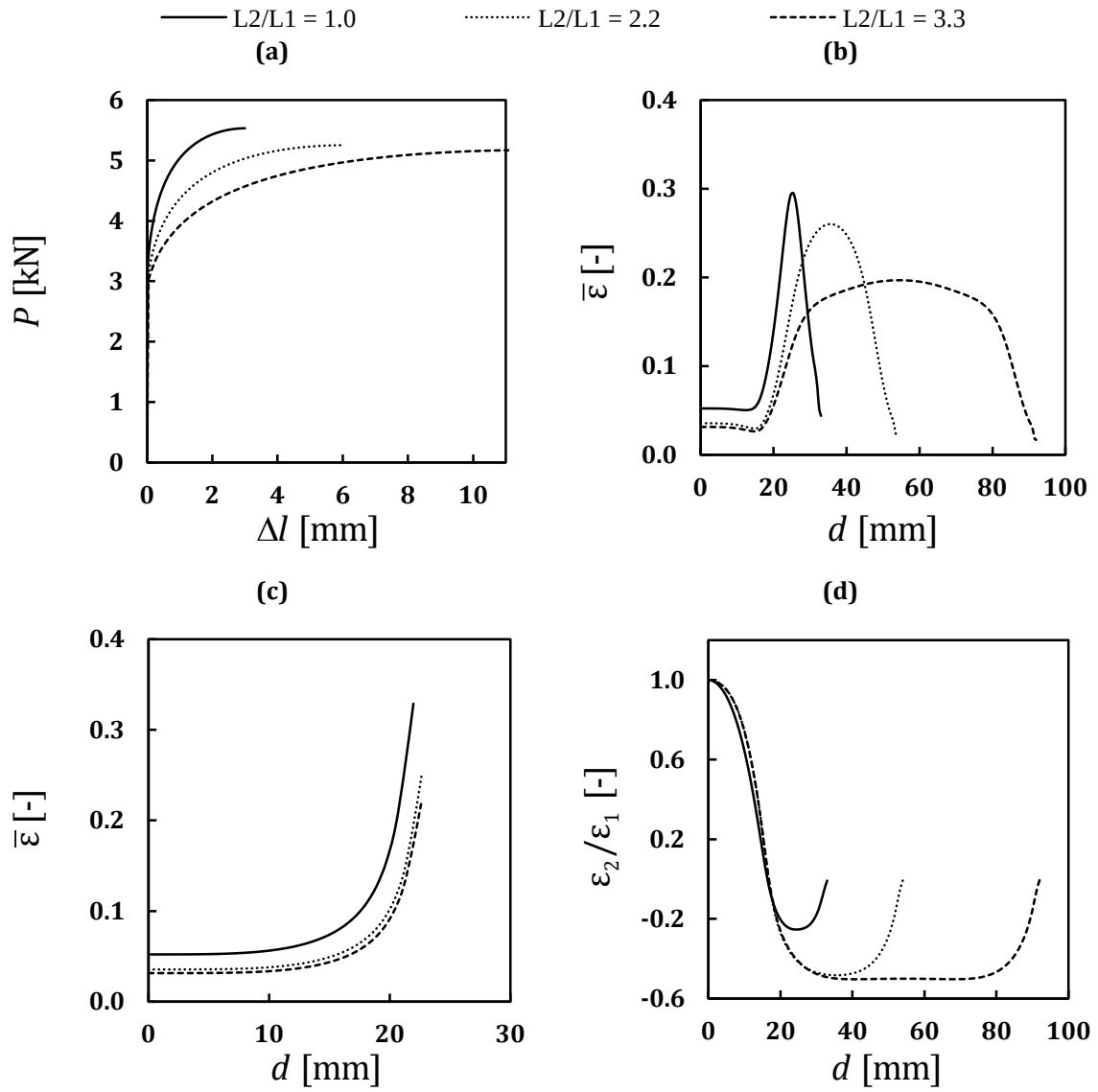

Figure A.6. Numerical simulation results for the L_2/L_1 values, $L_2/L_1 = 1.0$, $L_2/L_1 = 2.2$ and $L_2/L_1 = 3.3$: (a) P *vs.* Δl; (b) and (c) $\bar{\varepsilon}$ *vs.* d, along the 0x (or 0y) axis and along the axis at 45° with the rolling direction, respectively, and (d) $\varepsilon_2 / \varepsilon_1$ *vs.* d, along the 0x (or 0y) axis.

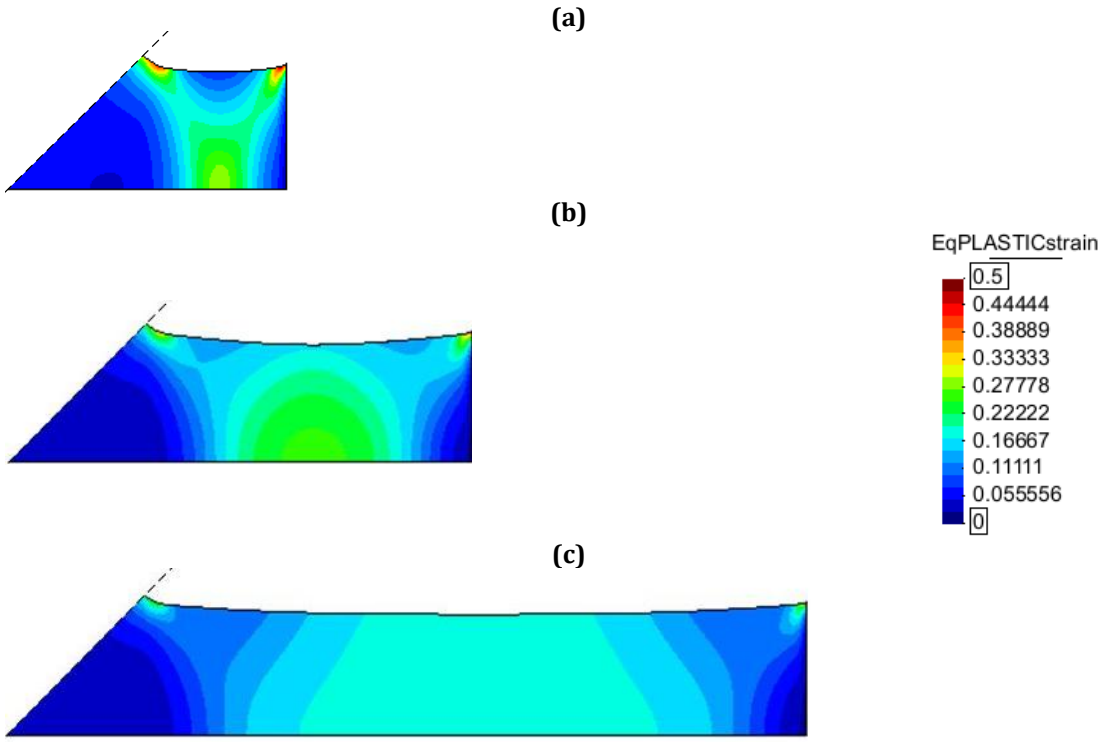

Figure A.7. Equivalent plastic strain fields measured on the surface of the cruciform sample, for L_2/L_1 values: (a) 1.0, (b) 2.2 and (c) 3.3. The dashed line indicates the material and geometric symmetry axes.

A.3.3 Opening angle of the arms, β

Lastly, the geometry sensitivity study is performed for the opening angle of the arms, β. Three values for β were considered: 3°, 6° and 9°. The remaining dimensions of the cruciform sample are R = 3mm, L_1 = 15mm and L_2 = 33mm. Figure A.8 shows the numerical results of the test, for the three values of β: P *vs.* Δl (see Figure A.8 (a)); $\bar{\varepsilon}$ *vs.* d, along the 0x (or 0y) axis (see Figure A.8 (b)) and along the axis at 45° with the rolling direction of the sample (see Figure A.8 (c)) and $\varepsilon_2 / \varepsilon_1$ *vs.* d, along the 0x (or 0y) axis (see Figure A.8 (d)). Figure A.9 shows equivalent plastic strain fields in the surface of the cruciform samples. The results in Figures A.8 (b), (c) and (d) and Figure A.9 are plotted for an instant immediately before maximum load (Δl = 5.7mm, 5.1mm and 4.5mm, for β equal to 3°, 6° and 9°, respectively).

The influence of the dimension β on the numerical results of the cruciform test can be summarised:

(i) The Δl value corresponding to the maximum load value decreases with the increase of β (Figure A.8 (a)). Also, the maximum load value increases with the increasing of β.

(ii) The maximum equivalent strain value, at the arms of the sample, decrease with the increase of β (Figure A.8 (b) and Figure A.9). The equivalent strain values in the central region of the cruciform sample increase with the increase of β. The equivalent strain value at the end of the arms approaches to zero with the increase of β.

(iii) The equivalent strain values near the fillet of the sample increase with the increasing of β (Figure A.8 (c) and Figure A.9); nevertheless, this does not causes a drastic reduction of the Δl value at the maximum load, even for the β angle equal to 9° (Figure A.8 (a)).

(iv) The range of strain paths allowed by each geometry is quite similar (Figure A.8) (d)). In all cases, $\varepsilon_2 / \varepsilon_1$ ranges from 1, at the centre of the cruciform sample, to -0.49, at the arms region.

Based on the results in Figure A.8 and Figure A.9, a β value equal to 9° was selected for the cruciform geometry. This angle allows a higher value of equivalent plastic strain in the centre of the sample than the remaining geometries with lower values of β. It is also advantageous for the numerical modelling of the boundary conditions, since the equivalent plastic strain values at the extremities of the sample are closer to zero. The β angles equal to 6° and 9° have the drawback that relatively high values of deformation occur near the fillet region, which can be mitigated performing the analysis for slightly smaller displacement values. Nevertheless, β angles of 3 and 6° could also have been selected.

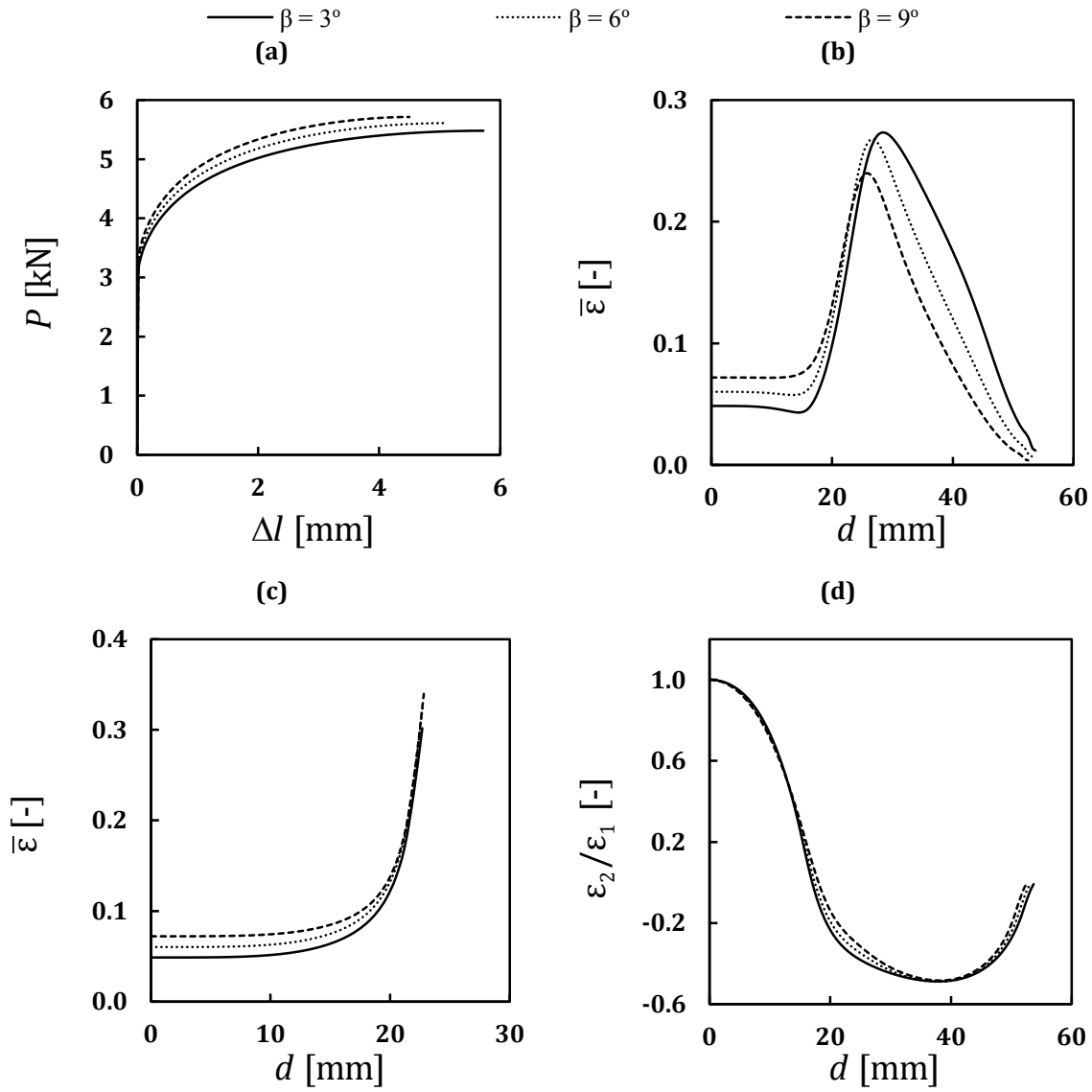

Figure A.8. Numerical simulation results for the β values, β = 3°, β = 6° and β = 9°: (a) P *vs.* Δl ; (b) and (c) $\bar{\varepsilon}$ *vs.* d , along the 0x (or 0y) axis and along the axis at 45° with the rolling direction, respectively, and (d) $\varepsilon_2 / \varepsilon_1$ *vs.* d , along the 0x (or 0y) axis.

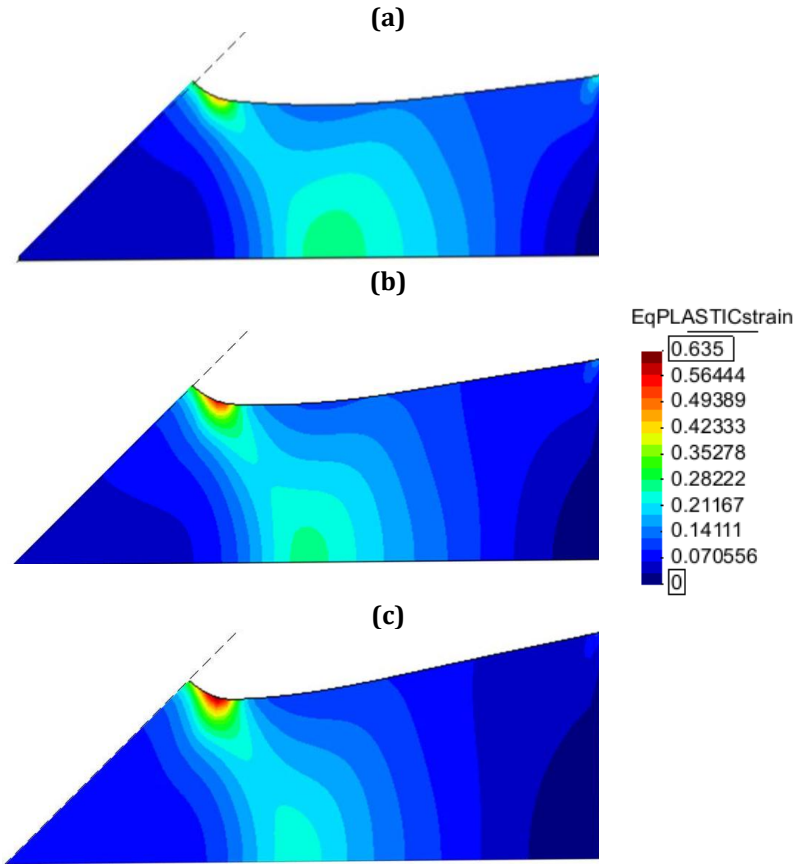

Figure A.9. Equivalent plastic strain fields measured on the surface of the cruciform sample, for β values: (a) 3°, (b) 6° and (c) 9°. The dashed lines indicate the material and geometric symmetry axes.

References

[1] Prates PA (2010) Metodologia de análise inversa para determinação simultânea dos parâmetros de leis constitutivas, com recurso a um provete cruciforme. MSc thesis, University of Coimbra.

[2] Chu TC, Ranson WF, Sutton MA, Peters WH (1985) Applications of digital-image-correlation techniques to experimental mechanics. Experimental Mechanics, 25, 232–244.

[3] Dinda S, Jarnes KF, Keeler SP, Stine PA (1981) How to Use Circle Grid Analysis for Die Tryout, ASM International, USA.

(Page intentionally left blank)